論文 / 著書情報
Article / Book Information

題目(和文)	巨視的非平衡系における普遍ゆらぎ：秩序化過程と界面成長に対する実験的検証
Title(English)	Universal fluctuations in macroscopic nonequilibrium systems: Experimental investigations on phase-ordering kinetics and interface growth
著者(和文)	Lisboa Almeida Renan Augusto
Author(English)	Lisboa Almeida Renan Augusto
出典(和文)	学位:博士(理学), 学位授与機関:東京工業大学, 報告番号:甲第11038号, 授与年月日:2019年3月26日, 学位の種別:課程博士, 審査員:大熊 哲,西森 秀稔,DAS BHANU PRATAP,藤澤 利正,平原 徹,竹内 一将
Citation(English)	Degree:Doctor (Science), Conferring organization: Tokyo Institute of Technology, Report number:甲第11038号, Conferred date:2019/3/26, Degree Type:Course doctor, Examiner:,,,,,
学位種別(和文)	博士論文
Type(English)	Doctoral Thesis

東京工業大学
Tokyo Institute of Technology

Doctorate Dissertation

Universal fluctuations in macroscopic nonequilibrium systems: Experimental investigations on phase-ordering kinetics and interface growth

Author:
Renan A. L. Almeida

Advisers:
Prof. Satoshi Okuma
Prof. Kazumasa A. Takeuchi

Submitted in partial fulfillment of the requirements
for the degree of PhD in Science

School of Science
Department of Physics

Tokyo, January 2019

Doctorate Dissertation

Universal fluctuations in macroscopic nonequilibrium systems: Experimental investigations on phase-ordering kinetics and interface growth

Author:

Renan A. L. Almeida

Committee attributed to the PhD qualification

Prof. Satoshi Okuma (Chair)

Prof. Bhanu Pratap Das

Prof. Toshimasa Fujisawa

Prof. Toru Hirahara

Prof. Hidetoshi Nishimori

Prof. Kazumasa A. Takeuchi

Tokyo, January 2019

Abstract

Fluctuations in nonequilibrium systems often display scaling invariance, which is theoretically expected to lead to universal properties. However, evidence for such universality remains scarce. Here, I experimentally investigate two types of nonequilibrium dynamics: the electrically-triggered ordering of two-dimensional twisted nematic liquid crystals (TNLC), and the (2+1)-dimensional growth of vacuum-deposited CdTe films. I show that universal fluctuations arise in both systems. TNLC ordering is accurately described by the model A class that, surprisingly, seems to coexist with critical percolation statistics. These findings suggest a generalisation of the fundamental scaling hypothesis for ordering dynamics. Regarding CdTe growth, by analysing height fluctuations at CdTe surfaces, I unveil a new transient scaling that may be generic in interface dynamics. Such a scaling precedes fluctuations in the Kardar-Parisi-Zhang class. This series of experiments provide compelling evidence for universal behaviours out-of-equilibrium. They also reveal non-trivial aspects of universality.

Acknowledgements

I express my gratitude to my parents, Geraldo and Adriana, for all we have been through hitherto. Who could have forecasted I would have the chance to study, and at such a level? Thanks to my father for being my example of simplicity and friendship. My gratitude to my wife, Míriam, for the patience, support and love during these years of scarce time for each other. I would not get here without you.

I am thankful to the supervisor of this Thesis, Prof. Kazumasa A. Takeuchi, for accepting me as his student. Prof. Takeuchi is an outstanding researcher, impeccable on his scientific demands and impressively dedicated to his work. I am grateful to Prof. Takeuchi, overall, for contributing with my opportunity to study abroad and to learn a bit about liquid crystals and statistical physics. Thanks for turning me into a much better researcher in all aspects. I am thankful to Prof. Satoshi Okuma as well, who promptly accepted me as his student after Prof. Takeuchi moved his laboratory to the University of Tokyo, where I spent my last six months in Japan.

Obrigado to the students belonging to the same research group for the kind way all of you received in the team. Let me cite, in particular, Dr Y. Fukai and Dr S. Zeraati since they considerably taught me how to build the thermal controller that I used in coarsening experiments; and in special Fukai who climbed mountain Fuji with me! I appreciate that Mr T. Iwatsuka provided me with excellent support to the Japanese language.

No one man is an island: nor in life, nor less in the academia. Therefore, it is a privilege to collaborate with Prof. Sukarno Ferreira – who was my host at the Universidade Federal de Viçosa where we cooperatively worked on the SiO_x project (not included in the thesis) – and with Prof. Tiago Oliveira, with whom I have been learning about universal aspects of surface growth since the undergraduate. Thanks for giving valuable comments on Chapter 4. I am in debt with Prof. Angélica da Mata that, patiently, understood my lack of time during the PhD which prevented me from completing our project on complex networks. Thanks for giving me the chance to give a talk at the Universidade Federal de Lavras. *Obrigado* to my colleagues Dr Ismael Carrasco, Dr Isnard Ferraz and Dr Frederico Vasconcellos that often contribute to parallel projects; and to, in addition to family members, continuously support me even from Brazil.

As a young scientist, I learned that is fundamental to listen to more experienced researches about our subject of interest. In this regard, I acknowledge the wisdom pieces of advice received from Prof. F. Aarão Reis, Prof. S. G. Alves (that taught me how to program in Fortran), Prof. J. J. Arenzon (that replied many of my long emails), Prof. C. Brito, Prof. L. F. Cugliandolo, Prof. S. C. Ferreira, Prof. S. O. Ferreira, Prof. T. Halpin-Healy, Prof. W. A. Moura-Melo, Prof. M. L. Munford, Prof. T. J. Oliveira, Prof. T. Ohta, Prof. O. Pierre-de-Louis, Prof. K. Takeuchi, and all those that, honestly, offered me a scientific advice along the PhD time.

Japan has a unique way to preserve its old culture amid a modern, capitalist-

demanded technology. It was a gift for me living here for two and a half years: my experience became cheerful because of the presence of Rodolpho Morine, David Anjos & his family (さゆりさん, 彩音, 夏姫, 唯華, and 一愛), Pe. Ambrosio L. da Silva, Pe. Léo, beyond Hygison Brandão, Maxim Ivanovich, Diego Rivota, in addition to all those from the Catholic community in Japan.

At this stage, I let here my deep thankfulness to the financial aid I received from the Japanese Society for the Promotion of Science. This aid contributed to my education, my development as a future scientist, and a few to the Japanese Science. I must apologise me with JSPS because I could not overcome some obstacles during the execution of the original project. Indeed, I consumed one and half year in this original project, despite it is not included in the Thesis. I am thankful for the housing support and the exemption of tuition fees conceived by the Tokyo Institute of Technology. Many thanks to Tokyo Tech., the Universidade Federal de Viçosa, and The University of Tokyo for letting me use their facilities along with the completion of the Thesis. Thanks for the committee of Professors that accepted to evaluate this dissertation.

Vanitas vanitatum et omnia vanitas.

CONTENTS

List of Figures

List of Tables

1

INTRODUCTION

We live in a nonequilibrium world. Matter continually exchanges energy, heat and particles with the environment in unbalanced rates. At a microscopic level of description, configurations for the building blocks – atoms, molecules, cells, *etc.* – from which the system is made evolve irreversibly, technically referred to as the breaking of detailed balance. In practice, such microscopic irreversibility renders the temporal changing of macroscopic observables, such as size, shape, phase, responses to external fields of the respective systems. This changing can occur in a wide range of time and length scales: as slow as, and as large as the cooling and the expansion of the universe from one hand, or as fast and small as collision processes of heavy ions producing quark-gluon plasmas, on the other. Without being extreme, nature decorates daily experience with the convective and the turbulent motion of fluids, with the roughening of the shapes of mountains, coastlines and other natural landscapes, or yet, in the biology realm, with the coordinated and hierarchical flights of bird flocks and school of fishes, just to name but a few. All these are examples of collective phenomena arising in *macroscopic* systems, where the typical length scale of their building blocks, $a_{\rm micro}$, is much smaller than the system size, $L_{\rm sys}$, so that $a_{\rm micro}/L_{\rm sys} \to 0$.

For nonequilibrium systems, however, there is no a counterpart of the celebrated Boltzmann-Gibbs (BG) ensemble [1–3], which would tell us about the probability of finding the macroscopic system at a given microscopic configuration at certain time t. Efforts have been proposed toward generalisations of BG statistics on the price of nonadditive entropies [4, 5], seemingly corroborated by some experimental data, but not yet comprehended from *principia*. Being more limited, as a matter of fact, for certain classes of nonequilibrium dynamics there are useful phenomenological approaches based on the concepts of *scale-invariance* and *universality*. Both concepts are inherited from the theory of critical phenomena [6, 7]

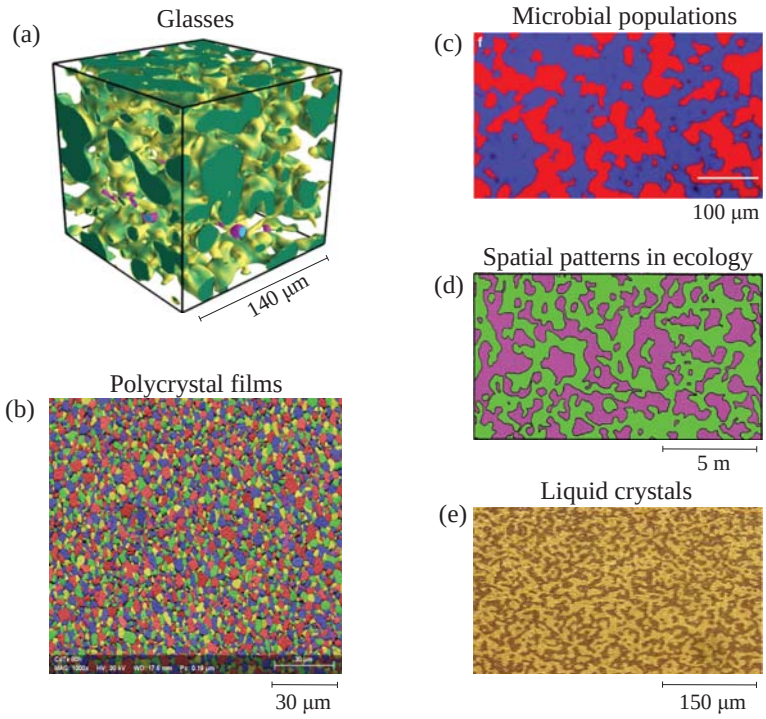

Figure 1.1: Examples of experimental systems with slow relaxation undergoing domain coarsening (or phase-ordering kinetics). (a) Reconstructed 3D image of X-ray tomography of barium-rich regions of a barium borosilicate glass that undergoes phase separation at $T = 1130\,^{\circ}\mathrm{C}$ [26]. (b) Reconstructed electron backscattering diffraction images of CdTe crystals in a 3.2 μm thick layer vacuum-deposited on Si(001) and then annealed in high vacuum at $T = 300\,^{\circ}\mathrm{C}$ during 80 hrs. Each colour represents a certain crystallographic orientation of grains. Courtesy of Prof. F. Vasconcellos and Prof. S. O. Ferreira from the Universidade Federal de Viçosa, Brazil. (c) Segregation of initially two well-mixed *Vibrio cholerae* strains with mutual T6SS-mediated killing [27]. (d) Incidence of *Calluna vulgaris* (pink) over a 10 m $\times$ 20 m planar region in the coniferous stand at Jädraås, Sweden [28]. (e) Electro-driven chiral deracemization of a quasi-bidimensional (5 μm $\times$ 1 cm^2) layer of bent-core liquid crystals after a quench from the isotropic liquid phase to the liquid-crystalline phase [29]. Different colours stand for regions with opposite chiralities [29]. Figures (a) and (e) are reprinted with the permission of American Physical Society, while (c) is reprinted with the permission of Springer Nature; (d) is a coloured version of Figure in [28].

for systems at equilibrium. In this theory – well successful thanks to the contributions of renormalisation group [8, 9] and of conformal invariance for the case of bidimensional systems [7, 10] – universality means that macroscopic properties of systems sharing global symmetries, dimensionality, and the number of components of a coarse-grained order parameter, $\tilde{\boldsymbol{\phi}}(\boldsymbol{r}, \boldsymbol{X})$, are described by the same scaling laws regardless of the nature of their building blocks and local interactions among them. Here, $\tilde{\boldsymbol{\phi}}$ is a n-vectorial ($n = 1, 2, ...$) quantity, $\boldsymbol{r}$ indicates the position of a (coarse-grained) degree of freedom embedded in a d-dimensional space and

$\boldsymbol{X}$ a vector in the Γ-dimensional phase space built from intensive thermodynamical variables (pressure, temperature, chemical potential *etc.*) related to the system thermodynamical state. Universal behaviour emerges when configurations of $\tilde{\boldsymbol{\phi}}(\boldsymbol{r}, \boldsymbol{X}_c)$, at a rather special critical point $\boldsymbol{X}_c$, become *statistically* invariant under scaling transformations. This property stems from a diverging correlation length ($\xi(\boldsymbol{X}_c) \to \infty$). Around $\boldsymbol{X}_c$, $\xi(\boldsymbol{X} \approx \boldsymbol{X}_c)$ becomes the single relevant length scale, such that, for $a_{\text{micro}} \ll |\boldsymbol{r}| \ll \xi$ microscopic details do not determine the macroscopic dynamics. That is the very reason why magnets at the Curie point and fluids at the terminal point along the liquid-vapour coexistence line share the same scaling laws with the idealised Ising model; they are said to belong to the same *universality class* [6, 7].

While scaling invariance arises only for exceptional conditions $\boldsymbol{X} = \boldsymbol{X}_c$ at equilibrium, there is ample theoretical evidence that nonequilibrium macroscopic phenomena may display scale-invariant fluctuations in much broader conditions [11–15]. These include cases where the invariance is *spontaneously* realised with no need to adjust external parameters [12, 13, 16]. Notice that $\tilde{\boldsymbol{\phi}}(\boldsymbol{r}, t)$ is now a time-dependent quantity. Pieces of evidence have been acquired most from the outcomes of continuum and simple discrete models conceived on the idealisation of universality. On a continuum, these models are Langevin-like equations:

$$\frac{\partial \tilde{\boldsymbol{\phi}}(\boldsymbol{r}, t)}{\partial t} \simeq \mathscr{Q}[\tilde{\boldsymbol{\phi}}] + \mathscr{W}[\tilde{\boldsymbol{\phi}}]\eta(\boldsymbol{r}, t), \tag{1.1}$$

where $\mathscr{Q}[\cdot]$ and $\mathscr{W}[\cdot]$ are functional forms that account for by effective interactions between the building blocks and $\eta(\cdot)$ is an effective noise stemming from fast, microscopic modes. The type of noise depends on the system under consideration and may stem from different contributions such as thermal effects, space-time inhomogeneities in the system or in the driving force itself. This phenomenology has provided a simplified description of the asymptotic dynamics occurring in some instances of macroscopic, nonequilibrium phenomena as below described.

I - Systems relaxing toward equilibrium. Consider a macroscopic system at equilibrium configuration $\tilde{\boldsymbol{\phi}}(\boldsymbol{r}, \boldsymbol{X})$. By suddenly changing external control parameters, *e.g.* performing a *quench*, via $\boldsymbol{X} \to \boldsymbol{X}'$, the system falls out of equilibrium and starts relaxing towards the new equilibrium configuration $\tilde{\boldsymbol{\phi}}(\boldsymbol{r}, \boldsymbol{X}')$. The relaxation can be either exponentially fast or *slow* [17] in the sense that the time required to achieve $\tilde{\boldsymbol{\phi}}(\boldsymbol{r}, \boldsymbol{X}')$ diverges with L_{sys}. There is no guarantee, however, whether the system is trapped into metastable configurations during its evolution. Systems with slow relaxation typically evolve by the ordering of locally-equilibrated phases that grow (or coarsen) until, possibly, restoring the global equilibrium [12, 14, 17]. Examples abound in nature; traditional ones are systems quenched through a phase transition such as magnets quenched through the paramagnetic-ferromagnetic phases and glassy materials through the glass-liquid phases [Fig. 1.1(a)]. Further instances include cellular structures such as foams and polycrystalline films [Fig. 1.1(b)], spatial segregations in biological populations [Fig. 1.1(c)], spatial incidence of

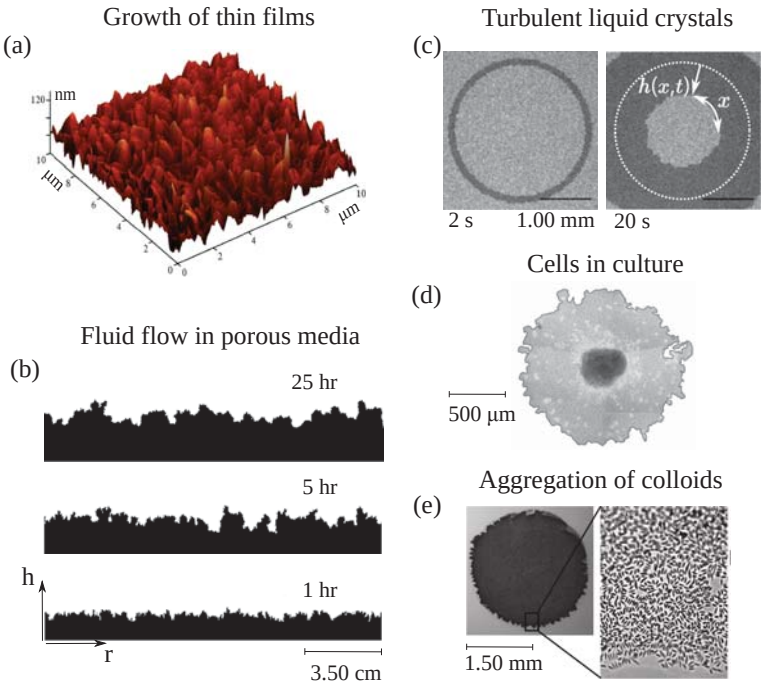

Figure 1.2: Examples of experimental growing interfaces. (a) Atomic force macroscopic image the rough surface of a polycrystalline CdTe film of thickness 3.2 μm vacuum-deposited on Si(001) substrates [43]. (b) Snapshots of ink imbibition (Pilot TC 42) in A4 sheets of newspaper as a function of time (from bottom to top). The ink layer (black) moves upward along the fibre directions of sheets producing a front shape that is dictated by the inhomogeneities of the medium [32]. (c) Left: Ring-shaped nucleation of dynamic scattering mode (DSM)2 phase (dark grey) over a DSM1 phase during the electro-driven turbulence of nematic liquid crystals. DSM1-DSM2 interfaces move towards DSM1 phase; meanwhile, DSM2 phase expands [31]. (d) Quasi-bidimensional colony of *Vero* cells cultured in Roswell Park Memorial Institute medium with 10% fetal serum maintained in 5% CO_2 atmosphere at $37\,^{\circ}\mathrm{C}$ [33]. A colloidal suspension of polystyrene ellipsoids after the liquid of the suspension was evaporated [34]. Polystyrene particles aggregate at the edge of evaporating drops and thus form aggregates with a rough front that advances from the edge to the centre of the drop. Figures (a-d) and Fig. (e) are reprinted with the permission of American Physical Society and Nature (Macmillan Publisher Limited), respectively.

vegetations in plant ecology [Fig. 1.1(d)], models for opinion formation [18] and so on. The common phenomenological understanding [12] for this myriad of phenomena is that, at asymptotic times $t \to \infty$, there is a single relevant length scale $l(t)$ – the typical domain size $l(t) \gg a_{\mathrm{micro}}$ – so that the statistics of $\tilde{\phi}(\boldsymbol{r}, t)$ become time-independent when $|\boldsymbol{r}| \mapsto |\boldsymbol{r}|/l(t)$. As for the case of critical phenomena, the statistics of these systems have been classified in terms of universality classes which encompass macroscopic behaviours sharing d, n, conservation laws and symmetries associated with $\tilde{\phi}$ evolution (this matter is addressed in detail in Chapter 2).

II - Driven systems. Gradients of temperature, pressure, chemical potential *etc.* can be applied (or stimulated) to a system. The presence of gradients promotes steady or time-dependent currents that prevent relaxation towards equilibrium. Examples of driven nonequilibrium phenomena are the Rayleigh-Bérnard convection in fluids [19], the electro-convection in liquid crystals [20], vibrated granular matter [21], catalytic reactions [22], the growth of interfaces [13] and so on. In the class of driven systems, we hereafter focus on surface (interface) growth phenomena. Surfaces are ubiquitous because matter has volume and surface. Surface physics is different from the bulk once building blocks at the surface have dangling bonds. This feature leads to surface reconstructions in crystalline facets, oxidation, conductive bands not present in bulk (such as in topological insulators), and roughening, to name but a few phenomena. When an interface is driven to grow because of an external source of particles, or by contact with an unstable phase, for instance, it generically develops a *rough* front. Figure 1.2 shows growing surfaces ranging from the deposition of thin films [Fig. 1.2(a)], fluid flow in porous media [Fig. 1.2(b)], invasion of turbulent phases in liquid crystals [Fig. 1.2(c)], culture of cells [Fig. 1.2(d)], to the aggregation of colloidal particles at the edge of evaporating drops [Fig. 1.2(e)]. The dynamics of such interfaces, which can be flat or curved, are in a first approximation modelled by Langevin-like equations [Eq. (1.1)] with $\tilde{\phi}(\boldsymbol{r},t) \mapsto h(\boldsymbol{r},t)$, where $h(\boldsymbol{r},t)$ is a scalar height field measured from flat (see Fig. 1.2(b)) or curved (see Fig. 1.2(c)) d_s-dimensional substrates. Overwhelming theoretical [13,23,24] and experimental [13,25] evidence shows that at asymptotic times, the statistics of the surface roughness $w(t) := [\langle h^2(\boldsymbol{r},t)\rangle_c]^{1/2}$ obey certain scaling laws, as we shall see in Chapter 4. This has lead to the proposition of classifying interface growth phenomena into dynamical classes of universality as well.

III - Nonequilibrium in the bulk. A flock of birds or a bunch of motile bacteria may form macroscopic systems where building blocks are, themselves, thermal machines constantly consuming (dissipating) energy from (to) the environment in individualised ways. The field of active matter has received a lot of attention particularly in the last two decades, *e.g.* [35–37]. One of the aims has been investigating whether model and experimental systems may also share universal macroscopic aspects as seemingly observed for the family of nonequilibrium processes I and II. Models have signalised the possible presence of spontaneous scale invariance [15, 37].

Despite the tantalising evidence for scale invariance in nonequilibrium macroscopic phenomena, largely upheld by models and experiments, observation of universal behaviour in real systems remains rather scarce (see a few precious examples in *e.g.* [38–45]). Even in realistic cases, there are many aspects of the associated universality class that remains to be substantiated yet. Indeed, we may say that the concept of universality, being one step epistemologically further from that of

scale invariance, very often seems to be hindered – or even destroyed – by system-dependent complexities not accounted for by idealised phenomenologies. These states of affairs have made experimental studies on universality issues a rather non-trivial task.

Strategies and aims of the Thesis

In this Thesis, we experimentally investigate the emergence of universal behaviours in macroscopic, nonequilibrium dynamics of type I and of type II. Toward this end, we need to choose a good experimental setup. Firstly, systems must comprise a large number of degrees of freedom so that $a_{\text{micro}}/L_{\text{sys}} \to 0$. They also must be of practical and safe handling, suitable for laboratory exploration, and shall have length and time scales that fit the demand for repetitive runs of experimental realisations. With the compromise to choose a natural system on the one hand, not only conceived for supplying a theoretical call, we also need an experimental system that fits the dimensionality, range interactions and other assumptions of the corresponding phenomenological theories on the other hand. Below we justify the experimental systems studied along this Thesis. The justifications are followed be the aims of each work.

Liquid crystals - We address Type I dynamics by using two-dimensional twisted nematic liquid crystals (TNLC) as an experimental system. We choose liquid crystals because they fulfil the requirements mentioned above. Furthermore, we noticed that they were studied in the context of phase-ordering kinetics in the past [38, 46, 47], where evidence of the so-called model A universality class (see Sec. 2.1 in Chapter 2) was given. In these studies, the authors analysed the (slow) relaxation dynamics that take place when TNLC is quenched between the high-temperature liquid phase and the low-temperature nematic liquid crystalline phase. The quench is induced by a gradient of temperature that, very different from phenomenological assumptions, takes several tens of seconds [38, 46, 47]. This time was enough to affect either partially [46] or even integrally [38] the sequential relaxation, and thus hampered good measurements of (expected) universal quantities [38]. To study phase-ordering kinetics using TNLC systems, but avoiding the drawbacks of previous studies, we designed a novel experimental setup involving an electrically-driven quench (that takes only ~ 10 ms) to achieve the following goals:

- (Aim 1) - Test theoretical predictions about universal behaviour in phase-ordering kinetics. As a first step, we explore experimental dynamics associated with the celebrated model A class to access universal aspects that remain to be substantiated for this case.

- (Aim 2) - Explore our (successful, as we shall see) model A experimental setup to investigate the surprising numerical-based observation [48, 49] on

the coexistence between model A universality class and critical percolation class (see Sec. 3.1 in Chapter 3) in phase-ordering dynamics.

Polycrystalline films - For dynamics type II, we focus on surface growth phenomena. We choose to study surface fluctuations of polycrystalline CdTe films because, despite their high complexity, they may exhibit universal fluctuations for certain growth conditions as shown previously by the Author and collaborators [43,50]. Specifically, by growing CdTe films on Si(001) substrates via hot wall technique, the authors showed that fluctuations at CdTe surface display a crossover from the universal Random-Deposition (RD) dynamics to the universal Kardar-Parisi-Zhang (KPZ) dynamics (described in Sec. 4.1 of Chapter 4). The RD-KPZ crossover time depends on thermally-activated mechanisms (diffusion, desorption, *etc.*) of mass redistribution along the surface. The higher the substrate temperature T, the shorter is the crossover time. At low deposition temperature, namely $T = 150\,^{\circ}\mathrm{C}$, these mechanisms are not operative enough to overcome energy barriers between crystalline domains. Thereby, crystals grow uncorrelated from each other and only the universal RD scaling arises. Once experimental evidence for universal fluctuations is very rare, we take advantage of the CdTe system to explore it in further directions. From the perspective of thin film science [51], the substrate face has a large impact on the formation of crystals and on the subsequent growth dynamics. Such substrate effects are not accounted for by phenomenological growth theories. That is said, our next aims of the Thesis are the following:

- (Aim 3) - Inquire about the effect of an amorphous (polymeric) substrate on the growth dynamics of CdTe films fabricated according to Almeida *et al.* protocol [43] in the low temperature deposition $T = 150\,^{\circ}\mathrm{C}$ regime.

- (Aim 4) - Explore our new observed time crossover (as we shall see), called Pseudo-Steady State (PSS) to KPZ dynamics, to test universal aspects of interface growth and KPZ statistics which shall be either firstly tested or better evaluated.

Scope of the Thesis

The Thesis is organised as follows. Chapters are written in a self-contained manner. At the beginning of Chapters 2, 3 and Chapter 4, there are elementary introductions to the respective subjects of research they encompass, namely, coarsening dynamics, percolation theory, and interface growth, respectively. These introductions are focused on the aspects required to comprehend the meaning and significance of the Author's research. Following the introductory text, one describes the material and experimental methods employed for performing each research.

Each Chapter has its notation and bibliography. A list of acronyms and symbols is regarded as an additional Section inserted before the list of references for

each Chapter. Chapter 5 contains the main conclusions and perspectives about the researches.

BIBLIOGRAPHY

[1] Boltzmann, L.: Weitere Studien ùber das Wârmegleichgewicht unter Gas molekùlen. Wien, Ber. **66**, 275 (1872).
Cited on page 1.

[2] Boltzmann, L.: Uber die Beziehung eines allgemeine mechanischen Satzes zum zweiten Haupsatze der Warmetheorie, Sitzungsberichte, K. Akademie der Wissenschaften in Wien, Math.-Naturwissenschaften **75**, 67 (1877).
Cited on page 1.

[3] Gibbs, J. W.: Elementary Principles in Statistical Mechanics. Charles Scribner's Sons, New York (1902).
Cited on page 1.

[4] Tsallis, C.: Possible generalization of Boltzmann-Gibbs statistics. J. Stat. Phys. **52**, 479 (1988).
Cited on page 1.

[5] Tsallis, C.: Introduction to nonextensive statistical mechanics: approaching a complex world. Springer Science & Business Media (2009).
Cited on page 1.

[6] Binney, J. J., Dowrick, N. J., Fisher, A. J., Newman, M.: The theory of critical phenomena: an introduction to the renormalization group. Oxford University Press, Inc. (1992).
Cited on pages 1 and 3.

[7] Nishimori, H., Ortiz, G. Elements of phase transitions and critical phenomena. Oxford University Press, Inc. (2010).
Cited on pages 1, 2, and 3.

[8] Wilson, K. G.: Renormalization group and critical phenomena. I. Renormalization group and the Kadanoff scaling picture. Phys. Rev. B **4**, 3174 (1971).
Cited on page 2.

[9] Wilson, K. G.: Renormalization group and critical phenomena. II. Phase-space cell analysis of critical behavior, Phys. Rev B **4**, 3184 (1971).
Cited on page 2.

[10] Belavin, A. A., Polyakov, A. M., Zamolodchikov, A. B.: Infinite conformal symmetry in two-dimensional quantum field theory. Nuclear Phys. B **241**, 333 (1984).
Cited on page 2.

[11] Hinrichsen, Haye.: Non-equilibrium critical phenomena and phase transitions into absorbing states. Adv. Phys. **49**, 815-958 (2000).
Cited on page 3.

[12] Bray, A. J.: Theory of phase-ordering kinetics. Adv. Phys. **51**, 481-587 (2002).
Cited on pages 3 and 4.

[13] Barabási, A.-L., Stanley, H. E.: Fractal Concepts In Surface Growth. Cambridge university press (1995).
Cited on pages 3 and 5.

[14] Henkel, M., Pleimling, M.: Non-Equilibrium Phase Transitions Volume 2: Ageing and Dynamical Scaling Far from Equilibrium. Springer Science & Business Media (2010).
Cited on page 3.

[15] Marchetti, M. C., Joanny, J. F., Ramaswamy, S., Liverpool, T. B., Prost, J., Rao, M., Simha, R. A.: Hydrodynamics of soft active matter. Rev. Mod. Phys. **85**, 1143 (2013).
Cited on pages 3 and 5.

[16] Bak, P., Tang, C., Wiesenfeld, K.: Self-organized criticality: An explanation of the 1/f noise. Phys. Rev. Lett. **59**, 381 (1987).
Cited on page 3.

[17] Cugliandolo, L. F.: Course 7: Dynamics of Glassy Systems. In: Barrat J. L., Feigelman M., Kurchan J., Dalibard J. (eds) Slow Relaxations and nonequilibrium dynamics in condensed matter. Les Houches-École d'ÉÉté de Physique Theorique, vol 77. Springer, Berlin, Heidelberg (2014).
Cited on page 3.

[18] Dornic, I., Chaté, H., Chave, Chave, J., Hinrichsen, H.: Critical coarsening without surface tension: the universality class of the Voter model. Phys. Rev. Lett. **87**, 045701 (2001).
Cited on page 4.

[19] Cross, M. C., Hohenberg, P. C.: Pattern formation outside of equilibrium. Rev. Mod. Phys. **65**, 851 (1993).
Cited on page 5.

[20] Kai, S., Zimmermann, W.: Pattern dynamics in the electrohydrodynamics of nematic liquid crystals. Prog. Theor. Phys. Supp. **99**, 458 (1989).
Cited on page 5.

[21] Kudrolli, A.: Size separation in vibrated granular matter. Rep. Prog. Phys. **67**, 209 (2004).
Cited on page 5.

[22] Winston, D., Arora, M., Maselko, J., Gáspár, V., Showalter, K.: Cross-membrane coupling of chemical spatiotemporal patterns. Nature, **351**, 132 (1991).
Cited on page 5.

[23] Halpin-Healy, T., Zhang, Y.-C.: Kinetic roughening phenomena, stochastic growth, directed polymers and all that. Phys. Rep. **254**, 215-414 (1995).
Cited on page 5.

[24] Krug, J.: Origins of scale invariance in growth processes. Adv. Phys. **46**, 139-282 (1997).
Cited on page 5.

[25] Krim, J., Palasantzas, G.: Experimental observations of self-affine scaling and kinetic roughening at sub-micron lengthscales. Int. J. Mod. Phys. B **9**, 599-632 (1995).
Cited on page 5.

[26] Bouttes, D., Guillart, E., Boller, E., Dalmas, D., Vandembroucq, D.: Fragmentation and limits to dynamical scaling in viscous coarsening: An interrupted *in situ* X-Ray tomographic study. Phys. Rev. Lett. **112**, 245701 (2014).
Cited on page 2.

[27] McNally, L., Bernardy, E., Thomas, J., Kalziqi, A., Pentz, J., Brown, S. P., Hammer, B. K., Yunker, P. J., Ratcliff, W. C.: Killing by Type VI secretion drives genetic phase separation and correlates with increased cooperation. Nat. Commun. **8**, 14371 (2017).
Cited on page 2.

[28] Diggle, P. J.: Binary mosaics and the spatial pattern of Heather. Biometric **37**, 531 (1981).
Cited on page 2.

[29] Sicilia, A., Arenzon, J. J., Dierking, I., Bray, A. J., Cugliandolo, L. F., Martínez-Perdiguero, J., Alonso, I., Pintre, C.: Experimental test of curvature-driven dynamics in the phase ordering of a two dimensional liquid crystal. Phys. Rev. Lett. **101**, 197801 (2008).
Cited on page 2.

[30] Almeida, R. A. L., Ferreira, S. O., Oliveira, T. J., Aarão Reis, F. D. A.: Universal fluctuations in the growth of semiconductor thin films. Phys. Rev. B **89**, 045309 (2014).
Cited on pages 4, 5, and 7.

[31] Fukai, Y. T., Takeuchi, K. A.: Kardar-Parisi-Zhang interfaces with inward growth. Phys. Rev. Lett. **119**, 030602 (2017).
Cited on page 4.

[32] Miranda, A. M., Menezes-Sobrinho, I. L., Couto, M. S.: Spontaneous imbibition experiment in newspaper sheets. Phys. Rev. Lett. **104**, 086101 (2010).
Cited on page 4.

[33] Huergo, M. A. C., Pasquale, M. A., González, P. H., Bolzán, A. E., Arvia, A. J.: Phys. Rev. E **84**, 021917 (2011).
Cited on page 4.

[34] Yunker, P. J., Still, T., Lohr, M. A., Yodh, A. G.: Suppression of the coffee-ring effect by shape-dependent capillary interactions. Nature Letter **476**, 308 (2011).
Cited on page 4.

[35] Vicsek, T., Czirók, A., Ben-Jacob, E., Cohen, I., Shochet, O.: Novel type of phase transition in a system of self-driven particles. Phys. Rev. Lett. **75**, 1226 (1995).
Cited on page 5.

[36] Chaté, H., Ginelli, F., Grégoire, G., Peruani, F., Raynaud, F.: Modeling collective motion: variations on the Vicsek model. Euro. Phys. J. B **64**, 451 (2008).
Cited on page 5.

[37] Ramaswamy, S.: The mechanics and statistics of active matter. Annu. Rev. Condens. Matter Phys., **1**, 323-345 (2010).
Cited on page 5.

[38] Orihara, H., Ishibashi, Y.: Dynamics of disclinations in twisted nematics quenched below the clearing point. J. Phys. Soc. Jpn. **55**, 2151-2156 (1986).
Cited on pages 5 and 6.

[39] Bramwell, S. T., Holdsworth, P. C. W., Pinton, J. F.: Universality of rare fluctuations in turbulence and critical phenomena. Nature **396**, 552 (1998).
Cited on page 5.

[40] Takeuchi, K. A., Kuroda, M., Chaté, H., Sano, M.: Directed percolation criticality in turbulent liquid crystals. Phys. Rev. Lett. **99**, 234503 (2007).
Cited on page 5.

[41] Takeuchi, K. A., Sano, M.: Universal fluctuations of growing interfaces: evidence in turbulent liquid crystals. Phys. Rev. Lett. **104**, 230601 (2010).
Cited on page 5.

[42] Bricard, A., Caussin, J. B., Desreumaux, N., Dauchot, O., Bartolo, D.: Emergence of macroscopic directed motion in populations of motile colloids. Nature **503**, 95 (2013).
Cited on page 5.

[43] Almeida, R. A. L., Ferreira, S. O., Oliveira, T. J., Aarão Reis, F. D. A.: Universal fluctuations in the growth of semiconductor thin films. Phys. Rev. B **89**, 045309 (2014).
Cited on pages 4, 5, and 7.

[44] Sano, M., Tamai, K.: A universal transition to turbulence in channel flow. Nature Phys. **12**, 249 (2016).
Cited on page 5.

[45] Lemoult, G., Shi, L., Avila, K., Jalikop, S. V., Avila, M., Hof, B.: Directed percolation phase transition to sustained turbulence in Couette flow. Nature Phys. **12**, 254 (2016).
Cited on page 5.

[46] Mason, N., Pargellis, A. N., Yurke, B.: Scaling behaviour of two-time correlations in a twisted nematic liquid crystal. Phys. Rev. Lett. **70**, 190-193 (1993).
Cited on page 6.

[47] Yurke, B., Pargellis, A. N., Majumdar, S. N., Sire, C.: Experimental measurement of the persistence exponent of the planar Ising model. Phys. Rev. E **56**, R40-R42 (1997).
Cited on page 6.

[48] Arenzon, J. J., Bray, A. J., Cugliandolo, L. F., Sicilia, A.: Exact results for curvature-driven coarsening in two dimensions. Phys. Rev. Lett. **98**, 145701 (2007).
Cited on page 6.

[49] Cugliandolo, L.: Geometric aspects of ordering phenomena. C. R. Physique **18**, 5-18 (2017).
Cited on page 6.

[50] Almeida, R. A. L., Ferreira, S. O., Ribeiro, I. R. B., Oliveira, T. J.: Temperature effect on (2+1)-experimental Kardar-Parisi-Zhang growth. Europhys. Lett. **109**, 46003 (2015).
Cited on page 7.

[51] Ohring, M.: Material Science of Thin Films – Deposition and Structure, 2nd. ed., Academic Press, Waltham (2001).
Cited on page 7.

2

ELECTRICALLY-TRIGGERED COARSENING IN TWISTED NEMATIC LIQUID CRYSTALS

In this Chapter, we investigate universal behaviours arising in the electrically-triggered coarsening dynamics of bidimensional twisted nematic liquid crystals (TNLC). First, an elementary introduction on the phenomenology of phase-ordering kinetics is given in Sec. 2.1. Nematic liquid crystals and their electro-convective regimes, which we explore in this research, are introduced in Sec. 2.2.1. In the Sec. 2.2.3, we describe our experimental setup, including the protocol behind the electrically-triggered coarsening. After that, we analyse the TNLC experimental system in detail: from the decay rate of defects in Sec. 2.3 to the asymmetrical roles played by twist states in Sec. 2.4. Then, we focus on two-point, spatial and temporal statistics [Sec. 2.5 and Sec. 2.6], respectively. Universal aspects of local persistence statistics enclose our exploration [Sec. 2.7]. Throughout the analysis, we make critical comparisons with model A universal statistics; some universal aspects of model A class are firstly probed here, while we also revisit standard ones. In Sec 2.8, we summarise the obtained results and highlight perspectives.

2.1 Elementary concepts on phase-ordering kinetics

2.1.1 Phenomenological equations and microscopic approach

Let $\tilde{\phi}(\boldsymbol{r}, t)$ be a coarse-grained, scalar order parameter field of a d-dimensional macroscopic system. For uniform systems, ruled by local microscopic interactions, we can ascribe a Landau-Ginzburg free energy $F[\tilde{\phi}]$ [1]:

$$F[\tilde{\phi}] = \int d^d r \left[\frac{a_1 |\nabla \tilde{\phi}|^2}{2} + V'(\tilde{\phi}) \right], \tag{2.1}$$

where $V'(\tilde{\phi})$ is a general potential. Higher-order terms and coupling with external fields can be additionated to the integrand of Eq. (2.1) depending on the system and the situation being dealt with. In anycase, $F[\tilde{\phi}]$ can account for phase transitions of macroscopic systems at thermal equilibrium [1]. For continuous phase transitions for example, the potential takes the form,

$$V'(\tilde{\phi}) = a_2(\boldsymbol{X})\tilde{\phi}^2 + \frac{a_3}{2}\tilde{\phi}^4, \tag{2.2}$$

where a_i ($i = 1, 2, 3$) are *phenomenological* quantities, nonuniversal functions of microscopic interactions. $\boldsymbol{X}$ is a vector in the phase space built from intensive thermodynamical variables such as pressure and temperature. The phase transition is modelled by the phenomenology of $a_2(\boldsymbol{X})$. Above the critical point $\boldsymbol{X}_c$, $a_2 > 0$, and the potential is minimized at $\tilde{\phi} = 0$; below the critical point, $a_2 < 0$, and the potential minimum occurs for $\tilde{\phi} = \pm\tilde{\phi}_{\text{eq}}$, where $\tilde{\phi}_{\text{eq}} = (|a_2(\boldsymbol{X})|/a_3)^{1/2}$; at $\boldsymbol{X}_c$, $a_2 = 0$. See how $V'(\tilde{\phi})$ schematically changes with a_2 as depicted in Fig. 2.1.

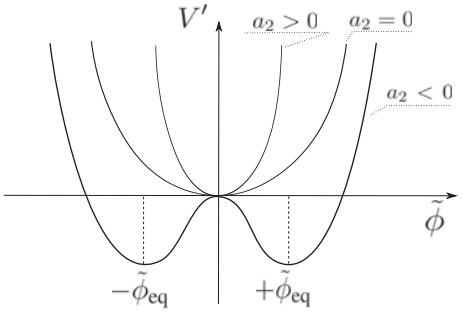

Figure 2.1: Schematics of the phenomenological potential used to model a second order phase transition in the Ginzburg-Landau approach.

We are interested in the nonequilibrium dynamics of systems relaxing between two equilibrium configurations. The evolution rules imposed to $\tilde{\phi}$ are constrained to the conservation laws present in each dynamical system. For a binary fluid, for instance, molecules of type A and type B can exchange their spatial configurations in time, while *locally* preserving the number of molecules of type A and type B. This is in sharp contrast with, *e.g.*, a ferromagnet, where neighbouring spins can interact without conserving the total number of spins "up" and "down" (in the language of Ising idealisation). Over coarse-grained scales, $\tilde{\phi}$ is then a conserved and a nonconserved quantity for dynamics compatible with the first and second examples cited above, respectively. An appropriate equation for the time evolution of *nonconserved* dynamics is the model A equation in the notation of Hohenberg and Halperin [2]:

$$\frac{\partial\tilde{\phi}(\boldsymbol{r},t)}{\partial t} = -\frac{\delta F[\tilde{\phi}]}{\delta\tilde{\phi}} + \zeta(\boldsymbol{r},t), \tag{2.3}$$

in which the system evolves by passing through configurations that progressively minimize F. For conserved dynamics, instead, the appropriate form is the so-called model B equation which is obtained after replacing $\delta F[\tilde{\phi}]/\delta\tilde{\phi}$ in Eq. (2.3) by $\nabla^2\delta F[\tilde{\phi}]/\delta\tilde{\phi}$ [2]. The stochastic (thermal) noise ζ is assumed as a Gaussian field, uncorrelated in space and time:

$$[\zeta(\boldsymbol{r},t)]_\zeta = 0; \quad [\zeta(\boldsymbol{r},t)\zeta(\boldsymbol{r}',t')]_\zeta = 2k_BT\delta^d(\boldsymbol{r}-\boldsymbol{r}')\delta(t-t'). \tag{2.4}$$

where $[...]_\zeta$ stands for averaging over independent realisations of the noise; k_B is the Boltzmann constant and T the temperature. From now on we assume changes only along the T axis of the vector $\boldsymbol{X}$. At $T = 0$, model A and model B equations are referred to as the time-dependent Ginzburg-Landau (TDGL) equation and Cahn-Hilliard equation, respectively.

Letting $a_2 < 0$ in Eq. (2.2), we can implement an abrupt phase transition (perform a quench) between $T_i > T_c$ (T_c is a critical temperature) and $T_f = 0$ by evolving the macroscopic system with Eq. (2.3) from an initial configuration $\tilde{\phi}(\boldsymbol{r},0)$ at T_i. Since at $T_i > T_c$ correlations are short-ranged, then a suitable initial condition is:

$$\langle\tilde{\phi}(\boldsymbol{r},0)\rangle = 0; \quad \langle\tilde{\phi}(\boldsymbol{r},0)\tilde{\phi}(\boldsymbol{r}',0)\rangle = \delta(\boldsymbol{r}-\boldsymbol{r}'); \tag{2.5}$$

where $\langle...\rangle$ means average over the space and over the ensemble of quench realisations. Notice that Eq. (2.5) shall be strictly valid for $T_i \to \infty$. However, any finite correlation at $T_i > T_c$ can be renormalised by scale transformations while approaching to the delta-correlated regime at $T_i \to \infty$. In the language of renormalisation group (RG), the flow for $T_i > T_c$ flows to the fixed point $T_i \to \infty$. The same can be argued for the final quench temperature; for $T_f < T_c$, the RG flow goes to the fixed point $T_f = 0$. Temperature dependences shall enter only through phenomenological quantities (such as a_i), but not in universal aspects of the relaxation that we focus below [3].

The model A equation in $d = 2$ after a quench from $T_i > T_c$ to $T = 0$ generates patterns as those shown in Fig. 2.2. From the images, we can realise the formation of locally-equilibrated domains that grow (coarsen) over time and compete between them to equilibrate the system asymptotically. This process is often referred to as domain coarsening, as well as to phase-ordering kinetics. Similar mosaics of domains takes place for model B dynamics. The phenomenological approach adopted in this section can be generalised to deal with systems with n-vectorial and even tensorial order parameter fields [3].

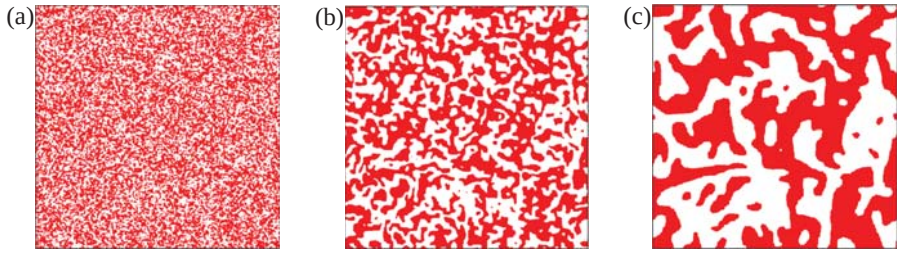

Figure 2.2: Typical patterns generated by models and real systems in the model A universality class. The mosaics were generated for the Ising model with nonconserved dynamics in a square lattice of 640 × 640 sites with periodic boundary conditions [4]. They refer to different simulation time steps (a) $t = 4$, (b) $t = 64$ and (c) $t = 512$ after the quench at $t = 0$ from $T \to \infty$ to $T = 0$. Figures reprinted with the permision of American Physical Society, extracted from Tartaglia *et al.* [4] with the permission of the authors.

Microscopic models

In addition to the phenomenological approach presented above, coarsening dynamics can also be investigated by stochastic microscopic models. These models are defined on a d-dimensional regular lattice comprising N degrees of freedom. The classic example is the Ising model placed into contact with a heat reservouir at temperature T. The Hamiltonian for the Ising model is $H(\{s_i\}) = -J\sum_{i,j} s_i s_j$ ($J > 0$), where the sum is performed over pairs of neighbouring spins, $i, j = 1, 2, ...N$, and $s_i = \pm 1$. A stochastic evolution for the configuration $\{s_i(t)\}$ can be imposed by stochastic rules for the spin flips $s_i(t) \to -s_i(t + \delta t)$ such that detailed balance is satisfied [5]; δt is a microscopic time step. For example, for each δt, one chooses a spin at i randomly and flip it with probability p, where p depends on $\Delta H \equiv H(\{s_i(t + \delta t)\}) - H(\{s_i(t)\})$. A suitable choice is $p = 1$ for $\Delta H \leq 0$ and $p = \exp(-\Delta H/k_B T)$, otherwise. The quench from the paramagnetic ($T > T_c$) to the ferromagnetic ($T < T_c$) phase can be, thereby, simulated by evolving $\{s_i(t)\}$ from an initial configuration where $\mathrm{sgn}\,[s_i(0)]$ is randomly distributed. The kinetic Ising model with *nonconserved* dynamics display domain coarsening [see Fig. 2.2]. In fact, the large-wavelength statistical properties of this model and model A equation are equivalent. They are said to belong to the model A universality class.

Further standard models used to study phase-ordering (not in model A class, however) are the kinetic Ising model with spin-exchange (or Kawasaki) dynamics [6], the Potts model [7] and the Voter model [8]; this last model is particularly fascinating because, despite being a pure kinetic model with no associated Hamiltonian, it contains a specially remarkable phase-ordering kinetics [9].

2.1.2 Dynamical scaling hypothesis

Many natural systems and artificial models evolve by developing ordered structures that grow amid a heterogeneous medium. Although coarsening theories have been traditionally developed in the language of continuous phase transitions, domain coarsening phenomena are not restricted to such a context. Segregation of bacterial populations, foams, polycrystalline films, spreading of vegetations in plant ecology, and first-order phase transitions, to name but a few, are all instances where coarsening behaviour arises (see Fig. 1.1 in Chapter 1 for an illustration).

The common assumption for this myriad of phenomena relies on the fundamental scaling hypothesis, which states the following [3]. In the asymptotic limit, $t \to \infty$ (for infinitely-large systems), there is a *single* emergent length scale $l(t)$ – the typical domain size – much larger than the typical defect width $\xi(T)$, such that the statistical properties of the order parameter field $\tilde{\phi}(\boldsymbol{r}, t)$ (or the microscopic configuration $\{s_i(t)\}$ for discrete models) for shall become time-independent at scales $r = |\boldsymbol{r}| \gg \xi(T)$, whenever $r \mapsto r/l(t)$.

The scaling hypothesis implies that, for instance, the two-point spatial correlator:

$$\tilde{C}_s(\boldsymbol{r}, t) := \langle \tilde{\phi}(\boldsymbol{r}', t)\tilde{\phi}(\boldsymbol{r} + \boldsymbol{r}', t)\rangle, \tag{2.6}$$

can be rewritten as:

$$\tilde{C}_s(\boldsymbol{r}, t) := \mathscr{F}(|\boldsymbol{r}|/l(t)), \tag{2.7}$$

with $\mathscr{F}(\cdot)$ a scaling function. For systems free from impurities and geometric frustration, domain size grows according to the *growth law*:

$$l(t) \sim t^{1/z} \tag{2.8}$$

where z is the dynamical exponent. Both z and $\mathscr{F}$ are *universal* quantities [3]. For d-dimensional systems, whose evolution rule is compatible with the symmetries and conservation laws of model A equation [Eq. 2.3], one predicts[1] $z = 2$ [10–12], while for model B dynamics $z = 3$ [12].

Simulations extensively support dynamical scaling, but its proof has been limited to a few simple models such as the one-dimensional Ising-Glauber chain [14, 15] and the d-dimensional nonconserved $O(n)$ model in the large n limit [16]. The exact functional form of $\mathscr{F}$ remains to be obtained yet. Approximate forms were proposed along an enormous deal of effort made around the 80's [17–19] and in the 90's [20–22], where two leading theories – the Ohta-Jasnow-Kawasaki (OJK) theory [18] and the theory of unstable growth (TUG) by Mazenko [19] – played

[1] Exceptions to the following law exists. They are the nonconserved one-dimensional XY model, that yields $z = 4$ [13], and the Voter model in $d = 2$, for which domains of all sizes appear (the largest size is delimited by the square root of the time in the Voter dynamics) [9].

the major roles. Nevertheless, experimental support for the OJK and TUG approximate forms, or for the universality of such a scaling function, has been surprisingly seldom reported. We will back to this subject in Sec. 2.5.

In general, microscopic systems, phenomenological equations and real experiments displaying coarsening dynamics can be grouped into dynamical universality classes. These classes are distinguished by the symmetries and conservation laws which are reflected in exponents and scaling functions such as z and $\mathscr{F}(\cdot)$. For convention, the classes are homonyms to the respective phenomenological equations they encompass. Therefore, for instance, the model A universality class embraces the family of models and real systems that share the universal statistics exhibited by the model A phenomenological equation.

2.1.3 Other universal quantities in the model A class & open questions

The value of $z = 2$ and the validity of scaling hypothesis are extensively corroborated by experiments using different materials, and in apparently different contexts – see Table 2.1. However, the universality of model A is not limited to z and $\mathscr{F}(\cdot)$, but involves additional exponents, correlation functions and amplitudes that *remain* to be experimentally substantiated. Although such quantities will be rigorously defined in the next sections, here we give an introduction to the matter in order to justify why they deserve experimental investigation. We highlight the open problems at the end of this section.

Universality in the time statistics

Beyond spatial statistics, *temporal* statitics of domain coarsening also display scale invariance with correlation functions of two- and infinitely-many points decaying algebraically in time [3, 30–32] (they are properly defined in see Sec. 2.6 and Sec. 2.7, respectively). As revealed by Fisher and Huse [33], the decay for the former functions involves an additional nonequilibrium exponent λ (Sec. 2.6, Eq. (2.32)), independent of z, which exhibits nontrivial dependence on the spatial dimensionality [33], on the number of order-parameter components n [34, 35] and on the presence of long-range order in the initial conditions [36, 37]. In the family of model A systems, exact results are available only for simple models, namely: the one-dimensional Ising-Glauber model [15], the one-dimensional TDGL equation [38], and the $O(n)$ model in the limit $n \to \infty$ [34, 35]. In $d = 2$, Fisher and Huse proposed a value $\lambda_{\text{FH}} = 5/4$ based on heuristic arguments and on a critical percolation result [33]. This conjecture has been supported by simulations of discrete [33, 36, 37] and continuous [39] models, as well as by an experiment involving the thermal-quench of twisted nematic liquid crystals [40]. However, the $\lambda_{\text{FH}} = 5/4$ value contrasts both with the prediction made from TUG ($\lambda_{\text{TUG}} \approx 1.29$) [41] – that is also upheld by finite-size scaling numerical results [42, 43] – and with the OJK outcome ($\lambda_{\text{OJK}} = 1$) [44] that has not been

Material	Dynamics	1/z	Ref.
Cu_3Au^a	1^{st} order	$0.50(3)$	[23]
Fe_3Al^a	2^{nd} order	≈ 0.5	[11, 24]
$Cu_{0.79}Pd^a_{0.21}$	Disorder-order	≈ 0.5	[25]
Nematic LC^b	1^{st} order	≈ 0.44	[26]
Cholesteric LC^b	1^{st} order	$0.5(1)$	[27]
Smectic LC^b	1^{st} order	$0.45(10)$	[28]
Bacteria^c (*Vibrio Cholerae*)	Phase separation	≈ 0.5	[29]

[a] Compounds are studied in the form of crystals. Experiments are performed inducing a phase transition between a disordered phase at high temperatures, where atoms randomly occupy the position of the unit crystalline cell, and an ordered, low temperature phase, where atoms respect stoichiometric configurations of the unity lattice.
[b] LC stands for liquid crystals. Experiments are performed inducing a phase transition between the isotropic (liquid) phase at high temperatures and a LC phase at low temperatures.
[c] Population of two antagonistic strains of bacterias evolve from a randomly mixed initial condition. Type VI secretion (T6SS) killing causes phase separation in the population.

Table 2.1: Some experimental systems reporting the dynamical exponent $1/z$ compatible with the model A universality class, for which $1/z = 0.5$.

empirically supported. In view of this scenario, a consensus on the universality of λ shall not be taken as settled yet.

Another challenging temporal aspect of coarsening is encoded in the fraction of degrees freedom that persistently maintain their state since a reference time [31, 32]. This fraction, also termed local persistence probability, is concerned with the full relaxation history and can be, therefore, faced as a correlation function of infinitely-many points. It generically exhibits algebraic decays dictated by an exponent θ (to be properly defined in Sec. 2.7, Eq. (2.37).) that turns out to be independent of z and of λ, but which is sensitive to the dimensionality of the system and to the conservation laws of the dynamics [32]. Some remarkable exact results are known in this case and include: the one-dimensional TDGL equation [45], the one-dimensional q-state Potts model [46, 47], the family of model systems with locally conserved dynamics (model B [2]) at $d \geq 2$ [48], and the two-dimensional diffusion equation [49]. The exponent θ has not been solved yet for two-dimensional model A systems. The most accurate estimation, obtained from lattice models, gives $\theta \approx 0.195$ [50], very close to the exact value derived for the

diffusion class, $\theta = 0.1875$ [49]. A previous experiment on thermal quench of liquid crystals measured $\theta = 0.19(3)$ [51], which is still not enough to distinguish between model A and diffusion classes. Another interesting aspect of persistence is that, along with the dynamics, remaining persistent degrees of freedom can be group into disconnected clusters featured by a rough contour and by a universasl fractal dimension d_f (Sec. 2.7) estimated in simulations of nonconserved Ising model as $d_f \approx 1.65$ [52]. Such dimensionality and related scaling functions, that we will introduce in Sec. 2.7, have not been experimentally measured (tested) for model A dynamics yet.

Universal functional forms

Beyond exponents z, λ, θ, and d_f, functional forms associated to these exponents are also universal. Although no functional form is analytically known in this case, there are approximated forms. Except by $\mathscr{F}(r/l^{1/z})$ – that is associated to z – similar universal functions related to λ, θ, and d_f have not been measured experimentally yet. Approximated functional forms theoretically proposed for describing the associated λ correlation function [Eq. 2.33, Eq. 2.34] has not been tested against experiments.

Summary of some open problems

In summary, this brief overview makes clear that many aspects of model A universality class, in $d = 2$, requires experimental investigation. We list some of them:

i) A lack of consensus on the value of λ calls for experimental tests;

ii) An experimental value for θ, accurate enough to allow a distinction from the value for the diffusion class, is in lack;

iii) The fractal exponent d_f of persistent clusters has not been measured;

iv) Rescaled scaling functions, related to λ, θ and d_f remain to be measured; theoretically proposed approximations for such correlation functions needs to be tested against experimental data.

In this Chapter, we discuss all of these aspects by employing an experimental setup that is suitable for studying phase-ordering dynamics. Since this Chapter is very extense, we introduce such quantities along with the comparison with the experimental results for the sake of better reading. In the next section, we present the materials and methods of our study.

2.2 Material and experimental methods

In Sec. 2.2.1 we introduce the nematic liquid crystalline phase and its property to, unlike fluids, store elasticity. Elasticity allows one to design specific configurations for the mesoscopic orientation of liquid crystals in a given confined geometry. By applying an electric field through a thin layer of certain nematic liquid crystals, the phenomenon of electro-convection arises. Several convective regimes exist depending on the amplitude of the electric field, but we focus on a specific nematic-turbulent regime in which topological defects fully fill the system. As contained in Sec 2.2.2, by suddenly turning off the voltage (performing a quench) from this turbulent phase, the system relaxes by the disentanglement and shrinking of defects in the meantime that locally-ordered domains grow, or coarsen. Although the coarsening of certain liquid crystals were studied in the past, several drawbacks of previous methodologies motivated us to employ a different, novel scheme for studying coarsening. In Sec. 2.2.3, we describe the methods used to carry out the research: the fabrication of our liquid crystal cell, the building of the experimental apparatus, and the experimental protocol to study the electrically-driven quench, which triggers an interesting coarsening dynamics.

2.2.1 Nematic liquid crystals and electro-convection

Nematic liquid crystals

Nematic liquid crystals consist of elongated, achiral organic molecules that, although randomly distributed in space, their spatial arrangement breaks the rotational symmetry of liquids [53] – see Fig. 2.3. This symmetry breaking manifests itself at larger scales as anisotropic responses (optical, electrical, *etc.*) in bulk. These responses can be decomposed into normal ($\perp$) and parallel ($\parallel$) components in reference to a director field $\boldsymbol{n}(\boldsymbol{r})$ [Fig. 2.3]. The director is a unit vector field describing the mesoscopic molecular orientation. Since the molecule is elongated, well approximated by a rod shape, the director field is invariant under operation $\boldsymbol{n} \rightarrow -\boldsymbol{n}$. Unlike usual liquids, liquid crystals can sustain stress in the form of splay, twist and bending of the nematic director [54]. Thanks to this nematic elasticity, an equilibrium bulk configuration of $\boldsymbol{n}(\boldsymbol{r})$ can be chosen by specifying its alignment at the surfaces of, *e.g.*, a container that encompasses the liquid crystal [55].

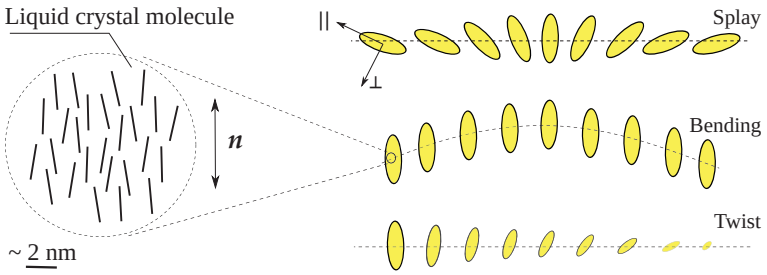

Figure 2.3: Sketch of nematic liquid crystals and conformation of the nematic director $\boldsymbol{n}$. The left of the figure illustrates a bunch of liquid crystal molecules which are represented by black rods. On a mesoscopic scale, the bunch of molecules has the orientation $\boldsymbol{n}(\boldsymbol{r})$ called the nematic director field. The nematic director, which is invariant $\boldsymbol{n} \to -\boldsymbol{n}$, is represented by yellow ellipses in the right part of figure. The director can splay, bend and twist.

Electro-convective dynamic scattering mode

When a thin layer ($\sim$ 10 μm to 100 μm) of nematic phase with negative dielectric constant ($\epsilon_\perp - \epsilon_\parallel < 0$) and positive electric conductance ($\sigma_\perp - \sigma_\parallel > 0$) is subjected to a voltage ($V \sim 10$ V [53]), a regime of electro-convection arises [56–60]. Upon gradual increasing of V, a rich sequence of patterns are formed [61–63] until the dynamics of $\boldsymbol{n}(\boldsymbol{r}, t)$ becomes turbulent. The turbulent regime splits into two states called dynamic scattering modes 1 (DSM1) and 2 (DSM2) [64–67]. DSM1 is an instance of anisotropic turbulence that preserves correlations with the lower-voltage patterns [68–70]. In turn, DSM2 is an isotropic nematic-turbulent phase that appears at voltages higher than those for DSM1. Indeed, DSM2 first nucleates [71] amid the DSM1 phase [Fig. 2.4(a)] to, then, locally grow [Fig. 2.4(a-b)], coalesce [Fig. 2.4(c-d)], and take over the whole system [Fig. 2.4(d)]. A nucleus of DSM2 comprises a high-density of line singularities for $\boldsymbol{n}(\boldsymbol{r}, t)$ referred to as disclinations (shown below). Disclinations are topological defects; in DSM2 the defects are constantly elongated, either split or intertwined, and transported amid the turbulent flow nearby. Because of these features, spatial and temporal correlations between $\boldsymbol{n}$ are of short range in DSM2. In particular, they are in the order of 1-3 μm and of 10 ms for the case of a 50 μm thick nematic layer [61].

2.2.2 Relaxation of defects and coarsening of TNLC domains

Since disclinations are line singularities, what happens if one suddenly turns (quench) off V from the DSM2 state? The answer is that a complicated relaxation dynamics takes place after setting $V = 0$ V as shown in Fig. 2.5(a-c). Defects disentangle and shrink in order to restore the corresponding equilibrium $\boldsymbol{n}(\boldsymbol{r})$ configuration of the layer. For a twisted nematic liquid crystal (TNLC) [72] for example – where equilibrium $\boldsymbol{n}$ configurations degenerate in either left- and right-handed twists – disclinations relax at the expense of the growth of twist phases. Since the equilib-

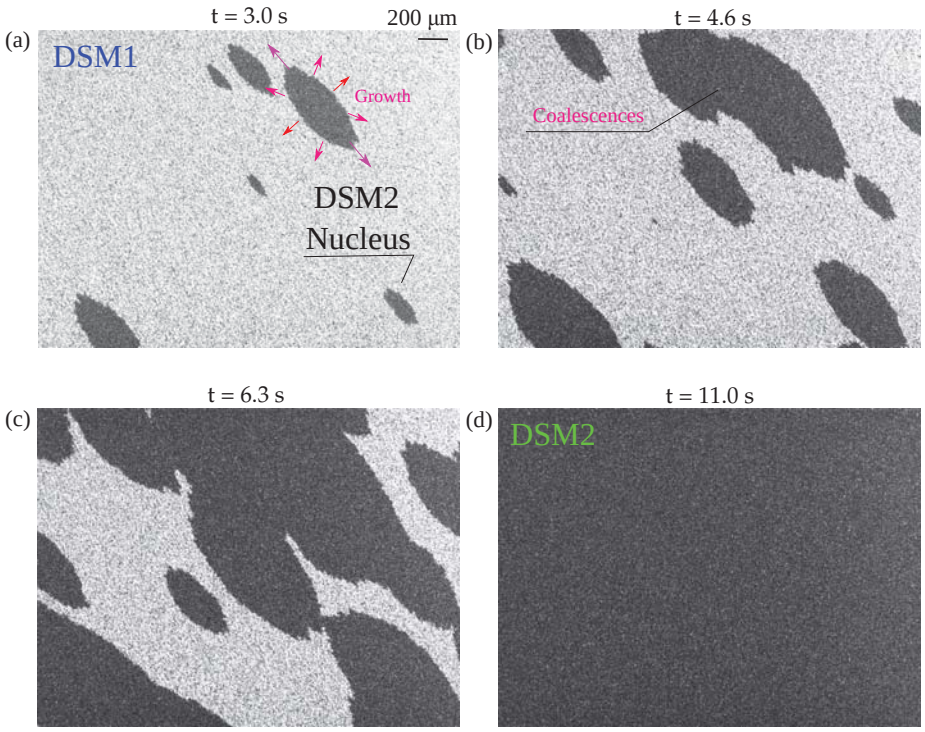

Figure 2.4: Optical microscopy images of a nematic liquid crystal layer in the nematic-turbulent regimes. The $t = 0$ s is the time in which a sinusoidal 100 Hz voltage $V = 50$ V is applied in the layer kept at $T = 25\,^{\circ}\mathrm{C}$. (a) Nucleation of DSM2 nucleuses in the DSM1 phase. DSM2 regions are darker. Arrows represent a sketch of the growth speed of a DSM2 patch. (b) Further stage after DSM2 nucleuses in (a) grew and some coalesced. (c) Intermediate stage where DSM1 and DSM2 area fractions are roughly similar. (d) DSM2 state.

rium conformation is energetically degenerated (or $\mathbb{Z}_2$ symmetric), the two possible twist states compete, via domain coarsening, to equilibrate the system. In this case, disclination lines are geometrically constrained to separate different twist phases as shown in Fig. 2.5(d). During the coarsening, the defect lines move to reduce their curvature and, thereby, the system free energy [73].

Thermally-activated TNLC domain coarsening

As briefly mentioned in Chapter 1, the coarsening of TNLC systems was studied in the past [26,40,51], where evidence of model A universality was given for a few quantities. In these studies, authors performed a *thermally*-driven quench through a *first-order* phase transition between the liquid phase and the nematic liquid crystal phase. A severe drawback of this methodology is the thermal operation itself which takes several tens of seconds [26, 40, 51]. The sequential coarsening dynamics is then affected either partially [40] or integrally [26] by a non-constant (noncontrollable) temperature. Worst, *slow* quench rates are known [74, 75] to largely modify

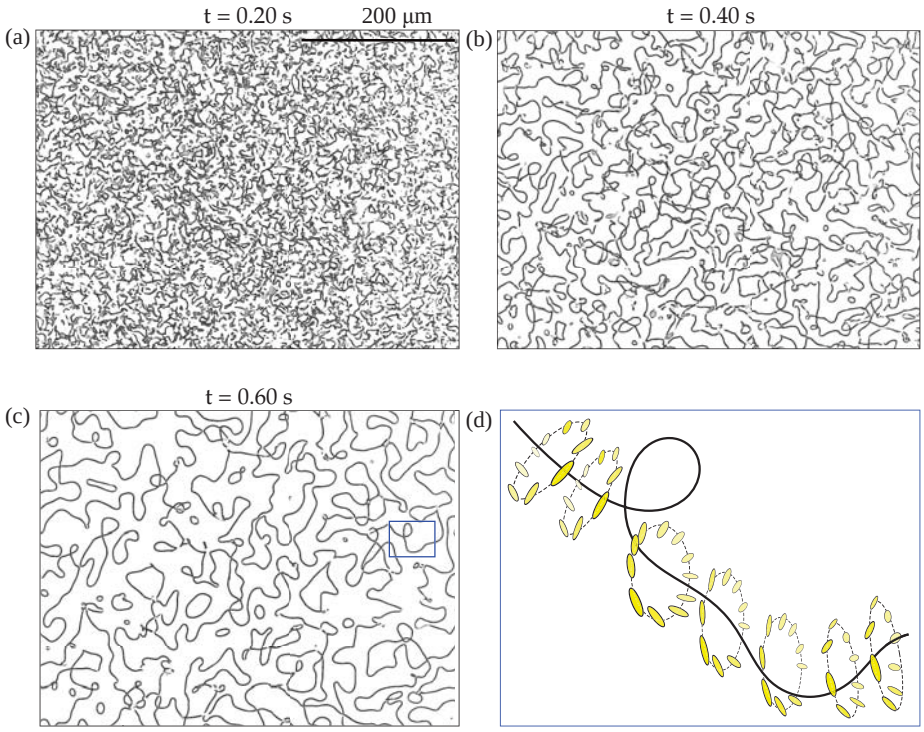

Figure 2.5: Disentangling and shrinking of disclinations after a sudden quench from DSM2 state to $V = 0$ V. The images are of optical microscopy and refer to patterns of the light transmitted through a 12 μm layer of twisted nematic liquid crystal. External voltage was turned off at $t = 0$. The width of the interfaces is artifficially enlarged for better visualization. The panel (d) is a "zoom in" the region inside the blue retangle in (c). The image in (d) is a simplified sketch of how the $\boldsymbol{n}(\boldsymbol{r}, t)$ (represented by yellow shaped ellipses) is expected to wrap around a disclination line for the case of a TNLC.

the initial density of defects, correlation lengths and, hence, the coarsening dynamics.

With the aim to conceive a suitable experimental platform to study coarsening dynamics, we designed an experimental setup, described in the next section, involving the electro-convective regimes of TNLC. Using nematic-turbulent DSM2 state to generate a disordered-like, short-ranged initial state, we explore the genuinely abrupt ($\sim$ 10 ms) quench from $V \sim 50$ V towards $V = 0$ V. The temperature of our experiment is kept constant within mK precision. Therefore, we avoid the noncontrollable feature of past studies and obtain a dynamics that is more compatible with the assumptions underlying coarsening theories. Although we study the simplest type of electrically-triggered TNLC coarsening as a first step, it is clear that quench operations from DSM2 towards other electro-convective regimes are equally feasible and controllable (but highly nontrivial); this is *per si* an enormous advantage of our setup.

2.2.3 Setup of the electrically-triggered coarsening

The TNLC cell

A liquid crystal container, or cell, was built as a capacitor of parallel plates filled with a nematic liquid crystal N-4-methoxybenzylidene-4-butylaniline (MBBA) (purity $> 98.0\%$, Tokyo Chem. Ind., Japan) doped with 0.01 wt$\%$ of tetrabutylammonium bromide (TBAB) (purity $\geq 99.0\%$, Tokyo Chem. Ind., Japan). Each plate was formed by a slab of glass covered by a transparent indium-tin oxide layer over which we coated a polyvinyl alcohol film. The film was mechanically rubbed by a handmade rubbing machine in order to specify an easy axis for the nematic director. The rubbing direction at a surface plate was set to be orthogonal to that set at the counterpart surface. This forced the nematic director to twist in the bulk after final assembly of the cell [Fig. 2.6(d)]. We constructed the capacitor geometry with polyester spacers so that its inner structure formed a quasi-bidimensional geometry of volume 14 mm $\times$ 14 mm $\times$ 12 μm. The inner volume was subsequently filled with the MBBA-TBAB solution by using the capillarity effect of the solution. The cell was then hermetically sealed, and electrical contacts were fabricated at both surfaces.

The setup

The temperature of the TNLC sample was kept constant at $25\,^{\circ}\mathrm{C}$ throughout all the experiments with in-plane, transversal and diagonal fluctuations less than 1 mK, 40 mK, and 50 mK respectively. We achieved this precision with a handmade thermo-controller that included two Peltier devices controlled via a proportional-integral-derivative feedback loop [Fig. 2.6(b)]. The devices were fed by a bipolar current supply that read the signal of a reference thermistor located at ~ 1 mm from the cell. Two sapphire windows were inserted in the thermo-controller in order to allow the passage of visible light through the TNLC cell and to measure its nematic orientation. The whole setup was put inside an adiabatic chamber, in which a constant temperature was maintained by an external thermal bath [Fig. 2.6(a)].

During the experiments, we emitted circularly polarised light through the TNLC sample, filtered it by an analyser, and recorded the transmitted light pattern with a charged-coupled device camera [Fig. 2.6(a)]. The primary light beam was produced by a halogen lamp of an Olympus inverted microscope IX73. Before reaching the sample, this beam passed through a green-light filter and a diffuser. A $\times 4$ objective was employed to observe coarsening mosaics in an area of $L_{\mathrm{sys}}^2 = 2.2$ mm $\times$ 2.9 mm.

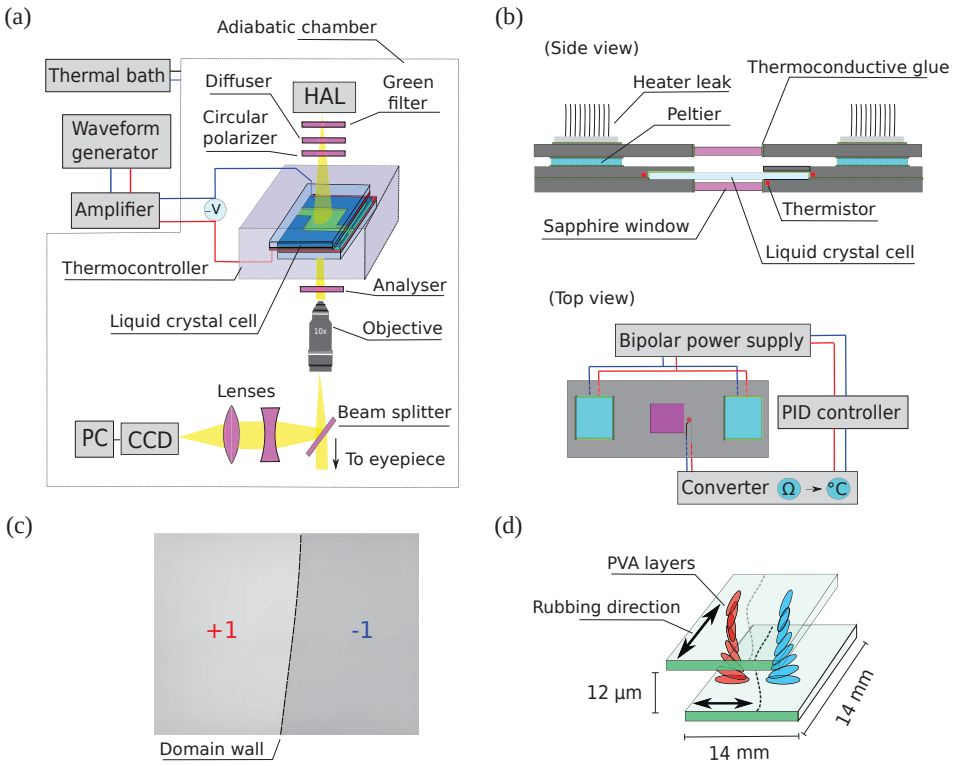

Figure 2.6: Schematics of the experimental methods. Panel (a) depicts the electro-optical setup employed to study the electrically-triggered coarsening dynamics of liquid crystals. (b) Handmade thermocontroller used to keep the temperature of the cell with $\sim$ mK precision when inserted within the adiabatic chamber in (a). The cell was prepared in such a way that the easy axes (rubbing directions) at the two surfaces were orthogonal to each other (d). This orthogonality allows the nematic director to conform in two approximately symmetric states at equilibrium, specifically, left- and right-handed twist states. Domains of opposite handedness are bordered by disclination lines. The two domains were distinguished by observing the transmitted pattern of a circularly polarized incident light through an analyser (c). We attributed to the twist states a scalar, local-order parameter $\phi(\boldsymbol{r}, t)$ that took the values ± 1 as represented in (c). Acronyms in (a) stand for: halogen lamp (HAL), charged-coupled camera (CCD), and personal computer (PC). In (b): proportional, integral and derivative (PID). In (d): polyvinyl alcohol (PVA).

Protocol of the electrical quench and image treatment

For each experiment, we first applied a 100 Hz sinusoidal voltage between the liquid crystal cell surfaces by using a wave generator and an amplifier. Voltage amplitude was set at $V = 70$ V to trigger the DSM2 turbulent regime. The liquid crystal cell was then kept at this condition during 120 s (approximately $\sim 10^4$ correlation times of the DSM2 state) before we suddenly turned off the applied voltage. From this time onwards, we recorded the transmitted light pattern over 2000 s at the speed of 3 frames per second. The experiment was repeated 20 times

to acquire sufficient statistics. Recorded images comprised 1028×1608 pixels with pixel size $a \approx 1.82$ μm. Our optical setup allowed us to distinguish domains of different twist states in terms of darker and brighter shades of grey colour in the images [Fig. 2.6(c)]. By image analysis, we attributed to each pixel a local state variable $\phi(\boldsymbol{r}, t)$ that took $\phi = -1$ at dark-grey colour pixels and $\phi = +1$ at white-grey colour ones. Disclinations appeared as dark lines of thickness $\xi \gtrsim a$ (it is not visually clear how much thick they precisely are) in the recorded images. Disclinations could not be fully distinguished from black-grey pixels; thus, during the binarisation step, they were absorbed into the $\phi = -1$ phase. The binary *approximation* is justified because we will be interested in the statistics of a certain length scale[2] $r^*(t)$ such that the ratio ξ/r^* is negligible in the limit that universal behaviour emerges.

2.3 Shrinkage law for interfaces

Figure 2.7 shows a few panels for the phase ordering in the TNLC system just after the quench at $t = 0$ s. A patchwork of hundred of TNLC domains, spatially shuffled in clusters of area nearly 10^2 μm^2 at $t \approx 5$ s, progressively evolves to reach a globally ordered state. Domains coarsen at the expense of smaller inner clusters that have the opposite twist handedness. Irregular contours of clusters at initial times are smoothed out as the coarsening proceeds; only approximately ten clusters on average, with locally smooth contour, are left at $t \approx 150$ s. Complete ordering is restored within the observation area, $L^2_{\rm sys}$, at a finite-size equilibration time $t^* \approx 1.2 \times 10^3$ s.

The phase-ordering is guided by minimisation of the excess of free energy stored at the interfaces. To quantify this process, we measure the interface density $\rho(t)$, here defined as the total number of neighbouring pairs $[\phi(\boldsymbol{r}, t), \phi(\boldsymbol{r} + \boldsymbol{a}, t)]$ with configuration $[\pm 1, \mp 1]$ divided by $L^2_{\rm sys}$ and averaged over the number of quench realizations. Figure 2.8 shows that $\rho(t)$ suggestively decreases algebraically in time. Indeed, assuming the law in Eq. (2.8), $\rho(t)$ shall be inversely proportional to $l(t)$ [3]:

$$\rho(t) \sim t^{-1/z}. \tag{2.9}$$

Defining the effective exponent $1/z_{\rm eff}(t) \equiv -\frac{d[\ln \rho(t)]}{d[\ln(t)]}$, we probe the existence of such a power law by observing whether a plateau appears in the $1/z_{\rm eff}(t)$ time series. The inset of Fig. 2.8(a) shows a salient plateau around $1/z_{\rm eff} \approx 0.50$ within the time window 7 s $\lesssim t \lesssim$ 60 s. Although this region is narrower than that the main panel of Fig. 2.8 would suggest, its result is certainly more reliable than a mere visual inspection [76]. Furthermore, the effective-exponent methodology automatically indicates a lower cutoff time (7 s) that is much larger than the microscopic

[2] The length scale $r^*(t)$ is quantitatively defined in Sec. 2.5, Eq. (2.14).

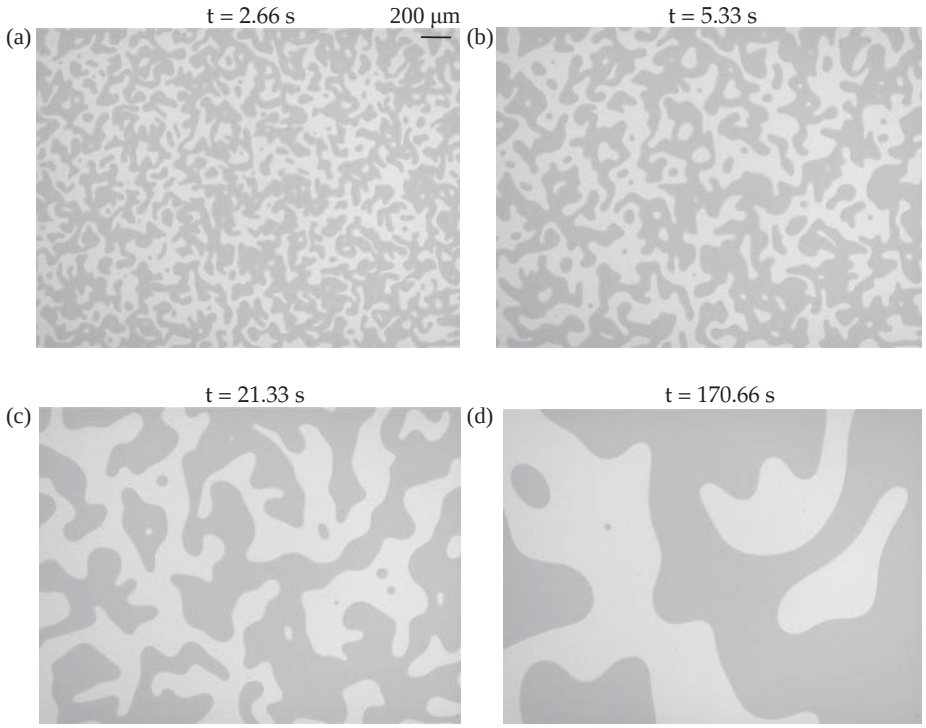

Figure 2.7: Typical images of the phase-ordering kinetics of two-dimensional TNLC systems. The dynamics is electrically-triggered by a sudden quench from a disordered (nematic-turbulent) regime to a state of null-applied electric field. Formation of twist phases starts just after $t = 0$ s. The two possible twist phases (with left- and right-handedness) are optically distinguished by different shades of grey. Liquid crystal molecule alignment is gradatively restored by the formation and grow of locally-ordered equilibrium TNLC phases that undergo coarsening as the system relaxes towards an equilibrium state where no interface remains.

time scale[3] $t_a \approx 0.5$ s, meanwhile it also indicates an upper cutoff time (60 s) much smaller (here, two orders of magnitude) than t^*. By taking the time average over the values of $1/z_{\text{eff}}(t)$ that are delimited by the cuttoff times, we obtain:

$$1/z = \begin{cases} 0.50(3) & \text{(time-averaged over } 1/z_{\text{eff}}(t) \text{ time series);} \\ 0.500(1) & \text{(best fit).} \end{cases} \tag{2.10}$$

The number into parentheses refers to the uncertainty (standard deviation) in the last digit. We also report the best-fitted value of $1/z$. In any case, our results are in striking agreement with that expected for model A dynamics, that is, $z = 2$ [10–12].

[3]The microscopic time t_a is here defined as the time for which the typical domain size [defined in Sec. 2.5, Eq. (2.14)] reaches the order of the TNLC cell gap (≈ 12 μm), so that system dynamics becomes effectively two-dimensional. From the results presented in Sec. 2.5, Fig. 2.11(b), one finds $t_a \approx 0.5$ s.

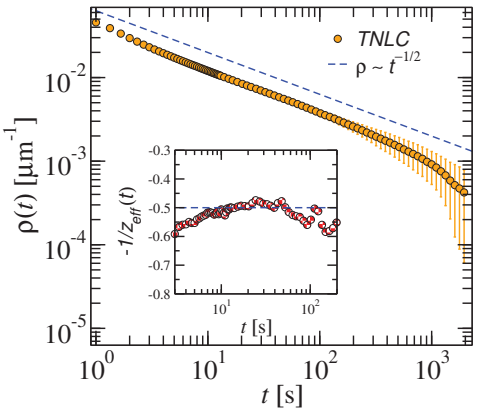

Figure 2.8: Total interface length per unit area at time t, $\rho(t)$, during the TNLC phase-ordering dynamics. The dashed blue line is a guide for eyes with slope -0.5. Inset shows time series of the effective exponent $1/z_{\text{eff}}(t) \equiv -\frac{d[\ln \rho(t)]}{d[\ln(t)]}$, with the exponent value -0.5 indicated by the horizontal dashed blue line.

2.4 Asymmetrical coarsening dynamics

The TNLC cells may not be perfectly $\mathbb{Z}_2$-symmetric regarding their twist states. There are two primary sources for breaking this symmetry. Rubbed polymeric layers are known to induce a finite angle between them and the $\boldsymbol{n}(\boldsymbol{r})$ in the plane perpendicular to the cell surfaces [77]. As a consequence, one of the two possible twist states becomes slightly favoured to the other. Moreover, a rotational misalignment between the top and bottom plates of the TNLC cell may also produce a bias for the coarsening dynamics [78].

Regarding the initial state of our experimental system, the nematic-turbulent character of DSM2 gives rise to an unbiased initial condition since even the surface anchoring of $\boldsymbol{n}(\boldsymbol{r})$ is destroyed in DSM2 phase [79]. Therefore, while the homogeneous and unbiased character of the initial condition may be experimentally realised here, similarly to typical numerical studies reported in the literature, a bias favouring one of the $\phi = \pm 1$ phases can be present in the dynamics. Despite that, TNLC systems are still rather suitable for investigating universal properties of relaxation dynamics, as it has been demonstrated in, *e.g.*, Refs. [26, 40, 51].

Figure 2.9 shows the area fraction,

$$A(t) = \langle L_{\text{sys}}^{-2} \sum_{\boldsymbol{r}} \phi(\boldsymbol{r}, t)_{|\phi=-1} \rangle, \tag{2.11}$$

where $\sum_{\boldsymbol{r}} \phi(\boldsymbol{r}, t)_{|\phi=-1}$ is the total number of pixels for which $\phi = -1$ in the configuration $\phi(\boldsymbol{r}, t)$. At very initial times ($t \ll 2.66$ s), the image is almost fully occupied by disclinations, or domain boundaries, that appear as black-coloured pixels in the bare images. Thus, we cannot fairly distinguish interfaces from $\phi = -1$ domains during this short initial transient. Therefore, the initial time region showing the decreasing of $A(t)$ is neglected. Afterwards, where binarization has

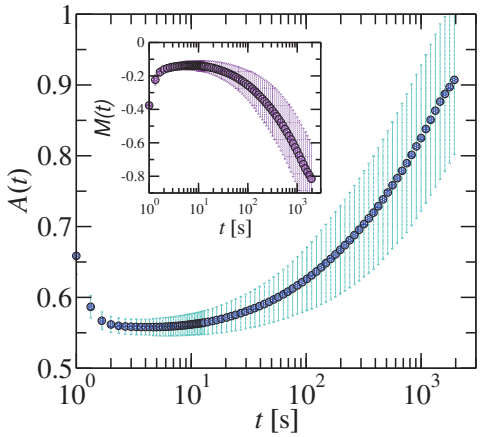

Figure 2.9: Area fraction of the TNLC domains in the biased ($\phi = -1$) phase as a function of time. Inset shows the "magnetization" $M(t) = 1 - 2A(t)$ during the coarsening. Notice that $M(t) \neq 0$ for any t. $M(t) = 0$ is expected for $\mathbb{Z}_2$-symmetric systems. Error bars are standard deviation over different experimental relaxations.

no effect on the data, $A(t)$ stays approximately constant (considering the errors bars), with mean $\overline{A} = 0.57(2)$ taken over the interval 2.66 s $\leq t \leq$ 76 s. This value corresponds to $\approx 14\%$ of deviation from the ideally $\mathbb{Z}_2$-symmetric situation for which $\overline{A} = 0.5$. Curiously, an almost identical value for this deviation, expressed by $\overline{A} = 0.576(16)$, was obtained for the thermally-induced TNLC coarsening in [51].

The evaluated asymmetric dynamics can also be expressed in terms of the "magnetization", here defined by $M(t) = 1 - 2A(t)$ [inset of Fig. 2.8(b)]. It directly gives $\overline{M} = -0.14(4)$ within 2.66 s $\leq t \leq$ 76 s, far from the $M(t) = 0$ expected for $\mathbb{Z}_2$-symmetric dynamics.

Because of the asymmetry between ϕ phases, our TNLC cell asymptotically orders always in the same $\phi = -1$ (biased) phase.

Bubble experiment

The asymmetry between the $\phi = \pm 1$ phases can also be observed in the shrinkage rate of approximate spherical domains (or bubbles) of phase ϕ surrounded by a "sea" in the $-\phi$ phase. For two-dimensional model A dynamics, the mean square radius $R^2(t)$ of a bubble at $t \geq t_0$ evolves as [11]:

$$R^2(t) - R^2(t_0) = 2D_{\text{AC}}(t - t_0) + \text{const.} \tag{2.12}$$

where D_{AC} is the Allen-Cahn diffusion constant.

We monitored $R^2(t)$ for 6 independent, isolated bubbles in our experiment; 3 of them in the $\phi = -1$ biased phase, and 3 of them in the $\phi = +1$. The results are shown in Fig. 2.10. By using Eq. (2.12), we estimate $D_{\text{AC}} = 118(3)\ \mu\text{m}^2\text{s}^{-1}$ for

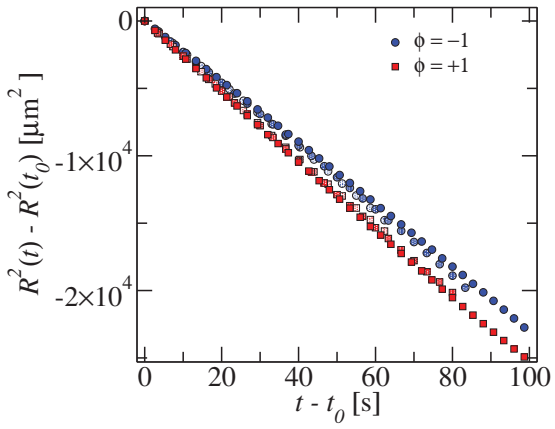

Figure 2.10: Evolution of the mean square radius $R^2(t)$ of approximate spherical TNLC domains of phase ϕ, surrounded by a "sea" of -ϕ phase. Circles (squares) stand for domains in the sligthly favoured (unfavoured) $\phi = -1$ ($\phi = +1$) phase. Curves with different shades of blue (red) stand for independent bubble experiments performed for $\phi = -1$ ($\phi = +1$) domains. t_0 is the time for which we start observing the shrinking of a bubble.

$\phi = -1$ domains and $D_{\mathrm{AC}} = 126(1)\ \mu\mathrm{m}^2\mathrm{s}^{-1}$ for $\phi = -1$ domains. An average between these values give an effective diffusion constant for our TNLC medium:

$$D_{\mathrm{AC}} = 122(4)\ \mu\mathrm{m}^2\mathrm{s}^{-1}. \tag{2.13}$$

These results show detailed evidence for the asymmetrical dynamical roles played by twist phases in the ordering process.

2.5 Two-point spatial statistics

In this section, we pay attention to the spatial statistics of two points. The celebrated growth law, defined in Eq. (2.8), is addressed in Sec. 2.5.1 by exploring the spatial correlator [Eq. (2.6)] as a measuring tool. In Sec. 2.5.2, the scaling hypothesis of coarsening theories, introduced in Sec. 2.1, Eq. (2.7), is experimentally tested. A universal amplitude exactly derived by Bray and Humayun, not observed in experiments yet, is our focus in Sec. 2.5.3.

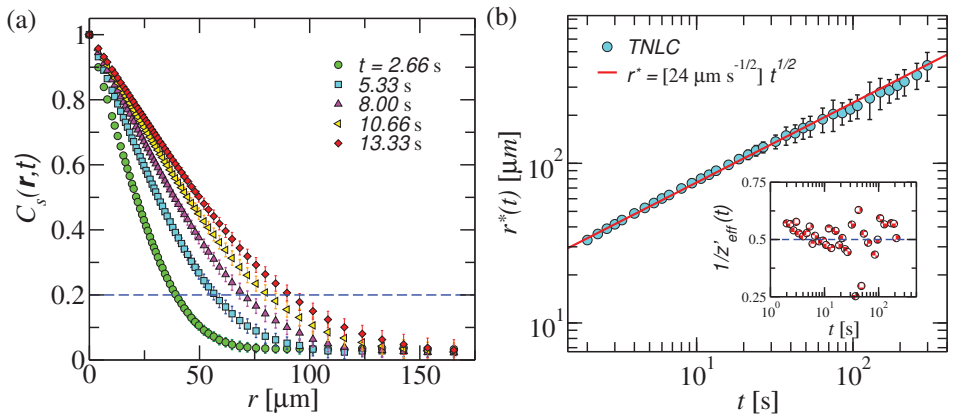

Figure 2.11: (a) Spatial covariance $C_s(\boldsymbol{r},t)$ against $r=|\boldsymbol{r}|$ at different times. The dashed blue line indicates the threshold for defining the typical scale $r^*(t)$ as the length for which $C_s(\boldsymbol{r},t)=0.2$. Error bars are defined as the standard deviation of the variable $C_s(|\boldsymbol{r}|,t)$ computed from the ensemble of quench realizations. (b) Typical length $r^*(t)$. The solid red line is a guide for eyes. Its slope corresponde to $1/z=2$, expected for scalar model A coarsening dynamics.

2.5.1 The growth law

Figure 2.11(a) shows the spatial covariance $C_s(\boldsymbol{r},t)$ [Eq. (2.6) with $\tilde{\phi}\mapsto\phi$] calculated in our TNLC experiment. We take the spatial average over all possible combinations of pairs $\phi(\boldsymbol{r}',t)$, $\phi(\boldsymbol{r}+\boldsymbol{r}',t)$ radially separated by $r=|\boldsymbol{r}|$ at t (isotropy is assumed) and then averaged over the ensemble of quench realizations from the random DSM2 states. The curves $C_s(\boldsymbol{r},t)$ show an exponentially-fast decay that depends on time. The time-dependence is due to the growth of TNLC domains. Notice that $C_s(\boldsymbol{r},t)\neq 0$ even for very large length scales. This occurs because, at such uncorrelated scales, $C_s(\boldsymbol{r},t)\approx\langle\phi(\boldsymbol{r},t)\rangle^2$; since the dynamics is asymmetric, then $\langle\phi(\boldsymbol{r},t)\rangle^2\neq 0$.

In order to quantify the growth of TNLC domains, we keep track of a typical length $r^*(t)$, defined by the distance that yields $C_s(\boldsymbol{r},t)\equiv 0.2$ for each time t. Figure 2.11(b) shows the extracted values $r^*(t)$ as a function of time. In agreement with the growth law [Eq. (2.8)], we find a power-law of kind:

$$r^*(t)\simeq C't^{1/z}\qquad(\xi\ll r^*(t)\ll L_{\rm sys}),\tag{2.14}$$

for more than two decades in time. The $1/z$ exponent is estimated from the plateau observed in the time series of $1/z'_{\rm eff}(t)\equiv d[\ln r^*(t)]/d[\ln t]$ shown in the inset of Fig. 2.11(b). From this analysis, we obtain:

$$1/z=\begin{cases}0.50(13) & \text{(time-averaged over } 1/z'_{\rm eff}(t) \text{ time series);}\\ 0.48(3) & \text{(best fit),}\end{cases}\tag{2.15}$$

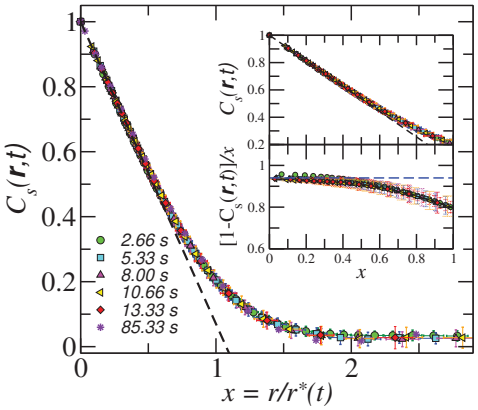

Figure 2.12: Experimental test of the scaling hypothesis. Spatial covariances $C_s(\boldsymbol{r},t)$ computed for different times and plotted against r normalized by the typical domain size $r^*(t)$. The dashed black line emphasizes the linear decay for small x with an angular coefficient $\alpha \approx 0.92$. The value of α is evaluated by plotting $[1-C_s(\boldsymbol{r},t)]/x$ as a function of x as shows the lower inset. The upper inset is a zoom in the main panel for the $x \leq 1$ region.

in good consistence with both our measurement from the interface density decay [Eq. (2.10)] and from the theoretical prediction $z = 2$ [10–12]. C' is a nonuniversal amplitude that we shall discuss in more detail in the next sections.

2.5.2 Experimental test of the scaling hypothesis

Now we are in position to experimentally test the dynamic scaling hypothesis summarized as in Eq. (2.7). We replot the covariances in Fig. 2.11(a) against the variable $x \equiv r/r^*(t)$ as shown in Fig. 2.12. The collapse of $C_s(\boldsymbol{r},t)$ data onto a single time-independent scaling function $\mathscr{F}(x)$ is remarkable, thus validating the scaling hypothesis in our experiment. Furthermore, the linear decay of $\mathscr{F}(x)$ at $x \ll 1$:

$$C_s(\boldsymbol{x},t) \approx 1 - \alpha x \qquad (\xi \ll r \ll r^*(t)), \tag{2.16}$$

expected from the Porod's law [80, 81], can also be clearly appreciated in our experimental data [see also the upper inset of Fig. 2.12].

The universal angular coefficient α is estimated by plotting $[1 - C_s(\boldsymbol{r},t)]/x$ as a function of x and by reading the value of its plateau as $x \to 0$. The bottom inset of Fig. 2.12 illustrates such a data. Taking the average over $0 \leq x \leq 0.5$ (approximately corresponding to the extension of the plateau), we obtain:

$$\alpha = 0.92(8). \tag{2.17}$$

By changing the interval of averaging (within the plateau region $x \leq 0.5$) α does not significantly change. As we shall see in the next section, the value of α can be used to access the nonuniversal amplitude C' defined in Eq. (2.14).

2.5.3 Bray-Humayun amplitude

The decay of $C_s(\boldsymbol{r},t)$ at $r \ll r^*(t)$ can be exactly derived for general d-dimensional, n-component vectorial coarsening dynamics (with $n \leq d$) [82,83]. By employing only geometrical arguments on the existence of topological defects, Bray and Humayun managed to explicitly find [83]:

$$C_s(\boldsymbol{r},t) = 1 + A'(d,n)\rho_{\text{Euc}}(t)r^n \qquad (\xi \ll r \ll r^*(t)), \tag{2.18}$$

where $\rho_{\text{Euc}}(t)$ is the interface density measured with the Euclidian metric and $A'(d,n)$ is a universal prefactor given by

$$A'(d,n) = \pi^{(n/2)-1}\frac{\Gamma(-n/2)\Gamma(d/2)[\Gamma((n+1)/2)]^2}{\Gamma((n+d)/2)\Gamma(n/2)}. \tag{2.19}$$

Here $\Gamma(\cdot)$ denotes the gamma function and n assumes only odd values[4]. Equation (2.18) is expected to hold regardless the validation of the dynamic scaling hypothesis since it is concerned to intra-domain scales. It is also independent of the presence of local and global conservation laws. Despite such a generality, such an exact relation between $C_s(\boldsymbol{r},t)$ and $\rho(t)$ has not been experimentally investigated yet.

For two-dimensional systems with $n = 1$ (our case), one has that $A'(2,1) = -4/\pi$. In order to investigate Eq. (2.18) using our TNLC data, we firstly shall convert $\rho_{\text{Euc}}(t)$ into the interface density $\rho(t)$ computed in the Manhattan metric, given this is the metric we used to count the total length of interfaces in the experiment [Fig. 2.8]. The conversion between the involved metrics can be performed by exploring the fact that, for an *isotropic* space, the average ratio between a piece of Manhattan length L'_{Man} and a piece of an Euclidian length L'_{Euc} is given by $L'_{\text{Man}}/L'_{\text{Euc}} = 4/\pi$ [83]. Therefore, Eq. (2.18) can be rewritten for the particular case $d = 2$, $n = 1$ as:

$$C_s(\boldsymbol{r},t) = 1 - A^*\rho(t)r \qquad (\xi \ll r \ll r^*(t)), \tag{2.20}$$

where the universal amplitude $A^* \equiv [-A'(2,1)\pi/4]$ is simply $A^* = 1$.

Now we test the prediction experimentally. From the data of the interface density $\rho(t)$ [Fig. 2.8], we already confirmed the shrinkage law $\rho(t) \simeq Ct^{-1/2}$, where here we also account for the nonuniversal prefactor C. By plotting $\rho(t)t^{1/2}$ against t, the plateau observed in the inset of Fig. 2.13 gives an estimate $C = 0.0379(5)$ $\text{s}^{1/2}\mu\text{m}^{-1}$. This value is to be compared with the asymptotic $r \to 0$ value of $[1 - C_s(\boldsymbol{r},t)]t^{1/2}/r$, which equals to A^*C according to Eq. (2.20) in the scaling limit. Figure 2.13 displays such a plot showing indeed a plateau that becomes larger as t increases. Reading the plateau value at small r, for curves corresponding to $t \geq 8.00$ s, gives $A^*C = 0.0378(3)$ $\text{s}^{1/2}\mu\text{m}^{-1}$. Then, using the value of $C = 0.0379(5)$ $\text{s}^{1/2}\mu\text{m}^{-1}$, we finally obtain

[4] The expression for even n can be found in Ref. [83].

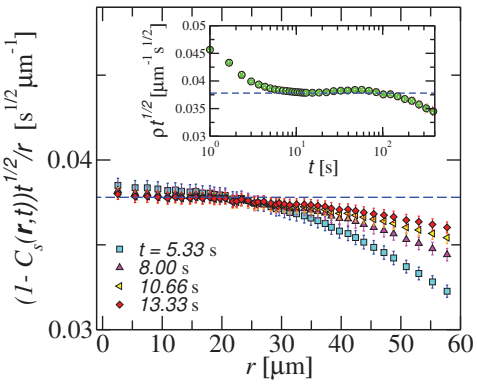

Figure 2.13: Experimental extraction of Bray-Humayun amplitude. Rescaled spatial covariances $[1 - C_s(\boldsymbol{r}, t)]t^{1/2}/r$ computed for different times and plotted against r. The dashed blue line marks the value of the non-universal amplitude $A^*C = 0.0379\ \mathrm{s}^{1/2}\mu\mathrm{m}^{-1}$. The inset displays $\rho t^{1/2}$ against t, in order to emphasize the amplitude C of the shrinkage law, $\rho(t) \simeq Ct^{-1/2}$. The horizontal dashed blue line is a guide for eyes at the plateau $C = 0.0379\ \mathrm{s}^{1/2}\mu\mathrm{m}^{-1}$.

$$A^* = 1.00(2), \tag{2.21}$$

which is in excellent agreement with $A^* = 1$ expected from Bray-Humayun's theory [83].

Notice that by comparing Eq. (2.16) with the exact relation in Eq. (2.20), one identifies α as $\alpha = A^*\rho(t)r^*(t)$. In terms of the prefactors we can write $\alpha = A^*CC'$. Since we estimate $A^*C = 0.0378(3)\ \mathrm{s}^{1/2}\mu\mathrm{m}^{-1}$ and $\alpha = 0.92(8)$ in Eq. (2.17), we obtain $C' = 24(2)\ \mu\mathrm{m/s}^{1/2}$ for the amplitude of $r^*(t) \simeq C't^{1/2}$, which accurately accounts for the experimental growth as the solid red line in Fig. 2.11(b) shows.

2.5.4 Experimental comparison with Gaussian theories

Since the first pieces of evidence for scaling in domain growth [84–86], exact functional forms $\mathscr{F}(\boldsymbol{r}/t^{1/z})$ remain unknown with exception of simple models, such as the Ising-Glauber chain [14, 15], the d-dimensional $O(n)$ model in the large n limit [16], and the one-dimensional XY model [13]. For scalar model A systems at $d = 2$, the Ohta-Jasnow-Kawasaki theory [18] and the theory of unstable growth [19], particularly[5], provide functional forms $\mathscr{F}(\cdot)$ which generically agrees with those extracted from the Ising-Glauber [88] and TDGL models [89]. From the experimental point of view, however, only the form predicted by the OJK

[5]There are other coarsening theories dealing with the functional forms $\mathscr{F}(\boldsymbol{r}/t^{1/2})$ for scalar systems, such as the Kawasaki-Yalabik-Gunton theory [17], the non-Gaussian theories [21, 87] and the perturbative ones [20, 22]. However, these theories generically recover OJK and TUG functional forms at the leading order.

theory has been tested: notably in thermally-driven TNLC coarsening [26] – for which agreement was limited to the linear decay $C_s(x) \approx 1 - \alpha x$ – and recently in polycrystalline layers of colloids [90], for which the fundamental growth law $l(t) \sim t^{1/2}$ underlying OJK theory is not obeyed. Here we take advantage of our accurate experimental system, that clearly shows $z = 2$, to investigate whether theories can account for our TNLC data.

In the scaling limit, the continuum field $\tilde{\phi}$ of a generic model A dynamics is $\tilde{\phi}(\boldsymbol{r}, t) = \pm\tilde{\phi}_{\rm eq}$ everywhere, except at interface positions $\boldsymbol{r}_i$, where $\tilde{\phi}(\boldsymbol{r}_i, t) = 0$ by definition[6]. A matter of mathematical concern about $\tilde{\phi}$ is that $|\nabla\tilde{\phi}(\boldsymbol{r}, t)| \rightarrow \infty$ when an interface is crossed. The idea used to OJK and TUG to avoid such divergences is to replace the description from $\tilde{\phi}$ to an auxiliary field that *smoothly* vary in the space. The way such auxiliary fields are introduced distintigues among the theories.

The OJK theory

The OJK model starts from the shrinking dynamics of interfaces [11], which can derived from TDGL equation [Eq. 2.3]:

$$v(\boldsymbol{r}_i, t) = -D_{\rm AC}[\nabla \cdot \boldsymbol{n}'(\boldsymbol{r}_i, t)], \tag{2.22}$$

where $v(\boldsymbol{r}_i, t)$ is the normal component of the velocity of a point $\boldsymbol{r}_i$ at interface, and $\boldsymbol{n}'(\boldsymbol{r}_i, t)$ is a unit vector normal to the interface (oriented in the direction of increasing $\tilde{\phi}(\boldsymbol{r}, t)$). One defines an auxiliary field $u(\boldsymbol{r}, t)$ that smoothly vary in space, such that $\tilde{\phi}(\boldsymbol{r}, t) = {\rm sgn}[u(\boldsymbol{r}, t))]$. Thus, $\boldsymbol{n}'(\boldsymbol{r}_i, t) = \nabla u(\boldsymbol{r}_i, t)/|\nabla u(\boldsymbol{r}_i, t)|$, which implies:

$$v(\boldsymbol{r}_i, t) = -\frac{D_{\rm AC}}{|\nabla u(\boldsymbol{r}_i, t)|}\sum_{j,k}^{d}[n'_j n'_k(\delta_{j,k}\nabla^2 - \nabla_j\nabla_k)u], \tag{2.23}$$

where $j,\ k = 1, 2, ..., d$ denote the spatial directions. At the coming frame of reference of the interface:

$$\frac{du(\boldsymbol{r}_i, t)}{dt} = |\nabla u|v + \frac{\partial u}{\partial t} \equiv 0. \tag{2.24}$$

Inserting $v(\boldsymbol{r}_i, t)$ from Eq. (2.24) into Eq. (2.23) leads to the nonlinear OJK equation:

$$v(\boldsymbol{r}_i, t) = -D_{\rm AC}\sum_{j,k}^{d}[n'_j n'_k(\delta_{j,k}\nabla^2 - \nabla_j\nabla_k)u]. \tag{2.25}$$

[6]Remember that in our experimental approach $\phi = \pm 1$ always because of the binarization treatment of images.

In order to simplify the expression above, OJK replaces $\nabla_j \nabla_k$ by its spherical average $\delta_{j,k}/d$ (OJK approximation). Physically, the approximation ignores correlations between the movement of mutually orthogonal directions of the interface. Equation (2.25) then becomes the diffusion equation:

$$\frac{\partial u(\boldsymbol{r}_i,t)}{\partial t} = -D_{\rm OJK}\nabla^2 u, \quad (D_{\rm OJK} \equiv (d-1)D_{\rm AC}/d), \tag{2.26}$$

which can be solved exactly by specifying boundary conditions. The further assumption of OJK is to treat $u(\boldsymbol{r}_i,0)$ as Gaussian field with spatial mean $\langle u(\boldsymbol{r}_i,0)\rangle = 0$ and correlator $\langle u(\boldsymbol{r}_i,0)u(\boldsymbol{r}_i+\boldsymbol{r},0)\rangle = \Delta\delta(\boldsymbol{r})$, with $\Delta > 0$ finite. Finally, backing to the original field – using $\tilde{\phi} = \mathrm{sgn}(u)$ – the model generates [3, 18]:

$$\mathscr{F}_{\rm OJK}(r/t^{1/2}, D_{\rm OJK}) = \frac{2}{\pi}\sin^{-1}\left[\exp\left(-\frac{1}{2}\left(\frac{r}{(4D_{\rm OJK}t)^{1/2}}\right)^2\right)\right], \tag{2.27}$$

where $\mathscr{F}_{\rm OJK}(\cdot)$ is the OJK functional form expected to be exact at $O(1/d^2)$ concerning the OJK assumption [91].

The TUG

In the TUG model one starts from TDGL equation [Eq. (2.3) with $T = 0$]. An auxiliary field $m(\boldsymbol{r},t)$ is introduced such that $d^2\tilde{\phi}[m]/dm^2 \equiv dV'(\tilde{\phi})/d\tilde{\phi}$. This equation gives $\tilde{\phi}(\boldsymbol{r},t)$ for a flat interface at *equilibrium* with $m(\boldsymbol{r},t)$ playing the (physical) role of the shortest distance between $\boldsymbol{r}$ and the nearby interface at $\boldsymbol{r}_i$. TUG cleverly explores this meaning in a nonequilibrium situation, where the interpretation of $m(\boldsymbol{r},t)$ is *locally* preserved. Thereby, the TDGL equation can be rewritten as, after multiplyied by $\tilde{\phi}(\boldsymbol{r}+\boldsymbol{r}',t)$ and taken the ensemble average:

$$\frac{\partial \tilde{C}_s(\boldsymbol{r},t)}{\partial t} = \nabla^2 \tilde{C}_s(\boldsymbol{r},t) + \left\langle \frac{d^2\tilde{\phi}(\boldsymbol{r}',t)}{dm^2}\tilde{\phi}(\boldsymbol{r}+\boldsymbol{r}',t)\right\rangle. \tag{2.28}$$

TUG *assumes* $m(\boldsymbol{r},t)$ as a Gaussian field (at all times). In this way the last term in Eq. (2.28) can be rewritten only in terms of $\tilde{C}_s(\boldsymbol{r},t)$ itself [3], thus allowing to obtain a differential equation for $\tilde{C}_s(\boldsymbol{r},t)$. Assuming the scaling hypothesis $\tilde{C}_s(\boldsymbol{r},t) = \mathscr{F}_{\rm TUG}(r/t^{1/2}, D_{\rm TUG})$ the TUG equation reads – in a convenient scale $g \equiv r/(4D_{\rm TUG}t)^{1/2}$ – with $D_{\rm TUG}$ a constant [19, 92]:

$$\frac{d^2\mathscr{F}_{\rm TUG}(g)}{dg^2} + \left(\frac{d-1}{g} + g\mu(d)\right)\frac{d\mathscr{F}_{\rm TUG}(g)}{dg} + \tan\left(\frac{\pi}{2}\mathscr{F}_{\rm TUG}(g)\right) = 0, \tag{2.29}$$

where $\mathscr{F}_{\rm TUG}(0) = 1$, and where $\mu(d)$ guarantees the integrability[7] of $\mathscr{F}_{\rm TUG}(g)$ in the limit $g \to \infty$. For the case of interest here $\mu(2) \approx 1.1042$ [92]. In the limit $g \ll 1$ one has the linear decay [92, 93]:

[7] Eq. (2.29) admits two linearly independent solutions at large ($g \gg 1$) scales: a Gaussian decay and an algebraic one. The general solution is given by a linear combination of both: $\mathscr{F}_{\rm TUG}(g \gg$

$$\mathscr{F}_{\rm TUG}(r/t^{1/2}, D_{\rm TUG}) \approx 1 - \left(\frac{1}{2D_{\rm TUG}\pi(d-1)}\right)^{1/2} \frac{r}{t^{1/2}}. \qquad (2.30)$$

Comparison between OJK and TUG with the experimental data

We can test Eq. (2.27) against our experimental data as follows. Since $D_{\rm OJK} = D_{\rm AC}/2$ for $d = 2$ [Eq. (2.26)], from our independent evaluation of $D_{\rm AC} = 122(4)$ μm^{2}s^{-1} [Sec. 2.4, Eq. (2.13)] we obtain $D_{\rm OJK} = 61(2)$ μm^{2}s^{-1}. In Fig. 2.14(a) we replot $C_s(\boldsymbol{r}, t)$ curves of TNLC and compare them with the OJK prediction generated with $D_{\rm OJK} = 61$ μm^{2}s^{-1} [Eq. (2.27)]. A clear visual agreement between the OJK and the TNLC curves is seen down to $C_s(\boldsymbol{r}, t) \approx 0.05$. This agreement, with no fit parameter, becomes even better for large times ($t \gtrsim 42.66$ s), where the experiment is in the scaling limit[8].

As an alternative route, notice that by making $\mathscr{F}_{\rm OJK}(r^*/t^{1/2}) = 0.2$ in Eq. (2.27), we are lead to $r^*(t) = \sqrt{8D_{\rm OJK}\ln[\sin(\pi/10)]}t^{1/2}$. Comparing this relation with the experimental law $r^*(t) \simeq C't^{1/2}$ in Eq. (2.14), with $C' = 24(2)$ μms$^{-1/2}$, we obtain $D_{\rm OJK} = 61(10)$ μm^{2}s^{-1}. This result sharply agrees with our direct estimation for $D_{\rm AC}$ that implies $D_{\rm OJK} = 61(2)$ μm^{2}s^{-1}.

In order to test TUG against the experimental data, we *assume* the universality of the angular coefficient in Eq. (2.30). Rewriting the $C_s(\boldsymbol{x}, t)$ decay in Eq. (2.16) in terms of $C_s(r/t^{1/2})$, with the help of Eq. (2.14), we achieve $C_s(r/t^{1/2}) \approx 1 - (\alpha/C')(r/t^{1/2})$. Comparing this relation with Eq. (2.30) on the basis of universality, one finds $D_{\rm TUG} = (C'/\alpha\sqrt{2\pi})^2$. Thereby, using $C' = 24(2)$ μm^{2}s^{-1} and $\alpha = 0.92(8)$ [Eq. (2.17)], we finally estimate $D_{\rm TUG} = 108(20)$ μm^{2}s^{-1}.

Now we are in position to evaluate Eq. (2.29). We integrated Eq. (2.29) in $d = 2$ via an Euler-Heuns discretization scheme with an uniform step $\delta g = 10^{-6}$. We started from the initial conditions $\mathscr{F}_{\rm TUG}(0) = 1$ and $\frac{d\mathscr{F}_{\rm TUG}(g)}{dg}|_{(g=0)} = (2/\pi)^{1/2}$. Figure 2.14(b) shows $\mathscr{F}_{\rm TUG}(r/t^{1/2}, 108\ \mu\text{m}^2\text{s}^{-1})$ compared with $\mathscr{F}_{\rm OJK}(r/t^{1/2}, 61\ \mu\text{m}^2\text{s}^{-1})$. Both functions are also compared with the TNLC data. For the sake of visualization, only curves from the experiment for $t = 42.66$ s and $t = 85.33$ s are plotted. The plot reveals the similar decays of OJK and TUG function for this way of rescaling. Such observation is consistent with previous simulations of discrete models [88, 89].

Although we fitted the initial decay of $\mathscr{F}_{\rm TUG}$ to the experimental data, the agreement between the curves, at large scales ($r/t^{1/2} \gg 1$ μms$^{-1/2}$), is fair considering the experimental error bars. Nevertheless, notice that agreement between the mean values of TNLC data and the TUG function can be improved by integrat-

1) $= F_0 g^{(d-\frac{\pi}{2\mu})} \exp\left(\frac{-\mu}{2}g^2\right) + F_1 g^{-\frac{\pi}{2\mu}}$, where F_0 and F_1 are constants. The power-law solution in TUG is neglected by Mazenko [92] based on the integrability of the correlation functions, which should decay to zero as $g \to \infty$. The value for $\mu(d)$ in the theory is then precisely defined as the value for which $\mathscr{F}_{\rm TUG}(g \gg 1)$ yields a solution with $F_1 = 0$.

[8] Please refer to the inset of Fig. 2.8, which shows $z = 2$ occurring around $t \approx 40$ s.

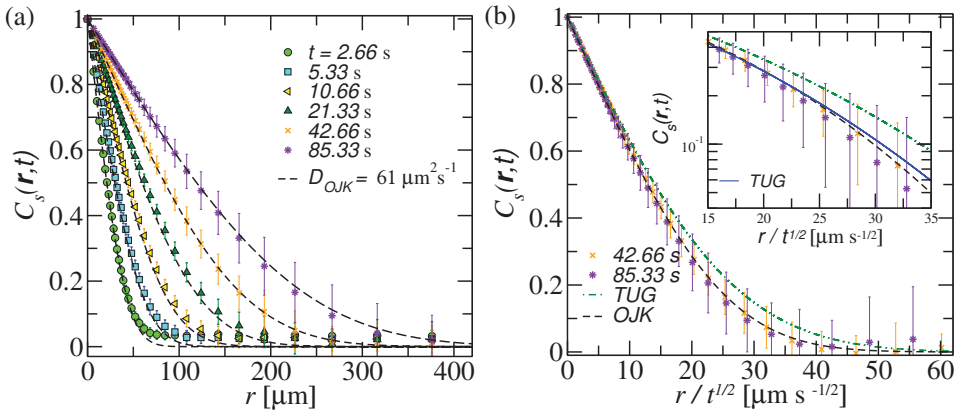

Figure 2.14: (a) Spatial covariances $C_s(\boldsymbol{r},t)$ calculated from the experiment (symbols) at several times. Dashed black lines are $C_s(\boldsymbol{r},t)$ generated from the OJK theory with $D_{\rm OJK} = 61\ \mu{\rm m}^2{\rm s}^{-1}$. (b) Rescaled $C_s(\boldsymbol{r},t)$ for the TNLC experiment at $t = 42.66$ s and $t = 85.33$ s (core of the scaling limit), compared with OJK (dashed black line) and TUG (dashed-point green line) functional forms using $D_{\rm OJK} = 61\ \mu{\rm m}^2{\rm s}^{-1}$ and $D_{\rm TUG} = 108\ \mu{\rm m}^2{\rm s}^{-1}$. Inset is a zoom in the main plot. The solid blue line is the TUG functional form predicted with $D_{\rm TUG} = 88\ \mu{\rm m}^2{\rm s}^{-1}$.

ing TUG equation with $D_{\rm TUG} = 88\ \mu{\rm m}^2{\rm s}^{-1}$: a value that is the lowest bound for our estimation $D_{\rm TUG} = 108(20)\ \mu{\rm m}^2{\rm s}^{-1}$. The insertion of Fig. 2.14(b) illustrates such a plot, where TUG approaches both to the TNLC and to the OJK functions.

In summary, OJK and TUG function can account for the TNLC data. These are nontrivial results given the experimental dynamics is asymmetric. OJK form agrees with TNLC down to $C_s \approx 0.05$ with no fit parameter; this improves the previous agreement between OJK and a real system obtained by Orihara and Ishibashi [26]. $\mathscr{F}_{\rm TUG}(r/t^{1/2}, D_{\rm TUG})$ is for the first time tested against an experimental data; it also agrees with TNLC within the error bars. Interesting, OJK and TUG may be indeed fair approximations to the exact, yet unknown universal scaling function $\mathscr{F}(r/t^{1/2})$ representative of two-dimensional scalar model A systems. In fact, the Gaussian assumption for $u(\boldsymbol{r},t)$ and $m(\boldsymbol{r},t)$ fields seem to be reasonable approximations, at least in $d = 2$, as very recently checked by integrations of the TDGL equation [94].

2.6 Two-time statistics

2.6.1 Topic introduction

Time correlations, typically probed by the time covariance or autocorrelation function,

$$\tilde{C}_t(t,t_0) := \langle \tilde{\phi}(\boldsymbol{r},t)\tilde{\phi}(\boldsymbol{r},t_0)\rangle \quad (t \geq t_0), \tag{2.31}$$

are generically found to decay slowly – that is, faster than exponentially – in a variety of nonequilibrium systems [95], such as spin glasses [96], colloidal suspensions [97], growing interfaces [98] and domain coarsening [40]. Particularly for coarsening dynamics, one anticipates [99] that this decay is algebraic in most of the cases[9] and can be written as $\tilde{C}_t(t,t_0) = \mathscr{H}(t/t_0)$, where:

$$\mathscr{H}(t/t_0) \sim (t/t_0)^{-\lambda/z} \quad (t, t_0 \gg t_{\text{micro}}, \quad t/t_0 \gg 1), \tag{2.32}$$

with $\mathscr{H}(\cdot)$ being a universal scaling function, t_{micro} a microscopic time scale, and λ the so-called autocorrelation exponent introduced by Fisher and Huse (FH) in the context of spin glasses [33].

For scalar model A systems at $d = 2$, there is no a clear consensus on the value of λ yet. Its value varies depending on the method of approximation. For instance, within the OJK linear theory, one has [3, 44]:

$$\mathscr{H}_{\text{OJK}}(y) = \frac{2}{\pi}\sin^{-1}\left(\frac{4y}{(1+y)^2}\right)^{d/4}; \quad \lambda_{\text{OJK}} = d/2, \tag{2.33}$$

where $y \equiv t/t_0$. In the $\lim y \to \infty, \mathscr{H}_{\text{OJK}}(y) \sim y^{-d/4}$. According to Eq. (2.32), one identifies $\lambda_{\text{OJK}} = d/2$ for dynamics with $z = 2$. Such a OJK time statistics, however, has not been observed in real and model systems yet.

The best-accepted value for λ is that obtained by the FH approach [33]. FH *assumes* that two-dimensional domain coarsening is an instance of critical percolation [107] if the competing phases occupy exactly 50% of the system area fraction. Relying on scaling hypothesis for a critical percolation theory [100], FH argues that $\lambda_{\text{FH}} = 5/4$. Despite lacking rigour, many discrete and continuum coarsening models support FH prediction [33, 36, 37, 39, 101]. An experiment of thermally-triggered coarsening of TNLC domains also reported $\lambda = 1.246(79)$ [40].

The FH approach provides only an estimate for the possible value of λ. A functional form, compatible with simulations of the Ising-Glauber model, however, is provided by a different approach; this more recent approach bases on a local scaling invariance (LSI). In the LSI theory [102], coarsening dynamics is *assumed* to be conformally invariant (CI). The CI hypothesis, entering as an additional symmetry into the dynamics, constrains scaling relations and the shape of correlation functions up to a few constants. For scalar model A dynamics, the phenomenology of a conjectured LSI predicts [101, 103]:

$$\mathscr{H}_{\text{LSI}}(y) = y^{\lambda/2}(y-1)^{-\lambda}\Phi\left(\frac{y+1}{y-1}\right) \quad (y \gg 1), \tag{2.34}$$

where $\Phi(q)$, $q \equiv (y+1)/(y-1)$, is a generic scaling function given by:

[9] One exception is the one-dimensional $O(2)$ model whose two-time covariance decays exponentially [13].

$$\begin{aligned}\Phi(q) = B_1 q^{2b-\lambda}\Big[&\Gamma(\lambda-2b)\,{}_2F_1(2\lambda-d-2b,\lambda-2b;\lambda+1-2b-d/2;-1/q)\\ &-\gamma(\lambda-2b,B_2q)\Big] + B_1 B_2^{-2b} q^{\lambda}\gamma(\lambda,B_2q) + B_3 B_2^{d/2-\lambda} q^{-\lambda}\gamma(\lambda,B_2q)\\ &+ B_1 B_2^{1-2b}\frac{2\lambda-d-2a}{\lambda+1-2a-d/2} q^{-\lambda}\Big[(B_2q)^{2b-1}\gamma(\lambda+1-2b,B_2q)-\gamma(\lambda,B_2q)\Big]\\ &+ B_3\Big[\Big(\Gamma(d/2)\,{}_2F_1(\lambda-d/2,d/2;1+2b+d/2-\lambda;-1/q)\\ &-\gamma(d/2,B_2q)\Big)q^{-d/2}\Big].\end{aligned} \tag{2.35}$$

In the expression above, ${}_2F_1(\cdot)$ is a hypergeometric function, $\gamma(\cdot)$ is the incomplete gamma function. With the constants $B_1 = -0.601$, $B_2 = 0.517$, $B_3 = 3.94$, $b = 1/z = 0.5$ and $\lambda = \lambda_{\text{FH}}$, the functional $\mathscr{H}_{\text{LSI}}(y)$ describes $\tilde{C}_t(t,t_0)$ for the Ising-Glauber model quenched to $T = 0$ for $y \gtrsim 3$ [101].

The exponent λ_{FH} is also very close to the approximate value yielded by the coarsening dynamics of the TUG model, namely $\lambda_{\text{TUG}} \approx 1.2887$ [41]. Very recent numerical evaluations of discrete and continuum coarsening models [42, 43] show agreement with λ_{TUG} instead of λ_{FH}. Although TUG theory does not provide a closed form for the funcional form $\mathscr{H}(y)$, its form is exptected to be well approximated by Eq. (2.35).

Given the universal value for λ is not even resolved in simulations yet, the previous experimental agreement with λ_{FH} reported in [40] shall not be a final answer; independent experimental measurements are required to support its universal character. Furthermore, the central scaling hypothesis $\tilde{C}(t,t_0) = \mathscr{H}(t/t_0)$, curiously, remains to be supported. We address these issues of universality for λ and $\mathscr{H}(y)$ using our electrically-triggered coarsening setup in the following section.

2.6.2 Autocorrelation exponent and scaling function

To compute $C_t(t,t_0)$ (which is $\tilde{C}_t$ for $\tilde{\phi} \mapsto \phi$) in our TNLC system, we performed an additional series of experiments in which the TNLC cell was rotated by π rad around its minor axis. This rotation translates into a colour inversion of the twist phases observed in the untreated images: domains which were previously detected as white-grey colour ($\phi = +1$) are now seen as black-grey colour ($\phi = -1$), and vice versa. The exception is for domain boundaries which, due to the strong scattering of the light, appear as a mixture of dark-black and dark-grey coloured pixels in any case. In summary, in this section we deal with two series of experiments: one for which $\phi(\boldsymbol{r}, t \to \infty) = -1$ (hereafter called Series A), and one for which $\phi(\boldsymbol{r}, t \to \infty) = +1$ (Series B).

Although Series A and B correspond physically to the same experiment, the *binarization* of images introduces an artificial difference between $C_t(t,t_0)$. Pixels corresponding to the domain boundaries are absorbed into the *biased* ($\phi = -1$)

phase in the case of Series A, but into the *unbiased* phase in the case of Series B. While the binarization scheme does not affect the other quantities we have investigated hitherto, it leads $C_t(t, t_0)$ function to behave differently when computed from Series A and Series B; Fig. 2.15(a) shows the results. Notice that $C_t(t, 2.66\text{s}) \approx 0.15$ for $t \gtrsim 200$ s in the Series A data because the interface pixels (counted as they were part of the biased phase) contribute to an artificial positive correlation at any $t \geq t_0$. On the other hand, $C_t(t, 2.66\text{s}) \approx 0.06$ for $t \gtrsim 200$ s considering the Series B data.

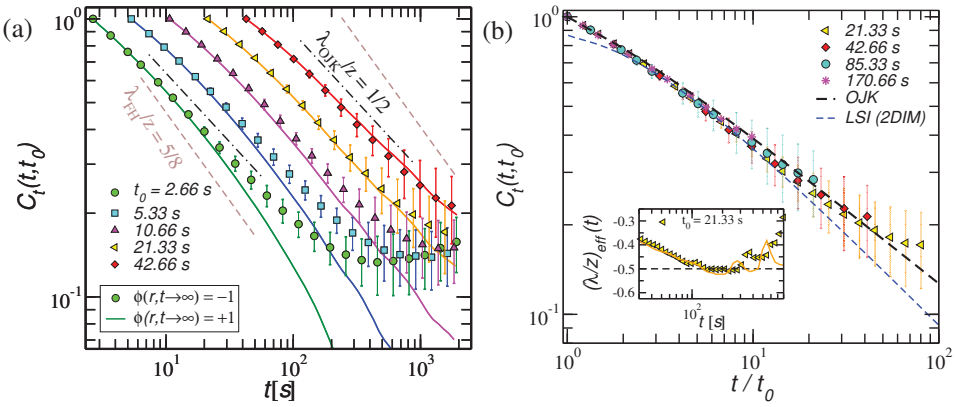

Figure 2.15: (a) Autocorrelation function $C_t(t, t_0)$ computed in the TNLC coarsening experiment for different reference times t_0. Symbols (lines) refer to the series of experiments performed such that the final equilibration is $\phi(\boldsymbol{r}, t \to \infty) = -1(+1)$. The difference between $C_t(t, t_0)$ results observed for $t_0 \lesssim 21.33$ s is artificial and comes from the binarization process. Dashed black and brown lines are guide to eyes and refer to the decay predicted by the OJK model [44] and the FH argument [33], respectively. (b) Experimental scaling function $C_t(t, t_0) = \mathscr{H}(t/t_0)$ compared to the OJK [Eq. (2.33)] (black solid line) and LSI (2DIM) [Eq. (2.35)] functional forms (blue dashed line), where 2DIM stands for two-dimensional kinetic Ising model with nonconserved dynamics. Inset shows the time series of the effective exponent $(\lambda/z)_{\text{eff}}(t) \equiv -\frac{d[\ln C_t(t;\, 21.33\text{ s})]}{d[\ln(t)]}$. Symbol (solid line) stands for the series of experiments such that $\phi(\boldsymbol{r}, t \to \infty) = -1(+1)$. The dashed black line at -0.5 is marked to the value predicted by the OJK model.

Before eliminating the spurious data, let us to call attention for the decay $C_t(t, 2.66\text{ s}) \approx t^{-5/8}$ for 10 s $\lesssim t \lesssim$ 100 s from Series B data. This decay would imply $\lambda \approx 5/4$, thus recovering the previous experimental result obtained in [40] which also was based on a binarization step. However, we know that such decay is spurious for our experimental data, at least. By looking at $C_t(t, t_0)$ for different t_0, it is clear that the decay $C_t(t) \approx t^{-5/8}$ cannot describe TNLC data for larger t_0 (see in particular $t_0 = 42.66$ s). In other words, $\lambda \approx 5/4$ does not seem to correspond to an actual λ in our case.

The spurious differences between $C_t(t, t_0)$ of Series A and Series B vanish when the interface density $\rho(t_0) \to 0$. From results in Fig. 2.15(a), this occurs when $t_0 \geq 21.33$ s since the $C_t(t, t_0)$ from both Series becomes equivalent – as

they must be.

Now we can safely proceed to read the decay of $C_t(t, t_0 \geq 21.33\ \text{s})$ from the effective exponent $(-\lambda/z)_{\text{eff}}(t) \equiv \frac{d[\ln C_t(t;\, 21.33\ \text{s})]}{d[\ln(t)]}$ shown in the inset of Fig. 2.15(b). The series $(\lambda/z)_{\text{eff}}(t)$ exhibits a narrow, but well defined plateau for $100\ \text{s} \lesssim t \lesssim 310\ \text{s}$. The plateau $(\lambda/z)_{\text{eff}}(t) = 0.50$ *does not* depend on $t_0 \gtrsim 21.33$ s nor on the Series. From such an analysis, we obtain for $z = 2$:

$$\lambda = \begin{cases} 1.00(2) & \text{(time-averaged over } (\lambda/z)_{\text{eff}}(t) \text{ time series);} \\ 0.998(2) & \text{(best fit);} \end{cases} \tag{2.36}$$

in striking agreement with the OJK outcome [Eq. (2.33)]. Our experimental results are significantly different from FH prediction.

Now we turn to the functional form $\mathscr{H}(y)$. In Fig. 2.15(b) we plot the rescaled experimental $C_t(t, t_0)$ curves for $21.33\ \text{s} \leq t_0 \leq 170.66\ \text{s}$. All the curves collapses onto a single $\mathscr{H}(y)$ curve that, when compared to $\mathscr{H}_{\text{OJK}}(y)$ in Eq. (2.33), reveals a reasonable agreement between TNLC and OJK model for $1 \leq y \lesssim 100$. Notice that the comparison does not involve fit parameters. We remark that similar y intervals are used in numerical simulations to discern among functional forms $\mathscr{H}(y)$ [101]. The experimental TNLC $\mathscr{H}(y)$ curve in Fig. 2.15(b) is also compared with $\mathscr{H}_{\text{LSI}}(y)$ [Eq. (2.34) and Eq. (2.35)]. The comparison unveils that $\mathscr{H}_{\text{LSI}}(y)$ does not describe the $y \lesssim 2$ region of our TNLC data. Furthermore, $\mathscr{H}_{\text{LSI}}(y)$ systematically deviates from the mean TNLC $C_t(t, t_0)$ curve as y increases. Although we cannot completly rule out $\mathscr{H}_{\text{LSI}}(y)$ from an agreement with the experiment within the error bars, $\mathscr{H}_{\text{LSI}}(y)$ is *not* expected to describe TNLC data in the scaling limit $y \to \infty$.

In summary, the experimental TNLC $C_t(t, t_0)$ function is accessible only for $t_0 \geq 21.33$ s. Otherwise, the data is artificially altered because of the binarized treatment applied to the images. We show that when the spurious data for $t_0 = 2.66$ s is analysed, consistency with the previous experimental report $\lambda \approx \lambda_{\text{FH}}$ [40] is obtained here. On the other hand, from our reliable data regime, TNLC data displays $\lambda = 1.00(2)$ [Eq. (2.36)]. This value may constitute the first experimental evidence compatible with the OJK statistics [Eq. (2.33)]. A further agreement with OJK is seen in the description of the experimental $\mathscr{H}(t/t_0)$. Form $\mathscr{H}_{\text{LSI}}(t/t_0)$ also gives an account for the experimental data, within the error bars, although limited by $3 \lesssim y \lesssim 40$. It is not clear yet, however, whether the asymmetric coarsening dynamics affects λ. In such a case, agreement with OJK could still have the chance to be merely accidental. We are currently investigating the effect of a biased dynamics in λ using simulations of Ising-Glauber model. Other remaining question is how to conciliate the two experimental values: λ_{FH} in [40] and λ_{OJK} here. Given λ_{FH} is not an artifact of binarization step, would λ be sensible to the initial conditions (isotropic liquid in [40] and DSM2 here)? The Author is currently performing thermal-quench experiments in the TNLC cell to answer this question.

2.7 Local persistence statistics

2.7.1 Topic introduction

Consider a d-dimensional stochastic system comprising N degrees of freedom whose microscopic state at time t is described by $\boldsymbol{Y}(t) := \{Y_1(t), Y_2(t), ..., Y_N(t)\}$. Without loss of generality, a local state variable $Y_i(t)$ with $i = 1, 2, ..., N$ can be defined so that it fluctuates in time with mean $\overline{Y_i(t)} \equiv 0$. By specifying an initial condition $\boldsymbol{Y}(t_0)$ from where we keep a record of the system evolution, an interesting question is then: what is the probability that the $\mathrm{sgn}(Y_i(t))$ has not *ever* changed up to time t since the reference time t_0? The answer for this question defines the *local persistence probability* $Q(t, t_0)$ [31, 32, 104], a quantity intimetely related to first-passage problems [105] and that surprisingly has been found to decay algebraically,

$$Q(t, t_0) \simeq (t/t_0)^{-\theta} \quad (t \gg t_0), \tag{2.37}$$

with a nontrivial exponent θ for a great variety of infinitely-large ($N \to \infty$) systems [32]. Examples include model systems [106, 107] and experiments [108–110] involving coarsening, simple diffusion [111–114], reaction-diffusion schemes [115, 116], as well as models [4] and real [98, 118–120] interface growth.

In the context of coarsening, the persistence exponent θ is exactly known for some simple models [45–49]. Among them, one finds the diffusion equation with random initial conditions at $d = 2$ [49]. For this case, Poplavskyi and Schehr managed to derive $\theta = 3/16$ by mapping the diffusive dynamics to Kac polynomials and from them, then, to the ensemble of truncated orthogonal random matrices [49].

Exact results are not available for the family of two-dimensional scalar model A systems. Approximate methods have estimated the exponent θ for this class. A variational and perturbative scheme working around Markovian processes predicts[10] $\theta \approx 0.19$ [121]. Such a value is indeed in good agreement with systematic $\theta = 0.199(3)$ [50] and earlier $\theta = 0.22(3)$ [106, 107] numerical simulations of the nonconserved Ising model. Yurke, Pargellis, Majumdar and Sire [51] measured $\theta = 0.190(31)$ for the thermally-induced coarsening of TNLC systems. Despite this remarkable experimental finding, the value $\theta = 0.190(31)$ is not accurate enough to allow a distinction from the exact result for the diffusion class ($\theta = 3/16$) [49], for which $z = 2$ as well. Furthermore, the dependence of the persistence probability $Q(t, t_0)$ [Eq. (2.37)] and its scaling with the reference t_0 remains unexplored in experimental systems despite being the central hypothesis in the persistence theory.

[10] The obtained prediction depends on the input used to initialise the perturbative scheme. If the TUG theory gives the input, authors obtain $\theta \approx 0.29$ in sharp disagreement with estimates from numerical simulations. The analytical prediction is improved by fitting a certain time correlator obtained from the Ising-Glauber model and using it as the new input for the perturbative scheme. This semi-analytical procedure gives then $\theta \approx 0.19$ [121].

In the following sections, we analyse the electrically-triggered TNLC data to revisit the experimental issue on the value of θ in the context of model A dynamics. At the same time, we compute $Q(t,t_0)$ for several reference times t_0 and investigate the collapse onto a single universal curve according to the scaling in Eq. (2.37). Finally but not least important, we turn to the morphological aspects of persistent clusters which are expected to encode universal characters as well [108, 122, 123]. Experimental evidence for this point, however, is in lack for the model A universality class.

2.7.2 The local persistent exponent

Figure 2.16(a) shows $Q(t,t_0)$ in the TNLC experiment. This quantity was computed as the fraction of $\phi(\boldsymbol{r},t)$ that has *never* changed the twist phase ϕ since t_0. Qualitative analogy with the behaviour of $C_t(t,t_0)$ in Sec. 2.6 can be made. Notice that $Q(t,t_0)$ explicitly depends on both t and t_0 and that $Q(t,t_0)$ decays algebraically for $t \gg t_0$. In order to characterize this decay, we rely on the effective persistence exponent $\theta_{\text{eff}}(t) \equiv -\frac{d[\ln Q(t,\,2.66\text{ s})]}{d[\ln(t)]}$ shown in the inset of Fig. 2.16(a). From the extended plateau of $\theta_{\text{eff}}(t)$ for 22 s $\lesssim t \lesssim$ 194 s one has:

$$\theta = \begin{cases} 0.194(2) & \text{(time-averaged over } \theta_{\text{eff}}(t) \text{ time series);} \\ 0.1941(1) & \text{(best fit).} \end{cases} \tag{2.38}$$

The accuracy of our results compares with that obtained by recent large-scale simulations of the nonconserved Ising model in $d = 2$ [50]: the experimental value $\theta = 0.194(2)$ is not only in sharp agreement with $\theta \approx 0.195$ – predicted by simulations performed with free boundary conditions [50] – but also rules out the exact value $\theta = 0.1875$ for simple diffusion [49]. The $Q(t,t_0)$ curves indeed collapses onto a single curve when rescaled by t/t_0 [Fig. 2.16(b)]. $Q(t/t_0)$ is singularly specified by the decay of θ since the prefactor in Eq. (2.37) is unity [inset of Fig. 2.16(b)]. The prefactor is fixed by the normalization requirement $Q(1) = 1$.

2.7.3 Morphology of persistent clusters

Now we turn to morphological properties of persistent clusters. For addressing this point, we define a local persistence index $u_{\text{pd}}(\boldsymbol{r},t)$ so that $u_{\text{pd}}(\boldsymbol{r},t) = 1$ if $\phi(\boldsymbol{r},t)$ has not ever changed since t_0, and $u_{\text{pd}}(\boldsymbol{r},t) = 0$ otherwise.

Figure 2.17 shows a few snapshots for the mosaic of TNLC domains in terms of $u_{\text{pd}}(\boldsymbol{r},t)$. The shape of persistent clusters has edges that become ragged at larger length scales as time elapses. This indicates the existence of a characteristic growing length, here denoted $r^*_{\text{pd}}(t)$, below which the initial cluster compactness of $u_{\text{pd}}(\boldsymbol{r},t_0)$ is destroyed. In order to confirm such a reasoning, we measure the dimension of persistent clusters, $d'(r,t)$. We count the number of $u_{\text{pd}}(\boldsymbol{r},t) = 1$ inside a box of lateral size $r \leq L_{\text{sys}}$ and refer to this number as the local mass

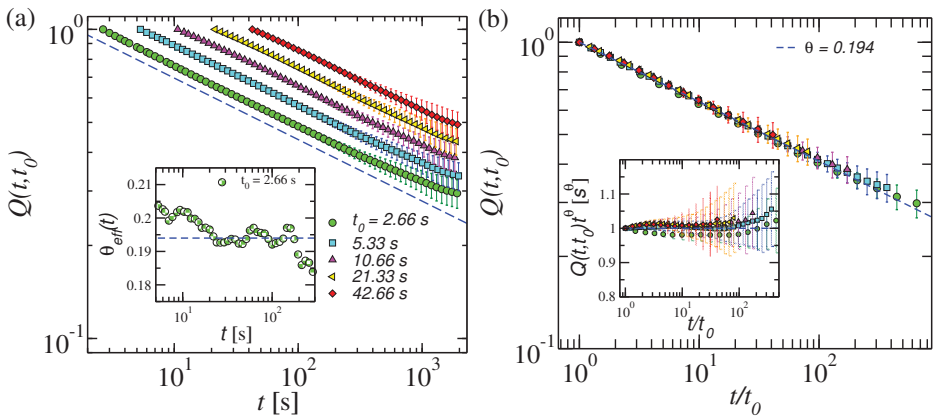

Figure 2.16: Persistence probability $Q(t, t_0)$ of TNLC domains during the electrically-triggered coarsening. (a) Decay of $Q(t, t_0)$ with t for several reference times t_0. Dashed blue line is a guide to the eyes and has slope -0.194. Inset shows the effective exponent $\theta_{\text{eff}}(t) \equiv -\frac{d[\ln Q(t,\, 2.66\,\text{s})]}{d[\ln(t)]}$ in time. Emphasis is given for the plateau 0.194 (dashed blue line) around which the experimental data fluctuates. (b) Same data as in (a) when plotted against t/t_0. Inset shows $Q(t, t_0)t^\theta$ versus t/t_0. The plateau $Q(t, t_0)t^\theta \approx 1$ (dashed blue line) corresponds to the unity prefactor of the scaling in Eq. (2.37).

$m_{\text{pd}}(r, t)$. The box then slides over a frozen picture of $u_{\text{pd}}(\boldsymbol{r}, t)$ and, from the i^{th} box position along the sliding procedure, we collect the respective $m^i{}_{\text{pd}}(r, t)$ value as far as $m^i_{\text{pd}} \in \mathbb{N}^*$. After completing the sliding protocol, the set $\mathbb{M}_{\text{pd}}(r, t) := \{m^i{}_{\text{pd}}(r, t)\}$ with $(i = 1, 2, ...)$ is obtained. We evaluate the total mass $M_{\text{pd}}(r, t)$ and the mean mass $\langle m_{\text{pd}}(r, t)\rangle$ respectively as:

$$M_{\text{pd}}(r, t) := \sum_{i=1}^{|\mathbb{M}_{\text{pd}}(r,t)|} m^i_{\text{pd}}(r, t); \qquad \langle m_{\text{pd}}(r, t)\rangle := M_{\text{pd}}(r, t)/|\mathbb{M}_{\text{pd}}(r, t)|, \tag{2.39}$$

where $|\mathbb{M}_{\text{pd}}(r, t)|$ is the cardinality of the set $\mathbb{M}_{\text{pd}}(r, t)$. One expects [125] that $|\mathbb{M}_{\text{pd}}(r, t)| \sim r^{-d'(r,t)}$, with $d'(r, t)$ taking a non-integer value d_f if objects are fractal, or $d'(r, t) = d$ otherwise. For a given configuration $u_{\text{pd}}(\boldsymbol{r}, t)$, the total mass $M_{\text{pd}}(r, t)$ is a constant. Thereby it follows from Eq. (2.39):

$$\langle m_{\text{pd}}(r, t)\rangle \sim r^{d'(r,t)}. \tag{2.40}$$

In Fig. 2.18(a) we plot $\langle m_{\text{pd}}(r, t)\rangle$ obtained from the experiment for different times. Distinct algebraic behaviours are seen, respectively, for $r \ll r^*_{\text{pd}}(t)$ and $r \gg r^*_{\text{pd}}(t)$ scales – notice that $r^*_{\text{pd}}(t)$ is formally defined as the crossover length of $\langle m_{\text{pd}}(r, t)\rangle$. The plot of the effective dimensional exponent $d'_{\text{eff}}(r, t) \equiv \frac{d\ln[\langle m_{\text{pd}}(r,t)\rangle]}{d[\ln r]}$ in Fig. 2.18(b) shows $d'_{\text{eff}}(r \gg r^*_{\text{pd}}(t), t) = 2$. On the other hand, $d_{\text{eff}}(r \lesssim r^*_{\text{pd}}(t), t)$ curves display a concave-like dependence along r with a minimum, $d'_{\text{eff}}(r^*_{\text{pd}}(t), t)$, that decreases with t [Fig. 2.18(b)]. These behaviours can

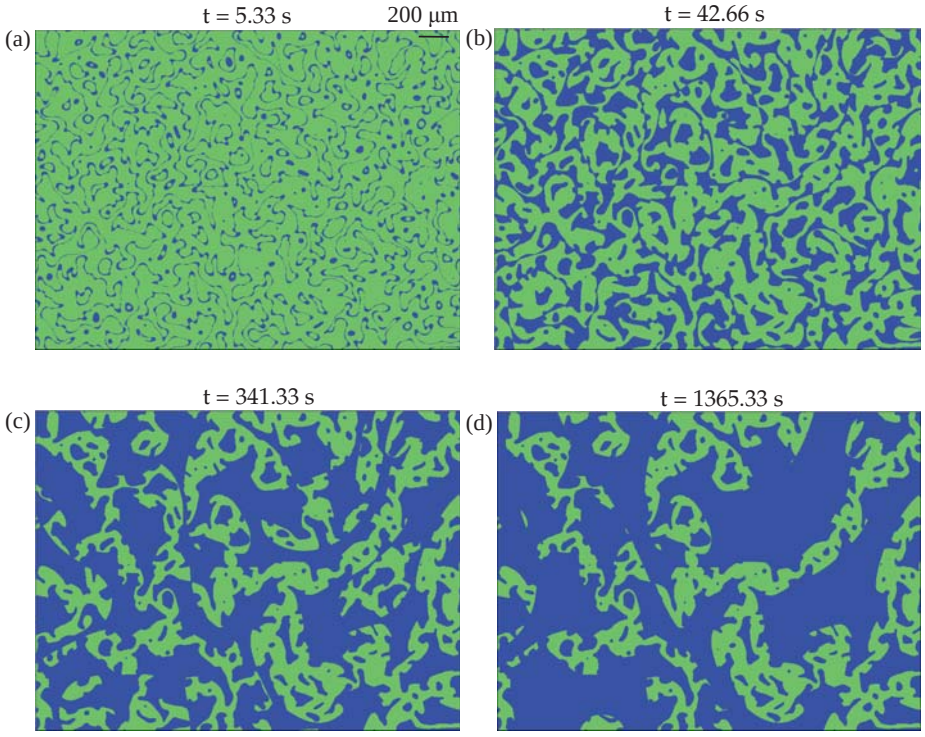

Figure 2.17: Typical spatial configuration of the persistent index $u_{\text{pd}}(\boldsymbol{r}, t)$ computed from the experimental eletrically-triggered coarsening of TNLC domains. Persistent spatial regions (in green) refer to areas that were never traversed by a domain wall since $t_0 = 2.66$ s. Persistent regions develop fractal clusters amid an increasing sea (in blue) of spatial points that were traversed by a domain wall at least once since t_0.

be traced back to finite-time and finite-size effects since $r^*_{\text{pd}}(t \gtrsim t_0) \approx a$ and $r \approx a$ at such regimes, respectively. In the limit $a \ll r \ll r^*_{\text{pd}}(t)$, one expects $d'_{\text{eff}} = d_f$. In fact, by progressively considering longer and longer times in the curves of Fig. 2.18(b), while seeking for a possible plateau in each one of them, we estimate $d_f \approx 1.65$ from the narrow plateau around $r \approx 100$ μm for $t = 1365.33$ s.

Two processes fabricate the fractal shape of persistent clusters. The first is the random position of interfaces seeded by the initial conditions which produces the irregular borders for both the physical domains and for the persistent clusters. The second process is concerned with the coarsening process itself. Since physical domains grow at the expense of the area of domains with high curvatures, the shrinkage of domains fabricates the holes observed in the persistent clusters [Fig. 2.17]. Notice that, nevertheless, the shrinkage movement of domain walls does not necessarily imply an update for $u_{\text{pd}}(\boldsymbol{r}, t)$ because walls may also move through nonpersistent regions. Thereby, there are two competing length scales in the problem: the mean separation of domains $r^*(t) \sim t^{1/z}$ and the mean size of nonpersistent regions which grows as $\sim t^{\theta}$. In our experiment one has $1/z > \theta$.

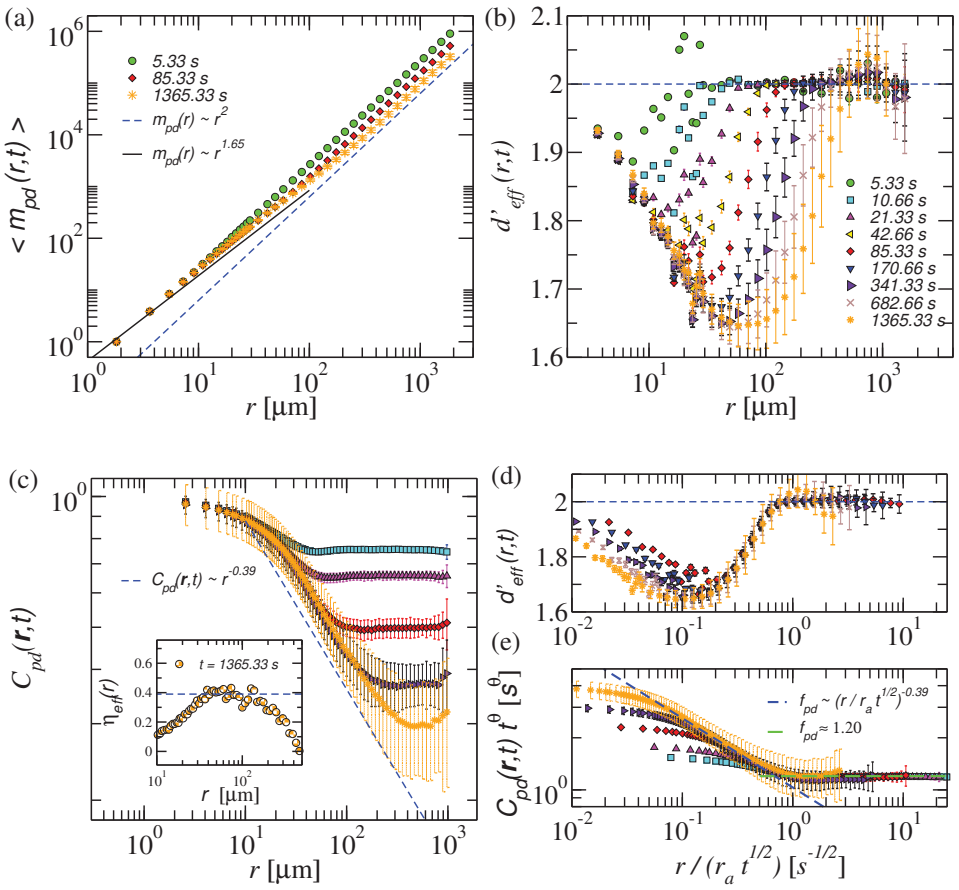

Figure 2.18: (a) Local mean mass $\langle m_{\rm pd}(r,t)\rangle$ for persistent clusters in the TNLC experiment (reference time, $t_0 = 2.66$ s). Solid black and dashed blue lines are guide to eyes and have semi-integer (1.65) and integer (2.00) inclinations, respectively. (b) Effective dimension $d'_{\rm eff}(r,t) \equiv \frac{d[\ln\langle m_{\rm pd}(r,t)\rangle]}{d[\ln r]}$ computed for different times. Dashed blue line demarks the value for which $d'_{\rm eff}(r,t) = 2$. (c) Persistence-related spatial covariance $C_{\rm pd}(\boldsymbol{r},t)$ shown for a few times; legend of symbols and colors are as described in (b). Inset depicts the changing of the effective $\eta_{\rm eff}(r) \equiv -\frac{d[\ln C_{\rm pd}(r,1365.33\,{\rm s})]}{d[\ln r]}$ with r. Emphasis is given on the plateau observed for 38 μm $\lesssim r \lesssim$ 150 μm that fluctuates around the dashed blue line at $\eta_{\rm eff} = 0.39$. (d) Effective dimension and (e) persistence-related spatial covariance rescaled so that r is normalized by $t^{1/2}$ and by the microscopic length scale $r_a \approx 10$ μm.

Thus, the dominating (and single relevant) scale is $r^*(t)$[11], which shall scale as $r^*_{\rm pd}(t) \sim r^*(t) \sim t^{1/2}$. The reasoning is supported by the collapse of $d'_{\rm eff}(r,t)$ onto a single curve when r is normalized by $t^{1/2}$ [Fig. 2.18(d)]. Deviations at short scales stem from finite-time effects.

[11] For cases where the opposite situation occurs, see model systems in [124].

Spatial correlation function

The spatial crossover from fractal to compact structures can be better captured by the persistence-related spatial covariance $C_{\rm pd}(\boldsymbol{r},t)$:

$$C_{\rm pd}(\boldsymbol{r},t) := \frac{\langle u(\boldsymbol{r}',t)u(\boldsymbol{r}+\boldsymbol{r}',t)\rangle}{\langle u(\boldsymbol{r}',t)\rangle}, \tag{2.41}$$

where the normalization factor $\langle u(\boldsymbol{r}',t)\rangle = Q(t,t_0)$. The $C_{\rm pd}(\boldsymbol{r},t)$ correlation function was computed for persistent clusters in the one-dimensional diffusion equation with random initial conditions [122], in an one-dimensional reaction-diffusion model [123], and in the two-dimensional Ising-Glauber model [52]. These numerical works suggest:

$$C_{\rm pd}(\boldsymbol{r},t) = Q(t) f_{\rm pd}(|\boldsymbol{r}|/r^*(t)), \qquad f_{\rm pd}(x) = \begin{cases} x^{-\eta} & \text{if} \quad x \ll 1; \\ \text{const.} & \text{if} \quad x \gg 1, \end{cases} \tag{2.42}$$

where η is a universal exponent that relates to z and θ,

$$\eta = z\theta; \tag{2.43}$$

$f_{\rm pd}(\cdot)$ is a universal scaling function.

The experimental $C_{\rm pd}(\boldsymbol{r},t)$ curves are shown in Fig. 2.18(c). The curves seem to exhibit a power-law decay, for more than one decade of range, better seen for large-enough times such as $t \gtrsim 10^3$ s. The effective exponent $\eta_{\rm eff}(r) \equiv -\frac{d[\ln C_{\rm pd}(r,1365.33\text{ s})]}{d[\ln r]}$ depicted in the inset of Fig. 2.18(c) shows a plateau for 38 μm $\lesssim r \lesssim$ 150 μm from where we measure:

$$\eta = \begin{cases} 0.39(4) & \text{(averaged over } \eta_{\rm eff}(r) \text{ series);} \\ 0.385(5) & \text{(best fit).} \end{cases} \tag{2.44}$$

The above outcomes are in fair agreement with $\eta = 0.428(7)$ observed for persisent clusters in the Ising-Glauber dynamics in $d = 2$ [52]. Combining the best-fitted values found for θ in Eq. (2.38) and for η in Eq. (2.44) we consistently reach $z = 1.98(3)$ after using Eq. (2.43).

Notice that the behaviour of $C_{\rm pd}(\boldsymbol{r},t)$, however, is *not* algebraic for $r \lesssim r_a$. Here $r_a \approx 10$ μm is a microscopic length scale related to the finite resolution of images [Fig. 2.18(c)]. Therefore, the expected universal scaling function $f_{\rm pd}(|\boldsymbol{r}|/r^*(t))$ shall accessed by plotting $C_{\rm pd}(\boldsymbol{r},t)t^\theta$ as function of $(|\boldsymbol{r}|/r_a)/t^{1/2}$ as we do in Fig. 2.18(e). Apart from finite-time corrections, we obtain a single-value function that behaves in agreement with Eq. (2.42), where the constant value $f_{\rm pd} \approx 1.20$ for $r \gg r^*(t)$. Both results in Fig. 2.18(d) and in Fig. 2.18(e) are additional pieces of evidence for the dynamical scaling hypothesis.

Relation between universal exponents

By noticing the relation between the mean mass and the spatial covariance [125],

$$\langle m_{\rm pd}(r,t)\rangle \propto \int_a^{r'=r} C_{\rm pd}(|\boldsymbol{r}|,t)d^d r', \tag{2.45}$$

the scaling form in Eq. (2.42) can be used to obtain, after integration:

$$\langle m_{\rm pd}(r,t)\rangle \sim \begin{cases} r^{d-\eta} & \text{if} \quad r \ll r^*_{\rm pd}(t); \\ r^d & \text{if} \quad r \gg r^*_{\rm pd}(t). \end{cases} \tag{2.46}$$

Bringing back Eq. (2.40) and the interpretation of results in Fig. 2.18(a), immediately one indentifies [125]:

$$d_f = 2 - \eta. \tag{2.47}$$

From our measurement of η in Eq. (2.44), one has $d_f = 1.61(5)$, which is in fair agreement with our previous estimate $d_f \approx 1.65$. Both values for the TNLC system are close to the numerical estimation, $d_f = 1.58 - 1.62$, for persistent clusters arising in the Ising-Glauber model [52].

2.8 Summary and concluding remarks

We studied the asymptotics coarsening dynamics of two-dimensional TNLC systems. The coarsening was electrically-triggered from a nematic-turbulent regime to an ordered state free from the applied external field. A detailed spatiotemporal statistical analysis was carried out based on twenty independent histories of relaxations monitored via optical microscopy. Despite TNLC coarsening being asymmetrical, the results agree with those either exactly derived or approximately obtained for the family of two-dimensional, $\mathbb{Z}_2$-symmetric scalar model A systems – see Table 2.8. This fact points out to the robustness of universal behaviours.

Our work goes beyond the mere comparison with experiments and previous experimental results; it provides empirical evidence for the universality of amplitudes, exponents and functional forms that hitherto had not been experimentally observed; they are:

i) the Bray-Humayun's amplitude [Eq. (2.21)];

ii) an accurate-enough persistent exponent θ that rules out simple diffusion process [Eq. (2.38)];

iii) the fractal dimension of persistent clusters d_f [Eq. (2.47)];

iv) central scaling functions such as $\mathscr{H}(t/t_0)$ [Fig. 2.15(b)] and others [Fig. 2.16(b), Fig. 2.18(d-e)].

Quantity	TNLC (here)	Model A ($d = 2$)	Ref.
$[1/z]$	$0.50(3)^a$	$1/z = 1/2$	[10–12]
$[\lambda]$	$1.00(2)^a$	$\lambda_{\text{OJK}} = 1; \lambda_{\text{FH}} = 5/4; \lambda_{\text{TUG}} \approx 1.29$	[33,41,44]
$[\theta]$	$0.194(2)^a$	${}^b\theta_{\text{WBC}} \approx 0.195 \quad \theta_{\text{PBC}} \approx 0.199(3)$	[50]
$[d_f]$	$1.61(5)$	$d_f = 2 - z\theta$	[123]
$[A^*]$	$1.00(2)$	$A^* = 1$	[83]
$[\alpha]^c$	$0.98(2)^d$	–	
$[C \times C']^e$	$0.9(1)^d$	–	

[a] Values obtained after averaging over a time-independent region (plateau) in the time series of the respective effective exponent.
[b] Subscripts stand for window boundary conditions (WBC) and periodic boundary conditions (PBC). Results obtained from large-scale simulations of the two-dimensional Ising-Glauber model.
[c] α defines the decay of the rescaled spatial covariance $C_s(\boldsymbol{x}) = 1 - \alpha x$, with $x \equiv r/r^*$ [Eq. (2.16)].
[d] Value depends on the definition of a coarsening length $r^*(t)$ through the spatial covariance $C_s(\boldsymbol{r}^*, t) \equiv 0.2$.
[e] $C \times C' \equiv \rho(t) r^*(t)$, where $\rho(t)$ is the interface density in the Manhattan scale, and the coarsening length $r^*(t)$ is measured in the Euclidian scale.

Table 2.2: List of the universal quantities measured in the electrically-triggered coarsening of TNLC domains compared to those either exactly derived or approximately obtained for two-dimensional model A systems.

We have compared the experimentally-obtained scaling function $\mathscr{F}(\boldsymbol{r}/t^{1/2})$ with both classical OJK and TUG functional forms $\mathscr{F}_{\text{OJK}}(r, D_{\text{OJK}})$ [Eq. (2.27)], and $\mathscr{F}_{\text{TUG}}(\boldsymbol{r}/t^{1/2}, D_{\text{TUG}})$ [Eq. (2.29)]. $\mathscr{F}_{\text{OJK}}$ is in remarkable agreement with the TNLC data without employing any sort of fit, while $\mathscr{F}_{\text{TUG}}$ also describes the experimental data, within the error bars [Eq. (2.14)(b)], given the Porod's decay of TUG is adjusted to be equal to that in TNLC data.

The time covariance $C_t(t, t_0)$ in the TNLC system is different from TUG (and Fisher-Huse) predictions, but compatible with both the $\lambda_{\text{OJK}} = 1$ [Eq. (2.36)] exponent and with the $\mathscr{H}_{\text{OJK}}(t/t_0)$ scaling function [Fig. 2.15(b)]. This outcome is nontrivial. From one hand, it might constitute the first observation of OJK decay beyond the OJK model itself. In this case, how to explain λ_{FH} found in the thermally-induced TNLC coarsening [40]? Perhaps, the difference in initial condi-

tions could play a role on λ. Further investigations are required. On the other hand, it is not clear whether the observed $\lambda = 1$ is a consequence of the $\mathbb{Z}_2$-symmetry violation. The Author is currently addressing these two points.

The accuracy of our results stems from the electrically-driven quench which is much faster and more controllable than the thermal ones generically used in the vast majority of related experimental studies.

We remark that electro-convection regimes in nematic liquid crystals are fertile fields where pattern formation and phase transitions arise [53, 71, 126]. This distinct feature enables us to experimentally explore quenches both from and to a corresponding critical state *a priori* [126]. The quench from a critical initial condition is theoretically expected to belong to a new universality class featured by $z = 2$, but by different scaling functions [127] and values of λ [36, 37] and θ [50]. However, experimental quantifications of this class remain untouched to the best of our knowledge. Furthermore, the type of quench performed in this study is an interesting candidate to study the relation between two-dimensional coarsening and critical percolation recently proposed [128, 129].

Overall, the suitability of our TNLC system to study diverse types of relaxation dynamics may play a distinct role either for corroborating or for unveiling novel universal aspects underlying the coarsening dynamics of two-dimensional systems.

2.9 Acronyms and Symbols

Acronym	Description
CCD	Charged coupled device
CI	Conformal invariance
DSM	Dynamic scattering mode
FH	Fisher-Huse
HAL	Halogen lamp
LSI	Local scaling invariance
MBBA	N-4-methoxybenzylidene-4-butylaniline
OJK	Ohta-Jasnow-Kawasaki
PBC	Periodic boundary conditions
PC	Personal computer
PID	Proportional-integral-derivative
PVA	Polyvinyl alcohol
RG	Renormalisation group
TBAB	Tetrabutylammonium bromide
TDGL	Time-dependent Ginzburg-Landau
TNLC	Twisted nematic liquid crystals
TUG	Theory of unstable growth
WBC	Window boundary conditions

Symbols

Latin Symbols	Description
a	Pixel size of the experimental images ($a \approx 1.82$ μm)
a_1 (a_2, a_3)	Phenomenological parameters of the Landau-Ginzburg free energy
A	Area fraction of the twist phase $\phi = -1$
A'	Universal Bray-Humayun amplitude
A^*	Bray-Humayun amplitude for $d = 2$, $n = 1$ with ρ in the Manhattan metric
b	Universal quantity in the LSI theory
$B_i (i = 1, 2, 3)$	Nonuniversal constants in the LSI theory
C	Amplitude of experimental shrinkage law $\rho(t)$
C'	Amplitude of experimental growth law $r^*(t)$

C_{pd}	Spatial covariance of the persistent index u_{pd}
C_s	Spatial covariance in the TNLC experiment
$\tilde{C}_s$	Spatial covariance for a generic system
$\tilde{C}_t$	Time covariance for a generic system
$\tilde{C}_t$	Time covariance for the TNLC experiment
d	Spatial dimension
d'	Dimension of persistent clusters
d'_{eff}	Effective dimensional exponent for persistent clusters
D_{AC}	Diffusion constant in the Allen-Cahn equation
D_{OJK}	Diffusion constant in the OJK equation
d_f	Universal fractal dimensional of persistent clusters
f_{pd}	Universal correlation function of persistent clusters
F_0 (F_1)	Constants in the TUG context
F	Landau-Ginzburg free energy
g	Dimensionless quantity in the TUG
H	Hamiltonian
i	Represents an integer number
j	Represents an integer number
J	Coupling constant of the Ising model
k	Represents an integer number
k_B	Boltzmann constant
l	Emergent length scale in phase-ordering theories
L_{sys}	Typical lateral size of the experimental images
$L'_{\text{Euc}}(L'_{\text{Man}})$	Piece of length in the Euclidian (Manhattan) space
m	Auxiliary field for the TUG
m_{pd}	Local mass of persistent clusters
m^i_{pd}	Local mass of persistent clusters within the i^{th} window
M	"Magnetization" of the TNLC configuration
M_{pd}	Total mass of persistent clusters
N	Total number of degrees of freedom of a microscopic model
$\boldsymbol{n}$	Nematic director field
$\boldsymbol{n}'$	Local unit vector normal to interfaces

p	Probability of flippling a spin
q	Defined in the LSI theory as $q = (y+1)/(y-1)$
Q	Local persistence probability
$\boldsymbol{r}$	Spatial vector
$\boldsymbol{r}_i$	Position of a domain boundary (interface)
r^*	Typical size of TNLC domains undergoing coarsening
r^*_{pd}	Typical length of nonpersistent clusters
r_a	Microscopic length scale of TNLC persistent degrees of freedom
R	Mean radius of a nearly spherical domain
R'	Local mean radius of a general interface profile
s	Ising spin variable
t	Elapsed time from quench operation
t^*	Equilibration time of TNLC system within a 2.2 mm $\times$ 2.9 mm area
t_0	Reference time $t_0 \leq t$
t_a	Time for which dynamics becomes bidimensional ($t_a \approx 0.5$ s)
t_{micro}	Microscopic time
T	Temperature
T_i	Initial temperature of quench
T_c	Critical temperature
T_f	Final temperature of the quench
u	Auxiliary field of the OJK theory
u_{pd}	Persistence index
v	Shrinking local velocity of an interface
V	Electrical voltage applied to a TNLC cell
V'	Landau-Ginzburg potential
x	Ratio $\lvert\boldsymbol{r}\rvert/r^*$
$\boldsymbol{X}$	Vector in the phase space of thermodynamical coordinates
$\boldsymbol{X}_c$	Critical point
y	Ratio t/t_0
$Y_i (i = 1, 2, 3...)$	Local state variable of the $i-th$ degree of freedom
z	Dynamical scaling exponent
z_{eff}	Effective dynamical exponent related to the shrinkage law
z'_{eff}	Effective dynamical exponent related to the growth law

Greek Symbols	Description
α	Universal angular coefficient for the decay of $C_s(x)$
γ	Incomplete γ function
Γ	Γ function
Δ	Constant $\Delta > 0$
ΔH	Difference in the time-dependent Hamiltonian between $t + \delta t$ and t
δt	Unit time step of a dynamical microscopic model
ζ	Thermal noise
η	Universal exponent for the decay of C_{pd} of persistent clusters
θ	Local persistent exponent
λ	Autocorrelation exponent
μ	Parameter of the TUG
ξ	Thickness of defects in the coarsening dynamics
ρ	Interface density in the Manhattan metric
σ	Scaling exponent associated to X_ξ of CP clusters
τ	Universal Fisher exponent
ϕ	Local order parameter of the TNLC experiment
$\tilde{\boldsymbol{\phi}}$	Local order parameter in phase-ordering theories
Φ	Scaling function in the LSI theory

Others	Description
$\perp$	Normal component of the nematic director field $\boldsymbol{n}$
$\parallel$	Parallel component of the nematic director field $\boldsymbol{n}$
${}_2F_1$	Hypergeometric function
$\epsilon_\perp(\epsilon_\parallel)$	Dielectric constants normal (parallel) to nematic axis $\boldsymbol{n}$
θ_{eff}	Effective local persistent exponent
$(\lambda/z)_{eff}$	Effetive exponent for the C_t decay in time
$\lambda_{\text{FH(OJK,TUG)}}$	Autocorrelation exponent for the FH (OJK, TUG) theory
ρ_{Euc}	Interface density computed in the Euclidian metric
ρ	Interface density
$\sigma_\perp(\sigma_\parallel)$	Electrical conductance normal (parallel) to nematic axis $\boldsymbol{n}$
$\mathbb{M}_{\text{pd}}$	Set of local masses for persistent clusters
$\mathscr{F}$	Universal two-point spatial scaling function

$\mathscr{F}_{\mathrm{OJK(TUG)}}$	OJK (TUG) two-point spatial scaling function
$\mathscr{H}$	Universal two-time scaling function
$\mathscr{H}_{\mathrm{LSI}}$	LSI two-time scaling function

BIBLIOGRAPHY

[1] Nishimori, H., Ortiz, G. Elements of phase transitions and critical phenomena. Oxford University Press, Inc. (2010).
Cited on pages 14 and 15.

[2] Hohenberg, P. C., Halperin, B. I.: Theory of dynamic critical phenomena. Rev. Mod. Phys. **49**, 435-479 (1977).
Cited on pages 15, 16, and 20.

[3] Bray, A. J.: Theory of phase-ordering kinetics. Adv. Phys. **51**, 481-587 (2002).
Cited on pages 16, 18, 19, 28, 38, and 41.

[4] Tartaglia, A., Cugliandolo, L. F., Picco, M.: Percolation and coarsening in the bidimensional voter model. Phys. Rev. E **92**, 042109 (2015).
Cited on page 17.

[5] Cugliandolo, L. F.: Geometric aspects of ordering phenomena. C. R. Physique **18**, 5-18 (2017).
Cited on page 17.

[6] Kawasaki, K.: Kinetics of Ising models, in Phase Transitions and Critical Phenomena, Vol. 2, C. Domb and M. S. Green eds. (Academic Press, London, 1972).
Cited on page 17.

[7] Wu, F. Y.: The Potts model. Rev. Mod. Phys. **54**, 235 (1982).
Cited on page 17.

[8] Clifford, P., Sudbury, A.: A model for spatial conflict. Biometrika **60**, 581 (1973).
Cited on page 17.

[9] See *e.g.*, Dornic, I., Chaté, H., Chave, Chave, J., Hinrichsen, H.: Critical coarsening without surface tension: the universality class of the Voter model. Phys. Rev. Lett. **87**, 045701 (2001).
Cited on pages 17 and 18.

[10] Lifshitz, I. M.: Kinetics of ordering during second-order phase transitions. Sov. Phys. JETP **15**, 939-942 (1962).
Cited on pages 18, 29, 34, and 52.

[11] Allen, S. M., Cahn, J. W.: A microscopic theory for antiphase boundary motion and its application to antiphase domain coarsening. Acta Mettall. **27**, 1085-1095

(1979).
Cited on pages 18, 20, 29, 31, 34, 37, and 52.

[12] Bray, A. J., Rutenberg, A. D.: Growth laws for phase ordering. Phys. Rev. E **49**, R27-R30 (1994).
Cited on pages 18, 29, 34, and 52.

[13] Newman, T. J., Bray, A. J., Moore, M. A.: Growth of order in vector spin systems and self-organized criticality. Phys. Rev. B **42**, 4514-4523 (1990).
Cited on pages 18, 36, and 41.

[14] Amar, J. G., Family, F.: Diffusion annihilation in one dimension and kinetics of the Ising model at zero temperature. Phys. Rev. A **41**, 3258-3262 (1990).
Cited on pages 18 and 36.

[15] Bray, A. J.: Universal scaling function for domain growth in the Glauber-Ising chain. J. Phys. A: Math. Gen. **23**, L67-L72 (1990).
Cited on pages 18, 19, and 36.

[16] Coniglio, A., Zanneti, M.: Multiscaling in growth kinetics. Europhys. Lett. **10**, 575-580 (1989).
Cited on pages 18 and 36.

[17] Kawasaki, K., Yalabik, M. C., Gunton, J. D.: Growth of fluctuations in quenched time-dependent Ginzburg-Landau model systems. Phys. Rev. A **17**, 455-470 (1978).
Cited on pages 18 and 36.

[18] Ohta, T., Jasnow, D., Kawasaki, K.: Universal scaling limit in the motion of random interfaces. Phys. Rev. Lett. **49**, 1223-1226 (1982).
Cited on pages 18, 36, and 38.

[19] Mazenko, G. F.: Theory of unstable thermodynamic systems. Phys. Rev. Lett. **63**, 1605-1608 (1989).
Cited on pages 18, 36, and 38.

[20] Bray, A. J., Humayun, K.: Towards a systematic calculation of the scaling functions for the ordering kinetics of nonconserved fields. Phys. Rev. E **48**, R1609-R1612 (1993).
Cited on pages 18 and 36.

[21] Mazenko, G. F.: Post-Gaussian approximations in phase ordering kinetics. Phys. Rev. E **49**, 3717-3726 (1994).
Cited on pages 18 and 36.

[22] Mazenko, G. F.: Perturbation expansion in phase-ordering kinetics: I. Scalar order parameter. Phys. Rev. E **58**, 1543-1567 (1998).
Cited on pages 18 and 36.

[23] Shannon, R. F., Nagler, S. E., Harkless, C. R.: Time-resolved x-ray-scattering study of ordering kinetics in bulk single-crystal Cu_3Au. Phys. Rev. B **46**, 40 (1992).
Cited on page 20.

[24] Park, B., Stephenson, G. B.: Development of fluctuations into domains during ordering in Fe_3Al. Phys. Rev. Lett. **68**, 1742 (1992).
Cited on page 20.

[25] Wang, X., Mainville, J., Ludwig, K., Flament, X., Finel A.: Ordering kinetics in the long-period superlattice alloy $Cu_{0.79}Pd_{0.21}$. Phys. Rev. B **72**, 024215 (2005).
Cited on page 20.

[26] Orihara, H., Ishibashi, Y.: Dynamics of disclinations in twisted nematics quenched below the clearing point. J. Phys. Soc. Jpn. **55**, 2151-2156 (1986).
Cited on pages 20, 24, 30, 37, and 40.

[27] Dierking, I.: Domain growth scaling at the Isotropic-to-Cholesteric liquid crystal transition. J. Phys. Chem. B **104**, 10642 (2000).
Cited on page 20.

[28] Sicilia, A., Arenzon, J. J., Dierking, I., Bray, A. J., Cugliandolo, L. F., Martínez-Perdiguero, J., Alonso, I., Pintre, C.: Experimental test of curvature-driven dynamics in the phase ordering of a two dimensional liquid crystal. Phys. Rev. Lett. **101**, 197801 (2008).
Cited on page 20.

[29] McNally, L., Bernardy, E., Thomas, J., Kalziqi, A., Pentz, J., Brown, S. P., Hammer, B. K., Yunker, P. J., Ratcliff, W. C.: Killing by Type VI secretion drives genetic phase separation and correlates with increased cooperation. Nat. Commun. **8**, 14371 (2017).
Cited on page 20.

[30] Henkel, M., Pleimling, M.: Non-Equilibrium Phase Transitions Volume 2: Ageing and Dynamical Scaling Far from Equilibrium. Springer Science & Business Media (2010).
Cited on page 19.

[31] Majumdar, S. N.: Persistence in nonequilibrium systems. Curr. Sci. **77**, 370-375 (1999).
Cited on pages 19, 20, and 45.

[32] Bray, A. J., Majumdar, S. N., Schehr, G.: Persistence and first-passage properties in nonequilibrium systems. Adv. Phys. **62**, 225-361 (2013).
Cited on pages 19, 20, and 45.

[33] Fisher, D. S., Huse, D. A.: Equilibrium behaviour of the spin-glass ordered phase. Phys. Rev. B **38**, 386-411 (1988).
Cited on pages 19, 41, 43, and 52.

[34] Newman, T. J., Bray, A. J.: New exponent for dynamic correlations in domain growth. J. Phys. A: Math. Gen. **23**, L279-L284 (1990).
Cited on page 19.

[35] Newman, T. J., Bray, A. J.: Dynamic correlations in domain growth: a 1/n expansion. J. Phys. A: Math. Gen. **23**, 4492-4507 (1990).
Cited on page 19.

[36] Humayun, K., Bray, A. J.: Non-equilibrium dynamics of the Ising model for T $\leq$ T_c. J. Phys. A: Math. Gen. **24**, 1915-1930 (1991).
Cited on pages 19, 41, and 53.

[37] Corberi, F., Villavicencio-Sanchez, R.: Role of initial state and final quench temperature on aging properties in phase-ordering kinetics. Phys. Rev. E **93**, 052105 (2016).
Cited on pages 19, 41, and 53.

[38] Bray, A. J., Derrida, B.: Exact exponent λ of the autocorrelation function for a soluble model of coarsening. Phys. Rev. E **51**, R1633 - R1636 (1995).
Cited on page 19.

[39] Brown, G., Rikvold, P. A., Sutton, M., Grant, M.: Speckle from phase-ordering systems. Phys. Rev. E **56**, 6601-6612 (1997).
Cited on pages 19 and 41.

[40] Mason, N., Pargellis, A. N., Yurke, B.: Scaling behaviour of two-time correlations in a twisted nematic liquid crystal. Phys. Rev. Lett. **70**, 190-193 (1993).
Cited on pages 19, 24, 30, 41, 42, 43, 44, and 52.

[41] Liu, F., Mazenko, G.: Nonequilibrium autocorrelations in phase-ordering dynamics. Phys. Rev. B **44**, 9185-9191 (1991).
Cited on pages 19, 42, and 52.

[42] Midya, J., Majumder, S., Das, S. K.: Aging in ferromagnetic ordering: full decay and finite-size scaling of autocorrelation. J. Phys.: Condens. Matter **26**, 452202 (2014).
Cited on pages 19 and 42.

[43] Vadakkayil, N., Chakraborty, S., Das, S. K.: Finite-size scaling study of aging during coarsening in non-conserved Ising model: The case of zero temperature quench. arXiv: 1806.00312v1 (2018).
Cited on pages 19 and 42.

[44] Yeung, C., Jasnow, D.: Two-time correlations, self-averaging, and an analytically solvable model of phase-ordering dynamics. Phys. Rev. B **42**, 10 523 - 10 535 (1990).
Cited on pages 19, 41, 43, and 52.

[45] Bray, A. J., Derrida, B., Godrèche, C.: Non-trivial algebraic decay in a soluble model of coarsening. Europhys. Lett. **27**, 175-180 (1994).
Cited on pages 20 and 45.

[46] Derrida, B., Hakim, V., Pasquier, V.: Exact first-passage exponents of 1D domain growth: Relation to a reaction-diffusion model. Phys. Rev. Lett. **75**, 751-754 (1995).
Cited on pages 20 and 45.

[47] Derrida, B., Hakim, V., Pasquier, V.: Exact exponent for the number of persistent spins in the zero-temperature dynamics of the one-dimensional potts model. J. Stat. Phys. **85**, 753-797 (1996).
Cited on pages 20 and 45.

[48] Lee, B. P., Rutenberg, A. D.: Persistence, poisoning, and autocorrelations in dilute coarsening. Phys. Rev. Lett. **79**, 4842-4845 (1997).
Cited on pages 20 and 45.

[49] Poplavskyi, M., Schehr, G.: Exact persistence exponent for the $2D$-Diffusion equation and related Kac Polynomials. Phys. Rev. Lett. **121**, 150601 (2018).
Cited on pages 20, 21, 45, and 46.

[50] Blanchard, T., Cugliandolo, L. F., Picco, M.: Persistence in the two dimensional ferromagnetic Ising model. J. Stat. Mech. **2014**, P12021 (2014).
Cited on pages 21, 45, 46, 52, and 53.

[51] Yurke, B., Pargellis, A. N., Majumdar, S. N., Sire, C.: Experimental measurement of the persistence exponent of the planar Ising model. Phys. Rev. E **56**, R40-R42 (1997).
Cited on pages 21, 24, 30, 31, and 45.

[52] Jain, S., Flynn, H.: Scaling and persistence in the two-dimensional Ising model. J. Phys. A.: Math. Gen. **33**, 8383-8388 (2000).
Cited on pages 21, 50, and 51.

[53] de Gennes, P.G., Prost, J.: The Physics of Liquid Crystals. International Series of Monographs on Physics, vol. **83**, 2nd ed. Oxford Univ. Press, New York (1995).
Cited on pages 22, 23, and 53.

[54] Frank, F. C.: I. Liquid crystals. On the theory of liquid crystals. Disc. Faraday Soc. **25**, 19-28 (1958).
Cited on page 22.

[55] Jérôme, B.: Surface effects and anchoring in liquid crystals. Rep. Prog. Phys. **54**, 391-451 (1991).
Cited on page 22.

[56] Williams, R., J. Chem. Phys. **39**, 384-388 (1963).
Cited on page 23.

[57] Carr, E. F.: Influence of electric fields on the molecular alignment in the liquid crystal p-(anisalamino)-phenyl acetate. Mol. Cryst. Liq. Cryst. **7**, 253-268 (1969).
Cited on page 23.

[58] Helfrich, W.: Conduction-induced alignment of nematic liquid crystals: Basic model and stability considerations. J. Chem. Phys **51**, 4092-4105 (1969).
Cited on page 23.

[59] Dubois-Violette, E., de Gennes, P. G., Parodi, O.: Hydrodynamic instabilities of nematic liquid crystals under a.c. electric fields. J. Phys. (Paris) **32**, 305-317 (1972).
Cited on page 23.

[60] Ribotta, E., Joets, A., Lei, L.: Oblique roll instability in an electroconvective anisotropic fluid. Phys. Rev. Lett. **56**, 1595-1597 (1986).
Cited on page 23.

[61] Joets, A., Ribotta, R.: Hydrodynamic transitions to chaos in the convection of an anisotropic fluid. J. Physique **47**, 595-606 (1986).
Cited on page 23.

[62] Kai, S., Zimmermann, W.: Pattern dynamics in the electrohydrodynamics of nematic liquid crystals. Prog. Theor. Phys. Suppl. **99**, 458-492 (1989).
Cited on page 23.

[63] Joets, A., Yang, X. D., Ribotta, R.: Singularities in the transitions to chaos of a convective anisotropic fluid. Physica D **23**, 235-239 (1986).
Cited on page 23.

[64] Heilmeier, G. H., Zanoni, L. A., Barton, L. A.: Dynamic scattering: A new electrooptic effect in certain classes of nematic liquid crystals. Proc. IEEE **56**, 1162-1171 (1968).
Cited on page 23.

[65] Sussman, A.: Secondary hydrodynamic structure in dynamic scattering. Appl. Phys. Lett. **21**, 269-272 (1972).
Cited on page 23.

[66] Nehring, J., Petty, M. S.: The formation of threads in the dynamic scattering mode of nematic liquid crystals. Phys. Lett. A,**40**, 307-308 (1972).
Cited on page 23.

[67] Chang, R.: "Secondary" dynamic scattering in negative nematic liquid crystal films. J. Appl. Phys. **44**, 1885-1887 (1973).
Cited on page 23.

[68] Krupowski, T., Ruszkiewicz, W.: Evidence for anisotropic expansion of secondary dynamic scattering. Mol. Cryst. Liq. Cryst. **49**, 47-54 (1978).
Cited on page 23.

[69] Nagaya, T., Takeda, T., Orihara, H.: Dynamic image analysis for dynamic scattering modes in nematic liquid crystal. J. Phys. Soc. Jpn. **68**, 3848-3852 (1999).
Cited on page 23.

[70] Strangi, G., Versace, C., Scaramuzza, N., Lucchetta, D. E., Carbone, V., Bartolino, R.: Photopolarimetric characterisation of the transition between two turbulent states in a nematic liquid crystal film. Phys. Rev. E **59**, 5523-5527 (1999).
Cited on page 23.

[71] Kai, S., Zimmermann, W., Andoh, M., Chizumi, N.: Spontaneous nucleation of turbulence in electrohydrodynamics and its similarity with crystal growth. J. Phys. Soc. Jpn. **58**, 3449-3452 (1989).
Cited on pages 23 and 53.

[72] Mauguin, Ch.: Sur les cristaux liquides de Lehmann. Bull. Soc. Fr. Miner. **34**, 71-117 (1911).
Cited on page 23.

[73] Geurst, J. A., Spruijt, A. M. J., Gerritsma, C. J.: Dynamics of $s = 1/2$ disclinations in twisted nematic. J. Physique **36**, 653-664 (1975).
Cited on page 24.

[74] Kibble, T. W. B.: Topology of cosmic domains and strings. J. Phys. A.: Math. Gen. **9**, 1387-1398 (1976).
Cited on page 24.

[75] Zurek, W. H.: Cosmological experiments in condensend matter systems. Phys. Rep. **276**, 177-221 (1996).
Cited on page 24.

[76] Stumpf, M. P. H., Porter, M. A.: Critical truths about power laws. Science **335**, 665-666 (2012).
Cited on page 28.

[77] Becker, M. E., Kilian, R. A., Kosmowski, B. B., Mlynski, D. A.: Alignment properties of rubbed polymer surfaces. Mol. Cryst. Liq. Cryst. **132**, 167-180 (1986).
Cited on page 30.

[78] Nagaya, T., Orihara, H., Ishibashi, Y.: Collective motion of an assembly of disclinations in the non-orthogonally twisted nematics quenched below the clearing point. J. Phys. Soc. Jpn. **56**, 3086-3091 (1987).
Cited on page 30.

[79] Fazio, V. S. U., Komitov, L.: Alignment transition in a nematic liquid crystal due to field-induced breaking of anchoring. Europhys. Lett. **46**, 38-42 (1999).
Cited on page 30.

[80] Porod, V. G.: Die Rontgenkleinwinkelstreuung von dichtgepackten kolloiden systemen I. Teil. Kolloid-Zeitschrift **124**, 83-114 (1951).
Cited on page 34.

[81] Porod, V. G.: Die Rontgenkleinwinkelstreuung von dichtgepackten kolloiden systemen II. Teil. Kolloid-Zeitschrift **125**, 51-57 (1952).
Cited on page 34.

[82] Bray, A. J., Puri, S.: Asymptotic structure factor and power-law tails for phase ordering in systems with continuous symmetry. Phys. Rev. Lett. **67**, 2670-2673 (1991).
Cited on page 35.

[83] Bray, A. J., Humayun, K.: Universal amplitudes of power-law tails in the asymptotic structure factor of systems with topological defects. Phys. Rev. E **47**, R9-R12 (1993).
Cited on pages 35, 36, and 52.

[84] Binder, K., Stauffer, D.: Theory for the slowing down of the relaxation and spinodal decomposition of binary mixtures. Phys. Rev. Lett. **33**, 1006-1009 (1974).
Cited on page 36.

[85] Marro, J., Lebowitz, J. L., Kalos, M. H.: Computer simulation of the time evolution of a quenched model alloy in the nucleation region. Phys. Rev. Lett. **43**, 282-285 (1979).
Cited on page 36.

[86] Furukawa, H.: Structure functions of quenched off-critical binary mixtures and renormalizations of mobilities. Phys. Rev. Lett. **43**, 136-139 (1979).
Cited on page 36.

[87] Wickham, R. A., Mazenko, G. F.: Phase ordering of the $O(2)$ model in the post-Gaussian approximation. Phys. Rev. E **55**, 2300-2313 (1997).
Cited on page 36.

[88] Humayun, K., Bray, A. J.: Scaling functions in phase-ordering dynamics: A comparison of theory and simulations. Phys. Rev. B **46**, 10594-10599 (1992).
Cited on pages 36 and 39.

[89] Brown, G., Rikvold, P. A., Grant, M.: Universality and scaling for the structure factor in dynamic order-disorder transitions. Phys. Rev. E **58**, 5501-5507 (1998).
Cited on pages 36 and 39.

[90] Lavergne, F. A., Aarts, D. G. A. L., Dulles, R. P. A.: Anomalous grain growth in a polycrystalline monolayer of colloidal hard spheres. Phys. Rev. X **7**, 041064 (2017).
Cited on page 37.

[91] Emmot, C. L.: Perturbative corrections to the Ohta-Jasnow-Kawasaki theory of phase-ordering dynamics. Phys. Rev. E **58**, 5508-5528 (1998).
Cited on page 38.

[92] Mazenko, G. F.: Theory of unstable growth. Phys. Rev. B **42**, 4487-4505 (1990).
Cited on pages 38 and 39.

[93] Mazenko, G. F.: Universal features in growth kinetics: Some experimental tests. Phys. Rev. B **43**, 8204-8210 (1991).
Cited on page 38.

[94] Yeung, C.: Direct test of the Gaussian auxiliary field ansatz in nonconserved order parameter phase ordering dynamics. Phys. Rev. E **97**, 062107 (2018).
Cited on page 40.

[95] Cugliandolo, L. F.: "Course 7: Dynamics of glassy systems." Slow Relaxations and Nonequilibrium Dynamics in Condensed Matter. Springer, Berlin, Heidelberg, 367-521 (2003).
Cited on page 41.

[96] Hérisson, D., Ocio, M.: Fluctuation-Dissipation ratio of a spin glass in the ageing regime. Phys. Rev. Lett. **88**, 257202 (2002).
Cited on page 41.

[97] Maggi, C., Di Leonardo, R., Dyre, J. C., Ruocco, G.: Generalized fluctuation-dissipation relation and effective temperature in off-equilibrium colloids. Phys. Rev. B **81**, 104201 (2010).
Cited on page 41.

[98] Takeuchi, K. A., Sano, M.: Evidence for geometry-dependent universal fluctuations of the Kardar-Parisi-Zhang interface in liquid-crystal turbulence. J. Stat. Phys. **147**, 853-890 (2012).
Cited on pages 41 and 45.

[99] Furukawa, H.: Multi-time scaling for phase separation. J. Phys. Soc. Jpn. **58**, 216-221 (1989).
Cited on page 41.

[100] Stauffer, D. Aharony, A.: Introduction to Percolation Theory, 2nd ed. Taylor and Francis group, London (1994).
Cited on page 41.

[101] Henkel, M., Piccone, A., Pleimling, M.: Two-time autocorrelation function in phase-ordering kinetics from local scale invariance. Europhys. Lett. **68**, 191-197 (2004).
Cited on pages 41, 42, and 44.

[102] Henkel, M.: Phenomenology of local invariance: from conformal invariance to dynamical scaling. Nucl. Phys. B **641**, 405-486 (2002).
Cited on page 41.

[103] Picone, A., Henkel, M.: Local scale-invariance and ageing in noisy systems. Nucl. Phys. B **688**, 217-265 (2004).
Cited on page 41.

[104] Aurzada F., Simon T.: Persistence probabilities and exponents. Lévy Matters V. Lectures Notes in Mathematics **2149**, 183-224 (2015).
Cited on page 45.

[105] Redner, S.: A guide to first-passage processes. Cambridge University Press, Cambridge, (2001).
Cited on page 45.

[106] Derrida, B., Bray, A. J., Godrèche, C.: Nontrivial exponents in the zero-temperature dynamics of the 1d Ising and Potts models. J. Phys. A.: Math. Gen. **27**, L357-L361 (1994).
Cited on page 45.

[107] Stauffer, D.: Ising spinodal decomposition at $T = 0$ in one to five dimensions. J. Phys. A.: Math. Gen. **27**, 5029-5032 (1994).
Cited on pages 41 and 45.

[108] Marcos-Martin, M., Beysens, D., Bouchaud, J. P., Godrèche C., Yekutieli, I.: Self-diffusion and 'visited' surface in the droplet condensation problem (breath figures). Physica A **214**, 396-412 (1995).
Cited on pages 45 and 46.

[109] Tam, W. Y., Zeitak, R., Szeto, K. Y., Stavans, J.: First-passage exponent in two-dimensional soap froth. Phys. Rev. Lett. **78**, 1588-1591 (1997).
Cited on page 45.

[110] Soriano, J., Braslavsky I., Xu, D., Krichevsky, O., Stavans, J.: Universality of persistence exponents in two-dimensional Ostwald ripening. Phys. Rev. Lett. **103**, 226101 (2009).
Cited on page 45.

[111] Majumdar, S. N., Sire, C., Bray, A. J., Cornell, S. J.: Nontrivial exponent for simple diffusion. Phys. Rev. Lett. **77**, 2867-2870 (1996).
Cited on page 45.

[112] Derrida, B., Hakim, V., Zeitak, R.: Persistent spins in the linear diffusion approximation of phase ordering and zeros of stationary Gaussian processes. Phys. Rev. Lett. **77**, 2871-2874 (1996).
Cited on page 45.

[113] Newman, T. J., Toroczkai, Z.: Diffusive persistence and the "sign-time" distribution. Phys. Rev. E **58**, R2685-R2688 (1998).
Cited on page 45.

[114] Wong, G. P., Mair, R. W., Walsworth, R. L.: Measurement of persistence in 1D diffusion. Phys. Rev. Lett. **86**, 4156-4159 (2001).
Cited on page 45.

[115] Krapivsky, P. L., Ben-Naim, E., Redner, S.: Kinetics of since-species annihilation. Phys. Rev. E **50**, 2474-2481 (1994).
Cited on page 45.

[116] Cardy, J.: Proportion of unaffected sites in a reaction-diffusion process. J. Phys. A.: Math. Gen. **28**, L19-L24 (1995).
Cited on page 45.

[117] Krug, J., Kallabis, H., Majumdar, S.N., Cornell, S.J., Bray, A.J., Sire, C.: Persistence exponents for fluctuating interfaces. Phys. Rev. E **56**, 2702-2712 (1997).
Cited on pages 45, 99, and 102.

[118] Dougherty, D. B., Lyubinetsky, I., Williams, E. D., Constantin, M., Dasgupta, C., Das Sarma, S.: Experimental persistence probability for fluctuating steps. Phys. Rev. Lett. **89**, 136102 (2002).
Cited on page 45.

[119] Merikoski, J., Maunuksela, J., Myllys, M., Timonen, J., Alava, M. J.: Temporal and spatial persistence of combustion fronts in paper. Phys. Rev. Lett. **90**, 024501 (2003).
Cited on page 45.

[120] Efraim, Y., H. Taitelbaum.: Persistence in reactive-wetting interfaces. Phys. Rev. E **84**, 050602(R) (2011).
Cited on page 45.

[121] Majumdar, S. N., Sire, C.: Survival probability of a Gaussian non-Markovian process: application to the $T = 0$ dynamics of the Ising model. Phys. Rev. Lett. **77**, 1420-1423 (1996).
Cited on page 45.

[122] Zanette, D. H.: Distribution of persistent sites in diffusing systems. Phys. Rev. E **55**, 2462-2464 (1997).
Cited on pages 46 and 50.

[123] Manoj, G., Ray, P.: Scaling and fractal formation in persistence. J. Phys. A.: Math. Gen. **33**, L109-L114 (2000).
Cited on pages 46, 50, and 52.

[124] Bray, A. J., O'Donoghue, S. J.: Unusual dynamical scaling in the spatial distribution of persistent sites in one-dimensional Potts models. Phys. Rev. E **62**, 3366-3375 (2000).
Cited on page 49.

[125] Vicsek, T.: Fractal Growth Phenomena. 2nd ed. World Scientific, Singapore (1992).
Cited on pages 47 and 51.

[126] Takeuchi, K. A., Kuroda, M., Chaté, H., Sano, M.: Directed percolation criticality in turbulent liquid crystals. Phys. Rev. Lett. **99**, 234503 (2007).
Cited on page 53.

[127] Bray, A. J., Humayun, K., Newman, T. J.: Kinetics of ordering for correlated initial conditions. Phys. Rev. B **43**, 3699-3702 (1991).
Cited on page 53.

[128] Arenzon, J. J., Bray, A. J., Cugliandolo, L. F., Sicilia, A.: Exact results for curvature-driven coarsening in two dimensions. Phys. Rev. Lett. **98**, 145701 (2007).
Cited on page 53.

[129] Blanchard T., Cugliandolo, L. F., Picco, M., Tartaglia, A.: Critical percolation in the dynamics of the 2D ferromagnetic Ising model. J. Stat. Mech. **2017**, 113201 (2017).
Cited on page 53.

3

CRITICAL PERCOLATION IN TWO-DIMENSIONAL COARSENING

The study of coarsening phenomena was largely focused on the statistics of space-time correlation functions [1, 2] and response functions [3–5] for more than 50 years. Much less attention was comparatively paid to the geometry of patterns, except by early efforts due to Lifshitz and Slyozov [6], Wagner [7], and by the study of systems with cellular structures [8, 9] such as polycrystalline films, soap froths and biological tissues. The situation has changed over the last decade; geometrical aspects of two-dimensional domains turn out to become in a centre of attention due to connections [10] with the universal critical percolation (CP) statistics [11]. Indeed, for CP and for critical phenomena at thermodynamical equilibrium, the geometry of clusters develops a fractal structure that is characterized by universal scaling exponents, as it happens in the paradigmatic d-dimensional Ising model at the Curie point ($d > 1$). Similar scenario takes place for absorbing (nonequilibrium) phase transitions at criticality [12]. In all these examples, however, scale-invariant behaviour arises only around a rather special point in the phase space, which is typically reached by tuning external control parameters. But what about dissipative systems that, via domain coarsening, relax towards an equilibrium state? In this Chapter, we tacke this question from an experimental approach. After a brief introduction on percolation in Sec. 3.1, we use the methods described in Sec. 3.2 to perform a morphological analysis for a *nonequilibrium* system undergoing coarsening. Specifically, we study the geometrical aspects of two-dimensional twisted nematic liquid crystals (TNLC) domains. Domains are spontaneously formed after a TNLC layer is electrically-quenched from a nematic-turbulent (disordered) phase towards a nearly $\mathbb{Z}_2$ symmetric phase. The TNLC coarsening dynamics belongs to the model A universality class, as shown by the Author in the previous Chapter. The

results of the current research, contained in Sec. 3.3, remarkably give evidence that, during the phase-ordering kinetics, TNLC system seems to *self-tune* to a CP state that renders fractal structures at length scales much larger than the typical TNLC domain size, here noted as $r^*(t)$. Recent simulations of two-dimensional coarsening dynamics suggest that such a coarsening-CP coexistence implies the existence of an additional length scale $r_p^*(t) \sim t^{1/z_p}$ that grows faster than $r^*(t) \sim t^{1/z}$ with a new dynamical exponent $z_p < z$ (z is the coarsening dynamical exponent). We are able not only to measure CP statistics in the nonequilibrium TNLC dynamics, but also to estimate z_p experimentally. Our results, therefore, also suggests that a correction in the fundamental scaling hypothesis for two-dimensional scalar model A systems shall be made. This result is in consonance with recent numerical results [13–16].

3.1 Topic introduction

Elementary concepts of scaling percolation theory and of its emergence in coarsening dynamics are presented. Section 3.1.1 introduces a few universal aspects of critical percolation. Consequences of CP statistics coexisting with two-dimensional coarsening, generically supported by numerical-based evidence, are described in Sec. 3.1.2.

3.1.1 Percolation phase transition

In disordered media where the connectivity between elements is random, such as in porous rocks and in fiber papers, the spreading of a fluid through the structure is a geometrical-dependent problem in the regime of weak external fields. The fluid is said to percolate when it entirely spreads from one side of the medium to the opposite side. Percolation processes, in a broader sense, deal with the influence of random media on the spreading of information and matter. The idea was introduced by Flory to study gelation in branched molecule mixtures [18], conceptually generalized in the seminal work by Broadbent and Hammerseley [19], and since then has been explored by physicists [11,20–23] and mathematicians [24–29] because of its simple definition, yet nontrivial geometrical (in some versions dynamical [12]) properties. At specific tuning parameters, percolation models may display scaling invariance and universality, with an intimate analogy to critical phenomena at thermal equilibrium [35].

Here we deal with the simplest type of percolation, namely undirected and uncorrelated percolation. To introduce it, we describe a particular family of models called *site* percolation models. Consider a d-dimensional regular lattice $\mathbb{Z}^d$ of lateral size L and coordination number Λ. Sites are independently occupied with probability p, but remain unoccupied otherwise. The set of occupied sites that are connected one to another by nearest-neighbour bonds is defined as a *cluster* – examples of clusters generated in the square lattice for $d = 2$ are shown in Fig. 3.1. A

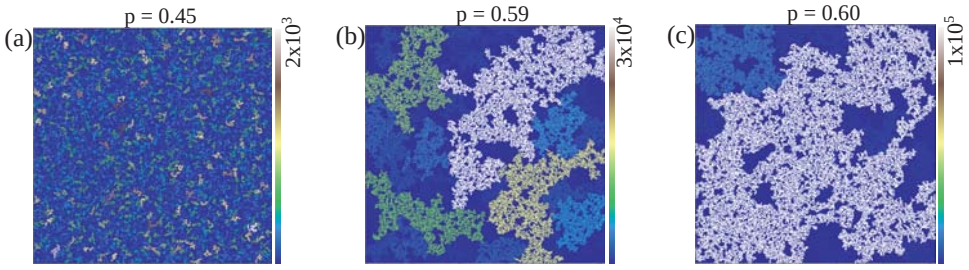

Figure 3.1: Clusters generated by the site percolation model in a square lattice, lateral size $L = 512$, for different occupation probabilities: well below (a) $p = 0.45$, sligthly below (b) $p = 0.59$, and sligthly above (c) $p = 0.60$ the critical threshold for the infinite lattice-size limit $p_c \approx 0.592746$ [31]. Colours refer to the sizes of clusters. The size is the number of sites belonging to a cluster.

cluster that spans, *i.e.* percolates, through the system appears with a finite spanning probability $P_s(p, L)$ if p is high enough. At the limit $L \to \infty$, these models display a percolation phase transition around a sharp critical point, $p_c(d, \Lambda)$, for which $\lim_{L\to\infty} P_s(p \leq p_c) = 0$[1], but $\lim_{L\to\infty} P_s(p > p_c) = 1$. The order parameter for the transition is the probability $P_\infty(p, L)$ that a site belongs to the spanning cluster[2]. The quantity $P_\infty(p) = \lim_{L\to\infty} P_\infty(p, L)$ is nonzero only for $p > p_c$ and continously grows with increasing p. Around $p_c(d, \Lambda)$, a conjecture predicts $P_\infty(p) \sim |p - p_c|^\beta$ in analogy to critical systems at thermodynamic equilibrium; β is a universal exponent.

Scaling hypothesis

The quantities of interest in percolation are related to the number and features x (x = perimeter, mass, hull area, *etc.*) of the formed clusters with corresponding values X. Around $p_c(d, \Lambda)$, scaling *hypothesis* for percolation [11, 20, 21] states there is a single relevant scale $X_\xi(p)$ into the problem that diverges as $X_\xi(p) \simeq |p - p_c|^{-1/\sigma_x}$ with the gap exponent $1/\sigma_x$. The number of clusters per lattice site, $n_x(p, X)dX$, with a certain geometrical feature x whose values are between X and $X + dX$ is written according to the *hypothesis* (first suggested in [30]), for large X as:

$$n_x(p, X) \sim X^{-\tau_x} f_x(X/X_\xi(p)) \qquad (|p - p_c| \to 0); \tag{3.1}$$

where τ_x is the Fisher exponent [36]; $f_x(\cdot)$ a scaling function with $f_x(0) \equiv C_x$ a universal constant. The set of exponents τ and $1/\sigma$ for the mass of clusters are

[1] It is rigorously known that no spanning cluster exists at $p = p_c$ only for $d = 2$ and $d \geq 19$ [32]. For other dimensions, there is a conjecture of analagous behaviour, but the proof itself has not been obtained yet.

[2] At this point you may wonder on the number of spanning clusters, $n_{\text{spam}}(p)$. It is proved [33] that, for periodic graphs, $n_{\text{spam}}(p)$ is either 0,1 or ∞ for $\forall\ p$. For $\mathbb{Z}^d$ lattices is proved [34] that $n_{\text{spam}}(p)$ is finite, hence, unity above p_c.

rigourously known in $d = 2$ [29]: $\tau = 187/91$ and $1/\sigma = 91/36$. Any other scaling exponent dealing with the mass of clusters can be written in terms of τ and $1/\sigma$ by using scaling relations [20]. The previously introduced β, for example, reads $\beta = (\tau - 2)/\sigma$.

Clusters formed around $p_c(p, \Lambda)$ are structures with scale-invariant statistics at scales $X \ll X_\xi(p)$. Therefore, universal CP statistics are contained at local length scales $l \leq L$, as far as l is smaller than the characteristic scale of clusters. For example, the *local* mean mass $\langle s_{\max}(l;p)\rangle_l$ of the largest cluster found in a d-dimensional hypercubic box of lateral size l, averaged over different boxes of volume l^d, is known to behave as [11]:

$$\langle s_{\max}(l;p)\rangle_l \sim l^{d_f} \qquad (|p - p_c| \to 0), \tag{3.2}$$

where $d_f < d$ is the fractal dimension of clusters that relates to d by:

$$d_f = d/(\tau - 1); \qquad (\text{for} \quad d = 2, \quad d_f = 91/48). \tag{3.3}$$

Exact results in CP statistics: Exceptional case in d = 2

Uncorrelated percolation models are simple to define, but exact results are scarce. Exact values for nonuniversal thresholds $p_c(d, \Lambda)$ [37–39] rigorously obtained for a few specific cases [25, 40, 41] do not include, for instance, the two-dimensional site percolation model on the square lattice[3] – used to generate Fig. 3.1 – nor the honeycomb lattice *etc.* [22]. Regarding the universal aspects of CP statistics, the situation in $d = 2$ is exceptional due to powerful predictions that conformal invariance (CI) can make at this dimension [43]. CI hypothesis was employed [45] to obtain a formula for the universal [44] crossing probability[4] in a finite retangle, which was shown to be in sharp agreement with results from simulations of discrete models [44], and was later rigorously derived [26, 27] by means of the Schramm-Löwner evolution (SLE) theory [46, 47]. The *proof* [28] that CI holds in the continuuum limit of site percolation model on a triangular lattice, in association with the body of acquired knowledge [26,27], culminated in the rigorous derivation of CP exponents [29].

Of notable interest is the exact result [48] for number density $n_h(A)dA$, for the *area of hulls*, *i.e.* the full area enclosed by the external perimeter of a cluster regardless its internal holes. Based on Coulomb gas and CI theories, Cardy and Ziff [48] obtained for CP models, in terms of Eq. (3.1):

$$n_h(A) \simeq A^{-2} C_h; \qquad C_h = 1/(8\pi\sqrt{3}) \qquad (p = p_c). \tag{3.4}$$

Comparing Eq. (3.4) with Eq. (3.1), one realizes:

[3] Evolving from nearly four decades [42], the p_c for site percolation on a square lattice remains a matter of research interest. In $d = 2$, $p_c = 0.59274601(2)$ have been recently obtained by transfer matrix techniques [31].

[4] The probability that a cluster spans horizontally (or vertically) inside a retangle.

$$\tau_h = 2; \qquad f_h(0) = C_h. \tag{3.5}$$

3.1.2 Critical percolation & coarsening

For two-dimensional scalar model A dynamics, domain boundaries *shrink* independently from domain to domain in the scaling regime (neither fission nor coalescences happen) [1]. The local velocity of shrinking $v(\boldsymbol{r}_i, t)$, normal to the interface at the point $\boldsymbol{r}_i$, is proportional to the local interface curvature $\kappa(\boldsymbol{r}_i, t)$ according to the Allen-Cahn equation [49]:

$$v(\boldsymbol{r}_i, t) = -\frac{\lambda_h}{2\pi}\kappa(\boldsymbol{r}_i, t), \tag{3.6}$$

where λ_h is a model-dependent diffusion coefficient, and 2π is a constant for later mathematical convenience. Notice that the time evolution $A(t, A_p)$ for the hull area, with initial area A_p at time t_p ($t_p \leq t$), can be obtained by integrating $v(\boldsymbol{r}_i, t)$ along the hull boundary:

$$\frac{dA(t, A_p)}{dt} = \oint v(\boldsymbol{r}_i, t)dr = -\frac{\lambda_h}{2\pi}\oint \kappa(\boldsymbol{r}_i, t)dr = -\lambda_h, \tag{3.7}$$

where dr is an infinitesimal length of the interface; the last equality results from the Gauss-Bonnet theorem. As described in the previous section, a key quantity for clusters in the percolation model is $n_x(p, X)$ [Eq. (3.1)]. By analogy, similar quantities can be inquired for mosaics arising in coarsening dynamics. The number density of hulls with area A at the mosaic at time t, $n_h(A, t)dA$, can be formally written in terms of its number density at the past $n_h(A_p, t_p)dA_p$ as:

$$n_h(A, t) = \int_0^\infty dA_p \delta[A - A(t, A_p)]n_h(A_p, t_p). \tag{3.8}$$

Since Eq. (3.7) provides $A(t, A_p)$ for two-dimensional scalar model A systems, the full time evolution of $n_h(A, t)$ is determined given $n_h(A_p, t_p)$ is available. But what is the exact form of $n_h(A_p, t_p)$? *Assuming* that $n_h(A_p, t_p)$ is given by the exact Cardy-Ziff result for CP statistics [Eq. (3.4)], Arenzon *et al.* [13] derived (using Eq. (3.8) and Eq. (3.7)):

$$n_h(A, t) = A^{-2}(2)f_h(A/\lambda_h t); \quad f_h(A/\lambda_h t) = \frac{C_h}{(1 + (A/\lambda_h t)^{-1})^2} \quad (t \gg t_p). \tag{3.9}$$

Here, $f_h(\cdot)$ is the (time-dependent) scaling function of Cardy-Ziff [Eq. (3.5)]. The factor two stems from the counting of hulls in the two phases of the coarsening dynamics (while Cardy-Ziff's result counts only hulls corresponding to occupied sites in the language of percolation models). Equation (3.9) is surprisingly in fine agreement with results obtained from the Ising-Glauber model quenched from the

paramagnetic to the ferromagnetic phase at zero temperature [13]. Only partial agreement, however, is obtained with data from a thermally-induced coarsening of chiral smectics [50]. The *hypothesis* of CP interplaying with coarsening at regimes $t \gg t_p$ was further explored by means of bimodal spin models in more detail [17], observed to accurately account for the crossing probabilities of model A dynamics [14, 15], and to hold in symmetric discrete model B systems [51, 52], voter dynamics [53], and to be robust against weak disorders [54–56]. No experimental result, beyond the effort to glimpse $n_h(A,t)$ in [54], however, upholds such a numerical-based knowledge.

The approach to CP statistics

The configuration $\{\phi(\boldsymbol{r}, t=0)\}$ of local order parameter $\phi = \pm 1$ in the two-dimensional Ising model on a square lattice at the infinite temperature limit, $\lim T \to \infty$, corresponds to the configuration $\{n(\boldsymbol{r}, p)\}$, with $n(\boldsymbol{r}, 1/2) := (\phi(\boldsymbol{r}, 0)+1)/2$, of the occupation number ($n = 0, 1$) in the site percolation model for $p = 1/2$. Since $1/2 < p_c$, $p_c \approx 0.59$ [31], there can not be spanning cluster at $t = 0$: $P_s(1/2) = 0$ [Fig. 3.2(a)].

By quenching the Ising model from $\lim T \to \infty$ to *any* subcritical T under either Glauber or Kawasaki dynamics (with isotropic interactions at the absence of external fields), overwhelming simulational data for nonconserved [16, 55, 57] and conserved [58, 59] dynamics *suggest* there exists a characteristic time t_p, time dependent on the system size,

$$t_p(L, \Lambda) \sim L^{z_p(\Lambda)}, \tag{3.10}$$

from which spanning domain(s) stabilize in the mosaic [example in Fig. 3.2]. Such spanning domain(s) turn out to dictate the fate of the phase ordering. $z_p(\Lambda)$ is a lattice-geometry dependent exponent ($z_p < z$). Existence of $t_p(L, \Lambda)$ implies that there is a typical percolation-related length, $r_p^*(t, \Lambda)$, that for nonconserved dynamics grows as $r_p^*(t, \Lambda) \sim t^{1/z_p(\Lambda)}$ [16, 57].

The approach to a percolative state at t_p occurs during the early regime $0 \leq t \ll t_p$. But how does it happen if $P_s(p = 1/2) = 0$ at $t = 0$? Notice that for unbiased coarsening dynamics, the ensemble averaged "magnetization" $\langle \sum_{\boldsymbol{r}} \phi(\boldsymbol{r}, t) \rangle / L^2$ is null as far as $t \ll L^z$. Within this period, length scales can be renormalized by the typical domain size $r^*(t)$ to wash out microscopic ingredients, such as the underlying lattice spacing a, and to recover the paramagnetic (disordered-like) configuration at scales $r \gg r^*(t)$. In terms of the percolation language, iterative renormalizations wash out a and, hence, one approaches to a percolation on *continuum*, for which $p_c = 1/2$ [60]. That is believed [17] to be the reason why coarsening dynamics self tune to a CP state.

Back to the coarsening context, the rapid approach to CP at $t_p(L, \Lambda)$ requires that a few exceptional[5] domains *coaslesce* – prior the scaling regime – in order

[5] In the sense of statistics of extreme events.

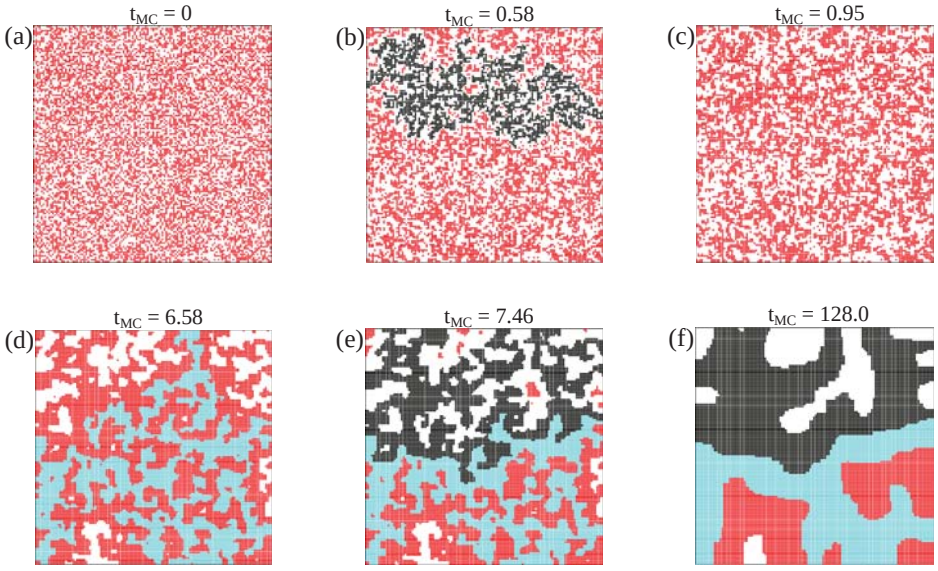

Figure 3.2: Configuration of Ising spins (red and white) during a simulation of the two-dimensional Ising-Glauber model on a square lattice ($L = 128$), free boundary conditions, quenched from $\lim T \to \infty$ to $T = 0$. Percolative domains of the red phase and white phase are highlighted as black and turquoise colours, respectively. The Monte Carlo times steps (t_{MC}) are shown on the top of each panel. (a) No percolative structure exists in the high-temperature phase. Although a spanning cluster appears after a few MC time steps (b), the spanning structure does not exhibit stability (c,d) before a certain characteristic time t_p (e). From t_p onwards, the spanning clusters keep their global shape for long times (f); actually, the shape is kept until the fate of the coarsening dynamics for $T = 0$. Figures reprinted with the permission from IOPscience, extracted from Blanchard *et at.* [16] with the permission of the authors.

to form extremely-large domains of size $r_p^*(t)$ that, due to the coalescences, grow faster than the average size $r^*(t)$.

3.2 Materials and experimental methods

The electrically-triggered coarsening dynamics of TNLC systems is herein analysed from a morphological point of view. We briefly recall the experimental setup we studied previously. The reader may take a look at Chap. 2 for additional information. Algorithms employed for detection of domains and hull areas in the TNLC mosaics are herein described.

3.2.1 The coarsening experiment

We prepared a quasi-bidimensional TNLC cell (14 mm $\times$ 14 mm $\times$ 12 μm) sandwiched between parallel slabs of glass covered with a transparent layer of indium-tin oxide (ITO). The cell was filled with a solution of N-4-methoxybenzylidene-4-butylaniline (purity $> 98.0\%$, Tokyo Chem. Ind., Japan) doped with 0.01 wt$\%$ of tetrabutylammonium bromide (purity $\geq 99.0\%$, Tokyo Chem. Ind., Japan). The ITO layer was, before assembly, coated with polyvinyl alcohol film and mechanically rubbed at mutually orthogonal directions. After filling the cell with liquid crystal, the rubbing directions induced the nematic director field to twist either in left- or right-hand orientation with nearly symmetric roles. We used a thermal controller to keep the cell temperature at 25°C with fluctuations in the order of 0.01°C during the experiment. The twist orientation, here attributed to the local order parameter $\phi(\boldsymbol{r}, t) = \pm 1$, was locally monitored via optical microscopy inside a bidimensional area of $L^2_{\rm sys} = 2.2$ mm $\times$ 2.9 mm. With a charge-coupled device (CCD), the images were taken at the frame rate of 3 s^{-1} and with spatial resolution of $a \approx 1.82$ μm. We prepared a short-range correlated, eletrically-driven nematic-turbulent phase by applying a 100 Hz sinusoidal voltage 70 V between the plates of the capacitor. This phase comprises a plenty of entangled disclination loops (topological defects), where ϕ is ill defined. After letting the system for 120 s in the nematic-disordered phase (corresponding to $\sim 10^4$ correlation times), the system was quenched at $t = 0$ s towards an equilibrium state at the absence of external field. Local twist states $\phi(\boldsymbol{r}, t) = \pm 1$ are formed at the expense of the disentangling and shriking of original disclination loops [Fig. 3.3(a)]. Twist domains grow and compete by space until $t \lesssim t^*(L_{\rm sys})$, with the equilibration time $t^*(L_{\rm sys}) \approx 2.0 \times 10^3$ s. The experiment was performed over 20 times to acquire statistics. We have shown in the previous Chapter 2 that the electrically-triggered coarsening dynamics is an experimental system in the model A universality class. Below, we describe the methodology for analysing the morphology of TNLC mosaics.

3.2.2 Algorithms of domains and hull detection

Domains

In order to detect domains in TNLC coarsening configurations, we used the optimized multi-label algorithm of Hoshen and Kopelman (HK) [61]. Images of the domain coarsening dynamics were regarded as a square lattice of unit spacing $a \approx 1.82$ μm. At each site (i, j) with $i = 1a, 2a, ..., 1028a$ and $j = 1a, 2a, ..., 1608a$, we defined a local variable $u(i, j) = \pm 1$ where $\phi = \pm 1$ and $u = 0$ at the location of interfaces between the twist phases. The width of interfaces was approximated to have the lattice spacing a. Sites for which $u(i, j)$ was equal to a specific value $u_{\rm HM}$, with $u_{\rm HM} = -1, 0, +1$, were considered as *occupied* (notice that only one, among the three possible values for $u_{\rm HM}$, was chosen as a parameter of the code).

For each occupied site (i, j), a cluster label $k_b \in \mathbb{N}$ was given (that is, we updated $u(i, j) \equiv k_b$); k_b refers to the k^{th} detected cluster and its b^{th} given label. Therefore, different sites belonging to the same k cluster could have different labels. These different labels were collected in a finite set $\{k_1, k_2, ..., k_s, ...\}$ where, among the members, only one was considered as the *proper* cluster label; for example, k_s. The proper label was defined as $\min\{k_1, k_2, ..., k_s, ...\}$. We then built a set of numbers $\{W(k_1), W(k_2), ..., W(k_s), ...\}$ with $W \in \mathbb{Z}$ to establish links between k_s and the k_b labels. In this set, only $W(k_s) > 0$, with $W(k_s)$ defined as the total number of sites belonging to the k^{th} cluster. All the other members of the set provided the connections between labels, *e.g.*, $k_1 = -W(k_2)$; $k_s = -W(k_1)$.

In practice, we scanned the $u(i, j)$ matrix column by column j, for each row i. At the first moment an occupied site was found, label counters k and b were set. When a generic occupied site (i, j) was hit, we inquired whether in its neighbourhood, namely sites $(i - 1, j)$ and $(i, j - 1)$, there were occupied sites as well. If there were occupied neighbours, then $u(i, j)$ was updated to the *smallest* proper name of the two neighbouring clusters; otherwise, a new cluster label was attributed using the k counter. Links $W(\cdot)$ were updated at each time an occupied site was analysed. This is the HK algorithm.

After implemented the HK code, the total number of clusters at the image was given by the final value of the k counter. We then relabeled all detected clusters so that sites (i, j) belonging to the k^{th} cluster were labelled to a *single* label (we updated $u(i, j) \equiv k$), where $W(k)$ provided the mass of the k^{th} cluster. Figure 3.3(a-b) shows a result of the domain detection algorithm applied on a mosaic of TNLC domains.

Hulls

A combination of algorithms were used to detect hulls. The final code employed the HK and the relabel sub-algorithms to detect domains. For each detected domain, label k, a biased walk was performed along its external perimeter. When the walker finished its percurse, the area enclosed by the external perimeter (the hull area) $A(k)$ was given. The biased walk code is based on codes by Grossman and Aharony [62], which were later largely modified (and improved for the current purpose) by Sicilia, Arenzon, Bray and Cugliandolo [17]. We describe the manner the code was implemented here. First, pixels at the bottom row $i = 1028a$ of the TNLC image were regarded as a flat substrate of height level $h(i = 1028a, j) \equiv 1a$ for $\forall\, j$. The h axis was vertically oriented from the bottom to the top of the image. This means $h(i, j) \equiv 1029a - i$ for $\forall\, j$. Now we describe the three main steps of the code.

(*Seed*) For each cluster (or domain) k, there is a seed site (i_s, j_s) for which one has $h(i_s, j_s) := \max\{h(i, j)\}$ for sites that satisfy $u(i, j) = k$. If $h(i_s, j_s)$ is not unique, we considered the site for which j_s was minimum. An area counter $A_0(k) = h(i_s, j_s)a$, and a height counter $H_0(k) = h(i_s, j_s)$ were set at this

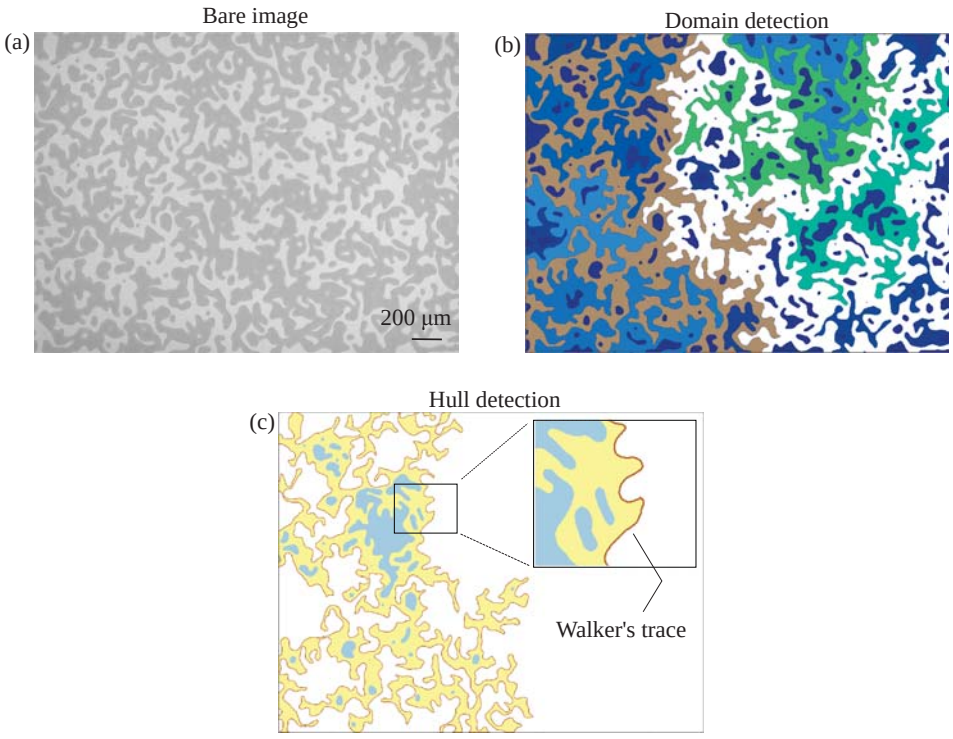

Figure 3.3: (a) Typical TNLC mosaic after 2.66 s from the electrically-triggered quench $t = 0$ s. Different shades of grey colour stand for distinct twist phases. The image is shown as acquired by a video camera. (b) Visualization of the resulting matrix $u(i, j)$ after the algorithm of domain detection was applied on the panel shown in (a). Different colours are used as a scale for the area of domains. (c) The second largest domain in (b) and its inner domains are highlighted with the yellow, grey-blue colours respectively. The path traced by a walker that, performing a biased walk according to the hull algorithm, is shown in brown colour. For the sake of visualization the width of this path (which is unity) was enlarged by a factor 2 to better visualization. Notice the walker goes along the external perimeter of the yellow domain (see zoom in).

stage.

(*Walk*) Starting from the seed (i_s, j_s), the walker tried to contour the external perimeter of a domain by following a clock-wise turn. In order to jumping to a neighbouring site, that is part of the cluster k, the walker initially tried to go towards the upward (2), right (3), down (4), and left (1) directions, respectively. The (q) possible directions of jumping are shown in Fig. 3.4. When a jumping was accepted towards the direction (3), for instance, the next order of jumping was updated to preserve the clock-wise movement; this forces the latest taken direction (3) to be the last option in the next trial. It means the updated order for this example was (4), (1), (2), (3). This reasoning was applied for other directions.

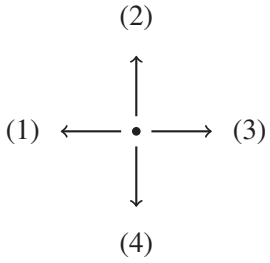

Figure 3.4: Possible directions of jumps performed by the walker. The central black dot stands for a current position (i, j) of the walker. Directions (1), (2), (3) and (4) refer to jumps toward $(i, j - 1a)$, $(i + 1a, j)$,$(i, j + 1a)$,$(i - 1a, j)$ sites, respectively.

(*Area*) Let the latest jumping direction of the walker at step t' be (q_{last}). When the next jumping at $t' + 1$ was accepted towards the (q_{next}) direction, the area counter was updated as $A_{t'+1}(k) = A_{t'}(k) + \Delta A(q_{\text{last}}, q_{\text{next}})$ and $H_{t'+1}(k) = H_{t'}(k) + \Delta H(q_{\text{last}}, q_{\text{next}})$, where $\Delta A(\cdot)$ and $\Delta H(\cdot)$ depend on the pair $(q_{\text{last}}, q_{\text{next}})$ as summarized in Tab. 3.1.

$(q_{\text{last}}, q_{\text{next}})$	ΔA	ΔH
(1,1)	$-a(h'_t(k) - a)$	0
(1,2)	$-a(h'_t(k) - a)$	a
(1,3)	a^2	0
(1,4)	0	$-a$
(2,1)	0	0
(2,2)	0	a
(2,3)	$ah'_t(k)$	0
(2,4)	$ah'_t(k)$	$-a$
(3,1)	a^2	0
(3,2)	0	a
(3,3)	$ah'_t(k)$	0
(3,4)	ah	$-a$
(4,1)	$-a(h'_t(k) - a)$	0
(4,2)	$-a(h'_t(k) - a)$	a
(4,3)	0	0
(4,4)	0	$-a$

Table 3.1: Updates of the area counter $\Delta A(q_{\text{last}}, q_{\text{next}})$ and height counter $\Delta h(q_{\text{last}}, q_{\text{next}})$ depending on the latest (q_{last}) and next (q_{next}) directions taken by the walker.

The code was iterated until the walker returned to the seed. There is an additional rule and one exceptional situation, however. The additional rule: if the last direction taken by the walker before returning to the seed was (1), then it is required to update $A_{t'+1}(k) = A_{t'}(k) - a(h(k) + a)$. There are exceptional situations in which the walker needs to pass twice over the seed until finishing the percurse. In these cases, the walker was sent to a second walking to the unexplored cluster

region. The final enclosed area was obtained by summing up contributions of the two excursions. A typical result for the hull detection applied to the experimenal data is shown in Fig. 3.3(c).

3.3 Results: CP statistics in TNLC coarsening

In Sec. 3.3.1 we revisit the celebrated growth law for coarsening, where we distinguish the contribution of each twist phase to the domain growth, separately. A new universal exponent is introduced to describe the decay of the number of domains in the asymptotic coarsening regime. The exact formula proposed by Arenzon *et al.* [13] is experimentally put in to test against the TNLC experimental data in Sec. 3.3.2. We measure the first exponent in the TNLC coarsening related to CP statistics in this part. Section 3.3.3 contains a detailed analysis for the statistics of extremely large domains. We extract a fractal dimension meaningful for inter-domains scales. The result is compared with the universal fractal dimension of clusters in the CP universality class. Based on our experimental evidence, and noting the numerical data in [57], model A coarsening may be interpreted as a CP model on an inflating lattice; consequences of such a way of thinking are directly probed in the experiment. Finally, still in Sec. 3.3.3, we estimate a value for the new percolation-related exponent $z_p(\Lambda)$. This is the first time that such quantities, universal exponents in CP universality class along with model A dynamics, are measured in an experimental system.

3.3.1 Average number of domains and the growth law

Figure 3.5(a) shows the total number of domains $\langle N_d(t;\phi)\rangle$ in the TNLC mosaic at time t averaged over the ensemble of quench realizations. $\langle N_d(t;\phi)\rangle$ reveals a slight dependence on the twist phase ϕ, not expected for $\mathbb{Z}_2$-symmetric systems. This observation is consistent with the asymmetrical roles played by the twist phases in TNLC systems, as we found previously (Chap. 2). Furthermore, the outcome $\langle N_d(t;-1)\rangle < \langle N_d(t;+1)\rangle$, except at $t \approx t^*(L_{\rm sys})$, might indicate that the ensemble averaged domain area, $\langle A(t;\phi)\rangle$, satisfies $\langle A(t;-1)\rangle > \langle A(t;+1)\rangle$. In that case, $\phi = -1$ domains shall coarsen faster than their competing $\phi = +1$ ones ($\phi = -1$ is the favoured twist phase) [Fig. 3.5(b)].

The time dependence of $\langle N_d(t;\phi)\rangle$ is common for both twist phases. The decay is algebraic over the full range of the relaxation dynamics [Eq. (3.11)], but crossover around $t_c \approx 25$ s:

$$\langle N_d(t;\phi)\rangle \sim t^{-2/\gamma}; \quad 2/\gamma = \begin{cases} 0.91(8) & 2.66\text{ s} \lesssim t \lesssim t_c; \\ 0.54(13) & t_c \lesssim t \lesssim 1000\text{ s}; \end{cases} \tag{3.11}$$

where γ is an exponent we introduce. The behaviour of $\langle N_d(t;\phi)\rangle$ is dictated by the most likely value, $A_{\rm ml}(t;\phi) := \mathrm{Argmax}(\rho_d(A,t;\phi))$ of the probability density

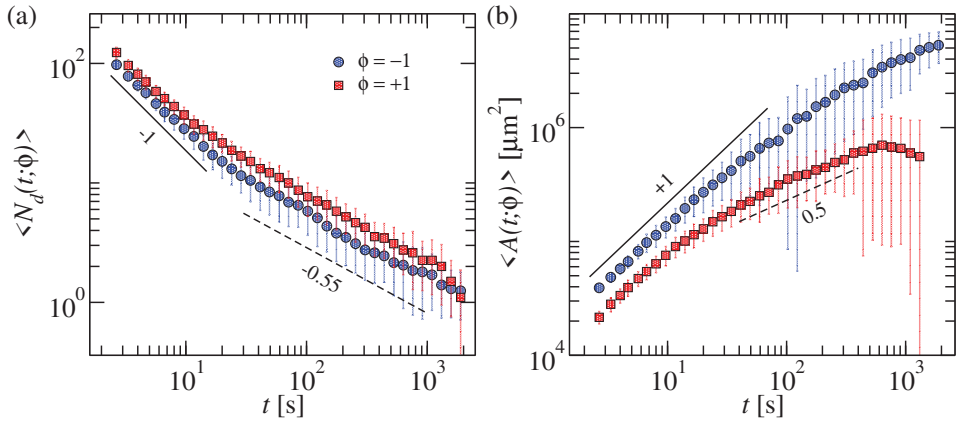

Figure 3.5: (a) Mean total number of domains (ensemble averaged), $\langle N_d(t;\phi)\rangle$, inside the area of observation $L^2_{\rm sys} = 2.2$ mm $\times$ 2.9 mm, for TNLC domains in the unfavoured (favoured) phase $\phi = +1$ ($\phi = -1$). Solid and dashed black line are guide to eyes and have slopes as indicated in the plot. (b) Domain mean area (ensemble averaged) $\langle A(t;\phi)\rangle$ as function of time. Solid black line is a guide to eye and represents the expected growth law for $\mathbb{Z}_2$-symmetric systems belonging to the model A universality class: $A(t;\phi) \sim t^{2/z}$, with $z = 2$.

function (PDF) for the area of domains $\rho_d(A,t;\phi)$. At very initial times ($0 \lesssim t \ll t_c$) domains are abundant and small (order of magnitudes in Fig. 3.5(a-b)). The PDF $\rho_d(A, t \ll t_p;\phi)$ shall be peaked at the typical domain area $(r^*(t))^2 \sim t^1$ with a narrow variance. Thereby $\langle N_d(t;\phi)\rangle \approx L^2_{\rm sys}/[r^*(t)]^2 \sim t^{-1}$, which explains the results in Eq. (3.11). At long times ($t \gg t_c$), however, a wide spectrum of domain areas sets in the mosaic. Notice that, *e.g.*, the domain with the largest area and the domain with a unit size count as the same for the quantity $N_d(t;\phi)$, but this discrepancy is relevant for the mean area. Thus it is easy to understand the relation $\langle N_d(t;\phi)\rangle \sim [r^*(t)]^{-2}$ should not hold in this regime ($t \gg t_c$). In fact, the relation $\langle N_d(t;\phi)\rangle \sim (A_{\rm ml}(t;\phi))^{-1}$ shall hold here, with the hypothesis $A_{\rm ml}(t;\phi) \sim t^{2/\gamma}$, from where we measured $\gamma = 3.70(96)$.

Now we turn to the average area $\langle A(t;\phi)\rangle$ displayed in Fig. 3.5(b). The growth law $\langle A(t;\phi)\rangle \sim t^{2/z}$ ($z = 2$), valid in the scaling regime [1] for model A coarsening dynamics, can be directly tested for each phase, separately. The asymmetry between twist phases affect not only the magnitude of $\langle A(t;\phi)\rangle$, but also the dynamical exponent z. Here we define z_- (z_+) for $\phi = -1$ ($\phi = +1$) and measure:

$$2/z_- = 0.93(8), \quad \text{for} \quad 2.66\ \text{s} \lesssim t \lesssim 100\ \text{s}; \tag{3.12}$$

$$2/z_+ = \begin{cases} 0.82(15) & 2.66\ \text{s} \lesssim t \lesssim t_c; \\ 0.50(12) & t_c \lesssim t \lesssim 400\ \text{s}. \end{cases} \tag{3.13}$$

Results are consistent with model A dynamics for $t \lesssim t_c$, since both phases are fairly described by $2/z = 1$. This result is valid until $t \approx 100$ s for the favoured

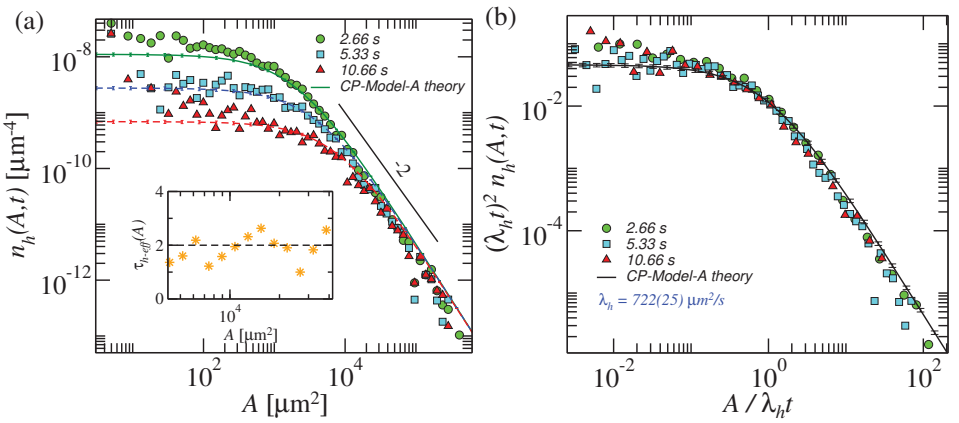

Figure 3.6: (a) Number density of hull areas per unit area, $n_h(A,t)$, computed in the experiment (symbols) for different times: $t = 2.66$ s, 5.33 s and 10.66 s. Solid black line is a guide to eyes with the universal slope $-\tau_h$, where $\tau_h = 2$ is the Fisher exponent for hull areas of clusters in the CP universality class. Dashed lines are the theoretical predictions of Eq. (3.9) (the CP-model-A theory) with $\lambda_h = 766(25)\ \mu\mathrm{m}^2/\mathrm{s}$ for $t = 2.66$ s, 5.33 s and 10.66 s, respectively from top to bottom. Inset shows the effective exponent $\tau^{\mathrm{exp}}_{h-\mathrm{eff}}(A) \equiv -d[\ln n_h(A, 2.66\mathrm{s})]/[d\ln(A)]$ as function of A. The dashed black line demarks the the universal $\tau_h = 2$ value, around which the experimental data oscillates. (b) Cardy-Ziff scaling function $f_h(A/\lambda_h t)$. Symbols are the same as in (a). Black line is generated with Eq. (3.9) using $\lambda_h = 766(25)\ \mu\mathrm{m}^2/\mathrm{s}$.

phase $\phi = -1$. The asymmetry between the phases is clearly observed for $t_c \lesssim t \lesssim 400$ s, where a much slower growth, with $2/z_+ \approx 0.50$ for the unfavoured phase, happens before the system equilibration.

Despite being simple quantities, $\langle N_d(t;\phi)\rangle$ and $\langle A(t;\phi)\rangle$ carry distinct aspects of the coarsening dynamics: they reveal the time behaviour of the most likely value and the mean value of the PDF $\rho_d(A, t \ll t_p;\phi)$, respectively. The former is dictated by a universal exponent γ [Eq. (3.11)], while the mean area follows the universal growth law $\langle A(t;\phi)\rangle \sim t^{2/z}$. Due to the asymmetry between the phases, z turns out to be significatively different for each twist phase at $t \gtrsim t_c$ [Eq. (3.12), Eq. (3.13)].

3.3.2 Number density of hull areas

According to Arenzon *et al.* [13], the number density of hull areas $n_h(A,t)dA$ is exactly derived for two-dimensional, scalar model A systems [Eq. (3.9)] by assuming the validity of CP statistics from some time t_p. A previous experimental endeavor, relying on the thermally-triggered quench of smectics [50], has tried to measure the universal CP properties encoded in the proposed form $n_h(A,t)$. Although a compatible decay with $\tau_h = 2$ has been glimpsed, the expected time-dependent plateau at $A \ll [r^*(t)]^2$ has not been detected (where the universal coefficient C_h [Eq. (3.4)] shall live).

Figure 3.6(a) displays $n_h(A,t)$ computed in the electrically-triggered quench of our TNLC system for different coarsening times, but constrained to $t \ll t_c$. At short-enough scales $A \lesssim 10^2\ \mu\mathrm{m}^2$, the $n_h(A,t)$ curves exhibit a time-dependent plateau, with exception for $A \lesssim 10\ \mu\mathrm{m}^2$, where spurious domains of nearly two or three pixels artificially affect the results. On the other scale regime, the behaviour for large areas is characterized by a power-law $n_h(A,t) \sim A^{-\tau_h^{\mathrm{exp}}}$ compatible with the universal CP statistics [Eq. (3.4)]. By defining an effective exponent $\tau^{\mathrm{exp}}_{h-\mathrm{eff}}(A) \equiv -d(\ln n_h(A, 2.66\ \mathrm{s}))/d\ln(A)$, we observe an area-independent value for the regime $4\times10^3\ \mu\mathrm{m}^2 \lesssim \mathrm{A} \lesssim 4\times10^4\ \mu\mathrm{m}^2$ [inset of Fig. 3.6(a)]; averaging over the points within this interval gives $\tau_h^{\mathrm{exp}} = 1.99(40)$, in good agreement with $\tau_h = 2$ [Eq. (3.5)].

Going back to the definition of λ_h in Eq. (3.6), we realize that $D_{\mathrm{AC}} \equiv \lambda_h/2\pi$ is the diffusion coefficient in the Allen-Cahn equation. In our previous study (Chap. 2), we measured $D_{\mathrm{AC}} = 122(4)\ \mu\mathrm{m}^2\mathrm{s}^{-1}$ from bubble shriking experiments. Therefore, $\lambda_h = 766(25)\ \mu\mathrm{m}^2\mathrm{s}^{-1}$ for our TNLC medium. Now we can test Eq. (3.9) against the experimental TNLC data with no fit parameter. Figure 3.6(a) displays this comparison. Solid lines referred to as CP-Model-A theory are generated from Eq. (3.9) with $\lambda_h = 766(25)\ \mu\mathrm{m}^2\mathrm{s}^{-1}$ for $t = 2.66$ s, 5.33 s and 10.66 s, respectively from top to bottom. The agreement between the proposed formula and the TNLC experiment is remarkable; it covers five orders of magnitude in $n_h(A,t)$ and nearly six decades in A. The $n_h(A,t)(\lambda_h t)^2$ curves are rescaled by the typical square area $(\lambda_h t)^2$ and plotted against $A/\lambda_h t$ so that the time-independent Cardy-Ziff scaling function $f_h(A/\lambda_h t)$ can be contemplated in Fig. 3.6(b). In summary, our results support the hypothesis of Arenzon *et al.* [13] that leads to Eq. (3.9). The Eq. (3.9) describes the TNLC data with notable accuracy by covering more than 5 decades in both vertical and horizontal axis. Our results uphold the universality of C_h, the universality of τ_h, and hence, the CP-model-A theory for two-dimensional systems.

3.3.3 Scaling of the maximum area

In this section we explore the statistics of the largest domain in the TNLC mosaics. The statitics of the extreme large domain allows us to characterize the fractal dimension for TNLC domains, which turn out to be in excellent agreement with d_f defined within the universal CP statistics [Eq. (3.3)]. The suggestion of a CP-coarsening coexistence, in the way it occurs (discussed in the text), conducts to the hypothesis, firstly proposed in [57], of the nonequilibrium coarsening dynamics being modelled as a CP model built on an inflating lattice. The hypothesis is herein supported by the experimental results. At the end of this section, we experimentally estimate the percolation-related dynamical exponent $z_p(\Lambda)$.

CP at uncorrelated scales

Consider the *local* area $A_{\max}(l;t)$ of the largest domain found inside a square box of lateral size $l \leq L_{\rm sys}$. The mean value $\langle A_{\max}(l;t)\rangle_l$, averaged over boxes that glide through the image of domain mosaics and over the ensemble of experiments, corresponds in $d = 2$ to the definition of the mean mass $\langle s_{\max}(l;p)\rangle_l$ of clusters in the percolation model [Eq. (3.2)]. Figure 3.7(a) shows $\langle A_{\max}(l;t)\rangle_l$ normalized by l^2 as a function of l for several coarsening times. For a fixed t, $\langle A_{\max}(l;t)\rangle_l/l^2$ crossover at a certain scale $l_c(t)$ from nearly a plateau regime – where $\langle A_{\max}(l \ll l_c;t)\rangle_l \approx l^2$ – towards an algebraic decay for $l \gg l_c(t)$. Interestingly, the characterization of such a decay:

$$\frac{\langle A_{\max}(l \gg l_c;t)\rangle_l}{l^2} \sim l^{D_f-2}; \quad D_f \approx 1.90 \tag{3.14}$$

is compatible with that expected for *clusters* in the CP universality class, where $d_f \approx 1.896$ [Eq. (3.3)]. D_f is the fractal dimension for TNLC domains.

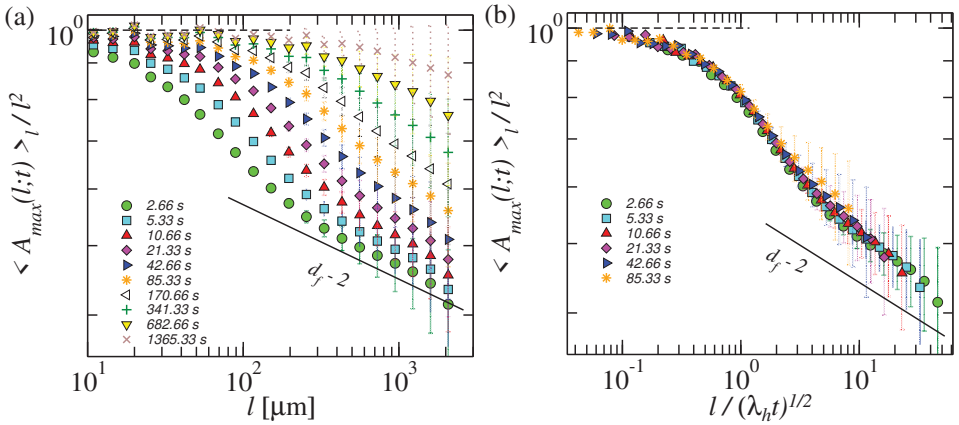

Figure 3.7: (a) Local area of the largest domain $\langle A_{\max}(l;t)\rangle_l$ found inside a square box of size $l \leq L_{\rm sys}$ for several times of the coarsening dynamics. The maximum area is normalized by l^2. Dashed and solid slopes are guide to eyes and represent the slopes for compact (null slope) and CP-like fractal clusters, respectively (d_f is the universal fractal dimension for CP statistics). (b) Universal, time-independent curve for $\langle A_{\max}(l;t)\rangle_l/l^2$ obtained from some curves shown in (a), but with the box size l rescaled by the typical domain coarsening size $r^*(t) \sim (\lambda_h t)^{1/2}$. The universal curve shows the crossover from compact to CP-like fractal clusters at scales $l \ll (\lambda_h t)^{1/2}$ and $l \gg (\lambda_h t)^{1/2}$, respectively.

The observed algebraic regime, however, becomes shorter as a function of time at the expense of the plateau stretching. This behaviour is controlled by the crossover length $l_c(t)$ which, according to the scaling hypothesis, shall behave as $l_c(t) \sim r^*(t) \sim t^{1/2}$. Indeed, Fig. 3.7(b) displays the same, but a few, data as in Fig. 3.7(a) all collapsed when rescaled by $l/(\lambda_h t)^{1/2}$. The collapse clearly reveals that the crossover between compact to the fractal-like structures of TNLC domains occur at intra- ($l \ll (\lambda_h t)^{1/2}$) and inter-domain ($l \gg (\lambda_h t)^{1/2}$) scales, respectively.

The fractal exponent $D_f \approx 1.90$ for domains, in good agreement with $d_f \approx 1.896$ for clusters in the CP class [Eq. (3.3)], is a further indicative that the system self-tuned to a CP state from some time t_p. According to data in Fig. 3.7(a), $t_p \ll 2.66$ s in our TNLC system.

Coarsening as CP clusters on an inflating lattice

The lesson from results above [Fig. 3.6(b), Fig. 3.7(b)] suggests that TNLC domains acquired a fractal structure compatible with the structure of CP clusters at uncorrelated scales $r \gg (\lambda_h t)^{1/2}$. Coarsening dynamics, in turn, manages to compactify the domains by building up correlations up to the scale $r^*(t) \sim t^{1/2}$. Therefore, one may think [57] the nonequilibrium coarsening process as a CP model that inflates in time such that CP statistics is preserved at long scales, but it is progressively destroyed at some dynamical (microscopic) length scale. As proposed in [57], the inflation can be mathematically inserted via the lattice spacing r_0 of a percolation model via $r_0 \mapsto r_0(t)$. Since in percolation models lengths and areas are measured in the unit of r_0 and $(r_0)^2$, respectively, we can rewrite Eq. (3.2) at p_c as (with the identification $A_{\max}(l;p) = s_{\max}(l;p)$ for $d = 2$):

$$\left\langle \frac{A_{\max}(l)}{(r_0)^2} \right\rangle_l \sim \left(\frac{l}{r_0} \right)^{d_f}. \tag{3.15}$$

Now, by defining the inflating CP model using $r_0 \mapsto r_0(t)$ so that $r_0(t) \sim t^{1/z}$ one finds:

$$\langle A_{\max}(l;t) \rangle_l \sim t^{\alpha} l^{d_f}, \quad \alpha \equiv \frac{2 - d_f}{z} \quad (\alpha = 5/96). \tag{3.16}$$

We test Eq. (3.16) by measuring $\langle A_{\max}(L_{\text{sys}};t) \rangle_l$ as a function of time in the TNLC system. Figure 3.8 shows the area of the 1st, 2nd and 3rd largest TNLC domains rescaled by L_{sys}^2 and multiplied by $t^{-\alpha}$. Experimental data for the 2nd and 3rd largest domains remarkably exhibit the expected plateaus for 3 s $\lesssim t \lesssim$ 300 s and 20 s $\lesssim t \lesssim$ 200 s, respectively. This behaviour is consistent with Eq. (3.16). For the largest domain, however, the plateau region is limited by a short time interval $t \lesssim t_c$, where $t_c \approx 25$ s [Fig. 3.5(b)]. The deviation is attributed to the asymmetry that favours the $\phi = -1$ phase. This asymmetry forces the area of the largest domain – which for any time is made of the phase $\phi = -1$ – to saturate faster than it would do it in the symmetric case. Such a reasoning is in consonance with the measurements for $\langle A(t;\phi) \rangle$ shown in Fig. 3.5(b).

The effective exponent $\alpha_{\text{eff}}(t) \equiv d[\ln(\langle A_{\max}(L_{\text{sys}};t) \rangle_l)]/[d \ln t]$ computed for the 2nd and 3rd largest domains is shown in the insertion of Fig. 3.8. The time series of $\alpha_{\text{eff}}(t)$ clearly shows a time-independent regime in which data for both 2nd and 3rd largest domains are around $\alpha_{\text{eff}}(t) \approx 0.05$. TNLC data is in agreement with $\alpha = 5/96$ expected from Eq. (3.16).

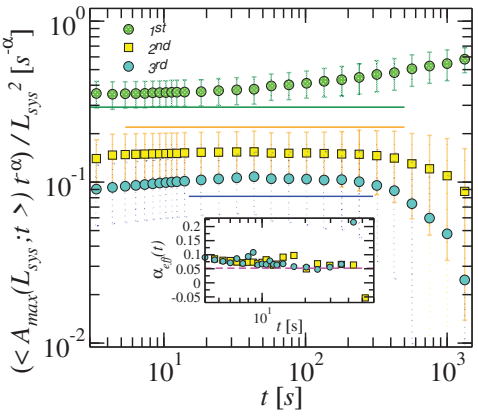

Figure 3.8: Mean area (ensemble averaged), $\langle A_{\max}(L_{\text{sys}};t)\rangle$, of the 1st, 2nd and 3rd largest domain inside the observational region $L^2_{\text{sys}} = 2.2$ mm $\times$ 2.9 mm as a function of time. The area is rescaled by t^{α}, where $\alpha \equiv (2-d_f)/z$, and normalized by L^2_{sys}. Solid green, orange and blue lines are plateaus working as a guide to eyes to be compared with data for the 1st, 2nd and 3rd largest domains, respectively. The hypothesis of coarsening as a CP model on an inflating lattice implies the curves shown in the plot shall exhibit plateaus in the scaling regime.

Percolation-related dynamical exponent

As proposed by simulations of discrete models (Sec. 3.1.2), the presence of a characteristic time $t_p(l,\Lambda) \sim l^{z_p(\Lambda)}$ [Eq. 3.10] implies the existence of an additional length $r^*_p(t,\Lambda)$. Such an existence is, *a priori*, in contradiction with the fundamental scaling hypothesis for coarsening dynamics since $z_p(\Lambda) \neq z$.

The results we obtained in Fig. 3.7, partially summarized in Eq. (3.14), tells us $\langle A_{\max}(l \gg l_c(t);t)\rangle_l \sim l^{D_f}$, where $D_f \approx d_f$. Given t_p really exists in our dynamics, dimensional consistence demands that:

$$\langle A_{\max}(l \gg l_c(t);t)\rangle_l = l^{D_f} g(t/t_p), \tag{3.17}$$

where $g(\cdot)$ is a (universal) scaling function. This argument has been recently employed [57] to estimate $z_p(\Lambda)$ in the coarsening dynamics of discrete models, but by using L instead of the local box l [57].

Inset of Fig. 3.9 shows $\langle A_{\max}(l \gg l_c(t);t)\rangle_l / l^{d_f}$ as function of t for three different local length scales $l = 466$ μm, 932 μm and 1864 μm. Notice that the curves are clearly distinct for each l. Relying on the expected scaling according to Eq. (3.17), we try to collapse the experimental curves after rescaling them by t/l^{z_p}. The analysis for each l, however, is limited by the range of time in which $\langle A_{\max}(l \gg l_c(t);t)\rangle_l \sim l^{D_f}$ holds. Based on Fig. 3.7(a), we estimate this range as approximately 20 s, 200 s and 500 s, respectively for $l = 466$ μm, 932 μm and 1864 μm. For the collapse methodology, we tested $z_p(\Lambda)$ as a parameter lying between 0 and 2.0; we varied $z_p(\Lambda)$ in steps of 0.1. The best collapse for the TNLC data, obtained for $z_p(\Lambda) = 0.4$, is shown in the main plot of Fig. 3.9.

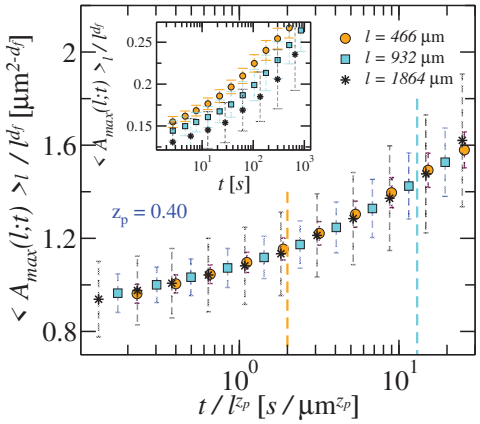

Figure 3.9: Best collapse for the mean local area $\langle A_{\max}(t;l)\rangle_l$ of the largest domain. The area is normalized by l^{d_f} and plotted as a function of the coarsening time normalized by the percolation-related time $t_p \sim l^{z_p}$ using $z_p = 0.4$ (main). Inset shows the bare data with no rescaling by l^{z_p}.

Orange and blue vertical dashed lines indicate the maximum scale t/l^{z_p} below which domains are fractal for $l = 466$ μm, 932 μm, respectively. Based on the collapse for other values of $z_p(\Lambda)$ (not shown) we estimate $z_p(\Lambda) = 0.45(5)$ for the TNLC dynamics. Such a value is rather distinct from $z = 2$. A meaning for $z_p(\Lambda) = 0.45(5)$, however, is less clear experimentally, where we do not handle with lattice systems. Nevertheless, 0.45 may be a combination of an effective coordination number with the range of interactions, as numerically observed [59]. Curiously, the value $z_p(4) = 2/5$, compatible with the experimental measurement, has been recently estimated for the zero-temperature coarsening dynamics of the Ising-Glauber model on a square lattice [57].

3.4 Summary and concluding remarks

We analysed the eletrically-triggered two-dimensional coarsening of TNLC domains, which is known to be in the model A universality class. Geometrical aspects of the domains, such as the number density of hull area and maximum area, are shown to behave rather differently below and above the typical domain size. Remarkably, inter-domain scales displays statistics compatible with that of the critical percolation class at $d = 2$. That is the first time we see such an agreement experimentally. In fact, the CP-model-A theory [13], hitherto supported in simulations [16, 17, 57], is here upheld experimentally in fine resolution.

The existence of an additional length scale $r_p^*(t) \sim t^{z_p(\Lambda)}$, conjectured by theoreticians [16], and here experimentally observed via z_p is a fundamental aspect. Although the link between this experimental value of z_p and an underlying TNLC lattice is vague, the existence of $z_p \neq z$ itself implies the generalisation of the fundamental scaling hypothesis, at least, for two-dimensional (continuum) model A

systems. Notice that our work experimentally support the recent scenario observed for discrete model systems [16, 57]. Concretely, correlation functions such as the spatial covariance $C(\boldsymbol{r},t) := \langle \phi(\boldsymbol{r'},t)\phi(\boldsymbol{r'}+\boldsymbol{r},t)\rangle$ shall become time-independent only when rewritten as $C(\boldsymbol{r},t) = \mathscr{F}\left(\frac{r}{t^{1/z}}, \frac{L}{t^{1/z_p}}\right)$ as recently shown for *discrete* models [16]. $\mathscr{F}(y,y_p)$ is a universal scaling function. When $\mathscr{F}(y,y_p \to 0)$, one recovers the classical single-argument scaling function; however, in the scaling limit $L \to \infty$ followed by $t \to \infty$ both $r^*(t)$ and $r_p^*(t)$ are always relevant. TNLC dynamics provide, finally, an evidence of CP in coarsening dynamics. Our experimental system can now be further explored; additional universal quantities in CP, such as the winding angle [55] and area-length relation of hulls [17], and correlation functions [55] recently computed in simulations of coarsening dynamics, are some, but a few examples deserving experimental investigations.

3.5 Acronyms and Symbols

Acronym	Description
CI	Conformal invariance
CP	Critical percolation
HK	Hoshen-Kopelman
ITO	Indium tin oxide
PDF	probality density function
SLE	Shramm-Löwner evolution
TNLC	Twisted nematic liquid crystals

Symbols

Latin Symbols	Description
a	Pixel size of the mosaic of TNLC domains
A	Generic element of area
$A_{\max}$	Area of the largest domain
A_{ml}	Most likely value for the area of a domain
A_p	Area enclosed by a hull at some previous time t_p
$A_{t'}$	Area counter for the hull algorithm at step t'
b	b^{th} label of a cluster in the multilable HK code
C	Two-point spatial correlation function
C_h	Amplitude for the number density of hull areas
C_x	Amplitude for the number density of x of CP clusters
d	Spatial dimension
d_f	Universal fractal dimension of clusters in CP
D_{AC}	Diffusion constant in the Allen-Cahn equation
D_f	Fractal dimensional of TNLC domains at large scales
f_h	Scaling function for the number density of hull areas
f_x	Scaling function for the number density of x of CP clusters
g	Scaling function for the area of the largest cluster
h	Height level of pixel in an image.
$H_{t'}$	Height counter for the hull algorithm at step t'

i	position of a row in a matrix
i_s	position of the row containing a seed of a domain
j	position of a column in a matrix
j_s	position of the column containing a seed of a domain
k	Label of a cluster in the HK code
l	Lateral size of a square box (window)
l_c	Crossover length scale in the TNLC experiment
L	Lateral size of a generic model system
L_{sys}	Typical lateral size of the experimental images
n_h	Number density of hull areas
n_x	Number density of a x (length, area *etc.*) of a cluster
N_d	Total number of domains
o	o^{th} label given to a cluster in the HK code
p	Occupation probability
p_c	Critical occupation probability
P_s	Probability of existence of a spanning cluster
q	Label of jumping directions
q_{last}	Latest jumping direction of a walker
q_{next}	Next jumping direction selected for a walker
$\boldsymbol{r}$	Spatial vector
r_0	Lattice spacing in the percolation model
r^*	Typical size of domains undergoing coarsening
r_p^*	Characteristic percolation-related length scale
$\boldsymbol{r}_i$	Position of a domain boundary (interface)
s	s^{th} label given to a cluster in the HK code
s_{max}	s_{max} mass of the largest d-dimensional cluster
t	Elapsed time from quench operation
t'	t'^{th} jump given by a walker
t^*	Equilibration time of a TNLC sample
t_c	Crossover time for N_d in the TNLC experiment
t_p	Time from which CP statistics sets in coarsening
T	Temperature

u	State variable of a pixel in the HK code
u_{HK}	Occupation control parameter the HK code
v	Shrinking local velocity of an interface
W	Link function of labels in a same cluster
x	Generic geometric feature: area, length, perimeter, *etc.*
X	Corresponding value of x
y	Ratio $r/t^{1/z}$
y_p	Ratio $L/t^{1/z_p}$
z	Dynamical scaling exponent
z_p	Percolation-related dynamical scaling exponent

Greek Symbols	**Description**
α	CP-model-A inflation exponent
β	Growth exponent the order parameter
γ	Exponent for the decay of N_d in the experiment
κ	Local mean curvature of an interface
Λ	Coordination number of a lattice
σ	Scaling exponent associated to X_ξ of CP clusters
τ	Universal Fisher exponent
ϕ	Local order parameter

Others	**Description**
P_∞	Fraction of sites belonging to the spanning cluster
X_ξ	Typical scale (length, area, volume...) of clusters in percolation
$z_-(z_+)$	Dynamical exponent for the twist phase $\phi = \pm 1$
α_{eff}	Effective CP-model-A inflation exponent in the TNLC experiment
λ_h	Diffusion coeficient in the Allen-Cahn equation
ρ_d	Probability density function of domain areas
σ_x	Scaling exponent for generic feature x of CP clusters
τ_h	Fisher exponent for hull areas in the CP class
τ_x	Fisher exponent for generic feature x of CP clusters
$\tau_{h-eff}^{\text{exp}}$	Effective Fisher exponent for TNLC hulls
$\mathscr{F}$	Universal two-point spatial scaling function

BIBLIOGRAPHY

[1] Bray, A. J.: Theory of phase-ordering kinetics. Adv. Phys. **51**, 481-587 (2002).
Cited on pages 70, 74, and 82.

[2] Puri, S., Wadhawan, V. (Eds.): Kinetics of Phase Transitions. Taylor and Francis Group (2009).
Cited on page 70.

[3] Calabrese, P., Gambassi, A.: Ageing properties of critical systems. J. Phys. A.: Math. Gen.**38**, R133 (2005).
Cited on page 70.

[4] Corberi, F., Lippiello, E., Zannetti, M.: Fluctuation dissipation relations far from equilibrium. J. Stat. Mech. **2007**, P07002 (2007).
Cited on page 70.

[5] Henkel, M., Pleimling, M.: Non-Equilibrium Phase Transitions Volume 2: Ageing and Dynamical Scaling Far from Equilibrium. Springer Science & Business Media (2010).
Cited on page 70.

[6] Lifshitz, I. M., Slyozov, V. V.: The kinetics of precipitation from supersaturated solid solutions. J. Phys. Chem. Solids **19**, 35-50 (1961).
Cited on page 70.

[7] Wagner, C.: Z. Elektrochem. **65**, 581-591 (1961).
Cited on page 70.

[8] Stavans, J.: The evolution of cellular structures. Rep. Prog. Phys. **56**, 733 (1993).
Cited on page 70.

[9] Thompson, C. V.: Grain growth in thin films. Annu. Rev. Mater. Sci. **20**, 245 (1990).
Cited on page 70.

[10] Cugliandolo, L.: Geometric aspects of ordering phenomena. C. R. Physique **18**, 5-18 (2017).
Cited on page 70.

[11] Stauffer, D. Aharony, A.: Introduction to Percolation Theory, 2nd ed. Taylor and Francis group, London (1994).
Cited on pages 70, 71, 72, and 73.

[12] Hinrichsen, Haye.: Non-equilibrium critical phenomena and phase transitions into absorbing states. Adv. Phys. **49**, 815-958 (2000).
Cited on pages 70 and 71.

[13] Arenzon, J. J., Bray, A. J., Cugliandolo, L. F., Sicilia, A.: Exact results for curvature-driven coarsening in two dimensions. Phys. Rev. Lett. **98**, 145701 (2007).
Cited on pages 71, 74, 75, 81, 83, 84, and 88.

[14] Barros, K., Krapivsky, P. L., Redner, S.: Freezing into stripe states in two-dimensional ferromagnets and crossing probabilities in critical percolation. Phys. Rev. E **80**, 040101(R) (2009).
Cited on pages 71 and 75.

[15] Olejarz, J., Krapivsky, P. L., Redner, S.: Fate of 2D kinetic ferromagnets and critical percolation crossing probabilities. Phys. Rev. Lett. **109**, 195702 (2012).
Cited on pages 71 and 75.

[16] Blanchard, T., Corberi, F., Cugliandolo, L. F., Picco, M.: How soon after a zero-temperature quench is the fate of the Ising model sealed? Europhys. Lett. **106**, 66001 (2014).
Cited on pages 71, 75, 76, 88, and 89.

[17] Sicilia, A., Arenzon, J. J., Bray, A. J., Cugliandolo, L. F.: Domain growth morphology in curvature-driven two-dimensional coarsening. Phys. Rev. E **76**, 061116 (2007).
Cited on pages 75, 78, 88, and 89.

[18] Flory, P. J.: Molecular size distribution in three dimensional polymers. I. Gelation. J. Am. Chem. Soc. **63** 3083-3090 (1941). *ibid* **63** 3091 (1941); *ibid* **63** 3096 (1941).
Cited on page 71.

[19] Broadbent, S. R., Hammersley, J. M.: Percolation processess. Math. Proc. Camb. Phil. Soc. **53**, 629-641 (1957).
Cited on page 71.

[20] Stauffer, D.: Scaling theory of percolation clusters. Phys. Rep. **54**, 1-75 (1979).
Cited on pages 71, 72, and 73.

[21] Essam, J. W.: Percolation theory. Rep. Prog. Phys. **43**, 833-912 (1980).
Cited on pages 71 and 72.

[22] Araújo, N. A. M., Grassberger, P., Kahng, B., Schrenk, K. J., Ziff, R. M.: Recent advances and open challenges in percolation. Eur. Phys. J. Special Topics **223**, 2307-2321 (2014).
Cited on pages 71 and 73.

[23] Saberi, A. A.: Recent advances in percolation theory and its applications. Phys. Rep. **578**, 1–32 (2015).
Cited on page 71.

[24] Kesten, H.: Percolation theory for mathematicians. Birkhauser, Boston (1982).
Cited on page 71.

[25] Grimmett, G.: What is Percolation?. In: Percolation. Grundlehren der mathematischen Wissenschaften (A Series of Comprehensive Studies in Mathematics), vol 321. Springer, Berlin, Heidelberg (1999).
Cited on pages 71 and 73.

[26] Lawler, G. F., Schramm, O., Werner, W.: Values of Brownian intersection exponents, I: Half-plane exponents. Acta. Math. **187**, 237 (2001).
Cited on pages 71 and 73.

[27] Lawler, G. F., Schramm, O., Werner, W.: Values of Brownian intersection exponents, II: Plane exponents. Acta. Math. **187**, 275 (2001).
Cited on pages 71 and 73.

[28] Smirnov, S.: Critical percolation in the plane: conformal invariance, Cardy's formula, scaling limits. C. R. Acad. Sci. Series I - Mathematics **333**, 239-244 (2001).
Cited on pages 71 and 73.

[29] Smirnov, S., Werner, W.: Critical exponents for two-dimensional percolation. Math. Res. Lett. **8**, 729 (2001).
Cited on pages 71 and 73.

[30] Stauffer, D.: Violation of dynamical scaling for randomly dilute Ising ferromagnets near percolation threshold. Phys. Rev. Lett. **35**, 394 (1975).
Cited on page 72.

[31] Jacobsen, J. L.: High-precision percolation thresholds and Potts-model critical manifolds from graph polynomials. J. Phys. A: Math. Theor. *47*, 135001 (2014).
Cited on pages 72, 73, and 75.

[32] Hara, T., Slade, G.: Mean-field behaviour and the lace expansion. In: Grimmett G. (eds) Probability and Phase Transition. NATO ASI Series (Series C: Mathematical and Physical Sciences), vol 420. Springer, Dordrecht (1994).
Cited on page 72.

[33] Newman, C. M., Schulman, L. S.: Number and density of percolating clusters. J. Phys. A: Math. Gen. **14**, 1735 (1981).
Cited on page 72.

[34] Aizenman, M., Kesten, H., Newman, C. M.: Uniqueness of the infinite cluster and continuity of connectivity functions for short and long range percolation. Commun. Math. Phys. **111**, 505 (1987).
Cited on page 72.

[35] Essam, J. W., Gwilym, K. M.: The scaling laws for percolation processes. J. Phys. C: Solid Stat. Phys. **4**, L228 (1971).
Cited on page 71.

[36] Fisher, M. E.: The theory of condensation and the critical point. Physics **3**, 255 (1967).
Cited on page 72.

[37] Sykes, M. F., Essam, J. W.: Some exact critical percolation probabilities for bond and site problems in two dimensions. Phys. Rev. Lett. **10**, 3 (1962).
Cited on page 73.

[38] Ziff, R. M., Scullard, C. R.: Exact bond percolation thresholds in two dimensions. J. Phys. A.: Math. Gen. **39**, 15083 (2006).
Cited on page 73.

[39] Grimmett, G. R., Manolescu, I.: Inhomogeneous bond percolation on square, triangular and hexagonal lattices. Ann. Prob. **41**, 2990 (2013).
Cited on page 73.

[40] Kesten, H.: The critical probability of bond percolation on the square lattice equals 1/2*. Commun. Math. Phys. **74**, 41 (1980).
Cited on page 73.

[41] Wierman, J. C.: A bond percolation critical probability determination based on the star-triangle transformation. J. Phys. A: Math. Gen. **17**, 1525 (1984).
Cited on page 73.

[42] Ziff, R. M.: Results for a critical threshold, the correction-to-scaling exponent and susceptibility amplitude ratio for 2d percolation. Phys. Proc. **15**, 106 (2011).
Cited on page 73.

[43] Henkel, M.: Conformal invariance and critical phenomena. Springer Science & Business Media (2013).
Cited on page 73.

[44] Langlands, R. P., Pichet, C., Pouliot, Ph., Saint-Aubin, Y.: On the universality of crossing probabilities in two-dimensional percolation. J. Stat. Phys. **67**, 553 (1992).
Cited on page 73.

[45] Cardy, J. L.: Critical percolation in finite geometries. J. Phys. A: Math. Gen. **25**, L201 (1992).
Cited on page 73.

[46] Schramm, O.: Scaling limits of loop-erased random walks and uniform spanning trees. Isr. J. Math. **118**, 221 (2000).
Cited on page 73.

[47] Schramm, O.: A percolation formula. Elect. Comm. in Probab. **6**, 115-120 (2001).
Cited on page 73.

[48] Cardy, J., Ziff, R. M.: Exact results for the universal area distribution of clusters in Percolation, Ising, and Potts models. J. Stat. Phys. **110**, 1 (2003).
Cited on page 73.

[49] Allen, S. M., Cahn, J. W.: A microscopic theory for antiphase boundary motion and its application to antiphase domain coarsening. Acta Mettall. **27**, 1085-1095 (1979).
Cited on page 74.

[50] Sicilia, A., Arenzon, J. J., Dierking, I., Bray, A. J., Cugliandolo, L. F., Martínez-Perdiguero, J., Alonso, I., Pintre, C.: Experimental test of curvature-driven dynamics in the phase ordering of a two dimensional liquid crystal. Phys. Rev. Lett. **101**, 197801 (2008).
Cited on pages 75 and 83.

[51] Sicilia, A., Sarrazin, Y., Arenzon, J. J., Bray, A. J., Cugliandolo, L. F.: Geometry of phase separation. Phys. Rev. E **80**, 031121 (2009).
Cited on page 75.

[52] Takeuchi, H., Mizuno, Y., Dehara, K.: Phase-ordering percolation and an infinite domain wall in segregating binary Bose-Einstein condensates. Phys. Rev. A **92**, 043608 (2015).
Cited on page 75.

[53] Tartaglia, A., Cugliandolo, L. F., Picco, M.: Percolation and coarsening in the bidimensional voter model. Phys. Rev. E **92**, 042109 (2015).
Cited on page 75.

[54] Sicilia, A., Arenzon, J. J., Bray, A. J., Cugliandolo, L. F.: Geometric properties of two-dimensional coarsening with weak disorder. Europhys. Lett. **82**, 10001 (2008).
Cited on page 75.

[55] Corberi, F., Cugliandolo, L. F., Insalata, F., Picco, M.: Coarsening and percolation in a disordered ferromagnet. Phys. Rev. E **95**, 022101 (2017).
Cited on pages 75 and 89.

[56] Corberi, F., Cugliandolo, L. F., Insalata, F., Picco, M.: Fractal character of the phase ordering kinetics of a diluted ferromagnet. arXiv:1811.12675 (2018).
Cited on page 75.

[57] Blanchard, T., Cugliandolo, L. F., Picco, M., Tartaglia, A.: Critical percolation in the dynamics of the 2D ferromagnetic Ising model. J. Stat. Mech. **2017**, 113201 (2017).
Cited on pages 75, 81, 84, 86, 87, 88, and 89.

[58] Tartaglia, A., Cugliandolo, L. F., Picco, M.: Phase separation and critical percolation in bidimensional spin-exchange models. Europhys. Lett. **116**, 26001 (2016).
Cited on page 75.

[59] Tartaglia, A., Cugliandolo, L. F., Picco, M.: Coarsening and percolation in the kinetic $2d$ Ising model with spin exchange updates and the voter model. J. Stat. Mech. **2018**, 083202 (2018).
Cited on pages 75 and 88.

[60] Zallen, R., Scher, H.: Percolation on a continuum and the localization-delocalization transition in amorphous semiconductors. Phys. Rev. B **4**, 4471 (1971).
Cited on page 75.

[61] Hoshen, J., Kopelman, R.: Percolation and cluster distribution. I. Cluster multiple labeling technique and critical concentration algorithm. Phys. Rev. B **14**, 3438 (1976).
Cited on page 77.

[62] Grossman, T., Aharony, A.: Structure and perimeters of percolation clusters. J. Phy. A.: Math. Gen. **19** L745-L751 (1986).
Cited on page 78.

4

SURFACE FLUCTUATIONS OF VAPOUR-DEPOSITED CDTE THIN FILMS

Herein we analyse surface fluctuations of polycristalline CdTe films. As briefly mentioned in Chap. 1, the height field of growing interfaces may display scaling invariance. Depending on certain scaling exponents, the statistics of such a height field can be grouped into a few dynamical universality classes. In this Chapter, we deal with the most prominent class concerned to a local, nonconserved interface growth dynamics: the so-called Kardar-Parisi-Zhang (KPZ) class. We devote attention to the (2+1)-dimensional KPZ case for which analytical solutions and experimental pieces of evidence are severely scarce. After the topic introduction in Sec. 4.1, we study surface fluctuations of polycristalline CdTe films. CdTe films play a relevant role in the industry of semiconductors as being a low-cost material for photovoltaic and optical-electronic technologies, such as solar cells and infrared detectors. Section 4.2 contains the materials and methods we use to grow and to analyse the films. In Sec. 4.3 we demonstrate that fluctuations at the surface of CdTe films, grown on polyimide substrates, belong to the KPZ class. This is supported by measurements with a wealth level of detail. Much beyond, we give experimental evidence of a general crossover expected for the distribution of the interface local width, which passes through a lognormal distribution regime. Interesting, we found that the short-time surface statistics of CdTe films grown on polyimide is featured by a peculiar regime christen (by the Author and collaborators) as Pseudo-steady state (PSS) – an analogy to the steady state of growing surfaces. We conclude pointing out to distinct interface dynamics where PSS scaling arises. The evidence for PSS scaling in different microscopic systems, including experiments and models, suggests PSS as a possible generic type of scaling that, however, has not been theoretically interpreted as such yet. Results here discussed

were published in [1].

Contribution

The research was done in collaboration with a Brazilian group in the Universidade Federal de Viçosa, Minas Gerais. With the experimental supervision of Prof. S. O. Ferreira and theoretical supervision of Prof. T. J. Oliveira, the Author was in front of all stages of the work: growth and experimental characterization of films; statistical characterization and analysis of CdTe surfaces, as well as of the writing of the research paper [1]. Prof. Ferreira and Prof. Oliveira discussed the results with the Author. Prof. Oliveira generated results for an one-dimensional model shown in Sec. 4.3.4. Dr. Ferraz contributed to grow a few additional films and performed some X-ray diffraction measurements during the period of time the Author was in Japan.

4.1 Dynamical scaling invariance of growing interfaces

This Section contains a sketch of scaling invariance hypothesis in growing interfaces. Subsections 4.1.1 and 4.1.2 provide an elementary introduction to the theme. Universal aspects of the KPZ class, which are of relevance for what comes in Sec. 4.3, are also described.

4.1.1 Elementary scaling concepts

Let a coarse-grained interface of lateral extent L be described by a continuous height field $h(\boldsymbol{r},t)$ measured from a flat d_s-dimensional substrate with $\boldsymbol{r} \in \mathbb{R}^{d_s}$ and $h,t \in \mathbb{R}_+$ [see an one-dimensional sketch in Fig. 4.1]. The simplest feature of an interface is its scale-dependent width or roughness, $W(L,t)$, defined as:

$$W(L,t) := \sqrt{\langle(\overline{h(\boldsymbol{r},t)^2} - \overline{h(\boldsymbol{r},t)}^2)\rangle}, \tag{4.1}$$

where,

$$\overline{h(\boldsymbol{r},t)} := \frac{1}{L^{d_s}} \int_0^L h(\boldsymbol{r},t) d^{d_s} r. \tag{4.2}$$

The brackets $\langle ... \rangle$ denote ensemble average over many different surfaces.

Over the last four decades, it was acquired overwhelming numerical, theoretical [2–4] and experimental [2, 5–7] evidence that statistical properties of growing surfaces can display scale invariance without fine-tuning. A fraction of these observations are compatible with the celebrated Family-Vicsek *ansatz* [8]:

$$W(L,t) = t^{\beta} f_{\text{FV}}(\xi(t)/L), \quad f_{\text{FV}}(y) \sim \begin{cases} \text{const.} & y \ll 1; \\ y^{-\alpha} & y \gg 1; \end{cases} \tag{4.3}$$

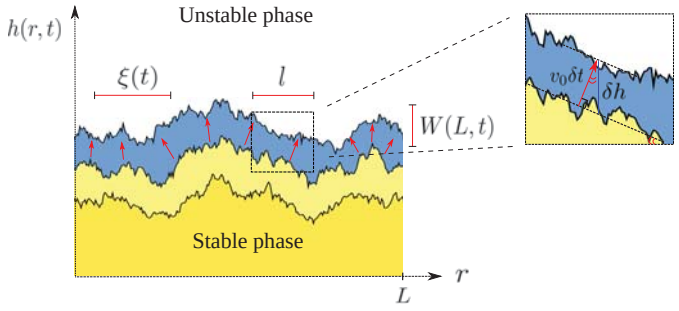

Figure 4.1: Sketch of (1+1)-dimensional growth process induced by the contact between a stable and an unstable phase. Profiles were numerically generated by integrating Eq. (4.7) with initial condition $h(r,0) = 0$. Layers of different colours correspond to different deposition times. The finite-size interface of lateral size L has global roughness $W(L,t)$ and correlation length $\xi(t)$. Local roughness $w(l,t)$ quantifies fluctuations inside a box of linear size $l \leq L$. Red arrows indicate the growth in the local normal direction of the profile. The zoom in a piece of interfaces generated at t and at $t + \delta t$ illustrates the normal growth mechanism, discussed in the main text.

where β, α and z are the growth, roughness, and dynamical exponents, respectively. In the Family-Vicsek scaling, $\beta \equiv \alpha/z$. The correlation length, $\xi(t)$, measured parallely to the substrate, follows the growth law:

$$\xi(t) \sim t^{1/z}. \tag{4.4}$$

Equation (4.3) and Eq. (4.4) stem from the invariance of interfaces under self-affine scale transformations:

$$\boldsymbol{r} \mapsto \varsigma \boldsymbol{r}; \quad t \mapsto \varsigma^z t; \quad h \mapsto \varsigma^{-\alpha} h, \tag{4.5}$$

where ς is a positive scale factor (isotropy is assumed).

It is worth remarking that scale-invariance is limited to the multilayer growth stage, in which many atomic species of size a_{micro} were incorporated to the growing phase so that $(\overline{h(\boldsymbol{r},t)}, \xi(t)) \gg a_{\text{micro}}$.

In the stage of validity, as properly accounted for by Eq. (4.3), interface dynamics has two regimes. When $y \ll 1$, the width is time-dependent and grows as $W(L,t) \sim t^{\beta}$. This is the *growth* regime. On the other hand, when $\xi(t) \sim L$, both $W(L,t)$ and $\xi(t)$ become time-independent and do not grow anymore even if the interface indefinitely advances over the unstable phase. This is called the *steady state* regime.

Microscopically distinct interfaces may rescale with the same scaling exponents α and z. This characteristic suggests their growth processes belong to the same dynamical universality class. Formally, α and z shall correspond to a fixed-point solution in the dynamical renormalisation group sense [10].

4.1.2 The simplest growth equations with local interactions

A continuum modelling accounting for by the growth dynamics should start from the general equation [11],

$$\frac{\partial h(\boldsymbol{r},t)}{\partial t} = v_0 + \mathscr{F}[(\nabla^i h)^j, \boldsymbol{r}, h, t] + \eta(\boldsymbol{r}, h(\boldsymbol{r},t), t), \tag{4.6}$$

where v_0 is the adsorption rate of atomic species in the expanding phase; $\mathscr{F}[\cdot]$ a functional that encodes interface relaxation mechanisms via combinations of $\nabla^i h$, $(\nabla h)^i$ and $(\nabla^i h)(\nabla h)^j$ $i, j \in \mathbb{N}$; $\eta(\cdot)$ is a function representing the noise contribution. The origins for the noise are thermal effects, spatial inhomogeneities in the medium and stochasticity of adsorptions [2].

The origin $(t_0, \boldsymbol{r}_0, h_0)$ chosen for describing the interface (and any other) dynamics is irrelevant to the dynamics itself. Thereby, invariance of Eq. (4.6) under translations in time ($t_0 \mapsto t_0 + \delta t$), in the substrate plane ($\boldsymbol{r}_0 \mapsto \boldsymbol{r}_0 + \delta \boldsymbol{r}$), and in the growth direction ($h_0 \mapsto h_0 + \delta h$) rules out explicit dependence of terms t, $\boldsymbol{r}$, h (and its higher order powers) in the functional $\mathscr{F}$. This is general. However, from now on we constrain the scope of physical description by including step-by-step additional symmetries that *some* interfaces are expected to satisfy.

Kardar-Parisi-Zhang equation

Assuming there is no privileged area to adsorptions occur at the interface[1], the dynamics shall be invariant under rotations ($\boldsymbol{r} \mapsto \mathscr{M}_{d_s}\boldsymbol{r}$ where $\mathscr{M}_{d_s}$ is the d_s-dimensional matrix of rotation) around the growth direction h. Invariance under rotational symmetry excludes terms of odd derivatives – *i.e.* $(\nabla^{2i+1}h)$ – from the functional $\mathscr{F}$. Thereby, the terms allowed to appear in $\mathscr{F}$ are now: $\nabla^{2i}h$, $(\nabla h)^{2j}$, and $(\nabla^{2k}h)(\nabla h)^{2n}$, $k, n \in \mathbb{N}$.

If we limit attention to the hydrodynamic limit ($L \to \infty$ and $t \to \infty$), where the contribution of high-order terms to fluctuations are irrelevant compared to the contribution of low-order ones [12], then the simplest nonlinear equation that can be written down is the so-called Kardar-Parisi-Zhang equation [13]:

$$\frac{\partial h(\boldsymbol{r},t)}{\partial t} = v_0 + \nu\nabla^2 h + \frac{\lambda}{2}(\nabla h)^2 + \sqrt{D}\eta(\boldsymbol{r},t). \tag{4.7}$$

Here, ν, λ and $\sqrt{D}$ are phenomenological constants representing the surface tension, the "excess of velocity" due to aggregations normally-oriented to the interface [Fig. 4.1], and the strength of the noise, respectively. For the sake of simplicity, $\eta(\boldsymbol{r},t)$ is hereafter assumed stemming from the randomness of adsorptions, which are usually modelled as a Gaussian process uncorrelated in space and time: $\langle\overline{\eta(\boldsymbol{r},t)}\rangle = 0$, and $\langle\overline{\eta(\boldsymbol{r},t)\eta(\boldsymbol{r}',t')}\rangle = \delta^{d_s}(\boldsymbol{r}-\boldsymbol{r}')\delta(t-t')$.

[1] This condition is not satisfied in many growth processes, including oblique vapour deposition, sputtering, diffusion-limited growth and others [2]. If the rotational symmetry around h is not satisfied, then odd derivatives such as ∇h and higher orders are allowed. In such cases, interface grows with nonlocal interactions.

The normally-oriented interface expansion contributes to an additional velocity in the total interface growth rate $v(L,t) = \frac{\partial \overline{h(\boldsymbol{r},t)}}{\partial t}$, that is, $v(L,t) = v_0 + \frac{\lambda}{2}\overline{(\nabla h)^2} + \overline{(\nabla^2 h)}$ [Fig. 4.1]. If the global interface shape has no residual curvature, $\overline{(\nabla^2 h)} = 0$. The additional nonlinear term implies that even when there is no an external flux of particles, $v_0 = 0$, the interface still grows $v(L,t) \neq 0$. In other words, the height of the expanding phase does not correspond to the total height of adsorbed particles if counted individually. Thereby, KPZ equation describes a type of *nonconserved* growth, in which the up-down symmetry $h(\boldsymbol{r},t) \mapsto -h(\boldsymbol{r},t)$ is not satisfied.

Edwards-Wilkison equation

The simplest linear continuum model that satisfies the up-down symmetry is the Edwards-Wilkison (EW) equation [14], which is nothing but the KPZ equation [Eq. (4.7)] with $\lambda = 0$. EW equation is soluble in any dimension (see, *e.g.* [4]), and satisfies Family-Vicsek scaling for $d_s \leq 2$. Scaling exponents can be easily obtained by assuming that EW equation is invariant under self-affine transformations [Eq. (4.5)]. The values of scaling exponents of the EW model are summarized in Tab. 4.1. A few model and experimental interface systems show scaling exponents compatible with EW exponents. They include the Family discrete model [15], surfaces in stacks of W/Si bi-layers sputtered on Si [16], and height fluctuations during the sedimentation of SiO_2 nanospheres from aqueous solutions [17]. These systems are said to belong to the EW dynamical universality class. In EW growth, the volume of the thick layer is *conserved*, which can be seen from the relation $v(L,t) = v_0$ for interfaces with no residual curvature.

Random-deposition equation

If the interface has no effective mechanism for mass redistribution, then the growth becomes noise-dominated in the asymptotic limit. Such a condition leads to the Random-deposition (RD) equation, that is Eq. (4.7) with $\nu = 0$ and $\lambda = 0$. In RD-generated surfaces, roughnes indefinitely grows as $W(L,t) = \sqrt{Dt}$. This implies $\beta = 1/2$ and $1/z = 0$ for any d_s [Tab. 4.1]. An interesting experimental example of RD growth is the (1+1)-dimensional deposition of spherical colloidal particles at the edges of evaporating drops [18], which – on the basis of universality – shall correspond to the aggregation dynamics of coffee powder at the edge of an evaporating drop of coffee that you spilled on the table. A further example, but for $(2+1)$-dimensional dynamics, is the surface of polycristalline CdTe films vapour-deposited deposited on Si(001) at low temperatures [19]. In this case, thermally-activated mass redistribution mechanisms at the interface (*e.g.* diffusion of CdTe molecules between grains) are not operative enough to overcome barrier energies between neighbouring crystals. The interface grows effectively uncorrelated, thus yielding $W(L,t) \sim t^{1/2}$ with nanometric roughness.

Exponent	EW ($d_s = 1$)	EW ($d_s = 2$)	RD ($d_s \geq 1$)
α	1/2	0	ill defined
β	1/4	0	1/2
$1/z$	1/2	1/2	0

Table 4.1: Universal scaling exponents (α, β, $1/z$) for the Edwards-Wilkison and Random Deposition universality classes for the substrate dimension d_s.

4.1.3 Some universal aspects of the Kardar-Parisi-Zhang equation

The KPZ equation has been intensively studied since its proposal in 1986. The equation itself is, indeed, a continuum model that belongs to what we call the KPZ class [2, 3, 13, 20–23]. The KPZ class encompasses a set of macroscopic systems that, at their asymptotic limit, displays the statistics displayed by the KPZ equation in the strong coupling regime[2]; it includes many discrete and experimental growing surfaces [2, 23], models for directed polymers in random media [3, 24], and for stirred fluids free from vortices [25], one-dimensional models of hopping particles on a discrete line [22, 23], beyond a model for magnetic flux lines in superconductors [26], and for density perturbations of the structure in the early universe [27], and so on.

General results

There is only one exact result in the KPZ theory valid for any d_s, which is the exponent relation

$$\alpha + z = 2. \tag{4.8}$$

This relation stems from the Galilean symmetry of the noisy Burgues equation [28] – a continuum model for stirred fluids – that can be mapped to the KPZ equation only if λ is scale invariant under self-affine transformations[3] [13, 25].

Another aspect of KPZ apparently valid for general d_s is the phenomenological evolution of $h(\boldsymbol{r}, t)$ but for only one point at interface, here noted $h(t)$. The variable $h(t)$ can be written in terms of parameters given by the Krug-Meaking theory [29, 30]:

[2] At $d_s > 2$, the nonlinear term $\frac{\lambda}{2}\langle(\nabla h)^2\rangle$ is not always relevant in the asymptotic limit $L \to \infty$, $t \to \infty$. The relevance is put in terms of a coupling constant $g = \lambda^2 D/\nu^3$ which serves as an effective parameter to describe whether, in the asymptotic limit, statistics of the KPZ equation goes to the strong coupling phase (nonlinear term is relevant) or to the weak coupling (EW statistics) phase [13].

[3] By applying the transformation $\boldsymbol{v}_B(\boldsymbol{r}, t) = -\nabla h(\boldsymbol{r}, t)$ in the KPZ equation, one arrives at the noisy Burgues equation for field velocity $\boldsymbol{v}_B(\boldsymbol{r}, t)$ of the stirred fluid: $\frac{\partial \boldsymbol{v}_B(\boldsymbol{r},t)}{\partial t} = \nu\nabla^2(\boldsymbol{v}_B) - \lambda(\boldsymbol{v}_B \cdot \nabla)\boldsymbol{v}_B - \nabla\eta(\boldsymbol{r}, r)$. Galilean symmetry, expected for fluids, $\boldsymbol{v}_B(\boldsymbol{r}, t) \mapsto \boldsymbol{v}_c + \boldsymbol{v}_B(\boldsymbol{r} - \boldsymbol{v}_c t, t)$, with $\boldsymbol{v}_c$ a constant relative velocity of two referential systems, is satisfied only if $\lambda = 1$ (constant). Therefore, λ shall be constant under scale transformations.

$$h(t) \simeq v_\infty t + \mathrm{sgn}(\lambda)(\Gamma t)^\beta \chi, \tag{4.9}$$

where v_∞ and Γ are KPZ-model dependent constants, and χ is a random variable. The constant Γ is actually defined by [30]:

$$\Gamma \equiv A^{1/\alpha}|\lambda|, \tag{4.10}$$

where A is also a model-dependent constant.

(1+1)-dimensional KPZ: Exact exponents, one-point statistics

The situation for the KPZ class is now well understood in $d_s = 1$. Exponents are exactly known since [13]. More recently, by starting with the solution of stochastic growth [31, 32] and hopping particles [33–35] models belonging to the KPZ class, the one-point interface statistics were also exactly derived from the KPZ equation itself for narrow-wedge like, [36–39], flat [40] and stationary [41, 42] initial conditions[4]. In short, it was proved that the distribution $p(\chi)$, with χ in Eq. (4.9), may be given by the Tracy-Widom (TW) distributions [43, 44] of random matrices theory depending on initial conditions[5]. Remarkably, experiments by Takeuchi *et al.*, involving liquid-crystal turbulence, were able to measure the TW distributions for $p(\chi)$ [46], thus confirming the dependence on the initial conditions for flat and curved cases [47, 48], beyond observing flat-to-stationary [49] and curved-to-flat crossovers [50]. There are many experiments showing agreement with the KPZ exponents in $d_s = 1$. Recent simulations of discrete models suggest [51], however, that one-point statistics in KPZ are very sensitive to the shape of the background space in which the interface develops.

(2+1)-dimensional KPZ: Estimation of exponents and one-point statistics

In contrast to the lower dimensional KPZ counterpart, there are no solvable models in KPZ for $d_s = 2$ (assuming isotropy). The body of KPZ knowledge has been taking shape by simulations of discrete models, renormalization group approaches, and a few experiments. The considered (up-to-date) best estimate $\alpha = 0.3869(4)$ obtained in a growth model [52] – consistent with nonperturbartive RG calculations [53, 54] – implies [Eq. (4.8)] $z = 1.6131(4)$ and $\beta = 0.2398(3)$. The last value agrees with an independent estimate recently made in [55]. Analogously to the (1+1)-dimensional case, $p(\chi)$ is found to be universal, but also initial-condition dependent [56–58]. In $d_s = 2$, possible initial conditions are spheres, cylinders, the flat plane and the stationary state.

[4] Narrow-wedge like means $h(r, 0) = -|r|/\delta, \delta \ll 1$. This initial condition generates a surface with macroscopic curved shape. The flat case is trivial: $h(r, 0) = 0$. The stationary initial condition means a *substrate* whose profile is given by the steady state ($t \to \infty$ for fixed L) of the KPZ equation, which actually is a Brownian path.

[5] The stationary initial condition [32, 41], and closely-related others [45] are examples of where Tracy-Widom distributions are not the limiting distributions for $p(\chi)$.

There are only a very few experiments reporting scaling exponents consistent with those expected for the (2+1)-dimensional KPZ case, despite a comparatively vast literature concerned to surface fluctuations in thin films. The rare pieces of evidence comes from sputtered Fe[15Å]/Au[21Å] crystalline multilayers on MgO(001) [59], amorphous SiO_2 films grown by chemical vapour deposition (CVD) [60], poly-(p-phenylene-vinylene)-type oligomer layers vapour-deposited on SiO_2 [61, 62], polycristaline CdTe films vapour-deposited on Si(001) [63], and now the pulsed galvanostatic electrodeposition of NiW films on polished steel [64]. However, evidence for universality beyond exponents was more recently obtained by Almeida *et al.* [63], and later than in [62, 64]. Below, we describe universal distributions that were, in $d_s = 2$, first experimentally measured in [63].

Squared roughness and maximal height distributions: past and open questions

Consider the *local* squared roughness $w_2(l,t)$, computed in a hypercubic box of lateral size $l \leq L$ [see Fig. 4.1], defined as:

$$w_2(l,t) := \overline{[h^2(\boldsymbol{r},t)]_l} - (\overline{[h(\boldsymbol{r},t)]_l})^2, \tag{4.11}$$

where,

$$\overline{[h(\boldsymbol{r},t)]_l} := \frac{1}{l^{d_s}} \int_r^{r+l} h(\boldsymbol{r},t) d^{d_s} r. \tag{4.12}$$

The squared global width, $W_2(L,t)$, is recovered for $l = L$. For a given growth process, the probability $p(w_2(l,t))dw_2$ of finding an interface, at time t, with squared roughness between $w_2(l,t)$ and $w_2 + dw_2$ can be written as:

$$p(w_2(l,t)) = \frac{1}{\langle w_2(l,t)\rangle} \Phi'\left(\frac{w_2(l,t)}{\langle w_2(l,t)\rangle}, \frac{\xi(t)}{l} \right). \tag{4.13}$$

where, here, brackets $\langle ... \rangle$ denote average over different boxes that span the interface and over the average over different samples. $\Phi'(x',y')$ is a scaling function. For the sake of clarity, it is worth to distinguish the ratio of local quantities such as $x' \equiv w_2(l,t)/\langle w_2(l,t)\rangle$ from the global ($l = L$) corresponding ones such as $x \equiv W_2(L,t)/\langle W_2(L,t)\rangle$. Equivalently, we distinguish $y' \equiv \xi(t)/l$ from y, and therefore $\Phi'(x',y')$ from $\Phi(x,y)$.

While in the growth regime one has $\Phi(x, y \ll 1) = \Phi'(x', y' \ll 1)$, in the steady state it follows $\Phi(x, y \gg 1) \neq \Phi'(x', y' \gg 1)$ in general [65]. Both steady steady functions are expected to be universal [66–68]. Exact results are available only for $d_s = 1$: $\Phi(x,y)$ for EW interfaces [69]; $\Phi(x, y \gg 1)$ for EW(KPZ) [66] and diffusion-dominated growth [67], and $\Phi'(x', y' \gg 1)$ for two types of Gaussian surfaces (including KPZ) [65]. In $d_s = 2$, the universality of $\Phi'(x', y' \gg 1)$ for KPZ systems was experimentally measured in CdTe surfaces by the Author and collaborators [63], guided by [72], where we compared curves obtained from discrete models with those from the experimental data. However, recent numerical

studies [73, 74] pointed out that more care should be taken to analyse the limit $y' \gg 1$.

A regime experimentally unexplored hitherto is the growth regime and its scaling function $\Phi(x, 0 \lesssim y \ll 1)$ expected to be superuniversal – that is, the functional form shall be unique for all types of growth dynamics, regardless d_s. First seen for EW interfaces at $d_s = 1$ [69], then in [74] for KPZ and other growth dynamics in $d_s = 1$ and $d_s = 2$, $\Phi(x, 0 \lesssim y \ll 1)$ was found, on the basis of simulations, to be well fitted by lognormal distribution function $f_{\rm LND}(x; \langle \ln(x) \rangle, \sigma_x)$:

$$f_{\rm LND}(x; \langle \ln(x) \rangle, \sigma_x) = \frac{1}{\sqrt{2\pi} x \sigma_x} \exp\left(\frac{-(\ln(x) - \langle \ln(x) \rangle)^2}{2\sigma_x^2} \right), \tag{4.14}$$

with $\sigma_x \equiv (\langle x^2 \rangle_c)^{1/2}$. We will return to this point in Sec. 4.3. For while, its is worth remarking that $\lim_{y \to 0} \Phi(x, y) = \delta(x - 1)$ since correlations are negligible in the $y \to 0$ scale regime and, therefore, the central limit theorem guarantees $\langle (W_2(L, t))^2 \rangle_c \sim O(L^{-d_s})$. In summary, an universal crossover from the Dirac delta distribution, to $f_{\rm LND}(x; \langle \ln(x) \rangle, \sigma_x)$, then to steady state distribution $\Phi'(x', y' \gg 1)$ and $\Phi(x, y \gg 1)$ is expected along the increasing y' and y axis, respectively.

To close this section we also mention a related quantity, namely, the maximal relative (to the mean) height:

$$m(l, t) := \max \{h(\boldsymbol{r}, t)\}_l - \overline{[h(\boldsymbol{r}, t)]_l}, \tag{4.15}$$

where $\max \{h(\boldsymbol{r}, t)\}_l$ is the maximum value of h inside a square box of size l. The probability $p(m(l, t))dm$ of finding a box at the interface of size $l \leq L$, at time t, with $m(l, t)$ between $m(l, t)$ and $m + dm$, can be written as:

$$p(m(l, t)) = \frac{1}{\sigma_m} \Upsilon' \left(\frac{m(l, t) - \langle m(l, t) \rangle}{\sigma_m}, \frac{\xi(t)}{l} \right). \tag{4.16}$$

with $\sigma_m = \langle m^2(l, t) \rangle_c$. The scaling function $\Upsilon'(u', y')$ and the global counterpart $\Upsilon(u, y)$ are expected to be universal as well. The exact PDF $p(m(L))$ is known for (1+1)-dimensional EW(KPZ) interfaces in the steady state for periodic boundary conditions (PBC) and free boundary conditions (FBC) [75, 76], checked in discrete growth models [77], and numerically estimated for KPZ models with PBC in $d_s = 2$ [78]. The universality of a local PDF $p(m(l, t))$ and its scaling fuction $\Upsilon'(u', y' \gg 1)$ was numerically and experimentally accessed for (2+1)-dimensional KPZ dynamics by Almeida *et al.* [63], revisited with proper care by Halpin-Healy and Palasantzas [62], and numerically confirmed to be independent of the initial conditions by Carrasco and Oliveira [74]. In the lower-dimensional KPZ case, Takeuchi's experimental data [21] suggests that $\Upsilon'(u', y' \gg 1)$ can be well described by the exact $\Upsilon(u, y \gg 1)$ derived from (1+1)-dimensional EW equation with FBC [75, 76].

4.1.4 Definition of ratio of cumulants

As discussed above, beyond scaling exponents, PDFs of height, roughness, and extreme height can be universal in interface growth phenomena. Usually, the comparison with expected universal PDFs is carried out by analysing dimensionless cumulants of the PDF $p(X)$, such as the coefficient of variance R, the skewness S and the Kurtosis K, defined as:

$$R := \frac{\langle X \rangle_c}{[\langle X^2 \rangle_c]^{1/2}}; \quad S := \frac{\langle X^3 \rangle_c}{[\langle X^2 \rangle_c]^{3/2}}; \quad K := \frac{\langle X^4 \rangle_c}{[\langle X^2 \rangle_c]^2} \tag{4.17}$$

where $\langle X^n \rangle_c$ is the n^{th} cumulant of X. S is a coefficient of asymmetry of the distribution in respect to the mean $\langle X \rangle_c$ (A symmetric PDF has $S = 0$). K quantifies how much the peak and the tails differ from the Gaussian distribution. PDFs with peaks higher (lower) than the Gaussian have $K > 0$ ($K < 0$) and, hence, their tails are heavier (lighter) than the tails of the normal PDF.

4.2 Materials and experimental methods

In this Section we describe properties of the materials and working principles of growth and characterization techniques for the films. At the end, we describe the experimental procedures employed to carry out our research.

4.2.1 Polycrystalline CdTe films

Cadmiun telluride is a zinc-blende structured semiconductor of the II-VI family whose direct gap energy, $E_{\text{gap}}(T) = 1.513(1)$ eV at $T = 300$ K [79], and high adsorption coefficient, $\alpha_{\text{abs}} \sim 10^4 - 10^6$ cm^{-1} for $1.5 - 3.5$ eV [80], render it and its relatives alloys – such as HgCdTe and CdZnTe – prominent materials for the photovoltaic [81, 82], infrared [83], X-ray and γ-ray detection [84] technologies. For instance, CdTe-based solar cells using glass substrates can already achieve conversion efficiencies around 16% [81, 82], while those using flexible substrates, such as polyimide foils, give 11% of efficiency [85, 86]. In the case of polyimide, this efficiency is obtained even for films vapour-deposited in low temperature conditions ($\lesssim 450\,^{\circ}$C), constrained by the polymer chemical stability.

From a fundamental point of view, the growth of large-area and high-quality CdTe crystals remains challenging compared to the case of IV (*e.g.* Ge, Si), and III-V (*e.g.* InSb, GaAs) semiconductors (see [87] for a review). The main reason is the omnipresence of grain boundaries (GBs), native point and other types of defects in CdTe layers. Such defects are attributed to the large mismatch between CdTe lattice constant ($a_{\text{lat}} = 6.48$ Å at $T = 300$ K [88]) and substrate lattice constants (*e.g.* Si $a_{\text{lat}} = 5.43$ Å at $T = 300$ K). Several techniques have been employed to grow large-area and defect-free CdTe thin films in order to, ultimately, improve the efficiency of film-based devices. Among these techniques, one stands

out metalorganic chemical vapor deposition [89], electrodeposition [90], molecular beam epitaxy [91], hot wall epitaxy (HWE) [92], sputtering [93], and others [87].

The difficulty around the CdTe growth, supplemented by its applied demand, have called attention to the fundamentals of its growth dynamics. Regarding the CdTe surface evolution, there is evidence for dynamical scaling invariance for films grown by HWE on glass covered by fluorine-doped tin oxide [94–96], and for films sputter-deposited on CdS/glass substrates [97]. In all these cases, large sets of scaling exponents are found to satisfy *anomalous* scaling relations [9]. In [94–96], these scaling relations are additionally dependent on the substrate temperature. The role of surface defects, mainly GBs, in the emergence of anomalous scaling has been recently emphasised [97]. Despite such non-trivial examples of fluctuations in polycrystalline CdTe surfaces, Almeida *et al.* [63] recently reported evidence for simple (Family-Vicsek [Eq. 4.3]) scaling and *universal* behaviour of surface fluctuations for CdTe films deposited on Si(001) by HWE [63]. Notably, it was shown that CdTe dynamics displays (2+1)-dimensional KPZ statistics [63] *regardless* the deposition temperature ($200\,^{\circ}\mathrm{C} - 300\,^{\circ}\mathrm{C}$) [19]. The lower T, the longer the characteristic time t_c from which surfaces start to display KPZ scaling. For films grown at $T = 150\,^{\circ}\mathrm{C}$, for example, the authors could not even observe the KPZ regime for films as thick as 3.2 μm. In this case, height fluctuations were observed to follow Random Deposition scaling as briefly mentioned in Sec. 4.1.2. But we shall wonder whether the observed RD scaling would be a (long) transient scaling preceding KPZ dynamics, as the Author here believe it is. In brief, the main conclusion about Almeida *et al.* works [19, 63] is that KPZ statistics arises at a crossover time t_c that is essentially controlled by the deposition temperature. Below t_c the statistics of surface fluctuations is given by RD.

From a thin-film point of view, it is known that the choice of the substrate can drastically affect the initial growth dynamics [98], or even the infinite-thickness regime regarding epitaxial processes [99]. To be precise, initial dynamics of CdTe films grown on Si(001) and on Si(111) substrates at same growth conditions were reported to be (qualitative and quantitative) different according to Lalev *et al.* [100]. The influence of the substrate on the grown CdTe layer is a matter of ample interest; it has been discussed [87] for the cases of Ge, Si, CdS, GaAs and $NbSe_2$ substrates. In terms of surface fluctuations, substrate-induced transient regimes shall be expected.

4.2.2 Hot Wall Epitaxy

Hot wall epitaxy (HWE) is a thermal evaporation technique developed in 1978 [101] for mainly growing II-VI compounds such as CdTe [102]. The key component of an HWE system is the tube that collimates the vapour beam from the source towards the substrate and can be heated for guaranteeing low material loss. As the tube severely constrains the angular dispersion of the beam, layers with uniform thickness are obtained. Growth is typically performed in high vacuum environment ($P \sim 10^{-7}$ Torr), with growth rates tuned between 0.01 Å/s and 3 Å/s. HWE is essentially limited for growing compounds that either sublimate congruently or that, at least, keep their stoichiometry after dissociation. The former case applies to CdTe in a wide range of the P-T phase diagram [101]. The HWE technique has been used, for instance, for growing CdTe epitaxial layers on Si(111) [92], Si(100) [100], glass [103], GaAs [104], beyond growing self-assembled CdTe quantum dots on Si(111) [105, 106].

4.2.3 Atomic Force Microscopy

The invention of scanning probe microscopes (SPM) [107, 108] in the 1980s revolutioned the study of surfaces by allowing access to atomic scales in real space. Nowadays, SPM techniques are widespread across fundamental and applied researches in surface science [109]. The working principle of SPM relies on a feedback-mediated scan of a sharp tip ($\sim 1 - 100$ nm radii) that glides along the surface of a specimen. The feedback mechanism can be mediated, for instance, by the tunneling current between the tip and a conducting surface, as in the case of scanning tunneling microscope (STM) [107], or by the forces experienced by the tip near the sample surface, as in the case of atomic force microscopy (AFM) [108].

In the AFM, surface forces as small as $\sim 10^{-18}$ N are measured by the deformation of a flexible cantiveler[6] that holds the tip at one of its ends. Several methods were proposed to measure surface forces, including STM [107], optical interferometry [110], capacitive methods [111], and piezoresistence [112]. Nevertheless, virtually all current AFM equipments employ an optical-lever based sensor [113, 114], in which deformations of the cantilever are monitored via deflections of a laser beam. The beam is focused at the cantilever face and reflected to a four-segmented photodetector that communicates with a controller. The controller manages the scanning operation. By applying voltages in piezoelectric devices, the controller promotes tip-surface movements in three spatial dimensions. Resolutions are $0.01 - 5$ nm in plane and $\sim 10^2$ nm in the vertical direction. The feedback mechanism works by reading the output signal coming from the photodetector, comparing the signal with a pre-determined setpoint value, and adjusting the voltages associated with the vertical movement of the piezo such that output-setpoint error is minimized. Voltages recorded along the scan are used to generate

[6] Cantilevers are typically $50 - 500$ μm long, $20 - 100$ μm wide and have a spring constant in the range of $0.01 - 100$ N/m.

an image in two spatial dimensions plus the dimension associated to the physical quantity probed by the tip (*e.g.* surface height, local coefficients of friction, stiffness, conductance, magnetization, *etc.* [109]).

The simplest mode of operation of AFM is the so-called contact mode [108, 109], used to measure the local surface height $h_{\mathrm{AFM}}(\boldsymbol{r})$. In this mode, the tip is approached to the surface until it experiences a repulsion force so that the cantilever bends up. The resulting deflection in the optical-lever sensor is used as a feedback control. The value of $h_{\mathrm{AFM}}(\boldsymbol{r})$ is measured relative to the minimum scanned height, $\min(h_{\mathrm{AFM}}(\boldsymbol{r}))$, inside the scanned area.

4.2.4 Growth and characterization of CdTe films

We grew CdTe films on polyimide foils (Kapton®HN, DuPont, USA) by HWE technique under high-vacuum ($\sim 10^{-7}$ Torr) environment. The wall of the HWE system is a cylinder 7 cm long with nearly 0.7 cm of diameter. Between one end of the wall and the substrate location, a manually controlled shutter was inserted to start and end the growth. High vacuum was achieved by a set of oil-based rotary and diffusion pumps. We inserted the polyimide substrate above the end of the wall. Prior deposition, substrate temperature was set to $T = 150\,^{\circ}\mathrm{C}$. Solid 4N CdTe material was smashed into grains of ~ 0.2 mm diameter, inserted into the HWE furnace source, and heated at $T = 510\,^{\circ}\mathrm{C}$. Both temperatures were monitored via a PID controller. The wall was not heated. Once the vacuum and both the temperatures became stable, the shutter was opened to start the deposition. After a pre-determined growth time t, the deposition was finished by closing the shutter, and cooling the sources. Films were removed from the HWE system roughly after two hours after stopping the deposition process. We grew a total of 14 independent CdTe films by repeating the experimental conditions above, but varying the growth time from 7.5 min to 5760 min.

Thickness of films were measured *ex-situ* by an optical profilometer (ContourGT-K, Brucker Corp., Germany) and a stylus profilometer (XP-1, Ambios Tech., United States). From thickness measurements, we estimate the CdTe growth rate as $F \approx 14$ nm/min (error less than 10%). We performed surface characterizations by AFM (NT-MDT Ntegra Prima SPM, Russia) with an optical-lever sensor operated in air, in contact mode, using Si cantilevers (CSG30, NT-MDT, Russia) of nominal radius 10 nm. For each film, we scanned an average of 10 different squared sub-regions of the CdTe surface with lateral size $L_{\mathrm{AFM}} = 10$ μm, and 512×512 pixels. Pixel size $a \approx 0.02$ μm. The lateral size was chosen so that both intra- and inter-grain morphology could be accessed simultaneously. AFM images were corrected by a second-order fit lines, and then used to data analysis by Fortran-language codes wrote by the Author. We also carried out measurements of X-ray diffractions (D8-Discover, Bruker, Germany) of the films in the coupled θ-2θ geometry.

4.3 Results: Kinetic roughening of CdTe surfaces

In the analysis of CdTe films, the lateral size of AFM images $L_{\text{AFM}} = 10\ \mu$m is referred to as the global scale L. Since we are concerned to the surface statistics, the statistics of the set $\{h_{\text{AFM}}(\boldsymbol{r},t)\}$ is, in this case, equivalent to that of the set $\{h(\boldsymbol{r},t)\}$, which has its reference in an ideal flat substrate. Without loss of generality for what is presented below, $h_{\text{AFM}}(\boldsymbol{r},t)$ is hereafter denoted by $h(\boldsymbol{r},t)$.

4.3.1 Film morphology and polycrystallinity

Figure 4.2 shows a few AFM images of film surfaces that well represent distinct growth regimes. Surface morphology is one of the aspects that notably changes during film deposition: for times within the interval 7.5 min $\lesssim t \ll 25$ min, the imaged surfaces are composed in part by a finite area fraction of the Kapton substrate and, in part, by CdTe islands that randomly nucleated over the substrate [Fig. 4.2(a)]. The average grain size[7] in this regime is $l_g(t) \approx 100$ nm. The exposed substrate area, nevertheless, becomes fully covered by the CdTe film around $t \approx 25$ min. During the subsequent interval 25 min $\lesssim t \lesssim 300$ min, CdTe surface shows a plenty of apparently rounded[8] and compacted grains that do not coarsen, but keep their size $l_g(t) \approx 100$ nm instead. Such grains are indeed CdTe crystals built in a few possible crystallographic orientations, as revealed by their X-ray diffraction spectra [Fig. 4.3(a)]. From $t \gtrsim 300$ min onwards, grains at the surface start to visibly coarsen, thus showing their faceted structure [Fig. 4.2(c,d)], which is better visualized in the inset of Fig. 4.2(c).

Although the CdTe film is polycrystalline, with grains following different crystallographic orientations in the bulk, one observes that the total volume of (111)-oriented crystals increases with the deposition time – compare the two X-ray diffraction spectra shown in Fig. 4.3(a). This effect, called (111) texturization [115], has generically been observed in CdTe layers deposited by different growth techniques (*e.g.*, sputtering [116], physical vapor deposition [117] and hot wall [19, 103]), and over different types of substrates, such as amorphous [103,116] and crystalline substrates [19]. Here we indirectly quantify film texturization by computing the scattering volume density $P((111),t)$ of (111)-oriented CdTe grains within the bulk as a function of the deposition time:

$$P((111),t) = \frac{I(2\theta_{111},t)/A_{\theta\text{-}2\theta}(\theta_{111},t)}{\sum_{\text{hkl}} I(2\theta_{\text{hkl}},t)/A_{\theta\text{-}2\theta}(\theta_{\text{hkl}},t)}, \tag{4.18}$$

where $I(2\theta_{\text{hkl}},t)$ refers to the intensity of (hkl)-oriented grains in the X-ray diffraction spectrum of the CdTe polycrystalline layer grown by t minutes, and $A_{\theta\text{-}2\theta}(\theta_{111},t)$ is the absorption factor function for the θ-2θ diffraction geometry [115]:

[7] The size we referred to is that estimated from a top view image, as depicted in Fig. 4.2.
[8] At the $l_g \approx 100$ nm scale, rounded shape could also be an artifact of the AFM tip scan.

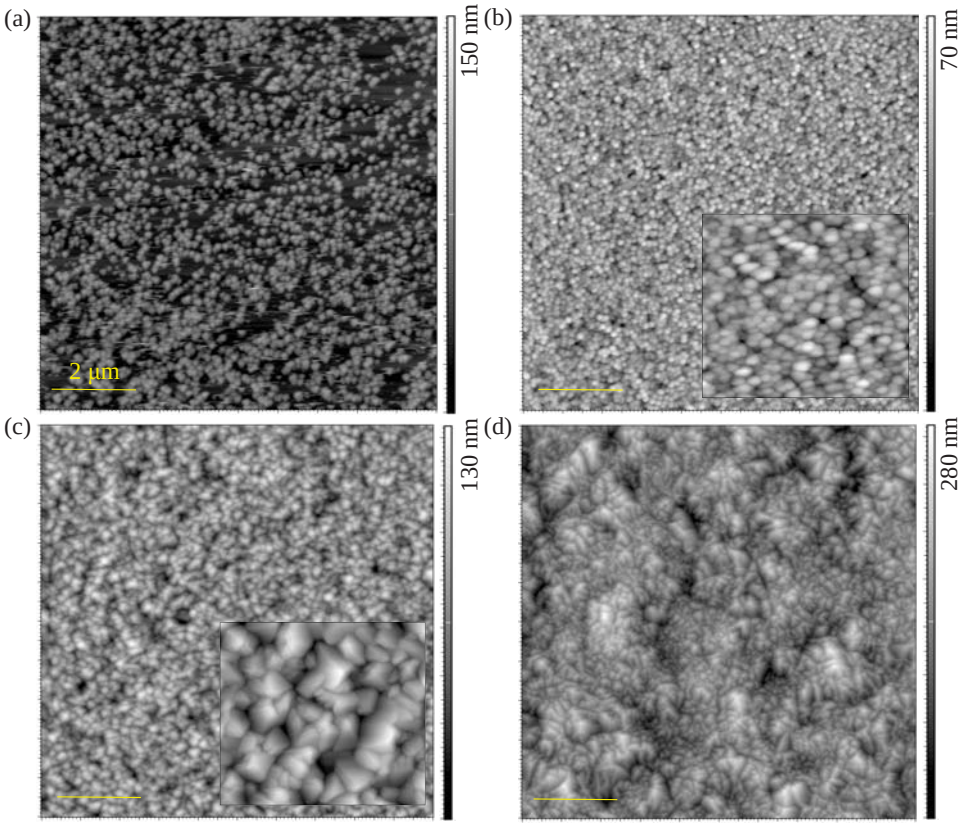

Figure 4.2: Typical 10 μm $\times$ 10 μm atomic force microscopic images of CdTe films thermally evaporated on Kapton substrates by hot wall technique (high-vacuum condition $\sim 10^{-7}$ Torr). Substrate temperature set at $T = 150\,^{\circ}\mathrm{C}$. Images show CdTe surfaces after (a) 7.5 min, (b) 25 min, (c) 360 min and (d) 2880 min of deposition. The deposition rate is adjusted so that film thickness grows at the average of 14.0 nm min^{-1}. Insertion in (c) is a 2 μm $\times$ 2 μm scanned region for films grown at 25 min, and 360 min, respectively. The insertion in (c) highlights the faceted structure of CdTe crystals.

$$A_{\theta\text{-}2\theta}(\theta_{\mathrm{hkl}}, t) = 1 - \exp\left(-\frac{2\mu\tau(t)}{\sin\theta_{\mathrm{hkl}}}\right), \tag{4.19}$$

with μ is the coefficient of linear attenuation for CdTe considering the $\lambda_{\mathrm{CuK}\alpha} = 0.151418\ \mathrm{nm}$ radiation. $\tau(t) \equiv Ft$ stands for the film thickness at time t.

Results in Fig. 4.3(b) show the progressive raising of $P((111), t)$ as function of time. Starting from $\approx 70\%$, $P((111), t)$ at $t = 25$ min goes over 95% at $t \approx 200$ min. For comparison, we include in the same panel the probability $P((111), t)$ measured from CdTe layers produced at same conditions, but grown on Si(001) substrates [19]. Notice that the (111) texture becomes similar for films grown both on Kapton and on Si(001) substrates only when large-enough times ($t \gtrsim 175$ min) are considered. Conversely, the probability $P((111), t)$ is significantly smaller for the Kapton case within the time interval 25 min $\lesssim t \lesssim 175$ min. This difference,

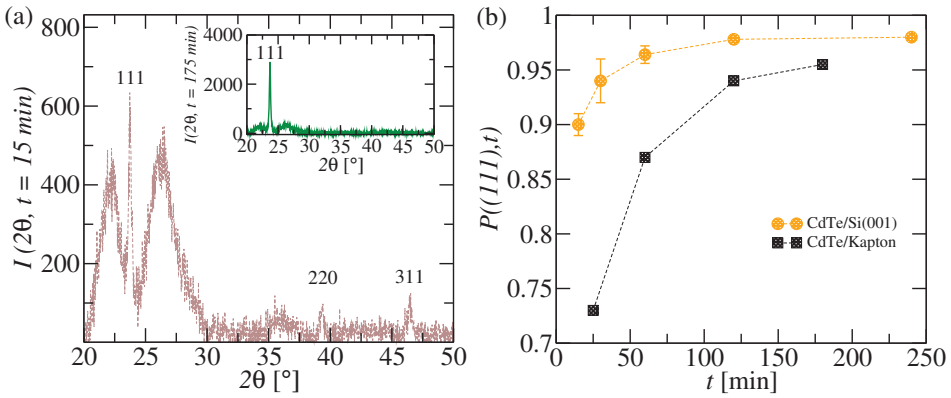

Figure 4.3: (a) X-ray diffraction spectra for CdTe films grown at $t = 15$ min (main) and $t = 175$ min (inset). CdTe diffraction peaks are labelled, on its top, with the corresponding crystallographic orientation. Broad peaks with no labels result from the amorphous scattering of the Kapton substrate. CdTe peaks for $50\,^\circ < 2\theta < 80\,^\circ$, if present in the film, were not distinguished within the experimental noise-intensity ratio. (b) Scattering volume density of (111)-oriented grains in the film as function of time.

stemming from a substrate effect, may indicate that substrate-induced transients could play a role in CdTe surface fluctuations.

4.3.2 From pseudo-steady state to Kardar-Parisi-Zhang scaling

Height fluctuations at CdTe surfaces display different regimes as function of time in a very similar manner as the morphological aspects do. For instance, the behaviour of the global width $W(L,t)$ – hereafter denoted by $W(t)$ – can also be divided in three stages [Fig. 4.4(a)]. In the first stage (7.5 min $\lesssim t \lesssim$ 25 min), $W(t)$ decreases from 28(3) nm to 14(2) nm. We shall argue below this is a smoothing regime that can be traced back to the complete wetting of the CdTe layer over the substrate. The second observed regime is comparatively longer than the early one: within the time interval 25 min $\lesssim t \lesssim$ 300 min, the surface manages to organize incoming atomic species so that $W(t)$ merely fluctuates around 15 nm with no apparent decreasing nor growing. Such a seemingly time-independent roughness behavior is compatible with the two-dimensional EW scaling, for which $\beta = 0$ [Tab. 4.1]. Indeed, by applying the scaling $W(t) \sim t^{\beta}$ [Eq. (4.3)] to the experimental data, we obtain $\beta = -0.01(7)$. For $t \gtrsim 300$ min, in constrast, $W(t)$ grows in time with $\beta = 0.24(7)$. Although $\beta = 0.24(7)$ is close to value found in (2+1)-dimensional KPZ model systems [Tab. 4.2], it also encompasses, within the error bars, the universal values for systems with linear ($\beta = 0.25$ [118]) and nonlinear ($\beta \approx 0.20$ [119]) diffusion-dominated dynamics. The crossover time t_c that characterizes the passage from the non-growing roughness regime to the growing roughness regime can be estimated from the time series of the effective exponent $\beta_{\text{eff}}(t;i)$, here defined as the average slope of i consecutive points in the $\log W(t) \times \log t$ plot. As shown in inset of

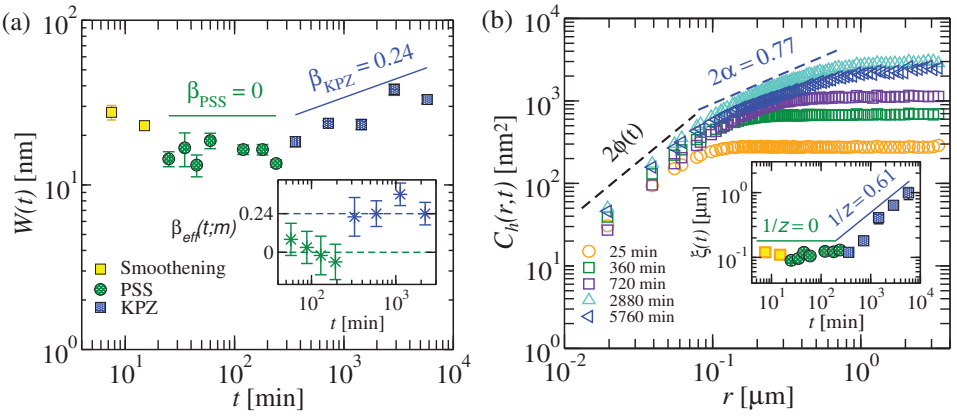

Figure 4.4: (a) Temporal evolution of the global roughness $W(t)$ of CdTe surfaces. Symbols of different colours refer to different scaling regimes. Green and blue solid lines are guide to eyes and have null and 0.24 slope coefficients, respectively. Inset shows the effective growth exponent $\beta_{\text{eff}}(t;5)$ (defined in main text). Dashed green and blue lines stand for the PSS ($\beta = 0$) and KPZ ($\beta = 0.24$) scaling exponents, respectively. (b) Height-height difference function $C_h(r,t)$ calculated for several growth times. Dashed lines are for visual reference: they indicate non-universal ($2\phi(t) \approx 1.2$) and KPZ universal ($2\alpha \approx 0.77$) slope coefficients. The inset shows the temporal variation of the correlation length $\xi(t)$. Solid lines are references for the Pseudo-steady state ($1/z = 0$) and KPZ scaling regime ($1/z \approx 0.61$) after assuming $\xi(t) \sim t^{1/z}$. Reprinted from Almeida *et al.* [1] under the Creative Commons license (Nature).

Fig. 4.4(a), $\beta_{\text{eff}}(t;5)$ seems to change abruptly from $\beta_{\text{eff}}(t;5) \approx 0$ for $t < t_c$ to $\beta_{\text{eff}}(t;5) \approx 0.24$ for $t > t_c$. This gives an estimation of $t_c \approx 300$ min. We checked the estimation of t_c is independent on the choice of i for $3 \leq i \leq 6$.

In order to complement the analysis, we now turn to interface fluctuations in space by paying attention to the equal-time, height-difference correlation function:

$$C_h(\boldsymbol{r},t) := \langle [h(\boldsymbol{r'},t) - h(\boldsymbol{r'}+\boldsymbol{r},t)]^2 \rangle. \tag{4.20}$$

Brackets represent average over all possible combinations of pairs of points in the AFM image that are separated by a radial distance $r = |\boldsymbol{r}|$ (isotropy is assumed), and average over different AFM images acquired from different regions of a same CdTe sample. For scaling-invariant surfaces with grainy features of mean size $l_g(t)$, this correlation function is expected to scale as [120, 121]:

$$C_h(r,t) \sim \begin{cases} r^{2\phi(t)} & (r \ll l_g(t)); \\ r^{2\alpha} & (l_g(t) \ll r \ll \xi(t)); \\ \text{const.} & (\xi(t) \ll r); \end{cases} \tag{4.21}$$

where $\phi(t)$ is a nonuniversal exponent related to the grain morphology [121], while α is the universal roughness exponent defined in Eq. (4.3).

Figure 4.4(b) shows the correlation function $C_h(r,t)$ computed from AFM images associated to CdTe surfaces at different times. For the range 25 min $\lesssim t \lesssim$ 720 min, the function exhibits only the initial $C_h(r) \sim r^{2\phi(t)}$ scaling before it saturates to a time-dependent value $C_h(r \gg \xi(t),t)$. Such a scaling is characterized by $\phi(t)$ increasing from $\phi(t) \approx 0.6$ to $\phi(t) \approx 0.8$ as the time elapses. These values indicate that the average shape of grainy structures undergoes a variation from a rounded to a sharper (faceted) shape [121], in consonance with direct observations made from AFM images [Fig. 4.2]. The single spatial crossover in the $C_h(r,t)$ curves signalizes that $\xi(t) \approx l_g(t)$, with both quantities being at the order of 100 nm. For $t \geq 720$ min, however, $l_g(t) \ll \xi(t)$ so that the intermediate scaling $C_h(r) \sim r^{2\alpha}$ can be detected in the experimental curves. Considering $C_h(r,t)$ for $t = 2880$ min and for $t = 5760$ min, for which the regime $l_g(t) \ll r \ll \xi(t)$ is clearer, we obtain $\alpha = 0.37(4)$. This value strongly suggests KPZ dynamics [Tab. 4.2], since it differs from values for linear ($\alpha = 1$ [118]) and nonlinear ($\alpha \approx 0.66$ [119]) diffusion-dominated dynamics.

Insertion of Fig. 4.4(b) shows how $\xi(t)$, estimated from the $C_h(r,t)$ curves, evolves in time. Curiously, data reveals that correlations *do not* spread parallely to the surface within the period 25 min $\lesssim t \lesssim t_c$. By assuming the growth law $\xi(t) \sim t^{1/z}$ [Eq. (4.4)], experimental data gives $1/z = -0.04(3)$ for such a regime. This measurement is crucial to rule out a possible EW scaling, for which $1/z = 1/2$ [Tab. 4.1]. On the other hand, the situation is distinct for surfaces grown beyond the crossover time $t \gg t_c$. For this regime, lateral correlations spread through the interface with $1/z \approx 0.63$, which is in good agreement with the behaviour displayed by (2+1)-dimensional KPZ model systems [Tab. 4.2].

4.3.3 Partial summary, discussions and height distributions

The analysis we have performed hitherto indicates that a kinetic scaling theory can be applied to CdTe films grown by $t \gtrsim 25$ min. Otherwise, the system is in the submonolayer growth stage with $W(t)$ showing non-monotic behaviour. We remind that $W(t)$ firstly increases from $W(0\text{ min}) \approx 6$ nm (Kapton substrate) to $W(7.5\text{ min}) = 28(3)$ nm, then decreases to $W(t) = 14(2)$ nm for $t \lesssim 25$ min [Fig. 4.4(b)]. The very initial increasing of $W(t)$ can be traced back to the nucleation of three-dimensional CdTe islands onto the substrate according to the Volmer-Weber (VW) growth mode. This reasoning is based on observations of AFM images (see Fig. 4.2(a) and its vertical scale), and based on the fact that VW mode operates CdTe growth in similar growth conditions [122]. The subsequent surface smoothing we measure should then be related to the substrate coverage regime. Indeed, during the coverage stage, initial three-dimensional CdTe islands that were isolated on the Kapton substrate eventually grow and come into contact with each other. This contact largely generates defects at grain boundaries (GBs) if neighbouring islands do not have the same crystalline orientation. Coalescences may occur otherwise. The deep valleys which are instantaneously formed after the contact of neighborhouring islands are expected to relax via reallocation of particles,

so that the free energy is minimized. This process implies that height differences between the originally isolated islands (now forming a continuous portion of the CdTe layer) tend to diminish, which explains the overall smoothing after summing up contributions over the whole film. Notice that this is a possible physical scenario compatible with the response of $W(t)$. To be precise about the operative microscopic mechanisms during and after the contact of CdTe islands, *in-situ* accessing to the sub- and few-monolayer regimes is required (not addressed here).

In the multilayer scaling regime, CdTe surface fluctuations display distinct dynamics depending whether the growth time t is below or above the crossover time $t_c \approx 300$ min. The short-time dynamics is featured by a non-developing roughness and no spreading of parallel correlations, so that it resembles (in a certain sense) the steady steady of interfaces for which both $W(L,t) \sim L^{\alpha}$ and $\xi(t) \approx L$ are saturated. Here, however, neither $W(t)$ nor $\xi(t)$ have indeed reached the saturation regime since they start growing after t_c. Thereby, it seems appropriate to call such a regime as a pseudo steady-state (PSS). The emergence of PSS can be glimpsed by comparing surface fluctuations of CdTe films grown at same growth conditions, but on different substrates. In the previous work by the Author and collaborators [19], PSS does not appear in the scaling of CdTe films grown on Si(001) substrates, under the same growth conditions, and within the same time interval in which PSS occurs here. Therefore, we may face the transient PSS scaling as a substrate-induced effect.

In fact, $t_c \approx 300$ min not only corresponds to the time in which the PSS-KPZ crossover occurs, but also it roughly corresponds to the time in which (111)-oriented CdTe grains dominate the film[9] [Fig. 4.3(b)]. We suggest that the PSS regime occurs during a combination between surface roughnening – induced by the incoming of atomic species – and surface smoothing that can be associated to the covering of non-(111)-oriented grains by (111)-oriented crystallites. The combination shall be equilibrated such that roughnening is counter-balanced by smoothing.

For $t \gg t_c$, exponent values indicate that interface fluctuations are in the KPZ class [Tab. 4.2]. Remarkably, this is a non-trivial result given that KPZ scaling has not been observed for CdTe films deposited at such a low substrate temperature [19]. We notice that the different surface dynamics (PSS and KPZ) are also accompanied by morphological and structural changes as discussed in Sec. 4.3.1.

The crossover from a PSS to the KPZ scaling is also manifested by the probability $p(h,t)dh$ of finding a height at surface $h(\boldsymbol{r},t)$ between h and $h+dh$ as shown in Fig. 4.5. $p(h)$ is the probability density function, or height distribution (HD). Dimensionless ratios between cumulants of $h(\boldsymbol{r},t)$, such as the skewness $S(t)$ and the kurtosis $K(t)$ [Eq. (4.17)], fluctuates around $S(t) \approx 0$ and $K(t) \approx 0$ within the PSS regime. However they show a crossover to values close to (2+1)-dimensional KPZ ones [Tab. 4.2] for $t \gg t_c$ [Fig. 4.5(a)]. The argument is more convincing

[9] Notice that the observable difference between P((111),t) for CdTe/Kapton and for CdTe/Si(001) systems tends to vanish for $t \approx t_c$ [Fig. 4.3(b)].

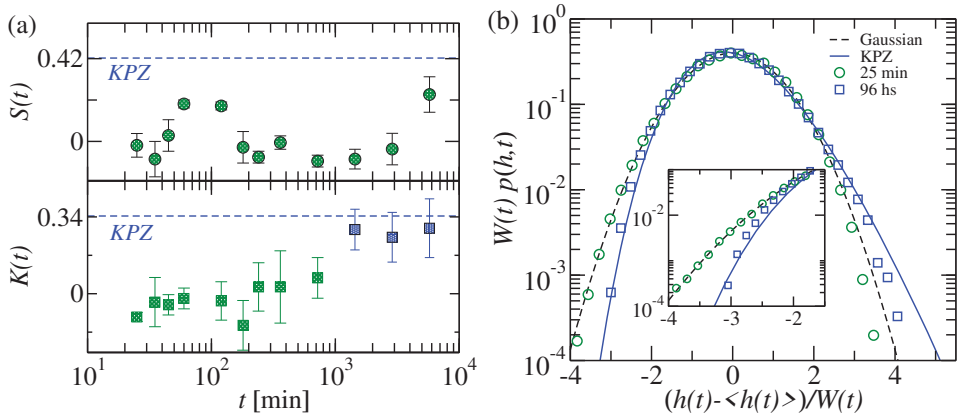

Figure 4.5: (a) Skewness, $S(t)$, (top) and Kurtosis, $K(t)$, (bottom) coefficients of HDs of CdTe surfaces at several times. Dashed blue line stands for the numerically estimates of $S(t \to \infty)$ and $K(t \to \infty)$ values observed in (2+1)-dimensional KPZ models [56,57]. (b) Rescaled CdTe-HDs (symbols) normalized to zero mean and unity variance. Dashed black and solid blue lines stand for the Gaussian-HD and KPZ-HD, respectively. The KPZ-HD is computed from (2+1)-dimensional KPZ models with flat initial condition [57]. Inset is a zoom in the left tail of the HDs. Reprinted from Almeida *et al.* [1] under the Creative Commons license (Nature).

Universal	25 min $\lesssim t \lesssim t_c$	$t \gg t_c$	KPZ class	Ref.
α	–[a]	0.37(4)	0.3869(4)	[52]
β	-0.01(7)	0.24(7)	0.241(1)	[55]
$1/z$	-0.04(3)	≈ 0.63	0.6199(2)[b]	[52]
$\alpha + z$	–[a]	≈ 1.96	2	[13]
S of $P(h)$	0.03(6)	0.24(9)	0.424(7)	[56]
K of $P(h)$	-0.06(8)	0.3(1)	0.346(8)	[56]

[a] Not measured in the experiment.
[b] Value obtained after using $\alpha + z = 2$ with α from [52].

Table 4.2: Universal exponents (α, β, $1/z$) and HDs coefficients, Skewness (S) and Kurtosis (K), measured in CdTe films grown on Kapton substrates for the early (25 min $\lesssim t \lesssim t_c$) and long time ($t \gg t_c$) scaling regime. Here, $t_c \approx 300$ min. The rightmost column shows estimates from numerical simulations of (2+1)-dimensional KPZ models. Experimental values of S and of K correspond to time averages for $t \lesssim t_c$, while the ones for $t \gg t_c$ are those measured for $t = 5760$ min.

looking at the $K(t)$ curve, which is known to converge faster than $S(t)$ in KPZ model systems. Figure 4.5(b) depicts two experimentally rescaled HDs in the PSS ($t = 25$ min) and in the KPZ ($t = 5760$ min) regime. To compare different times, we rescale HDs to have zero mean and unit variance. In this way, we are accessing $p(\chi)$ [with χ in Eq. (4.9)] also rescaled in the same manner. As indicated by $S(t)$

and $K(t)$, HDs are nearly Gaussians in the PSS scaling, but tend to crossover towards the universal KPZ-HD for $t \gg t_c$. Notice that the crossover is particularly clear at the left tail of rescaled HDs [inset of Fig. 4.5(b)].

4.3.4 Modelling: a toy model showing the Pseudo-steady state

In Ref. [19], we proposed an one-dimensional growth model that successfully reproduced the time scaling behaviour displayed by the average slope, $\langle\overline{(\nabla h(\boldsymbol{r},t))^2}\rangle$, of CdTe surfaces films grown at different substrate temperatures (from 150 °C to 300 °C). Interestingly, the same model might account for the PSS scaling here experimentally observed.

We define the model on a lattice of $L_{\text{mod}} = 2000$ sites with lattice spacing $a_{\text{mod}} = 1$ "nm" similar to that of CdTe crystals (~ 1 nm at $T = 300$ K [88]). The initial condition, $\{h_i(t=0)\}$ with $i = 1, 2, ..., L_{\text{mod}}$ is set to be one-dimensional profiles extracted from the experimental AFM-imaged CdTe surfaces. We use AFM images of CdTe surfaces grown by 60 min, since our goal is to account for the PSS scaling. Lateral AFM scan was $L_{\text{AFM}} = 2$ μm, in order to match with L_{mod}. The deposition rate, F, is also parametrized according with the experimental growth rate, namely, $F = 14$ monolayers (ML) of particles deposited per time step ("min") of the model. Particles are represented by a square of area a^2_{mod}. For each event of deposition, the relaxation rules are as follow. A site i at the interface is randomly selected to simulate the stochastic location of atomic adsorptions. A particle permanently aggregates at i, that is $h_i(t+\delta t) = h_i(t) + 1$ (with $\delta t = 1/F$) if the restricted solid-on-solid (RSOS) condition [123], $|h_i(t)+1-h_{i\pm1}(t)| \leq 1$, is satisfied. Otherwise, the particle randomly diffuses until finding a site in which the RSOS rule is respected [124]. This account for the expected diffusion of atomic species at the surface of a single crystal [125]. During a diffusive trajectory, the particle may find a site that corresponds to a grain boundary (GB). A GB separates crystalline domains with distinct orientations and is thereby a defect region. In our model, we approximate GB sites as the local minima appearing in the initial height profiles $\{h_i(t=0)\}$. An energy barrier of $E_{\text{GB}} = 0.10$ eV is locally assigned to all GB sites so that diffusion across a GB site occurs with probability $P_d = e^{-E_{\text{GB}}/k_BT}$, where k_B is the Boltzmann constant. Moreover, as observed experimentally [19, 63], CdTe crystals eventually coalesce to form larger mounds. This suggests that a rearrangement of particles at, and around the GB sites, might occur to facilite inter-grain mass transport (notice that adsorption of particles is uniform among all sites, regardless whether that site is a GB or not). It is not our purpose to specify how such a rearrangement works, but we focus only on its final effect. Thereby, we model relaxations at the GB sites so that when a particle is deposited there, the GB site might become a regular site with probability $P_R = e^{-E_{\text{R}}/k_BT}$, where $E_{\text{R}} = 0.30$ eV. Finally, we consider that diffusion and aggregation occur much faster than adsorption of atomic species. Therefore, each particle irreversibly aggregates at the interface before the arrival of the next one. The energy values $E_{\text{GB}} = 0.10$ eV and $E_R = 0.30$ eV for the barrier and the

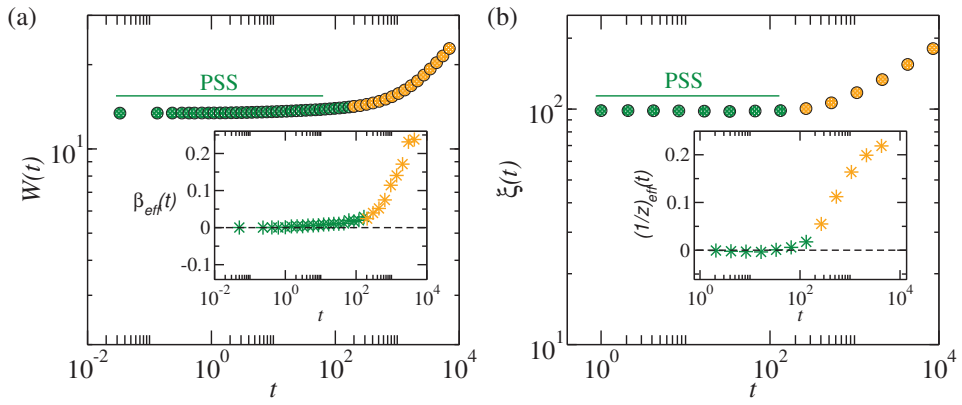

Figure 4.6: (a) Global roughness $W(t)$ and (b) correlation length $\xi(t)$ as function of time for interfaces generated by the one-dimensional lattice model described in the text. Insets show the time evolution of the effective growth exponent $\beta_{\text{eff}}(t)$ (a) and of the effective dynamical exponent $z_{\text{eff}}^{-1}(t)$ (b). Symbols of different colours used in both (a) and (b) plots refer to different scaling regimes: green symbols represent scaling for the PSS characterized by $\beta = 0$ and $1/z = 0$, while orange ones stand for a non-PSS scaling regime. Reprinted from Almeida *et al.* [1] under the Creative Commons license (Nature).

relaxation at GB sites, respectively, were found as those to better describe the experimental CdTe data in [19].

Figures 4.6(a-b) show how $W(t)$ and $\xi(t)$ of the interface generated by our model develops in time. By starting from $W(0) \approx 14$ nm and $\xi(0) \approx 100$ nm, both quantities do not increase until a certain model characteristic time $t_c^{\text{mod}} \approx 300$ "min" is approached. This is observed in the effective growth $\beta_{\text{eff}}(t) \equiv \frac{d\ln(W(t))}{d\ln t}$ and dynamical $z_{\text{eff}}^{-1}(t) \equiv \frac{d\ln(\xi(t))}{d\ln t}$ exponents, which behave as $\beta_{\text{eff}}(t) \approx 0$ and $z_{\text{eff}}^{-1}(t) \approx 0$ for $t \ll t_c^{\text{mod}}$ as shown in the insertions of Fig. 4.6(a-b), respectively. Curiously, there is even a quantitative agreement between t_c^{mod} and that of the experiment $t_c \approx 300$ min, once both correspond to times for which deposits are $\sim 10^3$ ML thick. For $t \gg t_c^{\text{mod}}$, $W(t)$ and $\xi(t)$ also grow in the artificial interface.

The crossover at t_c^{mod} characterizes the time for which most of GBs sites at interface relaxed, thus leading to grain coalescences and further interface roughening.

The outcomes of the toy model reveals that a combination of $i)$ relaxation of defects at GB sites and $ii)$ roughening might (minimally) account for the PSS scaling. Notice that this is not too far from what experimentally we measured. Since the volume of (111)-oriented CdTe grains increases over time, GBs formed due to the "collision" of (111) and non-(111) grains become less relevant to the interface dynamics. In fact, when $P((111), t) \sim 95\%$ most of GBs are arguably only due to the "collision" of (111) with (111) grains and interface fluctuations crossover from the PSS dynamics.

Despite a somewhat consistent picture with the experiment, we remark that the one-dimensional model is not built with the intention to reproduce the complex

CdTe polycrystalline dynamics, nor to explain the asymptotic KPZ scaling. The intention is to gain further evidence that minimal ingredients believed to be relevant to the real dynamics are enough to generate the PSS scaling, even when these ingredients are modelled in the simplest (toy-like) manner. Such a way of thinking is based on the concepts of universality.

4.3.5 Generalized scaling and lognormal distributions

The Family-Vicsek *ansatz* [Eq. (4.3)] can be generalized to account for the scaling of the n^{th} cumulant of the squared roughness, denoted as $\langle [w_2(l,t)]^n \rangle_c$. Partially based on simulations of nonconserved and conserved growth models and, partially, on exact relations for one-dimensional models in the EW and RD class, the authors from [74] propose that:

$$\langle [w_2(l,t)]^n \rangle_c = l^{2n\alpha} f_n(\xi(t)/l); \quad f_n(y') \sim \begin{cases} (y')^{z\gamma_n} & (y' \ll 1); \\ \text{const.} & (y' \gg 1). \end{cases} \tag{4.22}$$

Scaling functions $f_n(\cdot)$ are expected to be universal, as well as their associated γ_n exponents, which can be written as [74]:

$$\gamma_n = 2n\beta + [(n-1)d_s]/z. \tag{4.23}$$

Expected γ_n values for the $(2+1)$-dimensional KPZ class are summarized in Tab. 4.3. Notice that Family-Vicsek scaling is recovered in Eq. (4.22) for $n = 1$ and $l = L$.

In order to experimentally evaluate the proposed Eq. (4.22), we follow the time dependence of $\langle [w_2(l,t)]^n \rangle_c$ for $n = 2$ and $n = 3$ computed in the experiment for $20a \leq l \leq 160a$. The chosen interval corresponds to the regime where $\xi(t) \ll l$ and, hence, where $\langle [w_2(l,t)]^n \rangle_c \sim t^{\gamma_n}$ if Eq. (4.22) holds. Figures 4.7(a-b) show the curves for $\langle [w_2(l,t)]^n \rangle_c$ with $n = 2$ and $n = 3$, respectively. Both curves are in qualitative agreement with the behaviour of $W(t)$ shown in Fig. 4.4(a). For 25 min $\lesssim t \lesssim t_c$, we find $\gamma_n \approx 0$ regardless the size l of the window. This implies $\beta \approx 0$ and $1/z \approx 0$ according to Eq. (4.23), and shows consistence with the PSS scaling. On the other hand, for $t \gg t_c$ we measure $\gamma_n(l, t \gg t_c)$ exponents that systematically increase with l [Fig 4.8(a)]. By plotting the best-fitted $\gamma_n(l, t \gg t_c)$ exponents as function of $1/l$ and taking the asymptotic limit $1/l \to 0$ [Fig 4.8(a)], a simple linear extrapolation provides $\gamma_2(t \gg t_c) \approx 1.96(29)$ and $\gamma_3(t \gg t_c) \approx 3.60(52)$. These values agree, within the experimental error bars, with those numerically expected for (2+1)-dimensional KPZ systems [Tab. 4.3].

The whole set $\{w_2(l,t)\}$ defines $p(w_2(l,t))$ and, thus, its associated scaling function $\Phi'(x', y')$ [Eq. (4.13)]. The intriguing numerical evidence [74] that $\Phi'(x', y' \ll 1)$ is approximately given by $f_{\text{LND}}(x)$ [Eq. (4.14)] regardless the conservations laws of the dynamics can be here experimentally tested. Figures 4.8(b-c) show $\Phi'(x', y')$ computed in the PSS ($t = 120$ min, $\xi(t) \approx 0.1$ μm) and KPZ ($t = 720$

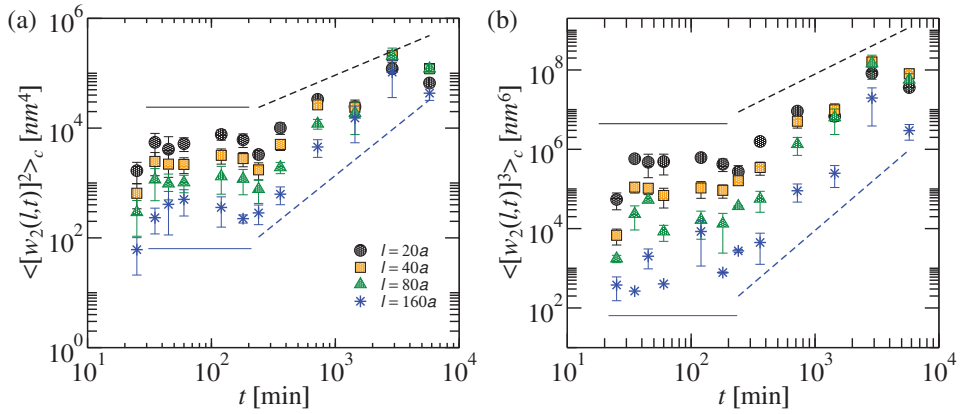

Figure 4.7: Time evolution of cumulants $\langle[w_2(l,t)]^n\rangle_c$ for (a) $n = 2$ and (b) $n = 3$ computed inside a window of lateral size l that span the whole CdTe surface. Solid and dashed lines are reference to eyes: they indicate the expected scaling for the PSS and KPZ regime, respectively. The difference of slope between dashed black and blue lines is due to finite-size l effects. Reprinted from Almeida *et al.* [1] under the Creative Commons license (Nature).

min, $\xi(t) \approx 0.2$ μm) regimes for $y' \approx 0.5, 0.125, 0.062$ and $y' \approx 1, 0.25, 0.125$, respectively (equivalently, for $l = 10a, 40a, 80a$). The data is compared with the $f_{\text{LND}}(x; \langle \ln(x) \rangle, \sigma_x)$ [Eq. (4.14)] built with the inputs directly measured from the CdTe surface. Therefore, comparisons contain no fit parameters. Remarkably, the experimental function $\Phi'(x', y' \ll 1)$ can be indeed well described by $f_{\text{LND}}(x)$ down to 10^{-2} as far as y' is small enough – that is, $y' \lesssim 0.25$. By decreasing y', the function becomes narrower, with a trend that supports $\lim_{y' \to 0} \Phi'(x', y') = \delta(x' - 1)$.

Deviation from $f_{\text{LND}}(x)$ also occurs if we increase y'. In the present case, $y' \gtrsim 0.5$ is enough to produce a clear difference between $\Phi'(x', y')$ and the $f_{\text{LND}}(x)$, as we show in the curves for $l = 10a$ in Fig.4.8(b-c).

Since now we understand the regimes $\Phi'(x', y')$ for which $f_{\text{LND}}(x)$ plays the role, we rescale $\Phi'(x', y' \ll 1)$ to zero mean and unit variance to provide compelling evidence that $f_{\text{LND}}(x)$ describes the experimental data regardless the type of surface scaling (PSS or KPZ, in this case). This upholds the conjecture made in [74]. Moreover, notice that $\Phi(x, y) = \Phi'(x', y')$ for $y' \ll 1$ given boundary

CdTe-γ_n ($t \gg t_c$)	KPZ-γ_n
$\gamma_1 = 0.57(12)$	$0.4830(30)$
$\gamma_2 = 1.96(29)$	$2.214(15)$
$\gamma_3 = 3.60(52)$	$3.946(27)$

Table 4.3: Asymptotic γ_n exponents [Eq. (4.23)] extracted from the experiment. Expected (2+1)-dimensional KPZ values were calculated using the estimates for α and β in [52, 55].

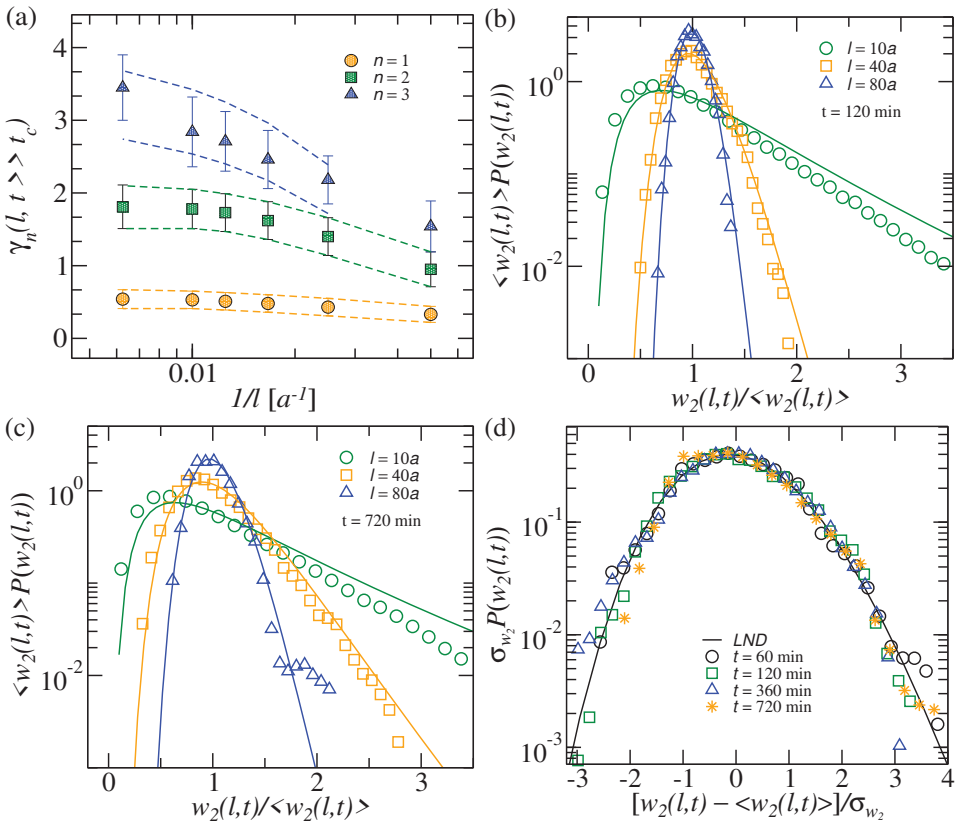

Figure 4.8: (a) Asymptotic exponents $\gamma_n(r, t \gg t_c)$ as functions of $1/l$ for $n = 1, 2, 3$. (b-c) Scaling function $\Phi'(x', y')$ [Eq. (4.13)] associated with the PDF $p(w_2(l,t))$ for CdTe surfaces (symbols) in the (b) PSS ($t = 120$ min) and (c) KPZ ($t = 720$ min) regimes. Solid lines stand for the respective $f_{\rm LND}(x; \langle \ln(x) \rangle_c, \sigma_x)$ [Eq. (4.14)] computed with inputs directly measured from the CdTe surfaces (that is, there is no fit parameter). CdTe surface statistics is well described by $f_{\rm LND}(x)$ for the $\xi(t) \ll l$ regime, which corresponds to curves for $l = 40a$ and $l = 80a$. In the limit $l \to \infty$, $\lim_{y' \to 0} \Phi'(x', y') = \delta(x' - 1)$, which is consistent with the trend of curves shown in (b-c). For $\xi(t) \gtrsim l$, $\Phi'(x', y \gtrsim 1')$ deviates from $f_{\rm LND}(x)$, as seen in data for $l = 10a$. (d) Scaling function $\Phi'(x', y' \ll 1)$, rescaled to mean null and unit variance, computed in the experiment (symbols) for different (PSS and KPZ) growth stages. Curves are compared to $f_{\rm LND}(x)$ (black solid line). Reprinted from Almeida *et al.* [1] under the Creative Commons license (Nature).

conditions are irrelevant in this limit. Thereby, our results are expected to be valid for $p(W_2(L,t))$ in the limit $L \to \infty$ followed by $t \to \infty$, so that $0 \ll y \ll 1$.

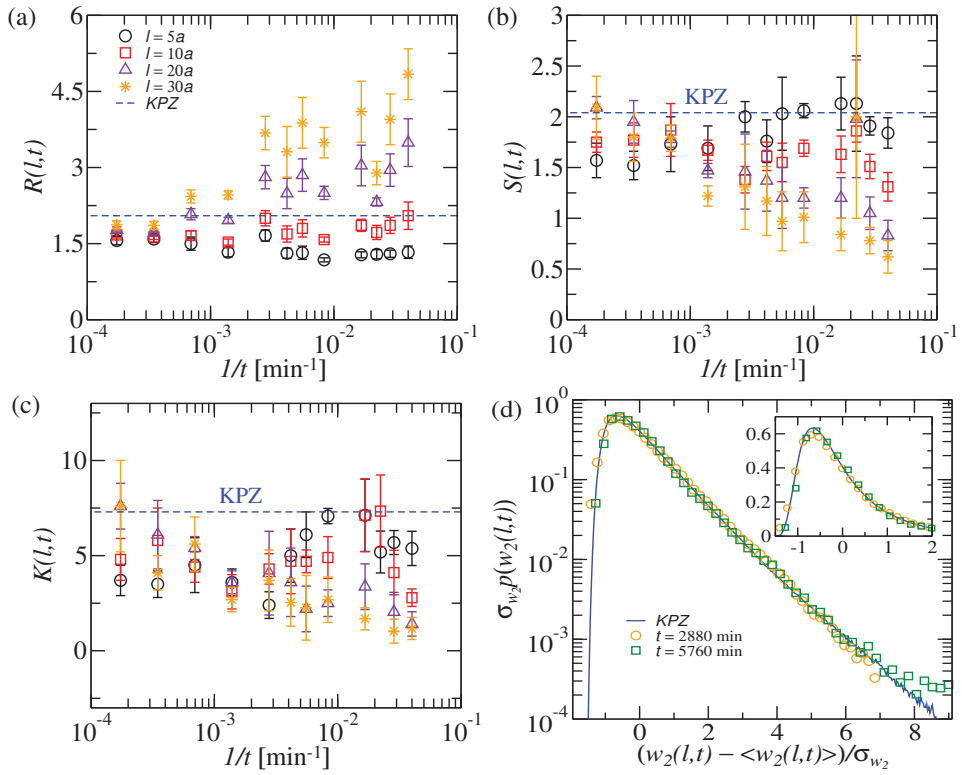

Figure 4.9: Dimensionless ratio between cumulant (a) $R(l,t)$, (b) $S(l,t)$ and (c) $K(l,t)$ related to $p(w_2(l,t))$ as function of $1/t$. Dashed blue lines refer to the universal values numerically found for (2+1)-dimensional KPZ stochastic models [Tab. 4.4]. (d) Universal $\Phi(x', y' \gg 1)$ scaling function for CdTe surfaces grown at $t = 2880$ min and $t = 5670$ min. Rescaled experimental distributions $p(w_2(l,t))$ are compared with the numerically estimated (2+1)-dimensional KPZ curve [74]. $\sigma_{w_2} = \langle w_2(l,t) \rangle_c^{1/2}$. Inset shows the same data contained in the main plot, but emphasizes the region around the peak in a linear $\times$ linear scale. Reprinted from Almeida *et al.* [1] under the Creative Commons license (Nature).

4.3.6 Universal stationary distributions

In order to continue the analysis and gain further evidence of KPZ scaling, in this section we focus on the stationary regime, $\xi(t) \gg l$ with $l \leq L$, for which $\Phi(x, y) \neq \Phi'(x', y')$ in general [65, 72], but where both scaling functions are universal. In fact, $\Phi'(x', y' \gg 1)$ was experimentally found for (2+1)-dimensional KPZ dynamics by Almeida *et al.* [63]. However, recent works [73,74] have stressed the role of (strong) finite-time and finite-size effects into access $\Phi'(x', y' \gg 1)$, which were not carefully taken into account in [63]. Therefore, we revisit the $\Phi'(x', y' \gg 1)$ issue to give a more reliable experimental test of its universality in CdTe surfaces.

We keep track of dimensionless cumulants $R(l,t)$, $S(l,t)$, $K(l,t)$ [Eq. (4.17)] related to the PDF $p(w_2(l,t))$ as function of $1/t$ [74]; we evaluated the quantities

for window sizes $5a \leq l \leq 30a$ [Fig. 4.9(a-c)]. The constrain to an upper limit $l = 30a$ was guided so that, for the thickest available film ($t = 5760$ min, $\xi \approx 1.0$ μm), one guarantees that $y' \gtrsim 1.7$. Now one knows [73] this is a safe limit to measure the universal $\Phi'(x', y' \gg 1)$ function. In fact, Fig. 4.9(a-c) reveals that the set $(R(l,t), S(l,t), K(l,t))$ shows negligible l-dependence for $20a \lesssim l \lesssim 30a$ at $1/t \sim 10^{-4}$ min^{-1}. We do not dare to extrapolate experimental data for $1/t \to 0$, as suggested by recent recipes [74], but constrain the analysis to the largest available time $t = 5760$ min. Analogously, instead of data extrapolation to $l \to \infty$ [74], we choose working with the "largest" l (here $l = 30a \approx 0.58$ μm) that is comparatively larger than $l_g(t) \approx 0.1$ μm, but still smaller than $\xi(t) \approx 1.0$ μm. The $(R(l,t), S(l,t), K(l,t))$ values measured in this limit are summarized in Tab. 4.4. They are in reasonable agreement with the numerically estimated KPZ values. However, we remark how "scattered" the curves for $R(l,t), S(l,t)$, and $K(l,t)$ are even at long times. Such a remark is a rephrasing of the numerically-based advertence [73, 74] about strong finite-size and time effects $\Phi'(x', y' \gg 1)$. Anyway, now we are in position the rescale the experimental $\Phi'(x', y' \gg 1)$ function at zero mean and unit variance, as suggested in [71], to compare it with the respective curve for (2+1)-dimensional KPZ model systems [74]. Figure 4.9(d) reveals the excellent data collapse down to $\sim 10^{-4}$ between experiment and simulations. The stretched exponential decay, hallmark of this KPZ scaling function [70], is thereby also observed.

Analogous analysis can be made for the PDF $p(m(l,t))$ [Eq. (4.16)] for the local maximal relative height and its universal scaling function $\Upsilon'(u', y')$. Following the path we run for calculating $p(w_2(l,t))$, we observe $R(l,t)$, $S(l,t)$ and $K(l,t)$ associated with the variable $m(l,t)$ [Fig. 4.10(a-c)]. Indeed, $S(l,t)$ and $K(l,t)$ converge to the numerically-estimated (2+1)-dimensional KPZ values when curves for $l = 30a$ and $t = 5760$ min are considered. Exception is for $R(l,t)$ that displays stronger finite-size effects than $S(l,t)$ and $K(l,t)$, as also occurs in KPZ models [74]. These scaling effects are eliminated by a non-linear extrapolation of $R(l,t)$ for $t = 2880$ min and $t = 5760$ min to $l \to \infty$ as $R(l) \times l^{-\Delta}$ with $\Delta = 0.17$, as shown in the inset of Fig. 4.10(a). The result pays off; it is in sharp agreement with the most accurated R estimated in KPZ systems [Tab. 4.4]. Finally, the universality of $\Upsilon'(u', y' \gg 1)$ is observed by the collapse of experimentally- and numerically-obtained curves down to 10^{-3} [Fig. 4.10(d)].

Analysis in the stationary state provides additional evidence that KPZ statistics rule the intergrain CdTe surface fluctuations even for films grown at such a low ($T = 150\,^{\circ}$C) substrate temperature.

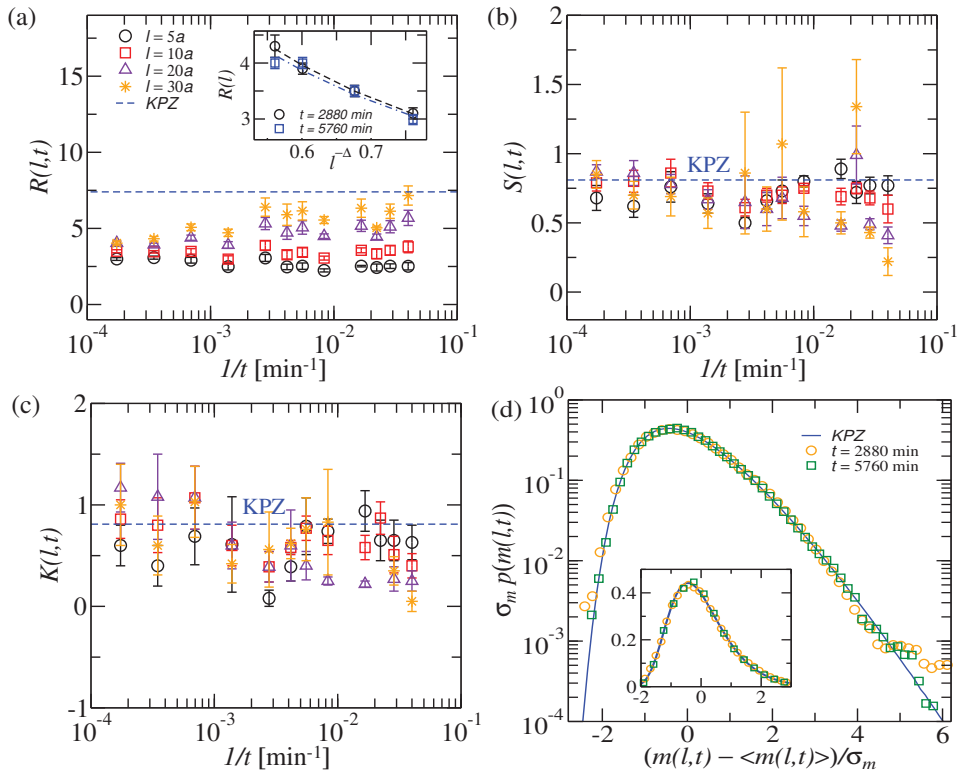

Figure 4.10: Dimensionless ratio between cumulant (a) $R(l,t)$, (b) $S(l,t)$ and (c) $K(l,t)$ related to the PDF $p(m(r,t))$ [Eq. (4.16)] as function of $1/t$. Dashed blue lines refer to the universal values numerically found for (2+1)-dimensional KPZ stochastic models [Tab. 4.4]. Inset of (a) shows the nonlinear extrapolation of $R(l) \times l^{-\Delta}$ with $\Delta = 0.17$ for $l \to \infty$ considering data for the largest times $t = 2800$ min and $t = 5760$ min. (d) Universal $\Upsilon'(x', y' \gg 1)$ scaling function for CdTe surfaces grown at $t = 2880$ min and $t = 5670$ min. Rescaled experimental PDF $p(m(r,t))$ are compared with the numerically estimated (2+1)-dimensional KPZ curve. Inset shows the same data contained in the main plot, but emphasizes the region around the peak by a linear $\times$ linear scale. Reprinted from Almeida *et al.* [1] under the Creative Commons license (Nature).

CdTe-$p[w_2]$	KPZ-$p[w_2]$	CdTe-$p[m]$	KPZ-$p[m]$
$R = 1.87(8)$	2.05(5)	$R = 7.3(5)$	7.3(4)
$S = 2.1(3)$	2.04(4)	$S = 0.83(9)$	0.84(2)
$K = 7.6(2.4)$	7.3(3)	$K = 1.19(34)$	1.14(5)

Table 4.4: Dimensionless cumulant ratios $R(l,t)$, $S(l,t)$ and $K(l,t)$ for stationary ($\xi(t) \gg l$) local squared roughness $p(w_2(l,t))$ and local maximal relative (to the mean) height $p(m(l,t))$ PDFs. Experimental values were computed for the largest available time ($t = 5760$ min), inside a square window of size $l \approx 0.58$ μm so that $\xi/l \approx 1.7$. (R, S, K) values for (2+1)-dimensional KPZ model systems were estimated in [74].

4.3.7 KPZ parameters & universal functional form

Based on the pieces of KPZ evidence in CdTe surfaces, we estimate system-dependent parameters following the KPZ scaling theory we described in Sec. 4.1.3. Looking

back at the *ansatz* in Eq. (4.9), the amplitude of $W_2(t)$ reads:

$$(\Gamma t)^{2\beta} \simeq W_2(t)/\langle\chi^2\rangle_c. \tag{4.24}$$

Using the numerically-estimated value $\langle\chi^2\rangle_c \approx 0.24$ [56], and our experimental measurements $W_2(t) \approx 1444$ nm^2 and $W_2(t) \approx 1089$ nm^2 for $t = 2880$ min and $t = 5760$ min [Fig. 4.4(a)], respectively, we obtain $\Gamma \approx 24 \times 10^3$ nm$^{1/\beta}$min^{-1} and $\Gamma \approx 7 \times 10^3$ nm$^{1/\beta}$min^{-1}. Differences are due to statistical fluctuations in $W_2(t)$.

We also pay attention to the non-universal amplitude A_h related to the stationary regime via the correlator:

$$C_h(r,t) = A_h r^{2\alpha} \quad (l_g(t) \ll r \ll \xi(t)). \tag{4.25}$$

Figure 4.11(a) shows $C_h(r,t)/r^{2\alpha} \times r$ curves for $t = 2880$ min and $t = 5760$ min. The clear plateau for $t = 2880$ min provides $A_h \approx 4400$ nm$^2\mu$m$^{-2\alpha}$. On the other hand, finding a plateau is a hard task for $t = 5760$ min. This difficulty is indeed expected since $C_h(r,$5760 min$) \times r$ scaling gives an exponent α slightly smaller than the KPZ one [Fig. 4.4(b)]. Nevertheless, a rough estimate $A_h \approx 3600$ nm$^2\mu$m$^{-2\alpha}$ for $t = 5760$ min might still be reached if one considers the maximum of the curve.

We remind the definition $\Gamma \equiv |\lambda|A^{1/\alpha}$ [Eq. (4.10)] that contains the non-universal constant A. This constant is related to A_h by the ratio $A_h/A \approx 0.646$, which is valid only in $d = 2 + 1$ [62]. Inserting the experimental estimates for Γ and A (or equivalently, A_h) into the relation $|\lambda| = \Gamma/A^{1/\alpha}$ with $\alpha \approx 0.39$ gives $|\lambda| \approx 6$ nm/s and $|\lambda| \approx 3$ nm/s for $t = 2880$ min and $t = 5760$ min, respectively. In our case, $|\lambda| = \lambda$ can be inferred from the positive skewness of HDs [Fig. 4.5(a-b)]. The averaged value $\lambda \approx 4.5 \times 10^{-2}$ has the same order of the experimental deposition flux $F \approx 23 \times 10^{-2}$ nm/s, but with $F/\lambda \approx 5$. Such a $5\times$ factor may be consistent with the long transient ($t_c \approx 300$ min) that precedes KPZ scaling.

The estimated KPZ-CdTe parameters, summarized in Tab. 4.5, can now be used to access the scaling of the correlator $C_s(\boldsymbol{r},t)$:

$$C_s(\boldsymbol{r},t) := \langle h(\boldsymbol{r'}+\boldsymbol{r},t)h(\boldsymbol{r'},t)\rangle - \langle h(\boldsymbol{r},t)\rangle^2, \tag{4.26}$$

which is expressed as (isotropy assumed):

$$C_s(r,t) \simeq (\Gamma t)^{2\beta}\Omega\left(\frac{1}{2}\frac{A_h r^{2\alpha}}{(\Gamma t)^{2\beta}}\right), \tag{4.27}$$

where $\Omega(q)$ is an universal scaling function [62]. In Fig. 4.11(b) and in its insertions, we compare $\Omega(q)$ found in KPZ model systems [126] with the experimentally obtained $\Omega(q)$ functions after using Eq. (4.27) with the non-universal parameters in Tab. 4.5. Comparison unveils the excellent collapse between the experiment and the outcome of KPZ models [126]. The agreement runs from $q \sim 10^{-2}$ to $q \approx 0.6$, which corresponds to $\Omega(q) \approx 0.24$ to $\Omega(q) \sim 10^{-3}$. Thereby, the universality of $\Omega(q)$ for (2+1)-dimensional KPZ systems is experimentally supported. Notice that

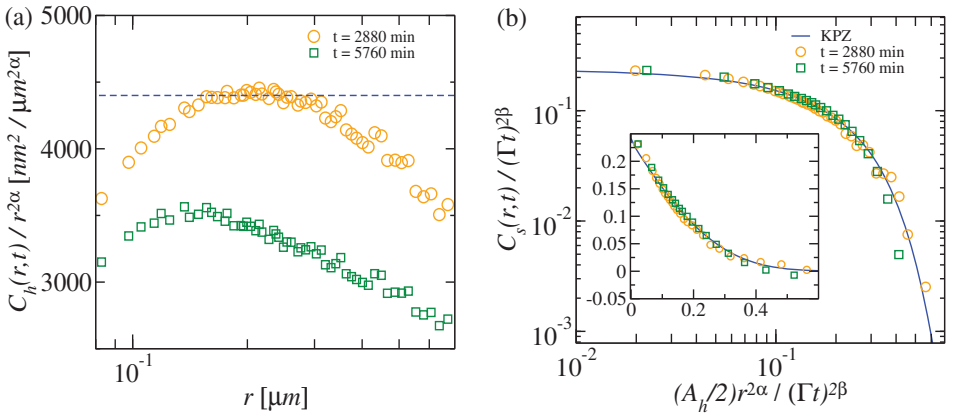

Figure 4.11: (a) Rescaled height-height correlation function $C_h(r,t)$ versus r for CdTe surfaces. We use $\alpha = 0.39$. The plateau observed in the plot represents the estimate of the non-universal parameter A_h (dashed blue line) for $t = 2880$ min. (b) Universal functional form $\Omega(\frac{1}{2}\frac{A_h r^{2\alpha}}{(\Gamma t)^{2\beta}})$ associated with two-point spatial covariance $C_s(r,t)$ of the KPZ class in $d = 2+1$ (blue solid line). This numerically-obtained curve [126] is compared with the spatial covariances calculated for CdTe surfaces at $t = 2880$ and $t = 5760$ min after rescaled using the KPZ-CdTe parameters A_h and Γ shown in Tab. 4.5. No fit is performed. Inset shows the same data of the main plot but in linear $\times$ linear scale. Reprinted from Almeida *et al.* [1] under the Creative Commons license (Nature).

we *do not* perform a fit in the q axis to adjust experimental data to the expected curve [62].

CdTe-KPZ	Γ [$\text{nm}^{1/\beta}\text{min}^{-1}$]	A [$\text{nm}^2\mu\text{m}^{-2\alpha}$]	λ [nm/s]
$t = 2880$ min	24×10^3	6811	6×10^{-2}
$t = 5760$ min	7×10^3	5572	3×10^{-2}

Table 4.5: Key non-universal KPZ parameters extracted from CdTe surfaces by following the KPZ scaling theory [29, 30].

4.4 Summary and concluding remarks

We analysed spatio-temporal height fluctuations at the surface of CdTe films vacuum-deposited on rough (≈ 6 nm) Kapton substrates by hot wall technique. The study is constrained to substrates heated at $T = 150\,^{\circ}\text{C}$ and to films deposited with a growth rate $F \approx 14$ nm/min. By imaging surfaces of the films with atomic force microscopy, we kept track of morphological and statistical properties of 14 independently grown CdTe films with deposition times between $t = 7.5$ min and $t = 5760$ min. Some aspects of the polycrystalline CdTe layer, such as its texturization, were addressed via X-ray diffractions.

Evolution of height fluctuations is coupled with surface morphological changes,

with both characterized by three distinct regimes [Fig. 4.2, and Fig. 4.4(a)]. For films grown between 7.5 min $\lesssim t \lesssim$ 25 min, fluctuations are smoothing-dominated as the surface width reveals; $W(t)$ decreases 50% of its initial 28(3) nm value within this period [Fig. 4.4(a)]. We *suggest* that smoothing stems from coalescences and mass-redistribution mechanisms between three-dimensional CdTe islands that, once nucleated onto the substrate, eventually come into contact during the substrate-coverage stage. In fact, while the surface at $t = 7.5$ min is composed in part by high-aspect ratio CdTe islands and, in part, by exposed areas of the Kapton [Fig. 4.2(a)], the surface is already fully covered by CdTe grains at $t = 25$ min [Fig. 4.2(b)]. Notice that the source of smoothing here observed does not seem to be directly related to the substrate roughness since $W(t)$ jumps from 6 nm at $t = 0$ min to $W \approx 28$ nm at $t = 7.5$ min and, only afterwards, it starts decreasing. This is fundamentally different from the substrate-induced smoothing studied in solid-on-solid growth models [127] and in theoretical approximations of linear growth equations [128]. A detailed *in-situ* characterization of CdTe nucleation and of island-island coalescences is required to precisely state which mechanisms play major roles in this regime.

For surfaces grown in the interval 25 min $\lesssim t \lesssim t_c$, with $t_c \approx 300$ min, height fluctuations display an unusual behaviour for which neither $W(t)$ nor the parallel correlation length $\xi(t)$ significantly change in time [Fig. 4.4]. According to the dynamical scaling hypothesis, this behaviour implies $\beta = 0$ and $1/z = 0$, respectively. We define this set of exponents and name its associated regime as Pseudo-steady state. The name PSS is an analogy with the stationary state of growing interfaces. For the PSS scaling here detected, height distributions are shown to be Gaussian [Fig. 4.5]. We remind that PSS scaling is more than a regime where surface smoothing is equilibrated by roughening, as in the case of (2+1)-dimensional EW dynamics. In the PSS, it is fundamental that the spreading of correlations parallel to the substrate does not diverge or does not even grow.

In the CdTe-on-Kapton experiment, we show that the time for which PSS scaling is measured coincides with the transient during which non-(111)-oriented CdTe grains at the surface are replaced by (111)-oriented grains [Fig. 4.3(b)]. This structural change explains why PSS is observed for CdTe films grown on the amorphous Kapton, which allows the formation of crystals in several directions [Fig. 4.3(a)], but does not appear for films grown on Si(001) [19], where most crystals are induced to be (111)-oriented since initial times. Although the microscopic mechanisms related to smoothing part of the PSS are not experimentally accessed, we *suggest* that it may be driven by relaxations at grain boundaries between the favoured (111)-oriented grains and non-(111)-oriented grains. An one-dimensional toy model supports that relaxations at GBs are enough to generate a PSS scaling.

We show that surface of films grown beyond $t_c \approx 300$ min displays (2+1)-dimensional KPZ scaling and, hence, may be in the KPZ class. The agreement with KPZ statistics is supported by a series of measurements that include i) scaling exponents (α, β, z) [Tab. 4.2], distributions of ii) height [Fig. 4.5], iii) local

square-width [Fig. 4.9] and distributions of iv) local maximal relative heights [Fig. 4.10], including their universal scaling functions $p((\chi - \langle\chi\rangle)/\sigma_\chi)$, $\Phi'(x', y')$ [Eq. (4.13)] and $\Upsilon'(x', y' \gg 1)$ [Eq. (4.16)], respectively. In addition, we also give support for v) the universality of the scaling function $\Omega(q)$ [Eq. (4.27)] related to the two-point spatial covariance of heights. In order to accomplish step v), we rely on the KPZ scaling theory [29, 30] to extract system-dependent growth parameters [Tab. 4.5], such as the "excess of velocity" of CdTe crystalline fronts $\lambda \sim 10^{-2}$ nm/s. Notice $\Omega(q)$ was experimentally found without fitting the u axis. Interesting, we provide evidence for the generalized Family-Vicsek scaling [Eq. (4.22) and Fig. 4.8], which can be employed to measure the *global* α and z (or β) exponents even in systems with anomalous scaling [74]. Associated with the evolution of $\langle(w_2(l,t)^n)\rangle_c$ for the regime where $\xi(t) \ll l \ll L$, we show that the experimental scaling function $\Phi'(x', y' \ll 1)$ is well described by $f_{\text{LND}}(x)$ [Eq. (4.14)], regardless whether the CdTe dynamics displays PSS or KPZ scaling. These findings support the long-standing model-based observation of Antal and Rácz [69], and the conjecture of Carrasco and Oliveira [74]. The trend of CdTe experimental data suggests $\lim_{y'\to 0} \Phi'(x', y') = \delta(x' - 1)$ [Fig. 4.8].

We remark that KPZ scaling has been found only after $\sim 10^3$ CdTe ML were deposited on the substrate: we had to grew films for up 4 days to observe one decade of KPZ scaling [Fig. 4.4(b)]. Long scaling transients preceding KPZ fluctuations are one of the reasons why KPZ is experimentally rare [60, 129]. Our results for CdTe-on-Kapton indicate that KPZ could appear after the RD scaling measured in CdTe-on-Si(001) films also grown at $T = 150\,^\circ\text{C}$ [19]. Furthermore, our results suggest that previous works on CdTe films grown on glass by HWE [95, 96] reported results only for transient dynamics. However, notice that, if CdTe is deposited under growth conditions that promotes shadowing, such as sputtering, asymptotic anomalous scaling may indeed takes place [97].

Grainy surfaces involve an additional grain length scale $l_g(t)$ that severely constrains the scaling regime $l_g(t) \ll r \ll \xi(t)$, in which the universal exponent α can be observed [121]. This situation, for instance prevented Almeida *et al.* [63] to measure α in CdTe-on-Si films. Anyhow, it seems important to rely on the analysis of other quantities beyond exponents, such as distributions of height and local quantities, in order to complement the study of fluctuations and gain further evidence of universality.

It is intriguing that KPZ fluctuations arise at the surface of polycrystalline systems. While fluctuations within a single crystal are believed to belong to a class of diffusion-dominated dynamics, the presence of defects in polycrystals conspires to complexify the scenario, which shows grains that coarsen and grow at different rates. The Author believe that conceiving a polycrystalline grain-growth model that displays diffusion-dominated and KPZ fluctuations at intra- and inter-grain scales, respectively, is an open and relevant task which should shed light to the possible conditions (and transients) related to KPZ in the vast realm of polycrystalline films.

Finally, we remark that height fluctuations in different systems may also dis-

play the PSS scaling. For instance, PSS is observed in parylene-C (poly(chloro-p-xylylene)) films ($W(0) \approx 6$ nm, $\xi(0) \approx 140$ nm) etched by RF plasma in rich O_2 atmosphere [130]. In the experiment, UV radiation and O_2 species break polymeric chains at the surface and terminate the end-chains with carbonyl group. Such a breaking decreases the molecular weight of chains and allow them to be easily desorbed in the vacuum or to diffuse and aggregate to form nano-islands. The underlying structure of unbroken polymers, however, although constantly loosing material, manages to stabilize its interface width so that $W(0)$ is kept constant until the film thickness is decreased by $\tau^* \approx \xi(0)$. During this transient, correlations also do not grow, and scaling hypothesis implies $\beta = 0$ and $1/z = 0$. This consitutes one example of where PSS scaling is likely induced by an initial rough substrate. Further examples in the same vein are the growth of SiO_2 films on polyethylene-2,6-napthalate (PEN) substrates by chemical vapor deposition with dielectric barrier discharge under ambient conditions [131], and the growth of Al_2O_3 films by atomic layer deposition also on PEN. For both cases $\beta = 0$ and $1/z \sim 0.1$ are reported [131]. Other examples where PSS emerges, but not induced by the substrate, rely on some discrete models. PSS is observed in a (2+1)-dimensional etching model that includes etching normally-oriented to the local surface (KPZ-like term), but also includes an inhomogeneous etching rate along the surface [132] that breaks rotational symmetry around h axis. In the model, crests at the surface react faster than valleys because the former structures partially overshadow the valleys. Thus, even if the substrate is initially flat, after a quick transient, shadowing mechanism self-adjusts fluctuations during etching so that $W(t)$ becomes constant and $\xi(t)$ does not grow [132]. Interesting examples of PSS in discrete models with local interactions are also observed in competitive models involving RD growth, for which $1/z = 0$, and the RSOS [123] model[10]. In conclusion, PSS scaling may be a general type of scaling that encompasses interface growth with local and nonlocal dynamics.

[10]Results of T. J. Oliveira show that PSS-to-KPZ scaling arises in the RD-RSOS model (private communication).

4.5 Acronyms and Symbols

Acronym	Description
AFM	Atomic force microscopy
CVD	Chemical vapour deposition
EW	Edwards-Wilkison
FBC	Free boundary condition
GB	Grain boundary
HD	Height distribution
HWE	Hot wall epitaxy
KPZ	Kardar-Parisi-Zhang
ML	Monolayer
PBC	Periodic boundary condition
PDF	Probability density function
PEN	Polyethylene-2,6-napthalate
PSS	Pseudo-steady state
RD	Random deposition
RF	Radio-frequency
RSOS	Restricted solid on solid
SPM	Scanning probe microscopy
STM	Scanning tunelling microscopy
TW	Tracy-Widom
UV	Ultraviolet
VW	Volmer-Weber
XRD	X-Ray Diffraction

Symbols

Latin Symbols	Description
a	Pixel size of AFM image
a_{latt}	CdTe lattice constant
a_{micro}	Microscopic length scale
a_{mod}	Lattice constant of the toy model
A	KPZ model-dependent parameter
A_h	Prefactor of the height-difference correlation function
C_h	Height-difference correlation function
C_s	Spatial covariance

d_s	Dimension of the substrate
$\sqrt{D}$	Amplitude of the white noise
E_{gap}	Energy gap
E_{GB}	Energy barrier at GBs sites
E_{R}	Relaxation energy barrier at the GBs of colided neighboring grains
f_{LND}	Lognormal distribution function
F	Growth rate of a film measured *ex-situ*
g	KPZ coupling constant
h	Height field of an interface measured from a flat substrate
h_0	Arbitrary referential height
h_{AFM}	Height field of probed by AFM
h_i	Surface height at site i of a discrete growth model
I_{hkl}	Intensity of peak hkl in a XRD spectrum
K	Coefficient of Kurtosis
K_{B}	Boltzman constant
l	Lateral size of a window that glides through the interface
l_g	Typical grain size
L	Lateral size of a finite-size interface
L_{AFM}	Lateral size of AFM image
L_{mod}	Size of the interface in a toy model for interface growth
$m(l)$	Local maximal height relative to the mean at scale l
P	Pressure
P_D	Probability of diffusion through a defect site
P_R	Probability of relaxation at a GB site
q	Defined as $A_h r^{2\alpha} = (\Gamma t)^{2\beta}$
$\boldsymbol{r}$	Spatial vector
$\boldsymbol{r}_0$	Arbitrary referential in space
R	Inverse of the coefficient of variance
S	Coefficient of Skewness

t	Growth time
t_0	Arbitrary time of reference
t_c	Crossover time
t_c^{mod}	Crossover time in a model for surface growth
T	Temperature of the substrate
u	Variable. Definition $\frac{m(l,t)-\langle m(l,t)\rangle}{\sigma_m}$
u'	Variable. Definition $\frac{m(L,t)-\langle m(L,t)\rangle}{\sigma_m}$
v	Average growth speed of an interface
v_0	Rate of deposition of atomic species at interface
v_∞	Asymptotic growth speed of an interface
$\boldsymbol{v}_B$	Velocity of a fluid in the Burgues equation
$\boldsymbol{v}_c$	Constant velocity shift
$w(l)$	Local roughness at scale l
$w_2(l)$	Squared local roughness at scale l
$W(L)$	Global roughness
$W_2(L)$	Squared global roughness
x	Variable. Definition $w_2(L)/\langle W_2(L)\rangle$
x'	Variable. Definition $w_2(l)/\langle w_2(l)\rangle$
y	Variable. Definition $\xi(t)/L$
y'	Variable. Definition $\xi(t)/l$
z	Dynamical scaling exponent

Greek Symbols	**Description**
α	Roughness scaling exponent
β	Growth scaling exponent
Γ	Nonuniversal parameter in the KPZ scaling theory
η	Noise
θ_{hkl}	Scattering angle of for the (hkl)-oriented crystal in a XRD measurement
λ	Factor of excess of growth speed of an interface
μ	Coefficient of linear attenuation
ν	Phenomenological coefficient of surface tension
ξ	Correlation length
ς	Scale factor
τ	Thickness of a thin film
Υ	Scaling function related to the PDF of the global relative maximal height

Υ'	Scaling function related to the PDF of the local relative maximal height
Φ	Scaling function related to the PDF of the global roughness
Φ'	Scaling function related to the PDF of the local roughness
χ	Random variable
Ω	Universal scaling function of the height covariance

Others	**Description**
$A_{\theta-2\theta}$	Absorption factor in a $\theta - 2\theta$ XRD geometry
z_{eff}^{-1}	Effective inverse dynamical exponent.
β_{eff}	Effective growth exponent.
γ_n	Universal exponent of $n - th$ order
$\delta h, \delta \boldsymbol{r}, \delta t$	Height, spatial and time shifts
$\lambda_{CuK\alpha}$	Wavelength emitted in a K_α transition from a Cu atom
σ_i	Standard deviation of a variable i
$\langle X^n \rangle_c$	n-th cumulant of the variable X

BIBLIOGRAPHY

[1] Almeida, R. A. L., Ferreira, S. O., Ferraz, I., Oliveira, T. J.: Initial pseudo-steady state & asymptotic KPZ universality in semiconductor on polymer deposition. Sci. Rep. (Nature) **7**, 3773 (2017).
Cited on pages 99, 114, 117, 119, 121, 122, 123, 125, and 127.

[2] Barabási, A.-L., Stanley, H. E.: Fractal Concepts In Surface Growth. Cambridge university press (1995).
Cited on pages 99, 101, and 103.

[3] Halpin-Healy, T., Zhang, Y.-C.: Kinetic roughening phenomena, stochastic growth, directed polymers and all that. Phys. Rep. **254**, 215-414 (1995).
Cited on pages 99 and 103.

[4] Krug, J.: Origins of scale invariance in growth processes. Adv. Phys. **46**, 139-282 (1997).
Cited on pages 45, 99, and 102.

[5] Krim, J., Palasantzas, G.: Experimental observations of self-affine scaling and kinetic roughening at sub-micron lengthscales. Int. J. Mod. Phys. B **9**, 599-632 (1995).
Cited on page 99.

[6] Cuerno, R., Vázquez, L.: Universality issues in surface kinetic roughening of thin solid films. In Advances in Condensed Matter and Statistical Physics (eds Korutcheva, E. & Cuerno, R.) 237–259, Nova Science (2004).
Cited on page 99.

[7] Cuerno, R., Castro, M., Muñoz-García, J., Gago, R., Vázquez, L.; Universal non-equilibrium phenomena at submicrometric surfaces and interfaces. Eur. Phys. J. Special Topics **146**, 427-441 (2007).
Cited on page 99.

[8] Family, F., Vicsek, T.: Scaling of the active zone in the Eden process on percolation networks and the ballistic deposition model. J. Phys. A.: Math. Gen. **18**, L75-L81 (1985).
Cited on page 99.

[9] Ramasco, J. J., López, J. M., Rodríguez, M. A.: Generic Dynamic Scaling in Kinetic Roughening. Phys. Rev. Lett. **84**, 2199 (2000).
Cited on page 108.

[10] Halperin, B. I., Hohenberg, P. C., S.-K. Ma.: Calculation of dynamic critical properties using Wilson's expansion methods. Phys. Rev. Lett. **29**, 1548 (1972).
Cited on page 100.

[11] Michely, T., Krug, J.: Islands, Mounds and Atoms. Patterns and Processes in Crystal Growth Far from Equilibrium. Springer-Verlag, Berlin, Heidelberg (2004).
Cited on page 101.

[12] Kardar, M.: Statistical physics of fields. Cambridge University Press (2007).
Cited on page 101.

[13] Kardar, M., Parisi, G., Zhang, Y.-C.: Dynamic scaling of growing interfaces. Phys. Rev. Lett. **56**, 889-892 (1986).
Cited on pages 101, 103, 104, and 117.

[14] Edwards, S. F., Wilkinson, D. R.: The surface statistics of a granular aggregate. Proc. R. Soc. Lond. A **381**, 17-31 (1982).
Cited on page 102.

[15] Family, F.: Scaling of rough surfaces: effects of surface diffusion. J. Phys. A: Math. Gen. **19**, L441-L446 (1986).
Cited on page 102.

[16] Salditt, T., Metzger, T. H., Peisl, J.: Kinetic roughness of amorphous multilayers studied by Diffuse X-ray Scattering, Phys. Rev. Lett. **73**, 2228-2231 (1994).
Cited on page 102.

[17] Salvarezza, R. C., Vázquez, L., Míguez, H., Mayoral, R., López, C., Meseguer, F.: Edward-Wilkinson behavior of crystal surfaces grown by sedimention of SiO_2 nanospheres. Phys. Rev. Lett. **77**, 4572-4575 (1996).
Cited on page 102.

[18] Yunker, P. J., Lohr, M. A., Still, T., Borodin, A., Durian, D. J., Yodh, A. G.: Effects of particle shape on growth dynamics at edges of evaporatin drops of colloidal suspensions. Phys. Rev. Lett. **110**, 035501 (2013).
Cited on page 102.

[19] Almeida, R. A. L., Ferreira, S. O., Ribeiro, I. R. B., Oliveira, T. J.: Temperature effect on (2+1)-experimental Kardar-Parisi-Zhang growth. Europhys. Lett. **109**, 46003 (2015).
Cited on pages 102, 108, 111, 112, 116, 118, 119, 128, and 129.

[20] Corwin, I.: The Kardar-Parisi-Zhang equation and universality class. Random Matrices Theory Appl.**1**, 1130001 (2012).
Cited on page 103.

[21] Halpin-Healy, T., Takeuchi, K. A.: A KPZ cocktail - shaken, not stirred...: Toasting 30 years of kinetically roughened surfaces. J. Stat. Phys. **160**, 794-814 (2015).
Cited on pages 103 and 106.

[22] Sasamoto, T.: The 1D Kardar-Parisi-Zhang equation: Height distribution and universality. Prog. Theor. Exp. Phys. **2016**, 022A01 (2016).
Cited on page 103.

[23] Takeuchi, K. A.: An appetizer to modern developments on the Kardar-Parisi-Zhang universality class. Physica A **504**, 77-105 (2018).
Cited on page 103.

[24] Kardar, M: Roughening by impurities at finite temperatures. Phys. Rev. Lett. **55**, 2923 (1985).
Cited on page 103.

[25] Forster, D., Nelson, D. R., Stephen, M. J.: Large-distance and long-time properties of a randomly stirred fluid. Phys. Rev. A **16**, 732 (1977).
Cited on page 103.

[26] Hwa, T.: Nonequilibrium dynamics of driven line liquids. Phys. Rev. Lett. **69**, 1552 (1992).
Cited on page 103.

[27] Berera, A., Fang, L.-Z.: Stochastic Fluctuations and Structure Formation in the Universe. Phys. Rev. Lett. **72**, 458 (1994).
Cited on page 103.

[28] Burguers, J. M.: The Nonlinear Diffusion Equation. Riedel, Boston (1974).
Cited on page 103.

[29] Krug, J., Meakin, P.: Universal finite-size effects in the rate of growth processes. J. Phys. A.: Math. Gen. **23**, L987-994 (1990).
Cited on pages 103, 127, and 129.

[30] Krug, J., Meakin, P., T. Halpin-Healy: Amplitude universality for driven interfaces and directed polymers in random media. Phys. Rev. A **45**, 638-653 (1992).
Cited on pages 103, 104, 127, and 129.

[31] Johansson, K.: Shape fluctuations and random matrices. Commun. Math. Phys. **209**, 437-476 (2000).
Cited on page 104.

[32] Phrähofer, M., Spohn, H.: Universal distributions for growth processes in 1 + 1 dimensions and random matrices. Phys. Rev. Lett. **84**, 4882-4885 (2000).
Cited on page 104.

[33] Ferrari, P. L., Spohn, H.: Scaling limit for the space-time covariance of the stationary tottaly asymmetric simple exclusion process. Commun. Math. Phys. **256**, 1-44 (2006).
Cited on page 104.

[34] Borodin, A., Ferrari, P. L., Prähofer, M., Sasamoto, T.: Fluctuation properties of the TASEP with periodic initial configuration. J. Stat. Phys. **129**, 1055-1080 (2007).
Cited on page 104.

[35] Tracy, C. A., Widow, H.: Asymptotics in ASEP with step initial condition. Commun. Math. Phys. **290**, 129-154 (2009).
Cited on page 104.

[36] Sasamoto, T., Spohn, H.: One-dimensional Kardar-Parisi-Zhang equation: An exact solution and its universality. Phys. Rev. Lett. **104**, 230602 (2010).
Cited on page 104.

[37] Amir, G., Corwin, I., Quastel, J.: Probability distribution of the free energy of the continuum directed random polymer in 1 + 1 dimensions. Comm. Pure Appl. Math. **64**, 466-537 (2011).
Cited on page 104.

[38] Calabrese, P., Le Doussal, P., Rosso, A.: Free-energy distribution of the directed polymer at high temperature. Europhys. Lett. **90**, 20002 (2010).
Cited on page 104.

[39] Dotensko, V.: Bethe ansatz derivation of the Tracy-Widom distribution for one-dimensional directed polymers. Europhys. Lett. **90**, 20003 (2010).
Cited on page 104.

[40] Calabrese, P., Le Doussal P.: Exact solution for the Kardar-Parisi-Zhang equation with flat initial conditions. Phys. Rev. Lett. **106**, 250603 (2011).
Cited on page 104.

[41] Imamura, T., Sasamoto, T.: Exact solution for the stationary Kardar-Parisi-Zhang equation. Phys. Rev. Lett. **108**, 190603 (2012).
Cited on page 104.

[42] Borodin, A., Corwin, I., Ferrari, P., Veto, B.: Height fluctuations for the stationary KPZ equation. Math. Phys. Anal. Geom. **18**, 20 (2015).
Cited on page 104.

[43] Tracy, C. A., Widom, H.: Level-spacing distribution and the Airy kernel. Commun. Math. Phys. **159**, 151-174 (1994).
Cited on page 104.

[44] Tracy, C. A., Widom, H.: On orthogonally and symplectic matrix ensembles. Commun. Math. Phys. **177**, 727-754 (1996).
Cited on page 104.

[45] Chhita, S., Ferrari, P. L., Spohn, H.: Limit distributions for KPZ growth models with spatially homogeneous random initial conditions. Ann. Appl. Probab. **28**, 1573-1603 (2018).
Cited on page 104.

[46] Takeuchi, K. A., Sano, M.: Universal fluctuations of growing interfaces: Evidence in turbulent liquid crystals. Phys. Rev. Lett. **104**, 230601 (2010).
Cited on page 104.

[47] Takeuchi, K. A., Sano, M., Sasamoto, T., Spohn, H.: Growing interfaces uncover universal fluctuations behind scale invariance. Sci. Rep. **1**, 34 (2011).
Cited on page 104.

[48] Takeuchi, K. A.,Sano, M.: Evidence for geometry-dependent universal fluctuations of the Kardar-Parisi-Zhang interfaces in liquid-crystal turbulence. J. Stat. Phys. **147**, 853-890 (2012).
Cited on page 104.

[49] Takeuchi, K. A.: Crossover from growing to stationary interfaces in the Kardar-Parisi-Zhang class. Phys. Rev. Lett. **110**, 210604 (2013).
Cited on page 104.

[50] Fukai, Y. T., Takeuchi, K. A.: Kardar-Parisi-Zhang interfaces with inward growth. Phys. Rev. Lett. **119**, 030602 (2017).
Cited on page 104.

[51] Carrasco, I. S. S., Oliveira, T. J.: Circular Kardar-Parisi-Zhang interfaces evolving out of the plane. arXiv:1810.11292v1 (2018).
Cited on page 104.

[52] Pagnani, A., Parisi, G.: Numerical estimate of the Kardar-Parisi-Zhang universality class in (2+1) dimensions. Phys. Rev. E **92**, 010101(R) (2015).
Cited on pages 104, 117, and 121.

[53] Canet, L., Chaté, H., Delamote, B., Wschebor, N.: Nonperturbative Renormalization Group for the Kardar-Parisi-Zhang Equation. Phys. Rev. Lett. **104**, 150601 (2010).
Cited on page 104.

[54] Kloss, T., Canet, L., Wschebor, N.: Nonperturbative renormalization group for the stationary Kardar-Parisi-Zhang equation: Scaling functions and amplitude ratios in 1+1, 2+1, and 3+1 dimensions. Phys. Rev. E **86**, 051124 (2012).
Cited on page 104.

[55] Kelling, J., Ódor, G., Gemming, S.: Universality of (2+1)-dimensional restricted solid-on-solid models. Phys. Rev. E **94**, 022107 (2016).
Cited on pages 104, 117, and 121.

[56] Halpin-Healy, T.: (2+1)-Dimensional Directed Polymer in a random medium: scaling phenomena and universal distributions. Phys. Rev. Lett. **109**, 170602 (2012).
Cited on pages 104, 117, and 126.

[57] Oliveira, T. J., Alves, S. G., Ferreira, S. C.: Kardar-Parisi-Zhang universality class in (2+1) dimensions: Universal geometry-dependent distributions and finite-time corrections. Phys. Rev. E **87**, 040102(R) (2013).
Cited on pages 104 and 117.

[58] Halpin-Healy, T.: Extremal paths, the stochastic heat equation, and the three-dimensional Kardar-Parisi-Zhang universality class. Phys. Rev. E **88**, 042118 (2013).
Cited on page 104.

[59] Paniago, R., Forrest, E., Chow, P. C., Moss, S. C.: Growth mode and asymptotic smoothing of sputtered Fe/Au multilayers studied by x-ray diffuse scattering. Phys. Rev. B **56**, 13442-13454 (1997).
Cited on page 105.

[60] Ojeda, F., Cuerno, R., Salvarezza, R., Vázquez, L.: Dynamics of rough interfaces in chemical vapor deposition: experiments and a model for silica films. Phys. Rev. Lett. **84**, 3125-3128 (2000).
Cited on pages 105 and 129.

[61] Palasantzas, G., Tsamouras, D., De Hosson, J. Th. M.: Roughening aspects of room temperature vapor deposited oligomer thin films onto Si substrates. Surf. Sci. **507**, 357-361 (2002).
Cited on page 105.

[62] Halpin-Healy, T., Palasantzas, G.: Universal correlators and distributions as experimental signatures of (2 + 1)-dimensional Kardar-Parisi-Zhang growth. Europhys. Lett. **105**, 50001 (2014).
Cited on pages 105, 106, 126, and 127.

[63] Almeida, R. A. L., Ferreira, S. O., Oliveira, T. J., Aarão Reis, F. D. A.: Universal fluctuations in the growth of semiconductor thin films. Phys. Rev. B **89**, 045309 (2014).
Cited on pages 105, 106, 108, 118, 123, and 129.

[64] Orrillo, P. A., Santalla, S. N., Cuerno, R., Vázquez, L., Ribotta, S. B., Gassa, L. M., Mompean, F. J., Salvarezza, R. C., Vela, M. E.: Morphological stabilization and KPZ scaling by electrochemically induced co-deposition of nanostructured NiW alloy films. Sci. Rep. (Nature) **7**, 17997 (2017).
Cited on page 105.

[65] Antal, T., Droz, M., Györgyi, G., Rácz, Z.: Roughness distributions for $1/f^{\alpha}$ signals. Phys. Rev. E **65**, 046140 (2002).
Cited on pages 105 and 123.

[66] Foltin, G., Oerding, K., Rácz, Z., Workman, R. L., Zia, R. K. P.: Width distribution for random-walk interfaces. Phys. Rev. E **50**, R639-R641 (1994).
Cited on page 105.

[67] Plischke, M., Rácz, Z., Zia, R. K. P.: Width distribution of curvature-driven interfaces: A study of universality. Phys. Rev. E **50**, 3589-3593 (1994).
Cited on page 105.

[68] Rácz, Z., Plischke, M.: Width distribution for (2+1)-dimensional growth and deposition processes. Phys. Rev. E **50**, 3530-3537 (1994).
Cited on page 105.

[69] Antal, T., Rácz, Z.: Dynamic scaling of the width distribution in Edwards-Wilkinson type models of interface dynamics. Phys. Rev. E **54**, 2256-2260 (1996).
Cited on pages 105, 106, and 129.

[70] Aarão Reis, F. D. A.: Numerical study of roughness distributions in nonlinear models of interface growth. Phys. Rev. E **72**, 032601 (2005).
Cited on page 124.

[71] Oliveira, T. J., Aarão Reis, F. D. A.: Finite-size effects in roughness distribution scaling. Phys. Rev. E **76**, 061601 (2007).
Cited on page 124.

[72] Paiva, T., Aarão Reis, F. D. A.: Height and roughness distributions in thin films with Kardar–Parisi–Zhang scaling. Surf. Sci. **601**, 419-424 (2007).
Cited on pages 105 and 123.

[73] Aarão Reis, F. D. A.: Scaling of local roughness distributions. J. Stat. Mech. **2015**, P11020 (2015).
Cited on pages 106, 123, and 124.

[74] Carrasco, I. S. S., Oliveira, T. J.: Width and extremal height distributions of fluctuating interfaces with window boundary conditions. Phys. Rev. E **93**, 012801 (2016).
Cited on pages 106, 120, 121, 123, 124, 125, and 129.

[75] Majumdar, S. N., Comtet, A.: Exact maximal height distribution of fluctuating interfaces. Phys. Rev. Lett. **92**, 225501 (2004).
Cited on page 106.

[76] Majumdar, S. N., Comtet, A.: Airy distribution function: From the area under a Brownian excursion to the maximal height of fluctuating interfaces. J. Stat. Phys. **119**, 777-826 (2005).
Cited on page 106.

[77] Schehr, G., Majumdar, S.: Universal asymptotic statistics of maximal relativa height in one-dimensional solid-on-solid models. Phys. Rev. E **73**, 056103 (2006).
Cited on page 106.

[78] Oliveira, T. J., Aarão Reis, F. D. A.: Maximal- and minimal-height distributions of fluctuating interfaces. Phys. Rev. E **77**, 041601 (2008).
Cited on page 106.

[79] Fonthal G., Tirado-Mejía, L., Marín-Hurtado J. I., Ariza-Calderón, H., Mendoza-Alvarez, J. G.: Temperature dependence of the band gap energy of crystalline CdTe. J. Phys. Chem. Solids **61**, 579-583 (2000).
Cited on page 107.

[80] Rakhshani, A. E.: Electrodeposited CdTe–optical properties. J. Appl. Phys. **81**, 7988 (1997).
Cited on page 107.

[81] Wu, S.: High-efficiency polycrystalline CdTe thin-film solar cells. Solar Energy **77**, 803-814 (2004).
Cited on page 107.

[82] Lee, T. D., Ebong, A. U.: A review of thin film solar cell technologies and challenges. Renewable Sustainable Energy Rev. **70**, 1286-1297 (2017).
Cited on page 107.

[83] Rogalski, A.: HgCdTe infrared detector material: history, status and outlook. Rep. Prog. Phys. **68**, 2267 (2005).
Cited on page 107.

[84] , Del Sordo, S., Abbene, L., Caroli, E., Mancini, A. M., Zappettini, A., Ubertini, P.: Progress in the development of CdTe and CdZnTe semiconductor radiation detectors for astrophysical and medical applications. Sensors **9**, 3491-3526 (2009).
Cited on page 107.

[85] Khrypunov, G., Romeo, A., Kurdesau, F., Bätzner, D. L., Zogg, H., Tiwari, A. N.: Recent developments in evaporated CdTe solar cells. Sol. Energy Mater. Sol. Cell **90**, 664-677 (2006).
Cited on page 107.

[86] Romeo, A., Khrypunov, G., Kurdesau, F., Arnold, M., Bätzner, D. L., Zogg, H., Tiwari, A. N.: High-efficiency flexible CdTe solar cells on polymer substrates. Sol. Energy Mater. Sol. Cell **90**, 664-677 (2006).
Cited on page 107.

[87] Triboulet, R., Siffert P.: CdTe and Related Compounds; Physics, Defects, Hetero- and Nano-structures, Crystal Growth, Surfaces and Applications. Part II. Crystal Growth, Surfaces and Applications. Elsevier Science (2010).
Cited on pages 107 and 108.

[88] Zanio, Z.: Semiconductors and Semimetals: Volume 13, Cadmium Telluride, Academic Press, New York (1978).
Cited on pages 107 and 118.

[89] Mohanty, D., Lu, Z., Sun, X., Xiang, Y., Wang, Y., Ghoshal, D., Shi, J., Gao, L., Shi, S., Washington, M., Wang, G.-C., Lu, T.-M., Bhat, I.: Metalorganic vapor phase epitaxy of large size CdTe grains on mica through chemical and van der Waals interactions. Phys. Rev. Mat. **2**, 113402 (2018).
Cited on page 108.

[90] Duffy, N. W., Peter, L. M., Wang, R. L., Lane, D. W., Rogers, K. D.: Electrodeposition and characterisation of CdTe films for solar cell applications. Electrochem. Acta **45**, 3355-3365 (2000).
Cited on page 108.

[91] Sporken, R., Sivananthan, S., Mahavadi, K. K., Monfroy, G., Boukerche, M., Faurie, J. P.: Molecular beam epitaxial growth of CdTe and HgCdTe on Si(100).
Cited on page 108.

[92] Lalev, G. M., Wang, J., Abe, S., Masumoto, K., Isshiki, M.: How wall epitaxy of high-quality CdTe/Si(1 1 1). J. Cryst. Growth. **256**, 20-26 (2003).
Cited on pages 108 and 109.

[93] Gupta, A., Compaan, A. D.: All-sputtered 14% CdS/CdTe thin-film solar cell with ZnO:Al transparent conductin oxide. Appl. Phys. Lett. **85**, 684-686 (2004).
Cited on page 108.

[94] Ferreira, S. O., Ribeiro, I. R. B., Suela, J., Menezes-Sobrinho, I. L., Ferreira, S. C., Alves, S. G.: Effect of temperature on the Hurst and growth exponents of CdTe polycrystalline films. Appl. Phys. Lett. **88**, 244102 (2006).
Cited on page 108.

[95] Mata, A. S., Ferreira, S. C., Ribeiro, I. R. B., Ferreira, S. O.: Anomalous scaling and super-roughness in the growth of CdTe polycrystalline films. Phys. Rev. B **78**, 115305 (2008).
Cited on pages 108 and 129.

[96] Nascimento, F. S., Ferreira, S. C., Ferreira, S. O.: Faceted anomalous scaling in the epitaxial growth of semiconductor films. Europhys. Lett. **94**, 68002 (2011).
Cited on pages 108 and 129.

[97] Kwon, D., Shim, Y., Amar, J. G., Compaan, A. D.: Grain growth, anomalous scaling, and grain boundary grooving in polycrystalline CdTe thin films. J. Appl. Phys. **116**, 183501 (2014).
Cited on pages 108 and 129.

[98] Ohring, M.: Material Science of Thin Films – Deposition and Structure, 2nd. ed., Academic Press, Waltham (2001).
Cited on page 108.

[99] Herman, M. A., Richter, W., Sitter, H.: Epitaxy: Physical principles and technical implementation. Vol. 62. Springer Science & Business Media (2013).
Cited on page 108.

[100] Lalev, G. M., Wang, J., Lim, J.-W., Abe, S., Masumoto, K., Isshiki, M.: Direct growth of CdTe(1 0 0) epilayers on Si(1 0 0) substrate by hot wall epitaxy. Appl. Surf. Sci. **242**, 295-303 (2005).
Cited on pages 108 and 109.

[101] Lopez-Otero, A.: Hot Wall Epitaxy. Thin Solid Films **49**, 3-57 (1978).
Cited on page 109.

[102] Rogalski, A., Piotrowski, J., Gronkowski, J.: A modified hot wall epitaxy technique for the growth of CdTe and $Hg_{1-x}Cd_xTe$ epitaxial layers. Thin Solid Films **191**, 239-245 (1990).
Cited on page 109.

[103] Ribeiro, I. R. B., Suela, J., Oliveira, J. E., Ferreira, S. O., Motisuke, P.: Low temperature growth of high quality CdTe polycrystalline layers. J. Phys. D: Appl. Phys. **40**, 4610-4613 (2007).
Cited on pages 109 and 111.

[104] Lischka, K., Fantner, E. J., Ryan, T. W., Sitter, H.: X-ray rocking curves from (100) and (111) CdTe grown on (100) GaAs by hot wall epitaxy. Appl. Phys. Lett. **55**, 1309-1311 (1989).
Cited on page 109.

[105] Ferreira, S. O., Paiva, E. C., Fontes, G. N., Neves, B. R. A.: Characterization of CdTe quantum dots grown on Si(111) by hot wall epitaxy. J. Appl. Phys. **93**, 1195-1198 (2003).
Cited on page 109.

[106] Suela, J., Ribeiro, I. R. B., Ferreira, S. O., Malachias, A., Fontes, G. N., Montoro, L. A., Ramirez, A. J.: Evolution of crystalline domain size and epitaxial orientation of CdTe/Si(111) quantum dots. J. Appl. Phys. **107**, 064305 (2010).
Cited on page 109.

[107] Binnig, G., Rohrer, H., Gerber, Ch., Weibel, E.: Surfaces studies by Scanning Tunneling Microscopy. Phys. Rev. Lett. **49**, 57-61 (1982).
Cited on page 109.

[108] Binnig, G., Quate, C. F., Gerber, Ch.: Atomic Force Microscope. Phys. Rev. Lett. **56**, 930-933 (1986).
Cited on pages 109 and 110.

[109] Eaton, P., West, P.: Atomic Force Microscopy. Oxford University Press Inc., New York (2010).
Cited on pages 109 and 110.

[110] Martin, Y., Williams, C. C., Wickramasinghe, H. K.: Atomic force microscope-force mapping and profiling on a sub 100-Å scale. J. Appl. Phys. **61**, 4723 (1987).
Cited on page 109.

[111] Goddenhenrich, T., Lemke, H., Hartmann, U., Heiden, C.: Force microscope with capacitive displacement detection. J. Vac. Sci. Tech. **8**, 383-387 (1990).
Cited on page 109.

[112] Tortonese, M., Barrett, R. C., Quate, C. F.: Atomic resolution with an atomic force microscope using piezoresistive detection. Appl. Phys. Lett. **62**, 834-836 (1993).
Cited on page 109.

[113] An atomic-resolution atomic-force microscope implemented using an optical lever. J. Appl. Phys. **65**, 164-167 (1988).
Cited on page 109.

[114] Alexander, S., Hellemans, L., Marti, O., Schneir, J., Elings, V., Hansma, P. K., Longmire, M., Gurley, J.: An atomic-resolution atomic-force microscope implemented using an optical lever. J. Appl. Phys. **65**, 164-167 (1988).
Cited on page 109.

[115] Birkholz, M.: Thin Film Analysis by X-Ray Scattering. John Wiley Sons, Weinheim, Germany (2006).
Cited on page 111.

[116] Becerril, M., Zelaya-Angel, O., Vargas-García, J. R., Ramírez-Bon, R., González-HernaÁndez J.: Effects of Cd vacancies on the electrical properties of polycrystalline CdTe sputtered films. J. Phys. Chem. Solids**62**, 1081-1085 (2001).
Cited on page 111.

[117] Saucedo, E., Corregidor, V., Fornaro, L. Cuña, A., Dieguez, E.: CdTe polycrystalline films for X-ray digital imaging applications. Thin Solif Films **471**, 304-309 (2005).
Cited on page 111.

[118] Wolf, D. E., Villain, J.: Growth with surface diffusion. Europhys. Lett. **13**, 389-394 (1990).
Cited on pages 113 and 115.

[119] Lai, Z.-W., Das Sarma, S.: Kinetic growth with surface relaxation: continuum versus atomistic models. Phys. Rev. Lett. **66**, 2348-2351 (1991).
Cited on pages 113 and 115.

[120] Oliveira, T. J., Aarão Reis, F. D. A.: Effects of grains' features in surface roughness scaling. J. Appl. Phys. **101**, 063507 (2007).
Cited on page 114.

[121] Oliveira, T. J., Aarão Reis, F. D. A.: Roughness exponents and grain shapes. Phys. Rev. E **83**, 041608 (2011).
Cited on pages 114, 115, and 129.

[122] Ferreira, S. O., Paiva, E. C., Fontes, G. N., Neves, B. R. A.: Characterization of CdTe quantum dots grown on Si(111) by hot wall epitaxy. J. Appl. Phys. **93**, 1195-1198 (2003).
Cited on page 115.

[123] Kim, J. M., Kosterlitz, J. M.: Growth in a restricted solid-on-solid model. Phys. Rev. Lett. **89**, 2289-2292 (1989).
Cited on pages 118 and 130.

[124] Kim, Y., Park, D. K., Kim, J. M.: Conserved growth in a restricted solid-on-solid model. J. Phys. A: Math. Gen. **27**, L533-L539 (1994).
Cited on page 118.

[125] Pimpinelli, A., Villain, J.: Physics of crystal growth. Cambridge university press, Cambridge (1999).
Cited on page 118.

[126] Carrasco, I. S. S., Takeuchi, K. A., Ferreira, S. C., Oliveira, T. J.: Interface fluctuations for deposition on enlarging flat substrates. New J. Phys. **16**, 123057 (2014).
Cited on pages 126 and 127.

[127] Assis, T. A., Aarão Reis, F. D. A.: Smoothening in thin-film deposition on rough substrates. Phys. Rev. E **92**, 052405 (2015).
Cited on page 128.

[128] Majaniemi96 S., Ala-Nissila, T., Krug, J.: Kinetic roughening of surfaces: Derivation, solution, and application of linear growth equations. Phys. Rev. B **53**, 8071 (1996).
Cited on page 128.

[129] Cuerno, R., Castro, M.: Transients due to Instabilities Hinder Kardar-Parisi-Zhang Scaling: A Unified Derivation for Surface Growth by Electrochemical and Chemical Vapor Deposition. Phys. Rev. Lett. **87**, 236103 (2001).
Cited on page 129.

[130] Bae, J., Lee, I. J.: A bifractal nature of reticular patterns induced by oxygen plasma on polymer films. Sci. Rep. (Nature) **5**, 10125 (2015).
Cited on page 130.

[131] Premkumar, P. A., Starostin, S. A., Vries, H., Creatore, M., Koenraad, P. M., MacDonald, W. A., Sanden, M. C. M.: Surface Dynamics of SiO_2-like films on polymers grown by DBD Assisted CVD at atmospheric pressure. Plasma Process. Polym. **9**, 1194-1207 (2012).
Cited on page 130.

[132] Drotar, J. T., Zhao, Y.-P., Lu, T.-M., Wang, G.-C.: Surface roughening in shadowing growth and etching in 2+1 dimensions. Phys. Rev. B **62**, 2118 (2000).
Cited on page 130.

5

CONCLUSIONS AND PERSPECTIVES

In this series of works, we experimentally studied scaling-invariant and universal behaviours emerging in macroscopic, nonequilibrium systems. We focused on two instances of nonequilibrium dynamics: the dissipative relaxation of two-dimensional systems towards an equilibrium state via domain coarsening, and the far-from-equilibrium growth of (2+1)-dimensional interfaces. The former process was addressed by the electrically-triggered coarsening of twist nematic liquid crystals (TNLC), while the interface dynamics was focused on the growth of polycrystalline (CdTe) films. We show that universal aspects arise in both of the studied systems. As expected, these aspects are accompanied by system-dependent complexities not accounted for by idealised theories; direct examples are the violation of the $\mathbb{Z}_2$-symmetry in TNLC systems and the substrate-induced effects in the growth of CdTe surfaces. Conversely, these additional ingredients reveal nontrivial aspects of universality and expand our knowledge on the robustness of scaling-invariant and universal behaviours. In the following, we summarise the main results of each work, along with their implications and prospects. Symbols used along each work are specified at the end of its respective Chapter.

Chapter 2: Electrically-triggered coarsening in twisted nematic liquid crystals

In Chapter 2, we designed a suitable experimental system to study coarsening dynamics in order to overcome the drawbacks of previous studies. By performing an instantaneous quench between the nematic-turbulent state and an equilibrium state of TNLC, we could obtain accurate evidence for behaviour in the model A universality class. We experimentally substantiate several aspects for this class for the first time, such as the Bray-Humayun amplitude and the universal morphology (fractal dimension and related scaling functions) of persistent clusters. The accuracy of results allows us to reinforce the universality of the dynamical exponent, and to obtain a value for the persistent exponent different from that in the diffusion class. The asymmetry between twist phases, not taken into account in idealised theories, unveils that even in such a biased dynamics most of the universal quantities obtained from the symmetric case are preserved. Both the Ohta-Jasnow-Kawasi model and the theory of unstable growth describes the functional form of the two-point spatial correlator. However, the two-point time statistics is not clear. Although the results suggest an agreement with the OJK model, we are not at the position to state whether this agreement is a unique property of the experiment or whether it is an effect of the $\mathbb{Z}_2$-symmetry violation. In summary, this work provides compelling and accurate evidence for the model A universality class, despite the presence of a biased dynamics. The experimental setup was built to play a relevant role to the studies of two-dimensional coarsening dynamics: unlike previous studies, the electrical quench is instantaneous; morevoer, it allows one to study different types of relaxations by performing the quench towards nonequilibrium electro-convective states.

Chapter 3: Critical percolation in two-dimensional coarsening

In Chapter 3, we reanalysed the model A coarsening dynamics of TNLC crystals from a morphological point of view. With the aim to investigate the relation between model A and critical percolation (CP) recently observed in simulations, we characterised the statistics of domains and hull areas. Our results demonstrate the validation of a CP-model-A theory, well represented by the Arenzon *et at.* [1] formula. The Fisher exponent for number density of hull area and the fractal dimension of the largest TNLC domain agree with those known for the CP universality class in $d = 2$. The hypothesis of coarsening as CP model on an inflating lattice is experimentally substantiated. Finally, we empirically measure a new percolation-related dynamical exponent, here $z_p = 0.45(5)$, for the TNLC dynamics. This result implies that the fundamental scaling hypothesis of two-dimensional (non-conserved $\&$ scalar) coarsening theories is incomplete. The scaling theory shall be modified to account for such a percolation-related length scale. Notice that is somewhat non-trivial, however, how the TNLC system self-tunes to a CP state even in the asymmetric dynamics. In summary, model A and CP universality classes rule the statistics of intra- and inter-domain scales. Further CP statistics recently uncov-

ered in the context of phase-ordering kinetic could be experimentally investigated in our system.

Chapter 4: Surface fluctuations of vapour-deposited CdTe thin films

We investigated height fluctuations of polycrystalline (CdTe) films vapour-deposited on polyimide substrates at low deposition temperature ($T = 150\,^{\circ}\mathrm{C}$). Our study reveals that, along with the growth process, surface fluctuations display three dynamical regimes: a submonolayer-related regime, a transient Pseudo-steady state (PSS), and a regime of Kardar-Parisi-Zhang (KPZ) dynamics. We briefly describe the main features for each regime below.

(Submonolayer) Occurs for deposition times $t \lesssim 25$ min. Surface width $W(t)$ behaves in a non-monotonic manner; it abruptly jumps from $W \approx 6$ nm at $t = 0$ min to $W \approx 28$ nm at $t = 7.5$ min, and then it smooths out to $W \approx 14$ nm at $t = 25$ min. We *suggest* that the first $W(t)$ increasing is triggered by the Volmer-Weber nucleation mode of CdTe islands onto the substrate, while the smoothening-dominated regime stems from the sequential formation of a (complete) CdTe layer that fully covers the substrate surface. Images of atomic force microscopy show that the coverage transition occurs within the period of time mentioned above.

(PSS) Occurs for 25 min $\lesssim t \lesssim$ 300 min. Both height fluctuations ($W(t) \approx 14$ nm) and spatial correlations ($\xi(t) \approx 100$ nm) are constant. These features resemble those found in the steady state of growing interfaces, where $W(t) \sim L^{\alpha}$ and $\xi \sim L$ are saturated. However, since this is not the case for the experimental regime, we christen it as a Pseudo-steady state. Scaling hypothesis implies that the PSS is characterized by $\beta = 0$ and $1/z = 0$. Comparison with our previous work on CdTe-on-Si(001) growth, where only Random-Deposition (RD) scaling takes place, reveals PSS as a substrate-induced regime in our case. X-ray diffraction measurements show that PSS regime coincides with the period in which non-(111)-oriented grains at the interface are replaced by (111)-oriented crystallites. We have not characterised the microscopic mechanisms leading to PSS, but an one-dimensional model predicts that relaxations at grain boundaries are enough to generate the PSS.

(KPZ) Occurs after PSS, for $t \gtrsim 300$ min. KPZ statistics arise in the *inter-grain* scale of a surface made of (111)-oriented CdTe grains. Evidence of KPZ behaviour is obtained by an exhaustive series of measurements that include $i)$ scaling exponents (α, β, z), distributions of $ii)$ height, $iii)$ local square-width, of $iv)$ the local maximal relative height, and the $v)$ two-point spatial height correlator. All these quantities provide evidence for a universal KPZ statistics. KPZ scaling theories were employed to extract the excess of the velocity of a CdTe surface, $\lambda \sim 10^{-2}$ nm/s, in the same order of the deposition rate.

The PSS-KPZ crossover is impressively long. KPZ scaling was observed only after the deposition of $\sim 10^3$ CdTe monolayers, which corresponded to 4 days of continuous deposition. This fact leads us to inquire whether the concepts of universality could have some practical meaning for the growth of thin films. In this regard, transients regimes such as the PSS found seem to be more meaningful. PSS-to-KPZ dynamics is itself nontrivial since it cannot be described by the KPZ equation, which only shows either RD-KPZ or EW-KPZ crossovers. Moreover, it is also nontrivial, and somewhat surprisingly, that PSS seems to appear in different experimental systems [2, 3] and discrete models with local [4] and nonlocal interactions [5], which do have relation with KPZ. These observations may suggest PSS as a general type of regime of interface growth.

It is intriguing why KPZ arises at inter-grain scales of polycrystalline systems [6–8]. It remains an open question to conceive a grain growth model displaying inter-grain KPZ fluctuations. The model could shed light on the essential ingredients leading to KPZ in the vast realm of polycrystalline films. Since experimental evidence of (2+1)-dimensional KPZ is rather scarce, CdTe surfaces are a suitable system to further exploration in the context of statistical physics. For instance, simulations of growth models predict that iso-height lines in KPZ growth are conformally invariant, according to the Schramm-Löwner evolution (SLE) theory [9]. Would be conformal invariance preserved at the experimental level? Another interesting perspective is to inquire about the (universal) *coarsening* dynamics of CdTe grains and whether and how this coarsening is related to the KPZ fluctuations. We are currently employing Electron Backscattering Diffraction techniques to image the evolution of a mosaic of grains distinguished by crystallographic orientations.

BIBLIOGRAPHY

[1] Arenzon, J. J., Bray, A. J., Cugliandolo, L. F., Sicilia, A.: Exact results for curvature-driven coarsening in two dimensions. Phys. Rev. Lett. **98**, 145701 (2007).
Cited on page 147.

[2] Bae, J., Lee, I. J.: A bifractal nature of reticular patterns induced by oxygen plasma on polymer films. Sci. Rep. (Nature) **5**, 10125 (2015).
Cited on page 149.

[3] Premkumar, P. A., Starostin, S. A., Vries, H., Creatore, M., Koenraad, P. M., MacDonald, W. A., Sanden, M. C. M.: Surface Dynamics of SiO_2-like films on polymers grown by DBD Assisted CVD at atmospheric pressure. Plasma Process. Polym. **9**, 1194-1207 (2012).
Cited on page 149.

[4] Oliveira, T. J. Private communication.
Cited on page 149.

[5] Drotar, J. T., Zhao, Y.-P., Lu, T.-M., Wang, G.-C.: Surface roughening in shadowing growth and etching in 2+1 dimensions. Phys. Rev. B **62**, 2118 (2000).
Cited on page 149.

[6] Almeida, R. A. L., Ferreira, S. O., Ribeiro, I. R. B., Oliveira, T. J.: Temperature effect on (2+1)-experimental Kardar-Parisi-Zhang growth. Europhys. Lett. **109**, 46003 (2015).
Cited on page 149.

[7] Almeida, R. A. L., Ferreira, S. O., Oliveira, T. J., Aarão Reis, F. D. A.: Universal fluctuations in the growth of semiconductor thin films. Phys. Rev. B **89**, 045309 (2014).
Cited on page 149.

[8] Almeida, R. A. L., Ferreira, S. O., Ferraz, I., Oliveira, T. J.: Initial pseudo-steady state & asymptotic KPZ universality in semiconductor on polymer deposition. Sci. Rep. (Nature) **7**, 3773 (2017).
Cited on page 149.

[9] Saberi, A. A., Niry, M. D., Fazeli, S. M., Tabar, M. R. R., Rouhani, S.: Conformal invariance of isoheight lines in two-dimensional Kardar-Parisi-Zhang surface. Phys. Rev. E **77**, 051607 (2008).
Cited on page 149.